
Theory of Large-Momentum-Transfer Atom Interferometry in the Quasi-Bragg Regime

Von der QUEST-Leibniz-Forschungsschule
der Gottfried Wilhelm Leibniz Universität Hannover
zur Erlangung des Grades

Doktor der Naturwissenschaften
Dr. rer. nat.

genehmigte Dissertation von

M. Sc. Jan-Niclas Kirsten-Siemß
geboren am 14. Dezember 1991 in Lübeck

Referent: Prof. Dr. Klemens Hammerer
Institut für Theoretische Physik
Leibniz Universität Hannover

Korreferent: Prof. Dr. Ernst M. Rasel
Institut für Quantenoptik
Leibniz Universität Hannover

Korreferent: Prof. Dr. Enno Giese
Institut für Angewandte Physik
Technische Universität Darmstadt

Tag der Promotion: 24.03.2023

Abstract

Atom interferometers are versatile instruments offering great accuracy and stability, suitable for fundamental science and practical applications. In usual setups, the sensitivity of the sensor to inertial forces including gravitational signals scales with the spatial separation of two atomic wave packets. Consequently, increasing this separation using large momentum transfer (LMT) promises to enhance the performance of today's devices by orders of magnitude. To date, despite several proof-of-principle experiments, only a handful of Bragg diffraction-based LMT implementations have yielded actual metrological gain. Hence, in this thesis we investigate the current sensitivity limits of Bragg interferometers resulting from the insufficient control of the atom-light interaction in two parts.

In the first part we develop an analytical theory for Bragg pulses based on the pivotal insight that the elastic scattering of atoms from time-dependent optical lattices can be accurately described using the adiabatic theorem. We show that efficient Bragg operations can be realized with any smooth pulse shape, suggesting that adiabaticity may be a necessary requirement. Moreover, we find that high-quality Gaussian pulses are exclusively adiabatic. Our model incorporates corrections to the adiabatic evolution due to Landau-Zener processes, as well as the effects of a finite atomic velocity distribution. We verify its accuracy by comparison with exact numerical descriptions of Gaussian pulses transferring four, six, eight, and ten photon recoils ($\hbar k$). We then extend our formalism to study the rich phenomenology of Bragg interferometers, which is quite different from that of a standard two-mode interferometer. We confirm the accuracy of our analysis through extensive numerical simulations for the example of a Mach-Zehnder interferometer. In particular, we determine the atomic projection noise limit of the interferometer and provide the means to saturate it. Furthermore, we evaluate the systematic errors intrinsic to the Bragg diffraction process, commonly known as the diffraction phase. We demonstrate their suppression by two orders of magnitude down to a few μrad using appropriate pulse parameters.

In the second part of this thesis, we present twin-lattice interferometry based on symmetric Bragg diffraction and Bloch oscillations combined with slowly expanding Bose-Einstein condensates. This method promises to address many of the constraints of previous LMT implementations enabling unprecedented momentum separations of up to $408 \hbar k$ in the QUANTUS-1 experiment. We model the experimental contrast decay with increasing momentum transfer and conclude that in particular the interaction of the atomic ensemble with a distorted laser beam leads to spatial decoherence and to contrast loss. The results presented in this thesis indicate that technical imperfections currently limit the scalability of the experiment and our theoretical analysis will be highly instrumental in the design of future sensors with momentum separations of up to one thousand photon recoils or more.

Keywords: Atom interferometry, Bragg diffraction, Large momentum transfer, Adiabatic theorem, Diffraction phase, Twin-lattice interferometry

Zusammenfassung

Atominterferometer sind vielseitige Instrumente mit hoher Genauigkeit und Stabilität, die sich sowohl für die Grundlagenforschung als auch für praktische Anwendungen eignen. In typischen Aufbauten skaliert die Sensitivität dieser Sensoren gegenüber Trägheitskräften, einschließlich Gravitationssignalen, mit dem räumlichen Abstand zwischen zwei atomaren Wellenpaketen. Folglich verspricht die Vergrößerung dieser Separation mittels großer Impulsüberträge erhebliche Leistungssteigerungen. Allerdings konnten bisher nur wenige auf Bragg-Streuung basierende Experimente einen messtechnischen Nutzen nachweisen. Gegenstand dieser Arbeit sind daher die derzeitigen Limitierungen von Bragg-Interferometern, die aus der Atom-Licht-Wechselwirkung resultieren.

Basierend auf dem adiabatischen Theorem entwickeln wir zunächst eine Beschreibung der elastischen Bragg-Streuung an zeitabhängigen optischen Gittern. Unsere Untersuchung legt nahe, dass Adiabaticität für stetig-differenzierbare Pulsformen eine notwendige Bedingung darstellt, und wir zeigen, dass dies für Gauß-Pulse der Fall ist. Unser Modell berücksichtigt nichtadiabatische Korrekturen aufgrund von Landau-Zener-Prozessen sowie die Auswirkungen einer endlichen atomaren Geschwindigkeitsverteilung und zeigt große Übereinstimmung mit exakten numerischen Lösungen für Gauß-Pulse, die vier, sechs, acht und zehn Photonenrückstöße ($\hbar k$) übertragen. Anschließend untersuchen wir die Phänomenologie von Bragg-Interferometern, die sich deutlich von der eines Zweimoden-Interferometers unterscheidet. Wir bestätigen die Genauigkeit unserer Analyse durch umfangreiche numerische Simulationen am Beispiel eines Mach-Zehnder-Interferometers. Insbesondere quantifizieren wir das atomare Projektionsrauschen des Interferometers und zeigen, wie diese fundamentale Schranke erreicht werden kann. Außerdem evaluieren wir die systematischen Fehler, die aus der Bragg-Streuung resultieren und allgemein als Streuphase ("diffraction phase") bekannt sind. Wir demonstrieren deren Unterdrückung um zwei Größenordnungen bis zu einigen μrad mittels geeigneter Pulsparameter.

Im zweiten Teil der Arbeit stellen wir das Prinzip der Doppelgitter-Interferometrie vor, die auf symmetrischer Bragg-Beugung und Bloch-Oszillationen in Kombination mit kollimierten Bose-Einstein-Kondensaten basiert. Dies verspricht, viele der Einschränkungen bisheriger LMT-Implementierungen zu überwinden und ermöglicht im QUANTUS-1-Experiment Impulsseparationen von bis zu $408 \hbar k$. Unsere Analyse zeigt, dass insbesondere die Wechselwirkung des atomaren Ensembles mit einem gestörten Lichtfeld zu räumlicher Dekohärenz und zu Kontrastverlust führt. Daher liegt es nahe, dass technische Unzulänglichkeiten derzeit die Skalierbarkeit des Experiments einschränken. In Zukunft wird die hier vorgestellte theoretische Analyse einen entscheidenden Beitrag zur Entwicklung neuartiger Sensoren mit Impulsüberträgen von bis zu $1000 \hbar k$ oder mehr leisten.

Schlagwörter: Atominterferometrie, Bragg-Streuung, Großimpulsübertragung, Adiabatisches Theorem, Streuphase, Doppelgitter-Interferometrie

Author contributions

Elements of this thesis have appeared elsewhere as peer-reviewed publications or on preprint servers. Here, I summarize my personal contributions to these publications. Please note that the contributions of other authors without my involvement are not explicitly listed. In the order of the corresponding chapters, these are:

Chapter 2:

J.-N. Siemß, F. Fitzek, S. Abend, E. M. Rasel, N. Gaaloul, and K. Hammerer, *Analytic theory for Bragg atom interferometry based on the adiabatic theorem*, *Phys. Rev. A*, **102(3):033709** (2020).

Author contribution: **Jan-Niclas Kirsten-Siemß (JNKS)** and KH developed the analytical scattering matrix formalism for Bragg diffraction. The comparison of the analytical results with exact numerical calculations was performed by **JNKS** with input from FF, NG, and KH. **JNKS** and KH wrote the manuscript with contributions from all authors.

Chapter 3:

J.-N. Kirsten-Siemß, F. Fitzek, C. Schubert, E. M. Rasel, N. Gaaloul, and K. Hammerer, *Large-Momentum-Transfer Atom Interferometers with μ rad-Accuracy Using Bragg Diffraction*, *Phys. Rev. Lett.* **131**, 033602 (2023).

Author contribution: **JNKS** extended the analytical description of single Bragg pulses to multistate Bragg atom interferometry sequences. **JNKS** and KH embedded the results of this approach in the context of phase estimation theory, obtaining contributions from FF, NG, and EMR. **JNKS** has carried out the calculations for the example of the Mach-Zehnder interferometer using numerical simulations provided by FF. **JNKS** was assisted in the interpretation of the results by FF, EMR, NG, and KH. **JNKS** wrote the manuscript with contributions from all authors.

Ruben Bösche, *Theory of atom interferometers in the Bragg regime*, Master thesis, October 2022, Leibniz Universität Hannover

Author contribution: **JNKS** contributed to the formulation of the tensorial representation of the Bragg scattering formalism and assisted in the supervision of the above Master thesis.

Chapter 4:

M. Gebbe, **J.-N. Siemß**, et al., *Twin-lattice atom interferometry*, *Nature Communications*, **12(1):2544** (2021).

Author contribution: **JNKS** developed the theoretical model for the contrast loss with input from NG. **JNKS** together with MG, SA, and EMR prepared the manuscript with contributions from all authors.

Acknowledgements

Here I am now. Not quite at the end of everything, but at the end of my PhD in theoretical physics. Admittedly, my journey was probably not as daunting as Frodo and Sam's conquest of Mount Doom, but it was definitely worth it. When I started my physics studies at Leibniz Universität Hannover (LUH), I was not sure what to expect, except that it would be a real challenge. Was it hard? Indeed. Did it push me to my limits? Absolutely. Was I so overwhelmed at times that I seriously doubted I could keep going? More often than I would like to admit. What I certainly did not foresee at the beginning is how collaborative the study of physics and later life as a physicist would be. What I will remember most from my time are all the inspiring and wonderful people I met along the way. These are people with whom I have been able to share my struggles, but who also share my fascination with solving the big and small quests on my way to becoming a PhD. In the future, if someone asks me, what is the best thing about studying physics, this is what I will tell them.

I would like to take this opportunity to thank you all for our time together and for all the support you have given me over the past 12 years:

The first group of people I would like to thank are Klemens Hammerer, Ernst M. Rasel, and Enno Giese, who kindly agreed to review my dissertation, and Benno Willke, as chair of my PhD committee. It is clear that I would never have come this far without my supervisors, who showed me the way many times, and therefore they deserve a great deal of thanks. First of all, there is Klemens Hammerer. Not only did you take me on as a new PhD student, but you were also open to exploring the field of atom interferometry together. Naturally, the path that has led us to today has been fraught with many twists and turns, but that has meant that it has always been exciting, and I am very happy and proud seeing where it has taken us. Whenever I felt overwhelmed with seemingly insurmountable physics problems, your door was always open and you had one or another physics trick up your sleeve. In addition, I have always found the supervision of students by you and the work in your working group, the AG Hammerer, very enriching. So thank you for letting me be a part of it and for your many years of support. On that note, I thank Julian and Ruben for letting me share my passion for Bragg atom interferometry with them.

It is the people who make the AG Hammerer special. Many thanks to former members Ondrej, Jonas, Jannis and Marius, with whom I shared an office for a while, and to Alexander, Corentin and Sahand. I have to admit, before joining you guys I would never have thought that theoretical physicists could be so crafty and that manufacturing one-of-a-kind PhD hats can be so much fun. And I very much enjoyed sharing this passion with the new generation of group members: Maja, Kasper, Ivan, Julian, Michi and Timm. And of course, there are Florian, my Bragg-Bloch-Buddy, and last but not least Victor. Dear Victor, I will eternally grateful that we went through the hardship of writing our theses together. Thank you for that and also thank you for being the best Dungeon Master I ever had! I enjoy

exploring the DnD universe together with Maja, Marius, Ivan and Kasper immensely.

My journey ends as a PhD of the AG Hammerer in the Institute of Theoretical Physics, but this is not where it began. In fact, I started studying math and physics (on my way to becoming a teacher) at LUH. Although it was clear from the beginning that teaching school children would never be my calling, I was lucky enough to meet some very passionate comrades in Anna, Jeannette, Felix and especially Stefan. You guys helped me through those early days, thank you for that! Also, after I fully focused on my bachelor in physics, I had the opportunity to make more friends. Thanks to Fabian, Steffi, Frederik, Friso, Lea, Pia and Philip for the many nice moments in and out of the university. During my master studies I then met Max, Jannis and Sabrina, who also turned out to be great friends and, in Max's case, bike buddies!

However, my first scientific projects took place in the group of Ernst M. Rasel and I stayed with you at the Institute of Quantum Optics (IQO) until the end of my master's. Dear Ernst, I am grateful for all the opportunities you and your group gave me during this time. My first steps doing experiments supervised by Felix Kösel and Sebastian Bode made me the theorist I am today. I particularly enjoyed the scientific and personal collaboration with the QUANTUS team, especially with Christian Schubert, Holger Ahlers, Sven Abend, Martina Gebbe and Matthias Gersemann. Despite the fact that providing theoretical analysis for a (magnificent) experiment is probably the biggest challenge I have faced during my PhD, I think that our results speak for themselves. I also want to thank Kulli and Torben for the brief but intense periods that we shared an office together. Es war mir immer ein Kirschblütenfest!

I consider myself lucky because I was also a founding member of a third group, and I have Naceur Gaaloul to thank for that. Naceur, you brought me into the fold, convinced me that there was a place for me in theoretical physics, and invited me into your "shadow group" which became the "T-SQUAD". You have gathered a group of exceptional young scientists around you and I cannot wait to see where Annie, Christian, Gabriel, Gina, Florian, Matty, Rui, Stefan, Timothé, Victor and your other members will go next. But it is clear that OGs Holger, Robin, Sina and Florian will always have a special place in my heart!

Engaging with the QUANTUS collaboration and my membership of the SFB 1227 (DQ-mat) also offered further exciting opportunities for discussions and collaborations, even outside the University of Hannover. In particular, I would like to thank Patrick Boegel, Matthias Meister, Maxim A. Efremov and Wolfgang P. Schleich from the University of Ulm for working together and sharing your insights with me.

Finally, I mustn't forget the people who work tirelessly in the background but are the heart and soul here in Hannover. Thank you, Fr. Goeldner, for our interactions and your efforts during my time at the IQO! Thank you, Birgit Gemmeke, for always being there for me, when I needed advice and doing a wonderful job making our lives as PhD students so much easier! Finally, I would also like to thank Birgit Ohlendorf for taking my hand navigating the treacherous waters of handing in my PhD thesis.

Analogous to my years as a graduate student, this dissertation is not just my work, but a collaborative effort. I am very grateful to all the people who gave me feedback during the

writing process: Thank you, Klemens, Naceur, Julian, Matty, Matthias, Michi and Jens! Special kudos to Florian, Stefan and Gabriel for your passionate comments! I also have to acknowledge the rigor of Christian, Victor, and my father, Rex, who combed through my pages and weeded out every mistake. And finally, thank you, Sina, for sharing some of your postdoc magic with me and holding my hand until the end! I won't forget this!

During my PhD time I could always complain and decompress with my old friends David and Niko. Thank you for keeping in touch and having an open ear for me over the last twelve years (!). I would also like to thank Jens, my siblings and my parents, Editha and Rex, for supporting me so energetically after I finished school and started my life here in Hannover.

And finally to you, Julia, my best friend, my partner, my wife, my life. You brought me to Hanover so I could do all these things and meet all these wonderful people. I will be forever grateful for your support during these sometimes challenging times and I look forward to our next adventures!

Contents

| | | |
|----------|--|-----------|
| 1 | Introduction | 1 |
| 1.1 | Example of an Inertial Matter-wave Sensor | 3 |
| 1.1.1 | Sensitivity to Linear Acceleration | 4 |
| 1.1.2 | Cold Atom Sources | 5 |
| 1.1.3 | Large Separation Times T | 6 |
| 1.1.4 | Large Momentum Transfer (LMT) | 7 |
| 1.1.5 | Accuracy Limits: Diffraction Phases | 8 |
| 1.2 | Thesis Outline | 9 |
| 2 | Theory for Bragg Atom Interferometry Based on the Adiabatic Theorem | 11 |
| 2.1 | Motivation and Research Problem | 11 |
| 2.2 | Review: Theory of Bragg Diffraction from Light Crystals | 12 |
| 2.2.1 | Bragg Hamiltonian | 13 |
| 2.2.2 | Diabatic Descriptions of Bragg Diffraction | 16 |
| 2.2.3 | Bloch-band Picture | 19 |
| 2.2.4 | Adiabatic Time Evolution | 21 |
| 2.3 | Bragg Diffraction as a Scattering Problem | 22 |
| 2.3.1 | Hamiltonian in the Momentum Basis | 23 |
| 2.3.2 | Hamiltonian in the Basis of Symmetric and Antisymmetric States | 25 |
| 2.3.3 | General Structure of the Bragg Scattering Matrix | 28 |
| 2.3.4 | Scattering Matrix for Adiabatic Bragg Pulses | 31 |
| 2.4 | Nonadiabatic Corrections and Doppler Detuning | 33 |
| 2.4.1 | Nonadiabatic Corrections: Landau-Zener (LZ) Phases | 34 |
| 2.4.2 | Bragg Pulse Area Condition | 39 |
| 2.4.3 | Nonadiabatic Corrections: LZ Losses | 39 |
| 2.4.4 | Doppler Detuning | 41 |
| 2.5 | Two-mode Bragg Scattering Matrix | 42 |
| 2.6 | Comparison to Numerical Simulations | 44 |
| 2.6.1 | Quality of Bragg Operations | 45 |
| 2.6.2 | Bragg Pulse Area Condition | 48 |
| 2.6.3 | Bragg Beam Splitters and Mirrors | 50 |
| 2.7 | Four-mode Bragg Scattering Matrix | 54 |

| | | |
|----------|--|------------|
| 2.7.1 | LZ Loss Parameters: γ, Γ | 58 |
| 2.7.2 | Phases | 60 |
| 2.8 | Conclusion and Comparison to Existing Theory | 62 |
| 2.8.1 | Diabatic Dynamics Described by an Effective Hamiltonian | 64 |
| 2.8.2 | Bloch-band Picture | 65 |
| 3 | LMT Bragg Atom Interferometers with μrad-Accuracy | 69 |
| 3.1 | Motivation and Research Question | 69 |
| 3.2 | Review: Concepts of Phase Estimation | 73 |
| 3.2.1 | Generalized Measurements | 73 |
| 3.2.2 | Cramér-Rao Bound (CRB) | 76 |
| 3.2.3 | Quantum Cramér-Rao Bound (QCRB) | 76 |
| 3.3 | Scattering Matrix for Bragg Interferometers | 77 |
| 3.4 | Mach-Zehnder (MZ) interferometer | 79 |
| 3.4.1 | MZ Scattering Matrix | 79 |
| 3.4.2 | Atom Number Signals | 82 |
| 3.4.3 | Tensorial Signal Calculus | 87 |
| 3.4.4 | Pulse Parameters for Fifth-order Bragg Diffraction | 90 |
| 3.5 | Analytical Signals of Bragg Atom Interferometers | 92 |
| 3.5.1 | Interferometer Including Parasitic Paths | 93 |
| 3.5.2 | Interferometer with Suppressed Parasitic Paths | 95 |
| 3.6 | Systematic Error: The Diffraction Phase | 96 |
| 3.6.1 | Phase Offset γ/\mathbf{n} | 97 |
| 3.6.2 | Diffraction Phases for Fifth-order Bragg Diffraction | 98 |
| 3.7 | Statistical Uncertainty: Phase Sensitivity | 103 |
| 3.7.1 | Sensitivity Bounds for Uncorrelated Particles | 104 |
| 3.7.2 | Statistical Uncertainty $\Delta\phi^{\text{est}}$ | 106 |
| 3.7.3 | Phase Uncertainty for Fifth-order Bragg Diffraction | 108 |
| 3.8 | Conclusion and Outlook | 111 |
| 4 | Atom Interferometry in a Twin Lattice | 113 |
| 4.1 | Motivation | 113 |
| 4.2 | Bose-Einstein Condensates | 116 |
| 4.2.1 | Gross-Pitaevskii Equation (GPE) | 118 |
| 4.2.2 | Effective One-dimensional GPE | 119 |
| 4.2.3 | Thomas-Fermi Approximation | 121 |
| 4.3 | Twin-lattice Beam Splitting | 122 |
| 4.3.1 | Ideal Twin-lattice Potential | 122 |
| 4.3.2 | Brief Review of Double Bragg Diffraction (DBD) | 124 |

| | | |
|----------|--|------------|
| 4.3.3 | Coherent Acceleration via Bloch Oscillations (BO) | 127 |
| 4.3.4 | Lattice Transport Fidelity | 133 |
| 4.4 | Realization in the QUANTUS-1 experiment | 136 |
| 4.4.1 | Twin-lattice Potential | 137 |
| 4.4.2 | Beam Splitter Fidelity | 139 |
| 4.4.3 | Twin-lattice Interferometer | 142 |
| 4.4.4 | Experimental Contrast Analysis | 146 |
| 4.5 | Contrast Model: Atom Loss | 148 |
| 4.6 | Contrast Model: Light Field | 151 |
| 4.6.1 | Single Particle Contrast | 152 |
| 4.6.2 | Contrast Loss in Open Interferometers | 154 |
| 4.6.3 | Contrast Loss due to Dephasing | 155 |
| 4.6.4 | Distorted Light-field Model | 158 |
| 4.7 | Combined Contrast Model and Conclusions | 161 |
| 5 | Summarizing Statements and Outlook | 167 |
| 5.1 | Bragg Diffraction from Pulsed Optical Lattices | 167 |
| 5.2 | Large-momentum-transfer Bragg Interferometry | 169 |
| 5.3 | Scalability of Twin-lattice Atom Interferometers | 171 |
| 5.4 | Future Prospects | 172 |
| A | Appendices for Chapter 2 | 177 |
| A.1 | Analytical Landau-Zener (LZ) Transition Amplitudes | 177 |
| A.2 | Doppler Detuning | 178 |
| A.3 | Hilbert Space Dimensionality and Numerical Integration | 180 |
| A.4 | Four-mode Bragg Scattering Matrix ($n = 2$) | 180 |
| B | Appendix for Chapter 3 | 183 |
| | List of Figures | 185 |
| | List of Tables | 187 |
| | Bibliography | 189 |

Abbreviations and Acronyms

| | |
|----------------|---|
| AC | Alternating current |
| BEC | Bose-Einstein condensate |
| BO | Bloch oscillations |
| CRB | Cramér-Rao Bound |
| DBD | Double Bragg diffraction |
| DKC | Delta-kick collimation |
| DLR | Deutsches Zentrum für Luft- und Raumfahrt |
| LMT | Large momentum transfer |
| MZ | Mach-Zehnder |
| TOF | Time of flight |
| QCRB | Quantum Cramér-Rao Bound |
| QUANTUS | Quantengase unter Schwerelosigkeit |
| ZARM | Zentrum für angewandte Raumfahrttechnologien und Mikrogravitation |
| H.c. | Hermitian conjugate |

1

Introduction

In 1923 *L. de Broglie* [1], formulated the foundational principle of matter-wave interferometry: A particle with mass M moving with velocity v can be described as a wave with an associated wavelength, $\lambda_{\text{dB}} = h/Mv$, that is proportional to the Planck constant h . Until this seminal discovery, the prevailing view was that wave-like properties could be associated with light but not matter. This was based on classical optics, where beam splitters and mirrors were used to separate and recombine light beams in interferometry experiments. The argument of de Broglie to apply this concept to matter waves in the first half of the 20th century was therefore nothing less than a revolution. Following the electron diffraction experiments of *C. Davisson* and *L. H. Germer* [2], as well as *G. P. Thomson* [3], to date matter-wave interferometry has been performed with electrons, neutrons [4,5], atoms [6–9], and molecules [10, 11].

Although delocalization and interference of massive particles are hallmarks of their quantum wave nature, they remain seemingly strange concepts that do not match observations in our mostly classical everyday life. For the wave properties of a particle to play a significant role, its wavelength λ_{dB} must reach a considerable size. This requires the particle to be slowed down, since $\lambda_{\text{dB}} \propto v^{-1}$ scales inversely proportional to its velocity. At room temperature, the thermal velocity of the particles, e.g., as part of an atomic cloud is in the order of m/s, translating into de Broglie wavelengths of a few tens of picometers, so that it is hardly possible to detect signs of the wave nature of matter [12].

In this context, the advent of atom optics began with the invention of the laser in the 1960s [13] and subsequent technological advances in stable monochromatic light sources. Decades of pioneering work followed with the goal of cooling and trapping atomic vapors with light at temperatures near absolute zero [14–16]. Since then, the suspension of neutral atoms in a vacuum and the ability to precisely control their internal and external degrees of freedom have paved the way for an incredible number of new scientific achievements. One of these is a distinctive demonstration of a particular state of matter: The Bose-Einstein condensate (BEC) was first realized in 1995 [17, 18] and is named after *S. Bose* and *A. Einstein*, who already predicted its existence in 1914 [19, 20]. It is reached when the temperature of a trapped cloud of bosonic atoms is sufficiently low so that the particles' de

Broglie wave length reaches the same order of magnitude as the average interparticle distance. As the matter waves start overlapping, the ensemble enters the so-called regime of quantum degeneracy.

These and similar advances in technology and fundamental science have opened the floodgates to the development of numerous new and increasingly precise measurements in recent decades. From a metrological point of view, atoms represent the ideal test particles, since two atoms of the same kind are indistinguishable and most of the atomic species used for experiments (alkali and alkaline earth metals) are relatively easy to handle and abundant on Earth. As massive particles with electromagnetic moments, they extend the possibilities of electrons and neutrons by coupling to all known (and potentially unknown) natural forces. This allows to probe a variety of effects with high controllability, rendering atom interferometry one of the most striking and versatile scientific innovations in atom optics.

Consequently, atom interferometry [21] has proven to be a powerful approach to test fundamental theories such as quantum electrodynamics [22–24]: To date, atom interferometers measuring the atomic recoil provide the most accurate determination of the fine structure constant [23, 24]. The inertial mass of the atoms makes these devices uniquely situated to probe the very interface between quantum particles and gravity [25]. This allows for some of the most rigorous constraints on quantum theory and general relativity, e.g., via complementary measurements of Newton’s gravitational constant [26] as well as tests of the equivalence principle [27–32]. Moreover, future devices may detect infrasound gravitational waves [33–40], realize quantum clocks [41–45] and contribute to the search for ultra-light dark matter [40, 46, 47]. Atom interferometers, however, not only provide answers to pressing questions in fundamental physics, but are also prime candidates for real-world applications [48] such as gravimetry [49, 50], gravity cartography [51], and inertial navigation [52, 53].

All these advances directly exploit the interferometers’ ability to perform absolute measurements of inertial forces with high precision and accuracy [54]. This is ultimately limited by the degree of control over their elementary atom optical elements. Some of the first interferometers were based on fixed gratings [7] or slits [6] to separate and recombine beams of cold atoms. But the success of atom interferometry is based on the high level of accuracy and stability provided by the realization of beam splitters or mirrors using pulsed counterpropagating laser beams [8, 9]. The goal of this thesis is to provide new theoretical insights into the interaction between light and matter in order to improve the performance of atom interferometric sensors.

1.1 Example of an Inertial Matter-wave Sensor

For this purpose, the principle of an inertial sensor is briefly explained. Any massive object can be accelerated by inertial forces such as gravity and the resulting motion generates a signal allowing to infer the force accelerating the object. Here, we assume a constant linear acceleration \mathbf{a} . The sensitivity of the device with respect to this force derives from the ability to track the relative motion of a freely falling test mass with respect to its environment for the duration of the measurement. For example, a freely falling test mass could be used to infer the acceleration of the experimental apparatus mounted on a ship or aircraft. Conversely, a stationary experimental unit on the ground could track the acceleration of the test mass in free fall to measure gravity. In both cases, the signal is encoded in the relative motion between the test mass and its environment. Measuring this signal can be accomplished by accurately tracking its relative position due to acceleration as a function of time in inertial sensors, and should be repeatable many times to ensure the statistical significance of the result. Inertial sensors based on atom interferometry are unique in that the atoms are free from manufacturing defects and mechanical wear, guaranteeing outstanding long-term stability. In addition, the spatial reference is typically an optical lattice implemented by counterpropagating laser beams, which promises a high degree of control and flexibility.

Figure 1.1(a) shows the example of a typical light-pulse atom interferometer in the standard Mach-Zehnder (MZ) configuration, consisting of two beam splitters and mirror pulse. Between pulses, the atoms move freely along the two paths reminiscent of an optical MZ interferometer. In this case, the incoming atomic wave packet is separated and recombined by via the interaction with the laser potential at three time points, which promotes transitions between two atomic states via stimulated emission and absorption of photons. The simplest form that the temporal profile of the laser intensity can take is that of a box pulse, in which the laser is abruptly switched on and off again. Figure. 1.1(b), on the other hand, shows a series of Gaussian light pulses, which we consider throughout this thesis. The difference of the center-of-mass momentum \mathbf{p} between two atomic states corresponds to the total photon recoil transferred during the atom-light interaction, $|1, \mathbf{p}\rangle \longleftrightarrow |2, \mathbf{p} + \hbar\mathbf{k}_{\text{eff}}\rangle$, where we have introduced the effective wave vector \mathbf{k}_{eff} and the reduced Planck constant $\hbar = h/2\pi$. Ideally, the pulses transfer either half (beam splitter, also called " $\pi/2$ -pulse") or the entire population between the two states (mirror, also called " π -pulse") and ensure that the trajectories of the two clouds perfectly overlap at the last pulse at $t = 2T$. Since the atoms interact with the optical lattice several times during the measurement cycle, each interaction imprints a phase on the atoms that depends on their position and consequently encodes their motion relative to the spatial structure of the lattice. The interferometer is therefore designed to derive the phase difference ϕ accumulated by the two atomic wave packets propagating along the two separate paths in Fig. 1.1(a). The measurement of ϕ is

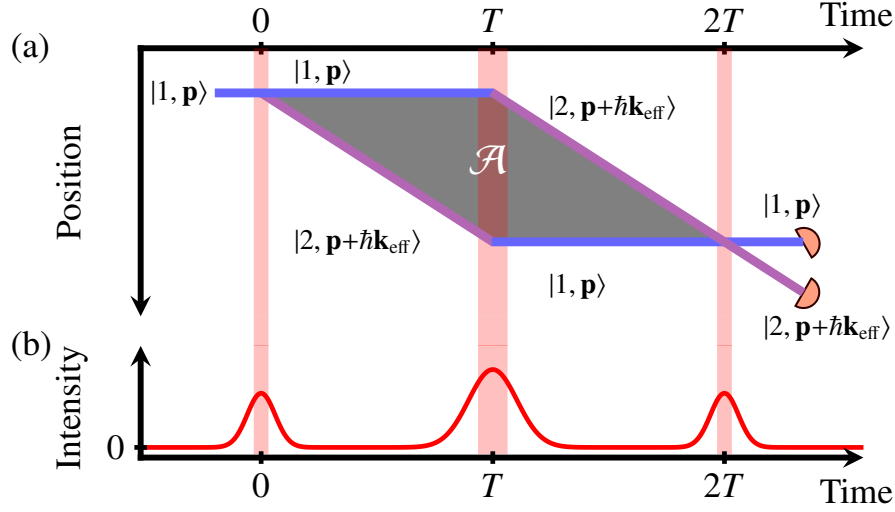


Figure 1.1: **Space-time diagram of a three-pulse Mach-Zehnder (MZ) matter wave interferometer.** (a) We show the center-of-mass trajectories of an incoming atomic wave packet in the freely falling frame. The wave packet is split, redirected and recombined via the interaction with three successive laser pulses at times $t = 0, T, 2T$. The atom-light interaction promotes transitions between the atomic states $|1, \mathbf{p}\rangle$ (blue) and $|2, \mathbf{p} + \hbar\mathbf{k}_{\text{eff}}\rangle$ (violet), where the effective momentum $\hbar\mathbf{k}_{\text{eff}}$ is transferred only to one part of the superposition. Here, $\hbar = h/2\pi$ is the reduced Planck constant. Because the phase imprinted during each interaction depends on the position of the wave packet with respect to the light fields, the relative phase ϕ accumulated along the two trajectories in Eq. (1.1) is proportional to the space-time area \mathcal{A} (gray shaded area) [55–57]. In this thesis, we consider laser intensities with a Gaussian time profile, as shown in (b).

made possible by the last pulse, which converts this relative phase into a population difference between the two states $|1, \mathbf{p}\rangle$ and $|2, \mathbf{p} + \hbar\mathbf{k}_{\text{eff}}\rangle$. The last beam splitter in a light interferometer plays a similar role, as it converts the relative phase between the two electric fields propagating along the two arms into an intensity difference between the two output ports.

1.1.1 Sensitivity to Linear Acceleration

The relative phase accumulated due to a linear acceleration \mathbf{a} by the two wave packets propagating along the two trajectories in Fig. 1.1(a) after a time $2T$ is given by [55–57]

$$\phi = \frac{M}{\hbar} \mathbf{a} \cdot \mathcal{A} = \mathbf{a} \cdot \mathbf{k}_{\text{eff}} T^2. \quad (1.1)$$

It is a function of the space-time area enclosed by the two arms of the interferometer, $\mathcal{A} = \hbar\mathbf{k}_{\text{eff}} T^2/M$, which we highlight in the figure (gray shaded area). Consequently, \mathcal{A} depends on the atomic mass M and scales linearly with the momentum separation \mathbf{k}_{eff} as well

as quadratically with the separation time T^2 . Therefore, \mathcal{A} serves as an amplifier, since the larger \mathcal{A} is, the more a change in acceleration affects the phase ϕ . The measurement of populations of quantum states is a probabilistic process, which is a key characteristic of quantum mechanics postulated by Born's rule. Hence, any estimate of ϕ will be subject to a statistical uncertainty, $\Delta\phi \geq 1/\sqrt{N_{\text{atoms}}}$, where N_{atoms} is the number of atoms taking part in the interferometer in one realization (also referred to as a "shot"). The scaling with $1/\sqrt{N_{\text{atoms}}}$ is a consequence of the fundamental uncertainty associated with the projective measurement in a two-level system for a fixed number of atoms and is therefore often referred to as atomic projection noise or shot noise [58]. If $\Delta\phi = 1/\sqrt{N_{\text{atoms}}}$ the measurement is only limited by the fundamental shot-noise and technical noise sources are negligible.

Accordingly, the scale factor in Eq. (1.1), $\mathbf{k}_{\text{eff}}T^2$, translates this into a corresponding statistical uncertainty in the measurement of \mathbf{a} , which is typically referred to as the sensitivity, $\Delta\mathbf{a}$. Assuming that both the force and the wave vector are aligned in parallel, $\mathbf{a} \cdot \mathbf{k}_{\text{eff}} = |\mathbf{a}||\mathbf{k}_{\text{eff}}| =: a k_{\text{eff}}$, so that the sensitivity of an interferometer with an ideal signal-to-noise ratio combined with an atomic source that produces N_{atoms} uncorrelated atoms per second becomes (see, e.g., [59])

$$\Delta a = \frac{\Delta\phi}{k_{\text{eff}}T^2} \geq \frac{1}{\sqrt{N_{\text{atoms}}}k_{\text{eff}}T^2}. \quad (1.2)$$

Improving the inertial sensitivity, either by increasing the atomic flux or the space-time region enclosed by the two arms, or both, has been the focus of tremendous efforts that have decisively shaped the field of atom interferometry over the past decade.

In the remainder of this introduction, we will briefly discuss some important developments that have already influenced the design of many of today's instruments, but will certainly prove to be groundbreaking for future generations. For a more comprehensive overview of the state of the art in this field, with a special focus on inertial sensing, we recommend the reader to refer to the recent reviews by *R. Geiger et al.* [54] and *F. A. Narducci et al.* [60] as well as the references therein.

1.1.2 Cold Atom Sources

If a measurement is shot-noise limited, increasing the atomic flux immediately improves the statistical significance of a single measurement run, as Eq. (1.2) suggests. This may reduce the total number of measurements required for a targeted level of sensitivity. Modern sources of laser-cooled atomic clouds produce circa 10^9 atoms/s [61], while thermal atomic beams can achieve an even larger flux [62], pushing the theoretical projection noise limit well below the mrad-level, $\Delta\phi < 100 \mu\text{rad}$. Meanwhile, the flux of the best current BEC sources is still orders of magnitude below that of thermal atoms [63]. However, comparing the two also requires taking into account the considerably larger expansion velocities of

thermal ensembles compared to condensed ones (see, e.g., Ref. [64, 65]), which can cause systematic errors in the interferometer [66–68] as well as lead to significant losses due to velocity sensitivity [69]. Moreover, the flux of BEC sources may be improved considerably in the intermediate future by the successful implementation of the atom laser [70, 71]. In addition, condensed ensembles offer the exciting prospect of using correlations between particles for improved scaling of $\Delta\phi$ with N_{atoms} [72, 73] up to the Heisenberg limit [74, 75], $1/N_{\text{atoms}}$.

Naturally, the development of compact and robust atomic sources has become an important focus [63, 76–78], as it is essential for the transition from laboratory-based experiments to portable devices that can be used in the real world [48]. In addition, extensive efforts have been made to better control the kinematic properties of the atomic source, which has sparked particular interest in BEC interferometry [79]. The reason is that small uncertainties in the position of the atomic clouds and a low expansion rate are indispensable when aiming for higher sensitivities by pushing the pulse separation time T and/or increasing the relative momentum $\hbar k_{\text{eff}}$ between the wave packets [see Eq. (1.2)].

1.1.3 Large Separation Times T

In conventional light-pulse interferometers, the atoms are in free fall between pulses, and the duration T is limited by the finite dimensions of the experimental apparatus. To prevent the atoms from falling out of the experiment, the free-fall time can be extended either in an atomic fountain, allowing up to $2T = 2.3$ s in 10 m setups on Earth, or by performing the experiment in a microgravity environment [52, 80–83], which promises a nearly force-free interrogation for the duration of several seconds [82, 83]. Alternatively, experiments have explored the possibility of suspending atoms via an external force [84–88], and although this method requires extremely good control over the quality of the levitating potential, the method has recently enabled coherence times of up to one minute [88].

Either approach has its own use case and presents a number of challenges, but they both require extremely low expansion rates of the atomic ensemble to avoid detrimental systematic effects stemming from the finite dimensions of the laser beams used to interrogate the atoms [88, 89]. The need for ultracold atomic ensembles makes BECs particularly interesting because of their inherently small cloud sizes and the ability to achieve expansion rates of less than $100 \mu\text{m/s}$ [65].

Developing inertial sensors based on condensed ensembles that can be deployed in extreme environments such as sounding rockets [90] or space [83] to perform matter-wave interferometry in microgravity has been a long standing goal of the QUANTUS (Quantengase unter Schwerelosigkeit) consortium [91]. This collaboration between several German universities and the German Aerospace Center (Deutsches Zentrum für Luft- und Raumfahrt, DLR [92]) has a strong focus on interferometry in microgravity environments [80, 81, 83,

90, 93], but also contributes to the innovation of the field of BEC interferometry in general [94, 95]. Most recently, the first-generation experiment QUANTUS-1 demonstrated the state of the art in splitting beams with large momenta [96].

1.1.4 Large Momentum Transfer (LMT)

Large-momentum-transfer (LMT) beam splitting takes advantage of the improved scaling of interferometer sensitivity with the momentum separation $\hbar k_{\text{eff}}$ of the coherent superposition of matter waves, as seen in Eq. (1.2). Several proof-of-principle experiments have demonstrated record-breaking separations [96–99] using various beam splitting techniques.

The first light-pulse atom interferometers used counterpropagating light fields to couple the hyperfine states of laser cooled atoms via Raman transitions [8, 9]. This makes the atom-light interaction insensitive to the relatively large velocity spread of the atomic ensembles available at the time¹, and enables selective detection of the two different electronic states. However, this limits the momentum splitting to $\hbar k_{\text{eff}} = 2\hbar k$, where k is the wave number of the optical lattice. Advances in laser cooling technology and BEC production, leading to atomic ensembles with momentum widths corresponding to a fraction of the photon recoil [64, 65], have brought into focus the utility of Bragg scattering of atoms from optical lattice potentials [101, 102] for atom interferometry.

Today, Bragg diffraction is at the heart of many elementary atom-optical operations in modern atom interferometry because it allows multiple photon recoils to be imparted to the atomic wave packets while precisely controlling the diffracted populations without changing the internal state of the atoms [64, 94, 96–98, 103–105]. The price to pay is the relatively strong velocity selectivity of the diffraction process [69] due to the relatively small energy splitting of the involved momentum states, which is in the order of the recoil frequency, $\omega_r = \hbar k^2/2M$ (\sim kHz). Nevertheless, Bragg diffraction enabled benchmark experiments to drive higher-order transitions up to $24\hbar k$ [103] and allowed for momentum separations of more than 100 photon recoils via sequential Bragg pulses [97]. In particular, high-fidelity Bragg pulses, often in conjunction with other methods such as Bloch oscillations (BO) [96, 106–111], are an indispensable tool for LMT atom interferometry [64, 94, 96–98, 103, 104, 109, 111]. Recently, the QUANTUS-1 experiment reported record-breaking momentum separation in an atom interferometer. Using "twin-lattice interferometry" the experiment combined a BEC source with two counterpropagating lattices to perform symmetric Bragg diffraction as well as BO, realizing MZ-type interferometers with at the time unprecedented momentum separations of more than $400\hbar k$ [96]. Since then the authors *T. Wilkason* et al. [99] have achieved comparable momentum separations combining inelastic scattering with methods of quantum control.

¹Because the detuning between the involved hyperfine states is typically in the GHz range, e.g., see the D2-line data for ⁸⁷Rb in Ref. [100].

1.1.5 Accuracy Limits: Diffraction Phases

Given these groundbreaking developments and several successful proof-of-principle experiments, it may seem counterintuitive that only a handful of atom interferometers have so far demonstrated a metrological gain implementing LMT beam splitters for matter waves [23,32,112,113], all of which rely on Bragg diffraction. Moreover, most sensitive inertial sensors are currently based on thermal atomic ensembles interrogated via two-photon Raman transitions [54]. The main reason for this is that current metrological tests of inertial forces are not necessarily bounded by the statistical uncertainty in Eq. (1.2). Instead, they suffer from inertial noise [24,114] or, more fundamentally, their accuracy is limited due to insufficient control over elementary atom-optical elements such as beam splitters or mirrors, often related to inhomogeneities of the light field acting on the atoms [85,86,88,96]. These imperfections are associated with the phase profile of the laser and are described as wavefront aberrations [66–68]. When they are related to the intensity distribution or the temporal pulse shape of the laser, they are often called "diffraction phases" [115–121]. In both cases, they lead to shifts in the relative phase in Eq. (1.1) contributing dominantly to the error budget of state-of-the-art experiments, e.g., see Refs. [23,24,68,122].

Since these imperfections are ultimately related to the relative motion of atoms in the laser beam caused by the finite size of the atomic ensemble and residual expansion, both Bragg and Raman interferometers face very similar challenges in this regard. However, the fact that Bragg diffraction inherently requires ultracold atomic ensembles with low expansion rates helps to mitigate some of these issues [54,89,123], albeit at the cost of significantly reduced atom numbers, as we have explained above. Furthermore, all the shortcomings caused by the inhomogeneities of the laser are further amplified when multiple photons are transferred either via Bragg transitions [98,103,124] or BO [84–86,88,118]. For this reason, lattice-depth-dependent phase shifts [116,119,120] lead to stringent requirements for experimental control of light field intensity in the context of Bragg diffraction and require appropriate mitigation strategies in the case of asymmetric momentum transfer [112,119,124]. Using single, multiphoton Bragg diffraction beam splitting pulses relaxes these requirements, but so far at the expense of smaller separations [103].

More importantly, in the case of Bragg scattering, the presence of multiple nearby transitions causes diffraction phases even under the assumption of a perfectly homogeneous light field in the form of a plane wave [116–121]. This makes it arguably more difficult to accurately determine the resulting diffraction phase shifts in Bragg interferometers compared to their Raman counterparts.

1.2 Thesis Outline

The inability to accurately estimate the systematic effects resulting from the atom-light interaction is a key factor limiting the sensitivity of modern LMT atom interferometers based on Bragg diffraction. A precise theoretical understanding of the atom optical elements is therefore essential to realize the full potential of interferometry with enhanced scale factors.

In the first part of this thesis, comprising the following two chapters, we present an analytical model for the signal from LMT Bragg atom interferometers using higher order Bragg diffraction in one dimension. Our treatment takes into account the multilevel properties of Bragg diffraction, which allows estimation of subsequent systematic effects and provides insight into appropriate mitigation strategies. These results provide the basis for future work to develop an analytical description of the interplay between three-dimensional Bragg atom interferometer geometries and the effects of realistic laser potentials, including wavefront errors and spatial laser intensity fluctuations. In the second part of this thesis, we investigate the limitations of current state-of-the-art LMT atom interferometers implemented in the QUANTUS-1 experiment focusing on the interaction between the atoms and the laser potentials.

This thesis is organized as follows. **Chapter 2** starts with a short overview of already existing theoretical descriptions of Bragg pulses. Motivated by the key insight that the dynamics of these pulses can be captured very accurately based on the adiabatic theorem, this is followed by a novel formulation of the problem within the framework of scattering theory. In the following, the measure of the pulse fidelity is introduced to compare the analytical predictions with exact numerical solutions of the dynamics of Bragg beam splitters and mirrors with Gaussian temporal pulse envelopes. This serves as a foundation for **Chapter 3**, which relates the metrological characteristics of Bragg interferometers to the multiport properties of the individual pulses. Using the popular Mach-Zehnder geometry as an example, it is shown that the physics of Bragg interferometers deviates significantly from the standard two-mode mode picture, leading to systematic errors and changing the standard shot-noise limit. Finally, ways to control and suppress intrinsic systematic errors by two orders of magnitude are presented. **Chapter 4** introduces the key ingredients to twin-lattice interferometry: Bose-Einstein condensates, symmetric (double) Bragg diffraction, and Bloch oscillations. After a brief description of the realization in the QUANTUS-1 experiment, the concepts of atom loss, open interferometer, and dephasing are discussed as the main causes of fringe contrast loss in the large-momentum-transfer atom interferometer. A theoretical model based on these aspects and tailored to the experiment is then compared with the measured data. **Chapter 5** summarizes these findings and concludes this thesis.

2

Theory for Bragg Atom Interferometry Based on the Adiabatic Theorem

2.1 Motivation and Research Problem

Bragg diffraction of atoms from optical lattice potentials [101, 102] is a cornerstone of light-pulse atom interferometry [125]. It is at the heart of most elementary atom optical operations in modern atom interferometry aimed at transferring several photon recoils and precisely controlling the diffracted populations without changing the internal state of the atom [64, 94, 96–98, 103–105]. In particular, high-fidelity Bragg pulses, often in conjunction with other methods, such as Bloch oscillations [96, 106–111], are an indispensable tool for LMT atom interferometry [64, 94, 96–98, 103, 104, 109, 111].

Theoretical models for Bragg diffraction of matter waves from light crystals have first covered the two limiting cases of short and intense as well as faint and long light pulses referred to as the Raman-Nath [126–128] or deep-Bragg regime [101, 102] respectively. Especially for rectangular pulses, both yield simple analytic solutions of the Schrödinger equation and thus provide compact descriptions of elementary atom optical operations and interferometers composed of them. However, neither allows for efficient LMT operations as desired for ultrasensitive atom interferometry. It has been found that efficient LMT operations can be achieved in between the two limiting cases of the Raman-Nath and deep-Bragg regime, in the so-called quasi-Bragg regime. As a result, LMT Bragg pulses in state-of-the-art atom interferometer experiments predominantly operate in the quasi-Bragg regime [23, 94, 96–98, 103–105, 109, 111]. In this regime, the approximations that led to analytic solutions in the previous cases are not applicable, and no simple analytic description of the Schrödinger dynamics generated by quasi-Bragg pulses with time-dependent envelopes has been known so far. As a matter of fact, for lack of manageable analytic descriptions, measured data in experiments are usually compared against numerical solutions of the Schrödinger equation [23, 94, 98].

The main focus of this chapter is to develop a comprehensive and relatively simple analytic theory for Bragg atom interferometers. The key insight of the work presented in the following is that the dynamics in the quasi-Bragg regime can, in fact, be captured very accurately by a model based on the adiabatic theorem [129]. We show that any smooth and adiabatic (in the sense of the adiabatic theorem) Bragg pulse can give rise to efficient atom optical operations. For the specific but widely used case of a Gaussian pulse we also show the reverse: Efficient beam splitter or mirror operations are generated exclusively by adiabatic pulses. Whether this is generally true, i.e., whether nonadiabatic Bragg pulses generating diabatic dynamics can lead to high-performance atom-optical operations at all, does not seem obvious to us based on the description developed in this chapter.

Before proceeding to formulate the problem of Bragg diffraction within the framework of scattering theory, in Sec. 2.2 we first briefly introduce the existing theoretical descriptions based on diabatic time evolution and point out the conceptual differences with our approach. The following Secs. 2.3 and 2.4 contain the formal derivation of the scattering matrix, where we exploit the symmetries of the Bragg Hamiltonian, apply the adiabatic theorem, and calculate first-order corrections to it. They take the form of Landau-Zener (LZ) losses and LZ phases as well as first-order Doppler shifts to perturbatively account for the finite momentum widths of atom wave packets. We summarize our findings in Sec. 2.5 and formulate the two-mode Bragg scattering matrix as a result. On this basis we study in Sec. 2.6 the fidelities of single Bragg beam splitter and mirror operations achievable with Gaussian pulses and show that our analytical model accurately reproduces the rich phenomenology exhibited by the numerical solutions of the Schrödinger equation. To improve accessibility of the results presented in this chapter and to facilitate further research all of the codes used to generate these results are available [120]. Finally, and in anticipation of Chapter 3 we extend our formalism in order to also describe the coherent coupling to undesired diffraction orders during higher-order Bragg processes in Sec. 2.7, while the outlook of this chapter indicates additional extensions and generalizations of the results developed in this thesis.

2.2 Review: Theory of Bragg Diffraction from Light Crystals

We start with a brief introduction of the Hamiltonian governing the dynamics of Bragg diffraction. For a more detailed derivation of the interaction of an atom with a classical radiation field, we recommend the textbook by *P. Meystre* [12] and would like to draw attention to the presentation of the individual contributions towards a better understanding of the diffraction of matter waves from optical lattices by *H. Müller et al.* [130].

2.2.1 Bragg Hamiltonian

Consider an atom (mass M) in a state which is localized in momentum space at an average momentum Mv_0 with a characteristic spread $\sigma_p \ll \hbar k$. Here, $k \equiv k_1 \approx -k_2$ is the wave number of two counterpropagating light fields with a laser phase ϕ_L forming the optical lattice as sketched in Fig. 2.1(a),

$$\begin{aligned} \mathbf{E}(\hat{\mathbf{x}}, t) &= E_0(\hat{\mathbf{x}}, t) \boldsymbol{\varepsilon} \{ \cos(k_1 \hat{z} - \omega_1 t + \phi_L) + \cos(k_2 \hat{z} - \omega_2 t - \phi_L) \} \\ &= 2E_0(\hat{\mathbf{x}}, t) \boldsymbol{\varepsilon} \{ \cos(k \hat{z} - \delta t + \phi_L) \cdot \cos(\omega_L t) \}. \end{aligned} \quad (2.1)$$

For simplicity we assume identical polarization vectors $\boldsymbol{\varepsilon}$ and homogeneous electric field amplitudes $E_0(\hat{\mathbf{x}}, t) = E_0(t)$ for both plane waves, so that $\mathbf{E}(\hat{\mathbf{x}}, t) = \mathbf{E}(\hat{z}, t)$. Moreover, in the second equality we have used the assumption that the frequency difference $2\delta \equiv \omega_1 - \omega_2$ is typically small compared to laser frequencies $2\omega_L \approx \omega_1 + \omega_2$, i.e., $\delta \ll \omega_L$, and employed the trigonometric relation $\cos(x) + \cos(y) = 2 \cos(\frac{x+y}{2}) \cos(\frac{x-y}{2})$. Note, that in this chapter we assume $\delta(t) = \delta$ but treat time-dependent detunings $\delta(t)$ later in Chapter 4. Since $\delta(t) \ll \omega_L$, we can assume throughout this thesis that $\omega_L(t) = \omega_L$. In case of a two-level atom consisting of a ground state $|g\rangle$ and a single excited state $|e\rangle$, its interaction with the electric field can be effectively described via a dipole potential contributing to the Hamiltonian

$$H^{\text{dip}} = \frac{\hat{\mathbf{p}}^2}{2M} + \hbar\omega_g |g\rangle\langle g| + \hbar\omega_e |e\rangle\langle e| - \hat{\mathbf{d}} \cdot \hat{\mathbf{E}}(\hat{\mathbf{x}}, t). \quad (2.2)$$

Operators $\hat{\mathbf{x}}$ and $\hat{\mathbf{p}}$ denote the centre-of-mass position and momentum operators for the atom that satisfy the commutation relations $[x_m, p_j] = i\hbar\delta_{mj}$. Since the operator $\hat{\mathbf{d}} = -e \hat{\mathbf{x}}_e$ accounts for the dipole moment of a single electron with charge e at position $\hat{\mathbf{x}}_e$ relative to the atom's center of mass, the dipole approximation is most accurate for hydrogen-like species such as alkali atoms. The dipole coupling due to the one-dimensional light-field in Eq. (2.1) simplifies to

$$-\hat{\mathbf{d}} \cdot \hat{\mathbf{E}}(\hat{z}, t) = \hbar\Omega_{eg}(t) \cos(k\hat{z} - \delta t + \phi_L) \left(e^{i\omega_L t} |e\rangle\langle g| + e^{-i\omega_L t} |g\rangle\langle e| + \text{H.c.} \right), \quad (2.3)$$

where we have introduced the coupling strength in terms of the Rabi frequency

$$\Omega_{eg}(t) = -\frac{E_0(t)}{\hbar} (\mathbf{d}_{eg} \cdot \boldsymbol{\varepsilon}). \quad (2.4)$$

It depends on the amplitude as well as the polarization of the electric field relative to the quantization axis of the atomic dipole given by the transition dipole moment \mathbf{d}_{eg} . Since the dynamics of Bragg diffraction is dictated by two very different time scales in the form of δ ($\approx 10^3 - 10^5$ Hz) and ω_L ($\approx 10^{15}$ Hz) according to the Hamiltonian in Eq. (2.2), it is convenient to change to a frame rotating at the laser frequency ω_L . This is achieved by

writing $H^{\text{dip}} = H_0^{\text{dip}} + H_I^{\text{dip}}$ and moving to an interaction picture, where the operators absorb the time evolution generated by

$$\hat{U} = \exp\left\{\left(-\frac{i}{\hbar}H_0^{\text{dip}}t\right)\right\}, \quad \text{with} \quad H_0^{\text{dip}} = \hbar\omega_g |g\rangle\langle g| + \hbar(\omega_e - \Delta) |e\rangle\langle e|. \quad (2.5)$$

Here, we have introduced the detuning of the laser from the transition frequency separating the two atomic levels $\Delta = (\omega_e - \omega_g) - \omega_L$. To suppress spontaneous emission during the Bragg interaction the detuning from the atomic resonance typically satisfies $\Gamma_{\text{nat}} \ll \Delta \ll \omega_L$, where Γ_{nat} denotes the natural line width of the atomic transition. This permits us to neglect the effect of spontaneous emission for now, but we will comment on its role for Bragg diffraction later.

We describe the evolution of the states solving the Schrödinger equation after transforming the residual terms,

$$H_I^{\text{dip}} = \frac{\hat{p}^2}{2M} + \hbar\Delta |e\rangle\langle e| + \hbar\Omega_{eg}(t) \cos(k\hat{z} - \delta t + \phi_L) \left(e^{i\omega_L t} |e\rangle\langle g| + e^{-i\omega_L t} |e\rangle\langle g| + \text{H.c.} \right), \quad (2.6)$$

into the interaction picture according to

$$H_I^{\text{dip}} \rightarrow \hat{U}^\dagger H_I^{\text{dip}} \hat{U} = \frac{\hat{p}^2}{2M} + \hbar\Delta |e\rangle\langle e| + \hbar\Omega_{eg}(t) \cos(k\hat{z} - \delta t + \phi_L) (|e\rangle\langle g| + \text{H.c.}) \quad (2.7)$$

In this last step, we have dropped fast oscillating terms with twice the laser frequency $\exp(\pm 2i\omega_L t)$ in the spirit of the *rotating wave approximation* since their dynamics is insignificant, e.g., on the time scale of a Bragg pulse.

Choosing detunings much larger than the Rabi frequency as well as the atomic recoil frequency, $\Delta \gg \Omega_{eg}(t)$, $\omega_r = \hbar k^2/2M$ affords another simplification by adiabatically eliminating the excited state's time evolution, e.g., see chapter 4 in Ref. [12]. Under this assumption the dynamic of the ground state $|g\rangle$ decouples and a time-dependent ac Stark potential drives the elastic Bragg scattering process of the atom remaining in $|g\rangle$. This gives rise to the Bragg Hamiltonian in the laboratory frame

$$\mathcal{H}^{\text{LF}}(t) = \mathcal{K} + 2\hbar\Omega(t) \cos^2(k\hat{z} - \delta t + \phi_L), \quad \mathcal{K} = \frac{\hat{p}^2}{2M}. \quad (2.8)$$

The two-photon Rabi frequency $\Omega(t) = \Omega_{\text{eg}}^2(t)/2\Delta$ determines the strength of the optical lattice potential in Eq. (2.8). Both $\Omega(t)$ and ϕ_L may have a time dependence which is controlled through the intensities and phases of the two applied fields. The laser phase ϕ_L , however, is assumed to be constant throughout our analysis and we will comment in the end of this chapter on the case of a time-dependent tuning of the laser phase. We assume a pulsed light pulses so that the Rabi frequency vanishes asymptotically, $\lim_{t \rightarrow \pm\infty} \Omega(t) = 0$, and is nonzero only for a time interval on the order of τ around $t = 0$. In Sec. 2.6, we will consider the widely used Gaussian pulse as a concrete example

$$\Omega(t) = \Omega e^{-\frac{t^2}{2\tau^2}}, \quad (2.9)$$

because the choice of a smooth envelope reduces populations of unwanted states and parasitic phase shifts [130]. In the following, we will explicitly state, whenever $\Omega(t)$ is assumed to be Gaussian function with a peak Rabi frequency of Ω .

As a result of n th-order Bragg diffraction a momentum $2n\hbar k$ shall be gained by the atom so that it is transferred to a final state with momentum $Mv_1 = Mv_0 + 2n\hbar k$, or, just as well, into an arbitrary superposition state of momenta Mv_0 and Mv_1 . If this is possible, the time-reversed process can be applied to any incoming superposition of momenta Mv_0 and Mv_1 too. Thus, for reasons of concreteness and without loss of generality, we can assume an incoming wave packet with average momentum Mv_0 as an initial condition. To transfer momentum efficiently the frequencies of the counterpropagating light fields depicted in Fig. 2.1(a) must be detuned with respect to each other so that

$$\delta = k(v_0 + \frac{n\hbar k}{M}) = kv_0 + 2n\omega_r. \quad (2.10)$$

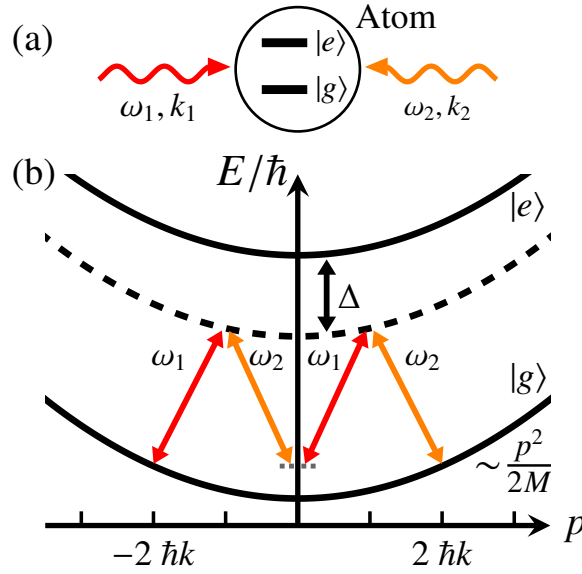


Figure 2.1: **Single Bragg diffraction setup.** (a) Schematic of an atom subjected to two counterpropagating light fields as in Eq. (2.1) with frequencies $\omega_L \approx \omega_1 \approx \omega_2$ and wave numbers $k \equiv k_1 \approx -k_2$. The light forms an optical lattice that can be pulsed and depending on the relative momentum between the atom and the optical lattice, the atom can undergo multiple $2n$ -photon transitions via stimulated absorption and emission, imparting $2n$ -photon recoils $\hbar k$ on the atom. The dispersion relation in the inertial frame comoving with the optical lattice (b) schematically shows the resonant coupling between the momenta $\pm n\hbar k$ (here, $n = 2$) via a multiphoton transition satisfying energy and momentum conservation. A prerequisite for this process is a large detuning of the laser frequency from the atomic resonance compared to the relative detuning of the light fields, i.e., $|\Delta| = |(\omega_e - \omega_g) - \omega_L| \gg |\omega_1 - \omega_2|$.

Figure 2.1(b) schematically represents the atomic energy levels and frequencies in the form of a dispersion relation in an inertial frame that moves with the lattice potential. This is useful for illustrating the so-called Bragg condition for matter waves, which in principle favors certain $2n$ -photon transitions over others due to the conservation of energy and momentum. This will be discussed in more detail in the next section. For the moment, suffice it to say that our chosen lattice velocity $v_L = \delta/k$ according to Eq. (2.10) ensures resonant Bragg diffraction between momenta $\pm n \hbar k$. We formally transfer Eq. (2.8) to the comoving frame and absorb a global phase Φ caused by the average ac Stark potential as well as a shift in kinetic energy in the process. The corresponding transformation is achieved by a unitary operator $\mathcal{G}(t) = \exp(-i(\hat{z} - \hat{p}t/M)Mv_L/\hbar + i\Phi_{\mathcal{G}}(t))$, where $\dot{\Phi}_{\mathcal{G}}(t) = \Omega(t) + Mv_L^2/2\hbar$. The Hamiltonian $\mathcal{H}^{\text{MF}} = i\hbar\dot{\mathcal{G}}\mathcal{G}^\dagger + \mathcal{G}\mathcal{H}^{\text{LF}}\mathcal{G}^\dagger$ in the moving frame is

$$\mathcal{H}^{\text{MF}}(t) = \mathcal{K} + \frac{\hbar\Omega(t)}{2} \left(e^{2i(k\hat{z} + \phi_L)} + e^{-2i(k\hat{z} + \phi_L)} \right). \quad (2.11)$$

In this frame the incoming atomic wave packet is initially composed of momentum components around an average momentum $M(v_0 - v_L) = -n \hbar k$, and the target momentum in n th-order Bragg diffraction is $M(v_1 - v_L) = n \hbar k$. The Hamiltonian in Eq. (2.11) is the usual starting point to describe Bragg pulses [12, 119, 130–132].

2.2.2 Diabatic Descriptions of Bragg Diffraction

The Fourier composition of the potential in Eq. (2.11) reveals the well-known property of the optical lattice potential to change the momentum of the atom only by a multiple of $2 \hbar k$. If in the initial wave packet n is an even (odd) number, then at a later point in time it will only consist of momentum components that are an even (odd) multiple of $\hbar k$. Therefore, the usual approach to solve the unitary time evolution as described by the Schrödinger equation for the electronic ground state wave function,

$$i\hbar\dot{\psi}_{\text{g}}(z, t) = -\frac{\hbar^2}{2M} \frac{\partial^2 \psi_{\text{g}}(z, t)}{\partial z^2} + \frac{\hbar\Omega(t)}{2} \left(e^{2i(kz + \phi_L)} + e^{-2i(kz + \phi_L)} \right) \psi_{\text{g}}(z, t), \quad (2.12)$$

stated here in position space, is to describe the Bragg diffraction process as diabatic transitions between different momentum components by expanding ψ_{g} in a basis of plane waves,

$$\psi_{\text{g}}(z, t) = \sum_{m=-\infty}^{\infty} c_m(t) e^{imkz}. \quad (2.13)$$

This procedure transforms Eq. (2.12) into an infinite set of ordinary differential equations¹,

$$i\dot{c}_m = m^2 \omega_r c_m + \frac{\Omega(t)}{2} \left(e^{2i\phi_L} c_{m+2} + e^{-2i\phi_L} c_{m-2} \right), \quad (2.14)$$

¹We note that the form of Eq. (2.14) implicitly assumes that the initial atomic wave packet can be approximated by a plane wave and would like to refer the reader to [133] for an extended derivation of the diabatic theory of Bragg scattering including finite velocity distributions.

which in the past has been the basis for numerous studies of Bragg diffraction in the context of atom interferometry, both analytically and numerically [69, 94, 118, 130, 132, 134–136]. In the following, we briefly discuss the known analytical solutions of Eq. (2.14) in the Raman-Nath as well as in the deep-Bragg regime and summarize the previous work to extend these methods to the quasi-Bragg regime.

The Raman-Nath Regime

The Raman-Nath regime is characterized by high laser intensities and short pulse durations. If the energy uncertainty is sufficiently large, i.e., $\tau \ll 1/\sqrt{2\Omega\omega_r}$ with the peak Rabi frequency $\Omega := \max_t \Omega(t)$, it is possible to neglect the kinetic energy term in Eq. (2.14). The resulting set of equations has a simple solution in form of the Bessel functions [130]

$$c_{2m}(t) = -(i)^m J_m \left(\int_0^t dt' \Omega(t') \right), \quad (2.15)$$

assuming a plane wave with zero momentum initially. While interferometry with Raman-Nath pulses has been demonstrated [98, 127] and this regime holds the potential for interesting applications such as multimode interferometry [137], the strong coupling to multiple diffraction orders makes it unsuitable for high efficiency beam splitter and mirror operations.

The deep-Bragg Regime

This is in stark contrast to the so-called Bragg or deep-Bragg regime, which in principle allows lossless operations of two-mode beam splitters and mirrors, even taking into account multiphoton transition, i.e., higher-order Bragg diffraction. The key idea is that, for longer pulse durations the kinetic energy giving rise to the quadratic dispersion relation shown in Fig. 2.1(b) plays a crucial role as energy and momentum must be conserved during the Bragg pulse. It is straightforward to illustrate in the inertial frame of the lattice, that only couplings to momentum states with the same kinetic energy as the initial state can be resonantly driven, which leads to an effective two-level system if the Bragg pulse is sufficiently long. In this regime, Eq. (2.14) can be formally reduced to two differential equations which, in the case of an initial momentum distribution centered around $\pm n \hbar k$, take the form

$$i\dot{g}_{-n} = \frac{1}{2}\Omega_{\text{eff}}(t)e^{2in\phi_L} g_n \quad \text{as well as} \quad i\dot{g}_n = \frac{1}{2}\Omega_{\text{eff}}(t)e^{-2in\phi_L} g_{-n}. \quad (2.16)$$

After all other states in Eq. (2.14) have been adiabatically eliminated ($n > 1$) they are coupled by an effective $2n$ -photon Rabi frequency

$$\Omega_{\text{eff}}(t) = \frac{\Omega^n(t)}{(8\omega_r)^{n-1} [(n-1)!]^2}. \quad (2.17)$$

States with larger absolute momenta naturally become off-resonant as the difference in kinetic energy from the initial and target states grows quadratically. To also average over the dynamics of the intermediate states, one needs to constrain the 2-photon Rabi frequency [130, 133]

$$\frac{\Omega}{2} \ll 4(n-1)\omega_r, \quad (2.18)$$

which immediately restricts the range of effective $2n$ -photon Rabi frequencies,

$$\Omega_{\text{eff}} \ll \frac{8(n-1)^n \omega_r}{[(n-1)!]^2}, \quad (2.19)$$

where similar to before $\Omega_{\text{eff}} := \max_t \Omega_{\text{eff}}(t)$. This limitation of Ω_{eff} as a result of the adiabatic elimination of off-resonant states is the reason why LMT pulses in the deep-Bragg regime require prohibitively long pulse durations even for ultracold atomic ensembles [64, 65]. This can be understood by studying the well-known Pendellösung of Eqs. (2.16),

$$g_{-n}(t) = \cos\left(\frac{1}{2} \int_{-\infty}^t \Omega_{\text{eff}}(t') dt'\right), \quad \text{and} \quad g_n(t) = -i \sin\left(\frac{1}{2} \int_{-\infty}^t \Omega_{\text{eff}}(t') dt'\right). \quad (2.20)$$

To realize a beam splitter or a mirror pulse, the integral in Eqs. (2.20) must at least evaluate to the value of $\pi/2$ or π respectively. This means that the laser intensities constrained due to Eq. (2.19) must be compensated for over the pulse duration, which in the case of a Gaussian pulse shape is characterized by τ . However, very long interaction times lead to Bragg diffraction pulses being extremely velocity selective and thus inefficient due to Doppler shifts resulting from the finite velocity distribution of the atom [69]. These effects were previously modeled numerically in the work published by *S. S. Szigeti* et al. [69], and analytically for the more complex case of double Bragg diffraction pulses involving a second optical lattice [94, 105] by *E. Giese* et al. [132]. In summary, the shortcomings of the deep-Bragg regime motivate the adoption of Bragg diffraction in the quasi-Bragg regime in the context of LMT atom interferometry.

Extension to the quasi-Bragg Regime

In particular, in combination with smooth (e.g., Gaussian) temporal pulse envelopes [130, 131] quasi-Bragg pulses are characterized by weak couplings to off-resonant states comparable to the Bragg diffraction regime while relaxing its requirement of long interaction times, which greatly improves diffraction efficiency with ultracold atomic ensembles [69, 130]. A rough estimate for typical 2-photon Rabi frequencies in the quasi-Bragg regime can be derived from Eq. (2.18)

$$\frac{\Omega(t)}{2} \lesssim 4(n-1)\omega_r. \quad (2.21)$$

Unfortunately, however, the residual couplings to off-resonant states significantly complicate the search for analytical solutions to the Schrödinger equation (2.12) in this regime, especially in case of time-dependent pulse shapes $\Omega(t)$. Existing approaches attempt to transfer the logic of deep-Bragg pulses to this intermediate regime by solving the effective dynamics of a two-level system after adiabatically eliminating all off-resonant couplings. In one of the most sophisticated descriptions along this line *H. Müller et al.* [130] arrive at an expression for the effective Rabi frequency $\Omega_{\text{eff}}(t)$ as a power series expansion in $\Omega(t)$ and $\dot{\Omega}(t)$ in Eq. (48) of [130]. They achieve this by systematically deriving an effective two-level Hamiltonian including $\Omega_{\text{eff}}(t)$ in a series expansion via the eigenvalues of the Mathieu equation. The Mathieu equation had already been used prior to that to describe the dynamics of an atom in a nonresonant standing light wave [138, 139]. This result, however, requires in particular to either numerically calculate the eigenvalues a_n and b_n of the Mathieu equation and to ensure their convergence for the desired orders in $\Omega(t)$ or to find closed expressions for these parameters (see Appendix B in Ref. [130]). Notwithstanding its accuracy, this series expansion results in rather cumbersome formulas for practically relevant parameters.

2.2.3 Bloch-band Picture

An alternative ansatz to describe the diffraction of an atom from a light crystal is to employ Bloch states. The picture of Bloch bands in optical lattices, which are the eigenenergies of the Hamiltonian in Eq. (2.11), is the natural framework to treat matter wave diffraction via Bloch oscillations [106–108]. This approach has previously been shown to provide analytical expressions for diffraction amplitudes [140] and phases [116] adequate in the weak lattice limit ($\Omega(t) \lesssim 2\omega_r$). Recently, *Gochbauer et al.* [119] have used the Bloch solutions to analyze quasi-Bragg pulses, which agree well with experimental results for the specific pulse shapes studied in their case. To do that, they numerically extract the Bloch energy bands by diagonalizing the Hamiltonian in Eq. (2.11) without restricting the potential depth. Since the Bloch-band picture is closely related to the formalism we develop in this chapter, it is worth summarizing its connection to quasi-Bragg diffraction as outlined in [119] at this point.

Figure 2.2 shows the lowest-energy bands $E_{n_B, q_B}(\Omega)$ ($n_B = 0, 1, \dots, 5$) of the Hamiltonian in Eq. (2.11) in the first Brillouin zone for quasimomenta $q_B \in]-k, k]$ and for different fixed values of the Rabi frequency increasing from $\Omega = 0$ to $30\omega_r$. For a free atom, that is, for $\Omega = 0$, a narrow wave packet with mean momentum $-n\hbar k$ (in the rest frame of the lattice) consists of a superposition of Bloch states around the points of degeneracy of the n -th and the $(n-1)$ -th band in the Bloch spectrum. For odd n this degeneracy occurs at a quasimomentum $q_B = \pm k$, and for even n at $q_B = 0$ (see panel for $\Omega = 0$ in Fig. 2.2). When the

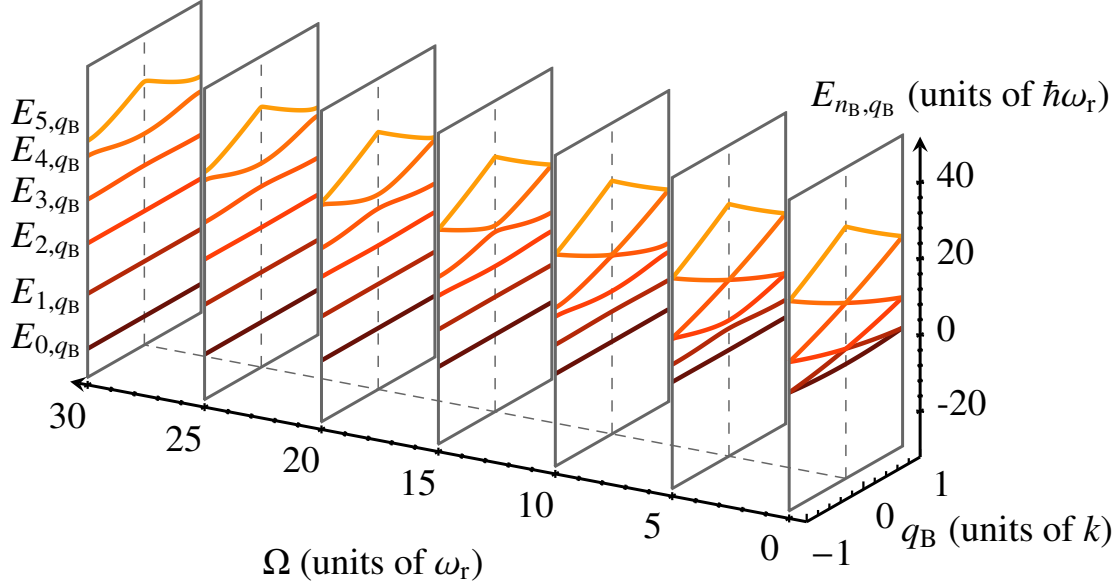


Figure 2.2: **Bloch energy bands.** The lowest six energy bands $E_{n_B, q_B}(\Omega)$ ($n_B = 0, 1, \dots, 5$) in the first Brillouin zone for Bloch-band quasimomenta $q_B \in [-k, k]$ and different values of the Rabi frequency Ω . They are obtained by diagonalizing the Hamiltonian in Eq. (2.11) after truncating orders $n > 5$. In the case of $\Omega = 0$, always two energy bands are degenerate either at the edges ($q_B = \pm k$) or the center ($q_B = 0$) of the Brillouin zone. For nonzero values of Ω the degeneracy is lifted and the bands separate. Figure adapted from *J.-N. Siemss et al., Phys. Rev. A* **102**, 033709 (2020), Copyright 2022, American Physical Society (Ref. [120]).

optical lattice is ramped up adiabatically², the atom remains in the superposition of states in the n -th and the $(n - 1)$ -th band the degeneracy of which will now be lifted (see panels in Fig. 2.2 for $\Omega > 0$). Based on this picture *Gochbauer et al. [119]* explain that the band gap is equivalent to the effective Rabi frequency for oscillations between the states in Eq. (2.16), i.e., the momentum eigenstates $|\pm n \hbar k\rangle$ coupled by the Bragg pulse. This explanation was confirmed by a comparison of numerically calculated band gaps and experimentally determined Rabi frequencies measured at constant potential depth. *Gochbauer et al.* also show that the Bragg diffraction is accompanied by a global phase (diffraction phase) which corresponds to the energetic shift of the center of the band gap with respect to the position of the degeneracy point at vanishing potential. Despite not directly producing analytical results, this study clearly shows that the Bloch-band picture offers important insight into the functioning of quasi-Bragg diffraction.

²Here, adiabaticity refers to the temporal slope of the Rabi frequency $\Omega(t)$. The criterion for a Gaussian pulse duration given in [119], $\tau \gg [4(n - 1)\omega_r]^{-1}$, is derived considering the energy separation to the states closest in energy similarly to Eq. (2.21), but now compared to the rate of change of the potential depth.

2.2.4 Adiabatic Time Evolution

However, we emphasize that the very concept of an effective Rabi frequency alludes to the idea of diabatic dynamics described by an effective Hamiltonian. We hope that the results presented in this chapter will convince the reader that it is much more economic and appropriate to analytically describe Bragg diffraction in the sense of the adiabatic theorem. Before deriving our analytical theory, we would like to explain why applying the adiabatic theorem is natural and provides an intuitive picture of the physics of an atom being elastically scattered from a pulsed optical lattice. If the atom is exposed to two counter-propagating light fields as shown in Fig. 2.1(a) with δ chosen according to Eq. (2.10) and if we idealize both the initial and the final state of the atom, being Bragg diffracted, as plane waves, we can write them as

$$\begin{aligned} e^{-inkz} &= \cos(nkz) - i \sin(nkz) \\ e^{+inkz} &= \cos(nkz) + i \sin(nkz). \end{aligned} \quad (2.22)$$

Previously, we have argued that the states in Eq. (2.22) are degenerate in kinetic energy in the inertial frame of the lattice potential, and that the resonant coupling of these states via $2n$ -photon transitions is therefore allowed in terms of energy and momentum conservation [see Fig. 2.1(b)]. Moreover, the expansion of the initial and final momentum eigenstates based on their symmetric ($\cos(nkz)$) and antisymmetric ($\sin(nkz)$) components according to Eq. (2.22) reveals that a Bragg pulse ideally imprints a differential phase between these basis states. This differential phase is exactly π for a mirror pulse and $\pi/2$ for a beam splitting pulse.

In the following sections, we demonstrate that the evolution of this differential phase over the course of the pulse can be well understood by calculating the evolution of the eigenenergies associated with the states (2.22) according to the adiabatic theorem,

$$\Theta^{\text{dyn}} = \frac{1}{\hbar} \int_{-\infty}^{\infty} dt (E_{n+}(t) - E_{n-}(t)). \quad (2.23)$$

The phase Θ^{dyn} can be seen as the equivalent of the time integral over the effective Rabi frequency [see Eqs. (2.20)], typically referred to as the "pulse area". However, before we are able to show that the eigenenergies in equation (2.23) can be easily calculated by diagonalizing finite-dimensional Hamiltonians, we need to decompose the Hilbert space associated with the Bragg Hamiltonian (2.11) into its symmetric and antisymmetric components, similar to equation (2.22), and formulate the Bragg diffraction process in terms of a scattering problem.

2.3 Bragg Diffraction as a Scattering Problem

We use the adiabatic theorem [129] in combination with analytic methods from scattering theory to determine the transfer or scattering matrix for single quasi-Bragg pulses. To understand and describe Bragg diffraction as a scattering process it is suitable to assume an asymptotic initial condition for the state of the atom. This means that for $t \rightarrow -\infty$ we require that the incoming atomic wave packet $|\psi(t)\rangle$ satisfies

$$|\psi(t)\rangle \xrightarrow{t \rightarrow -\infty} e^{-i\mathcal{K}t/\hbar} |\psi^{\text{in}}\rangle, \quad (2.24)$$

and $|\psi^{\text{in}}\rangle$ is chosen to match the initial conditions discussed in Sec. 2.2.1. In an interaction picture with respect to the kinetic energy \mathcal{K} the asymptotic initial condition assumes the simpler form $|\psi^I(t)\rangle = \exp(i\mathcal{K}t/\hbar) |\psi(t)\rangle \xrightarrow{t \rightarrow -\infty} |\psi^{\text{in}}\rangle$.

The problem we are going to address in this section is to solve the Schrödinger equation for the time evolution operator $\mathcal{U}(t, t_0)$ in the interaction picture,

$$i\hbar \frac{d}{dt} \mathcal{U}(t, t_0) = \mathcal{H}^I(t) \mathcal{U}(t, t_0), \quad (2.25a)$$

$$\mathcal{H}^I(t) = \frac{\hbar\Omega(t)}{2} e^{-i\mathcal{K}t/\hbar} \left(e^{2i(k\hat{z} + \phi_L)} + e^{-2i(k\hat{z} + \phi_L)} \right) e^{i\mathcal{K}t/\hbar}, \quad (2.25b)$$

from which we construct the scattering (or transfer) matrix corresponding to the Bragg pulse:

$$\mathcal{S} = \lim_{\substack{t \rightarrow \infty \\ t_0 \rightarrow -\infty}} \mathcal{U}(t, t_0). \quad (2.26)$$

In order for the limits in Eq. (2.26) to be well defined, it is important to consider the time evolution in the interaction picture, where the Hamiltonian (2.25b) vanishes asymptotically for $t \rightarrow \pm\infty$. The Bragg scattering matrix maps asymptotic incoming onto asymptotic outgoing wave packets:

$$|\psi^{\text{out}}\rangle = \mathcal{S} |\psi^{\text{in}}\rangle. \quad (2.27)$$

In Sec. 2.3 we will derive the general structure of the Bragg scattering matrix without making any further assumption regarding the pulse shape $\Omega(t)$. We will then determine the specific shape that the scattering matrix takes, when the Rabi frequency is changed adiabatically. Moreover, we show that for efficient Gaussian Bragg pulses as in Eq. (2.9) adiabaticity is a necessary condition. To solve the equation of motion (2.25a) we will first use symmetries of the Hamiltonian (2.11) to divide it into sub-blocks, enabling the application of the adiabatic theorem in the first place. In addition, this greatly reduces the complexity of the problem of Bragg diffraction as a whole and will allow us to make quite general statements without assuming much about the specific shape $\Omega(t)$ of the Bragg pulse, and whether it operates in a diabatic or an adiabatic regime.

2.3.1 Hamiltonian in the Momentum Basis

First, we exploit the aforementioned property of the optical lattice potential to change the momentum of the atom only by a multiple of $2\hbar k$. The observation that, depending on whether n is an even (odd) number, a Bragg pulse maps a wave packet originally centered about $-n\hbar k$ to even (odd) momentum components only is formally reflected by expanding the Hamiltonian (2.11) in the momentum basis. In doing so, we group the momentum eigenstates $|m\hbar k + p\rangle$ into bins with $m \in \mathbb{Z}$ and introduce the (quasi)momentum $p \in [-\hbar k/2, \hbar k/2]$. From now on, the momentum variable p is always limited to this interval. Since efficient Bragg diffraction of atomic wave packets crucially depends on its narrow momentum width $\sigma_p \ll \hbar k$ [69] we can further constrain the (quasi)momenta p by assuming

$$\epsilon(p) = \frac{p}{\hbar k}, \quad (2.28)$$

to be a small parameter. This will allow us to solve the dynamics of the Bragg pulse for $p = 0$ and take into account first-order corrections in p perturbatively. The Hamiltonian in Eq. (2.11) then decomposes into blocks,

$$\mathcal{H}^{\text{MF}} = \int_{-\hbar k/2}^{\hbar k/2} dp \left\{ \mathcal{H}_e^{\text{MF}}(p) + \mathcal{H}_o^{\text{MF}}(p) \right\}, \quad (2.29)$$

where the components $\mathcal{H}_\alpha^{\text{MF}}(p)$ act on disjunct subspaces $\mathcal{H}_{p\alpha} = \text{span}\{|m\hbar k + p\rangle\}_{m \in \mathbb{Z}_\alpha}$ corresponding to even and odd momentum states for $\alpha = e, o$, respectively. We denote the set of even and odd integers by $\mathbb{Z}_e = 2\mathbb{Z}$ and $\mathbb{Z}_o = 2\mathbb{Z} + 1$. The total Hilbert space is $\mathcal{H} = \oplus_{p\alpha} \mathcal{H}_{p\alpha}$. Depending on whether n of the initial mean momentum is even or odd, the dynamics of the $(m\hbar k + p)$ -momentum components of the wave-packet are governed either by $\mathcal{H}_e^{\text{MF}}(p)$ or $\mathcal{H}_o^{\text{MF}}(p)$. We will see that these Hamiltonians have a very similar structure, but still feature important differences. With the notation

$$\hat{\sigma}_{m,j}(p) := |m\hbar k + p\rangle\langle j\hbar k + p|, \quad (2.30)$$

$m, j \in \mathbb{Z}$, the components of the Hamiltonian in subspace $\mathcal{H}_{p\alpha}$ can be expressed as

$$\mathcal{H}^{\text{MF}} = \int_{-\infty}^{\infty} dp \left\{ \frac{p^2}{2M} |p\rangle\langle p| + \frac{\hbar\Omega(t)}{2} \left(e^{2i\phi_L} |p + 2\hbar k\rangle\langle p| + \text{H.c.} \right) \right\} \quad (2.31)$$

$$= \int_{-\hbar k/2}^{\hbar k/2} dp \sum_{m=-\infty}^{\infty} \left\{ \frac{(m\hbar k + p)^2}{2M} |m\hbar k + p\rangle\langle m\hbar k + p| \right. \quad (2.32)$$

$$\left. + \frac{\hbar\Omega(t)}{2} \left(e^{2i\phi_L} |(m+2)\hbar k + p\rangle\langle m\hbar k + p| + \text{H.c.} \right) \right\} \quad (2.33)$$

$$= \int_{-\hbar k/2}^{\hbar k/2} dp \left\{ \mathcal{H}_e^{\text{MF}}(p) + \mathcal{H}_o^{\text{MF}}(p) \right\}, \quad (2.34)$$

where

$$\mathcal{H}_\alpha^{\text{MF}}(p) = \mathcal{K}_\alpha(p) + \sum_{m \in \mathbb{Z}_\alpha} \frac{\hbar \Omega(t)}{2} \left(e^{2i\phi_L} \hat{\sigma}_{m+2,m}(p) + \text{H.c.} \right), \quad (2.35)$$

$$\mathcal{K}_\alpha(p) = \sum_{m \in \mathbb{Z}_\alpha} \frac{(m \hbar k + p)^2}{2M} \hat{\sigma}_{m,m}(p), \quad (2.36)$$

for $\alpha \in \{e, o\}$. The summation in these equations is defined over even or odd numbers \mathbb{Z}_e or \mathbb{Z}_o , respectively. We note that the symbols in Eq. (2.30) were already used by Shankar et al. [141] in the context of atomic optics. We also would like to point out to the reader that (quasi)momentum variable p is not identical, but closely related, to the quasimomentum q_B in the sense of the Bloch theorem introduced in Sec. 2.2.3. Our choice is motivated by the fact that it naturally provides us with the decomposition of the Hilbert space into even and odd momentum bins in Eq. (2.29) and allows us to describe the dynamics of even and odd diffraction orders equally. It will be useful to expand the kinetic energy in two terms, $\mathcal{K}_\alpha(p) = \mathcal{L}_\alpha(p) + \mathcal{M}_\alpha(p)$, where the last term collects the components of the kinetic energy which are linear and quadratic in the (quasi)momentum variable p . That is,

$$\mathcal{L}_\alpha(p) = \sum_{m \in \mathbb{Z}_\alpha} \hbar \omega_r m^2 \hat{\sigma}_{m,m}(p), \quad (2.37)$$

$$\mathcal{M}_\alpha(p) = \sum_{m \in \mathbb{Z}_\alpha} \left(2\hbar \omega_r m \epsilon(p) + \frac{p^2}{2M} \right) \hat{\sigma}_{m,m}(p), \quad (2.38)$$

where we have expressed the kinetic energy in terms of the atomic recoil frequency ω_r and we have used $\epsilon(p)$ introduced in Eq. (2.28). We now move to an interaction picture with respect to the term $\mathcal{M}_\alpha(p)$. In this picture the asymptotic initial condition in Eq. (2.24) becomes

$$|\psi(t)\rangle \xrightarrow{t \rightarrow -\infty} e^{i\mathcal{M}_\alpha(p)t/\hbar} e^{-i\mathcal{K}t/\hbar} |\psi^{\text{in}}\rangle = e^{-in^2\omega_r t} |\psi^{\text{in}}\rangle. \quad (2.39)$$

Here, we leverage that the initial state $|\psi^{\text{in}}\rangle$ is localized in the momentum bin around $-n \hbar k$. The Hamiltonian in this interaction picture is

$$\mathcal{H}_\alpha(p) = \sum_{m \in \mathbb{Z}_\alpha} \hbar \omega_r m^2 \hat{\sigma}_{m,m}(p) + \frac{\hbar \Omega(t)}{2} \left(e^{2i(\phi_L + 2\epsilon(p)\omega_r t)} \hat{\sigma}_{m+2,m}(p) + \text{H.c.} \right). \quad (2.40)$$

The time dependence in the lattice potential reflects the Doppler shift of the two counter-propagating lattice beams seen by the components of the wave packet with (quasi)momentum p in $\mathcal{H}_{p\alpha}$. It is straightforward to check that if the unitary operator $\mathcal{V}_\alpha(p, t, t_0)$ on the subspace $\mathcal{H}_{p\alpha}$ is a solution of

$$i\hbar \frac{d}{dt} \mathcal{V}_\alpha(p, t, t_0) = \mathcal{H}_\alpha(p, t) \mathcal{V}_\alpha(p, t, t_0), \quad (2.41)$$

then the time evolution operator solving Eq. (2.25a) on the same subspace is

$$\mathcal{U}_\alpha(p, t, t_0) = \exp(i\mathcal{L}_\alpha(p)(t - t_0)/\hbar) \mathcal{V}_\alpha(p, t, t_0). \quad (2.42)$$

Our strategy will be to solve Eq. (2.41), and use this solution to construct the scattering matrix (2.26) using Eq. (2.42). So far, no approximation has been made. We now exploit the fact that the initial state is a narrow wave packet with a momentum spread $\sigma_p \ll \hbar k$ which amounts to $|\epsilon(p)| \ll 1$ for all (quasi)momentum components of the wave packet. Furthermore, we assume now that for the duration τ of the Bragg pulse we have $n\omega_r\tau\sigma_p \ll \hbar k$ for n th-order Bragg scattering, which is readily fulfilled when describing the coupling of atomic ensembles with narrow momentum widths in the quasi-Bragg regime. With this assumption we can expand the time-dependent phase in Eq. (2.40) to first order in $\epsilon(p)$. Performing a Taylor expansion $\epsilon(p)$ and collecting the terms of zeroth and first order in $\epsilon(p)$ one finds

$$\mathcal{H}_\alpha(p) = H_\alpha(p) + \epsilon(p)V_\alpha(p), \quad (2.43)$$

where

$$H_\alpha(p) = \sum_{m \in \mathbb{Z}_\alpha} \left\{ \hbar\omega_r m^2 \hat{\sigma}_{m,m}(p) + \frac{\hbar\Omega(t)}{2} \left(e^{2i\phi_L} \hat{\sigma}_{m+2,m}(p) + \text{H.c.} \right) \right\}, \quad (2.44a)$$

$$V_\alpha(p) = i2\hbar\Omega(t)\omega_r t \sum_{m \in \mathbb{Z}_\alpha} \left(e^{2i\phi_L} \hat{\sigma}_{m+2,m}(p) - \text{H.c.} \right). \quad (2.44b)$$

We recall that the Hamiltonian $\mathcal{H}_\alpha(p)$ acts on the subspace $\mathcal{H}_{p\alpha}$. Its components $H_\alpha(p)$ and $V_\alpha(p)$ in Eqs. (2.44) are structurally identical for all (quasi)momentum p . It is just the strength $\epsilon(p)$ of the perturbation $V_\alpha(p)$ in Eq. (2.43) due to the Doppler shift which has a nontrivial dependence on the (quasi)momentum p . In the next sections we will consider only the zeroth-order Hamiltonian (2.44a). The perturbation (2.44b) will be treated later on in Sec. 2.4.4.

2.3.2 Hamiltonian in the Basis of Symmetric and Antisymmetric States

Within each subspace $\mathcal{H}_{p\alpha}$ we introduce a new basis which consists of (anti)symmetric states $|p, m, \pm\rangle$ defined by

$$|p, m, \pm\rangle := \frac{1}{\sqrt{2}} \left(e^{im\phi_L} |m\hbar k + p\rangle \pm e^{-im\phi_L} |-m\hbar k + p\rangle \right), \quad (2.45a)$$

for $m \in \mathbb{N}/0$. We recall that ϕ_L is the laser phase. For $m = 0$ there is a single state in \mathcal{H}_{pe} :

$$|p, 0, +\rangle := |p\rangle. \quad (2.45b)$$

The total Hilbert space is $\mathcal{H} = \oplus_{p\alpha\pm} \mathcal{H}_{p\alpha\pm}$, where $\mathcal{H}_{p\alpha\pm} = \text{span}\{|p, m, \pm\rangle\}_{m \in \mathbb{Z}_\alpha}$ are the subspaces of symmetric and antisymmetric states in $\mathcal{H}_{p\alpha}$. When the Hamiltonian H_α in Eq. (2.44a) is expressed in this new basis it decomposes further into a sum of two terms,

$$H_\alpha = H_{\alpha+} + H_{\alpha-}, \quad (2.46)$$

which act on the disjunct spaces $\mathcal{H}_{p\alpha\pm}$. Before we explicitly construct the components $H_{\alpha\pm}$ we give an argument for why H_α has to be block diagonal in the basis of (anti)symmetric states. Consider the Hermitian operator

$$\Pi := \sum_{\alpha=\pm,0} \int_{-\hbar k/2}^{\hbar k/2} dp \Pi_\alpha(p), \quad (2.47)$$

$$\Pi_\alpha(p) = \sum_{m \in \mathbb{Z}_\alpha} e^{2mi\phi_L} \hat{\sigma}_{m,-m}(p), \quad (2.48)$$

which fulfills $\Pi^2 = 1$. Its eigenvalues are ± 1 , and the corresponding eigenvectors are the (anti)symmetric states, $\Pi|p, m, \pm\rangle = \pm|p, m, \pm\rangle$. It can be easily shown that H_α in Eq. (2.44a) is invariant under conjugation with Π , that is, $\Pi H_\alpha \Pi = H_\alpha$. Therefore, the commutator of these two operators vanishes, $[\Pi, H_\alpha] = 0$, and H_α cannot couple states corresponding to different eigenvalues with respect to Π . In other words, H_α has to be block diagonal as in Eq. (2.46). We note that Π is connected to reflections in momentum space, but is not equivalent to the parity operator. Setting the laser phase to zero, $\phi_L = 0$, the operators $\Pi_\alpha(p)$ generate reflections in momentum space about (quasi)momentum p in $\mathcal{H}_{p\alpha}$. The symmetry we are exploiting here will ultimately be broken by the Doppler detuning (2.44b). However, it will be almost conserved for sufficiently narrow initial wave packets and perturbation theory will be well suited to account for the effects of Doppler-induced breaking of this symmetry. We note that the basis of (anti)symmetric states in Eqs. (2.45) has been used recently also to analyze Bloch oscillations [142].

In order to identify the components $H_{\alpha\pm}$ of the Hamiltonian in Eq. (2.46) we define, in correspondence to (2.30),

$$\hat{\sigma}_{m,j}^\pm(p) := |p, m, \pm\rangle \langle p, j, \pm|. \quad (2.49)$$

Here, m and j are nonnegative integers and the operator $\hat{\sigma}_{m,j}^-(p)$ acting on the antisymmetric subspace is defined only for $m, j \neq 0$. The change to the basis of (anti)symmetric states and the transformation of the Hamiltonian (2.43) are straightforward given a few useful relations:

$$\hat{\sigma}_{m,m} + \hat{\sigma}_{-m,-m} = \hat{\sigma}_{m,m}^+ + \hat{\sigma}_{m,m}^-, \quad (m > 0), \quad (2.50)$$

$$\hat{\sigma}_{0,0} = \hat{\sigma}_{0,0}^+, \quad (2.51)$$

and for the case $n \geq 2$

$$e^{2i\phi_L}(\hat{\sigma}_{m+2,m} + \hat{\sigma}_{-m,-(m+2)}) + \text{H.c.} = \hat{\sigma}_{m+2,m}^+ + \hat{\sigma}_{m+2,m}^- + \text{H.c.}, \quad (2.52)$$

as well as

$$e^{2i\phi_L}(\hat{\sigma}_{2,0} + \hat{\sigma}_{0,-2}) + \text{H.c.} = \sqrt{2}(\hat{\sigma}_{2,0}^+ + \text{H.c.}), \quad (2.53)$$

$$e^{2i\phi_L}\hat{\sigma}_{1,-1} + \text{H.c.} = \hat{\sigma}_{1,1}^+ - \hat{\sigma}_{1,1}^-. \quad (2.54)$$

The result of this transformation is different for the Hamiltonian acting on the even and the odd subspace, i.e., for Bragg scattering of even or odd order n . One finds for the Hamiltonians acting on the even subspaces $\mathcal{H}_{pe\pm}$

$$\begin{aligned} H_{e-} &= \sum_{\substack{m \in \mathbb{N}_e \\ m \neq 0}} \left\{ \hbar\omega_r m^2 \hat{\sigma}_{m,m}^- + \frac{\hbar\Omega(t)}{2} (\hat{\sigma}_{m+2,m}^- + \text{H.c.}) \right\} \\ H_{e+} &= \sum_{\substack{m \in \mathbb{N}_e \\ m \neq 0}} \left\{ \hbar\omega_r m^2 \hat{\sigma}_{m,m}^+ + \frac{\hbar\Omega(t)}{2} (\hat{\sigma}_{m+2,m}^+ + \text{H.c.}) \right\} + \frac{\hbar\Omega(t)}{\sqrt{2}} (\hat{\sigma}_{2,0}^+ + \text{H.c.}), \end{aligned} \quad (2.55a)$$

and one finds for the Hamiltonians acting on the odd subspace $\mathcal{H}_{po\pm}$

$$H_{o\pm} = \sum_{m \in \mathbb{N}_o} \left\{ \hbar\omega_r m^2 \hat{\sigma}_{m,m}^\pm + \frac{\hbar\Omega(t)}{2} (\hat{\sigma}_{m+2,m}^\pm + \text{H.c.}) \right\} \pm \frac{\hbar\Omega(t)}{2} \hat{\sigma}_{1,1}^\pm. \quad (2.55b)$$

Thus, in both even and odd subspaces $\mathcal{H}_{p\alpha}$ the symmetric and antisymmetric subspaces $\mathcal{H}_{p\alpha\pm}$ decouple in zeroth order of the Doppler detuning, as expected. In writing the Hamiltonians (2.55) we have suppressed the (quasi)momentum p in all arguments. This can be done without loss of information, since all these Hamiltonians, just like the Hamiltonian of zeroth order in Eq. (2.44a), are structurally identical for all (quasi)momenta p . To simplify the notation, we therefore adhere to the following convention in this and all subsequent sections dealing exclusively with the zeroth-order Hamiltonian: The argument of $\hat{\sigma}_{m,j}^\pm$ and $\hat{\sigma}_{m,j}$ – as well as of all operators composed thereof – is p everywhere, unless stated otherwise. We will also suppress the momentum p in writing the basis vectors

$$|p, m, \pm\rangle \equiv |m, \pm\rangle, \quad (2.56)$$

and explicitly state the momentum p as an argument again, when we treat Doppler detuning in Sec. 2.4.4. In both even and odd subspaces the Hamiltonians in Eqs. (2.55a) and (2.55b) for the symmetric and antisymmetric subspace are very similar, but still show important differences: In the even subspace \mathcal{H}_{pe} the symmetric (+) subspace contains the state $|0, +\rangle$, while no such state exists for the antisymmetric (–) subspace. As a consequence, the Rabi frequency of the coupling between the states $|0, +\rangle$ and $|2, +\rangle$ [see last term in Eq. (2.55a)] is

enhanced by a factor of $\sqrt{2}$ compared to the coupling of other levels $|2m, \pm\rangle \leftrightarrow |2m + 2, \pm\rangle$ for $m > 0$. In order to make this more transparent, and for later reference, we give here a truncated representation of the Hamiltonians in the basis $(|6, -\rangle, |4, -\rangle, |2, -\rangle)$ for H_{e-} , and $(|6, +\rangle, |4, +\rangle, |2, +\rangle, |0, +\rangle)$ for H_{e+} :

$$H_{e-} = \hbar\omega_r \begin{pmatrix} 36 & w & 0 \\ w & 16 & w \\ 0 & w & 4 \end{pmatrix}, \quad H_{e+} = \hbar\omega_r \begin{pmatrix} 36 & w & 0 & 0 \\ w & 16 & w & 0 \\ 0 & w & 4 & \sqrt{2}w \\ 0 & 0 & \sqrt{2}w & 0 \end{pmatrix}, \quad (2.57a)$$

where we introduced $w \equiv w(t) := \Omega(t)/2\omega_r$. In the odd subspace \mathcal{H}_{po} the levels $|1, \pm\rangle$ have energies $\hbar\omega_r \pm \frac{\hbar\Omega(t)}{2}$ shifted proportionally to the Rabi frequency in opposite directions for the symmetric and the antisymmetric subspace [see last term in Eq. (2.55b)]. The energies of higher lying levels $|2m + 1, \pm\rangle$ for $m > 0$ are independent of the Rabi frequency. In a truncated basis $(|7, \pm\rangle, |5, \pm\rangle, |3, \pm\rangle, |1, \pm\rangle)$ one finds,

$$H_{o\pm} = \hbar\omega_r \begin{pmatrix} 49 & w & 0 & 0 \\ w & 25 & w & 0 \\ 0 & w & 9 & w \\ 0 & 0 & w & 1 \pm w \end{pmatrix}. \quad (2.57b)$$

After transforming the Hamiltonian to the basis of (anti)symmetric states we also have to consider, how the initial condition in Eq. (2.39) reads in this basis. An initial wave packet $|\psi^{\text{in}}\rangle$ composed of momentum states around an average momentum $-n\hbar k$ corresponds to an odd superposition of states in the symmetric and the antisymmetric subspace, $|-n\hbar k + p\rangle = \exp(in\phi_L)(|p, n, +\rangle - |p, n, -\rangle)/\sqrt{2}$. If we were to perform, e.g., a mirror pulse transferring a momentum $2n\hbar k$ to the atom, the challenge is to change this state into the even superposition $\exp(-in\phi_L)(|p, n, +\rangle + |p, n, -\rangle)/\sqrt{2} = |n\hbar k + p\rangle$. This is expressed more formally in terms of the scattering matrix.

2.3.3 General Structure of the Bragg Scattering Matrix

Based on the decomposition of the Bragg Hamiltonian into its sub-blocks (2.55) we will now determine the scattering matrix (2.26) for a Bragg pulse. To zeroth order in the Doppler detuning, the dynamics in the subspace $\mathcal{H}_{p\alpha}$ is governed by the Hamiltonian $H_\alpha(t)$ in Eq. (2.46) which is block-diagonal in the subspaces $\mathcal{H}_{p\alpha\pm}$. Therefore, the unitary evolution operator will be of the form

$$U_\alpha(t, t_0) = U_{\alpha+}(t, t_0) + U_{\alpha-}(t, t_0), \quad (2.58)$$

where $U_{\alpha\pm}(t, t_0)$ acts on $\mathcal{H}_{p\alpha\pm}$ only, and fulfills the Schrödinger equation

$$i\hbar \frac{d}{dt} U_{\alpha\pm}(t, t_0) = H_{\alpha\pm}(t) U_{\alpha\pm}(t, t_0). \quad (2.59)$$

In zeroth order of Doppler detuning, i.e., in zeroth order of $\epsilon(p)$, the formal solution (2.58) provides already the solution to Eq. (2.41). Using $\mathcal{V}_\alpha(t, t_0) = U_\alpha(t, t_0)$ in Eq. (2.42), we find that the Bragg scattering matrix from Eq. (2.26) on the subspace $\mathcal{H}_{p\alpha}$ is

$$\mathcal{S}_\alpha = \lim_{\substack{t \rightarrow \infty \\ t_0 \rightarrow -\infty}} \exp(i\mathcal{L}_\alpha(t - t_0)/\hbar) U_\alpha(t, t_0) = \mathcal{S}_{\alpha+} + \mathcal{S}_{\alpha-}. \quad (2.60)$$

The block diagonal structure of the formal solution (2.58) and the diagonal form of \mathcal{L}_α [cf. Eq. (2.37)] imply that the scattering matrix is also block diagonal in the (anti)symmetric basis.

Single n th-order Bragg diffraction pulses are supposed to couple the momentum eigenstates in the incoming wave packet $| -n \hbar k + p \rangle \longleftrightarrow | n \hbar k + p \rangle$ (for $n > 0$), and ideally execute $\pi/2$ or π pulses in this two-dimensional subspace. What ultimately enters in an interferometer sequence is not the full Bragg scattering matrix of Eq. (2.60), but rather its projection into this two-dimensional subspace. In terms of the basis of (anti)symmetric states this subspace is spanned by the states $|n, \pm\rangle$, see Eq. (2.45a). Due to the block-diagonal structure, the projection of the scattering matrix in (2.60) yields a diagonal matrix in the basis $(|n, +\rangle, |n, -\rangle)$:

$$\begin{aligned} \mathcal{S}_\alpha &= \sum_{s, s' = \pm} \mathcal{S}_{ss'} |n, s\rangle \langle n, s'|, \\ S &= \begin{pmatrix} e^{-i\theta_{n+} - \gamma_{n+}} & 0 \\ 0 & e^{-i\theta_{n-} - \gamma_{n-}} \end{pmatrix}, \end{aligned} \quad (2.61)$$

where

$$e^{-i\theta_{n\pm} - \gamma_{n\pm}} = \langle n, \pm | \mathcal{S}_{\alpha\pm} | n, \pm \rangle = \lim_{\substack{t \rightarrow \infty \\ t_0 \rightarrow -\infty}} e^{in^2\omega_r(t-t_0)} \langle n, \pm | U_{\alpha\pm}(t, t_0) | n, \pm \rangle. \quad (2.62)$$

The parameters $\theta_{n\pm}$ and $\gamma_{n\pm}$ describe scattering phases and population loss from the states $|n, \pm\rangle$. Since the scattering matrices $\mathcal{S}_{\alpha\pm}$ are unitary in the idealized lossless case, we have $\gamma_{n\pm} \geq 0$. It is important to note that the general form of the scattering matrix S applies regardless of the exact shape $\Omega(t)$ of the Bragg pulse. Moreover, it is instructive to write the projected Bragg scattering matrix (2.61) in the basis of momentum states $(|+n \hbar k + p\rangle, |-n \hbar k + p\rangle)$. The transformation from the (anti)symmetric states $|n, \pm\rangle$ to momentum states can be read off from Eqs. (2.45):

$$T = \frac{1}{\sqrt{2}} \begin{pmatrix} e^{in\phi_L} & e^{-in\phi_L} \\ e^{in\phi_L} & -e^{-in\phi_L} \end{pmatrix}. \quad (2.63)$$

With Eq. (2.61) one finds the projected Bragg scattering matrix in the momentum basis, $B := T^\dagger S T$, yielding

$$B(\Phi_n - i\Gamma, \Theta_n - i\gamma) = e^{-i\frac{\Phi_n - i\Gamma}{2}} \begin{pmatrix} \cos\left(\frac{\Theta_n - i\gamma}{2}\right) & -ie^{-i2n\phi_L} \sin\left(\frac{\Theta_n - i\gamma}{2}\right) \\ -ie^{+i2n\phi_L} \sin\left(\frac{\Theta_n - i\gamma}{2}\right) & \cos\left(\frac{\Theta_n - i\gamma}{2}\right) \end{pmatrix}. \quad (2.64)$$

We define the differential phase between the symmetric and the antisymmetric state $|n, \pm\rangle$ and the global phase imprinted on this subspace,

$$\Theta_n = \theta_{n+} - \theta_{n-}, \quad \Phi_n = \theta_{n+} + \theta_{n-}, \quad (2.65)$$

and the corresponding parameters characterizing differential and total loss:

$$\gamma = \gamma_{n+} - \gamma_{n-}, \quad \Gamma = \gamma_{n+} + \gamma_{n-}. \quad (2.66)$$

We remind the reader that ϕ_L denotes the relative laser phase between the two light fields generating the optical lattice. We also note that the global phase Φ should not be confused with the global phase Φ_G which includes the average ac Stark shift and has been gauged out in the picture of the fundamental Hamiltonian (2.11).

Comparison to Ideal Bragg Operations

Comparison of the scattering matrix in Eq. (2.64) to the one corresponding to an ideal n th-order Bragg pulse, the form of which is well known (see, e.g., [125]),

$$\mathcal{S}_{\Theta_n}^{\text{ideal}} = \int_{-\hbar k/2}^{\hbar k/2} dp \sum_{s,s'=\pm} [B_{\Theta_n}]_{ss'} |s n \hbar k + p\rangle \langle s' n \hbar k + p|, \quad (2.67)$$

allows us to identify conditions to achieve high-quality pulse operations. For a beam splitter pulse ($\Theta_n = \pi/2$) the matrix B_{Θ_n} in Eq. (2.67) takes the form

$$B_{\pi/2} = \frac{1}{\sqrt{2}} \begin{pmatrix} 1 & -ie^{-i2n\phi_L} \\ -ie^{+i2n\phi_L} & 1 \end{pmatrix}, \quad (2.68a)$$

and for a mirror pulse ($\Theta_n = \pi$),

$$B_{\pi} = \begin{pmatrix} 0 & -ie^{-i2n\phi_L} \\ -ie^{+i2n\phi_L} & 0 \end{pmatrix}. \quad (2.68b)$$

This should also be true for the matrix in Eq. (2.64), albeit only in an ideal hypothetical limit. To achieve this, the differential phase collected between symmetric and asymmetric subspace needs to be tuned to $\Theta_n = \pi/2$ for a beam splitter and to $\Theta_n = \pi$ for a mirror pulse. Hence, it can be seen that the differential phase Θ_n is identical to what is usually referred to as the pulse area. The global phase Φ_n does not necessarily have to be nulled in order to achieve a good pulse quality, but it must be controlled and included in the phase budget of an interferometer (cf. [98, 116, 119, 135]). Finally, to maintain the population in the subspace $|n, \pm\rangle$ and avoid losses to other momentum states, ideally the condition $\gamma_{n\pm} = 0$ should be fulfilled. In view of Eq. (2.62) this is tantamount to

$$\lim_{\substack{t \rightarrow \infty \\ t_0 \rightarrow -\infty}} |\langle n, \pm | U_{\alpha\pm}(t, t_0) | n, \pm \rangle| = 1, \quad (2.69)$$

where the unitaries $U_{\alpha\pm}(t, t_0)$ are the solutions to the Schrödinger Eqs. (2.59). Thus, in both the symmetric and the antisymmetric subspace an initial population of $|n, \pm\rangle$ ultimately has to return to this state. This presents a highly nontrivial constraint in view of the fact that the Hamiltonians $H_{\alpha\pm}(t)$ in these two subspaces differ structurally but are controlled through the same Rabi frequency $\Omega(t)$.

The challenge is to identify a pulse $\Omega(t)$ that meets all of these requirements. As we will establish in the next section, a sufficient condition on $\Omega(t)$ for achieving this is that the Rabi frequency is tuned adiabatically in the sense of the adiabatic theorem: thereby the initial population of $|n, \pm\rangle$ is maintained at all times in a corresponding instantaneous energy eigenstate of $H_{\alpha\pm}(t)$, and is thus perfectly restored to $|n, \pm\rangle$ at the end of the pulse, satisfying Eq. (2.69). As an ideal adiabatic tuning requires infinitely long pulse durations, it is important to consider also effects of nonadiabaticity, and to determine the impact of a finite pulse duration on the Bragg pulses. We do so in Secs. 2.4.1 and 2.4.3. In Sec. 2.6 we will show for the specific but most relevant case of a Gaussian pulse [see Eq. (2.9)] that each pair of peak Rabi frequencies Ω and pulse durations τ leading to a high-quality Bragg $\pi/2$ - or π -pulse with losses at an acceptable level does indeed correspond to adiabatic dynamics with first-order nonadiabatic corrections. Thus, for Gaussian pulses adiabaticity in the sense of the adiabatic theorem is a necessary and sufficient condition. It is interesting, but beyond the scope of this thesis, to ponder, whether a nonadiabatic Bragg pulse $\Omega(t)$, i.e., a pulse that produces real transitions among the instantaneous energy eigenstates of $H_{\alpha\pm}(t)$, can at all give rise to high-quality atom optics operations.

2.3.4 Scattering Matrix for Adiabatic Bragg Pulses

We now consider the important special case of an adiabatic tuning of the Rabi frequency $\Omega(t)$. As shown in Fig. 2.3, the energy spectrum of the Hamiltonians $H_{\alpha\pm}$ is nondegenerate for any fixed value of Ω , and no level crossing occurs. This means that the quantum numbers labeling the eigenstates $|m, \pm\rangle$ corresponding to eigenenergies $m^2\hbar\omega_r$ for vanishing Rabi frequency, $\Omega = 0$, remain good quantum numbers also for $\Omega \neq 0$. Here, we note that this is only the case because we are working in an interaction picture with respect to the Doppler shift term in Eq. (2.38). For a time-dependent Rabi frequency $\Omega(t)$ we denote the instantaneous eigenstates and eigenenergies by

$$H_{\alpha\pm}(t) |m, \pm; t\rangle = E_{m\pm}(t) |m, \pm; t\rangle. \quad (2.70a)$$

with $m \in \mathbb{N}_\alpha$ and $m > 0$. For $\alpha = e$ and $m = 0$ there is only one eigenstate,

$$H_{e+}(t) |0, +; t\rangle = E_{0+}(t) |0, +; t\rangle. \quad (2.70b)$$

In the asymptotic limits, where $\lim_{t \rightarrow \pm\infty} \Omega(t) = 0$, we have

$$\lim_{t \rightarrow \pm\infty} |m, \pm; t\rangle = |m, \pm\rangle. \quad (2.71)$$

The instantaneous eigenstates and eigenenergies can be calculated from Eqs. (2.55a) and (2.55b) for a given Rabi frequency $\Omega(t)$ with a suitable truncation of the Hilbert space. Due to the block decomposition of the Hamiltonian excellent results can be achieved for a relatively low order of truncation, as will be seen in Sec. 2.6. In the following, we will express all the results in a form that requires only the numerical calculation of the instantaneous energy eigenvalues, which is an efficient subroutine. The much more involved calculation of energy eigenstates can be avoided by suitable approximations.

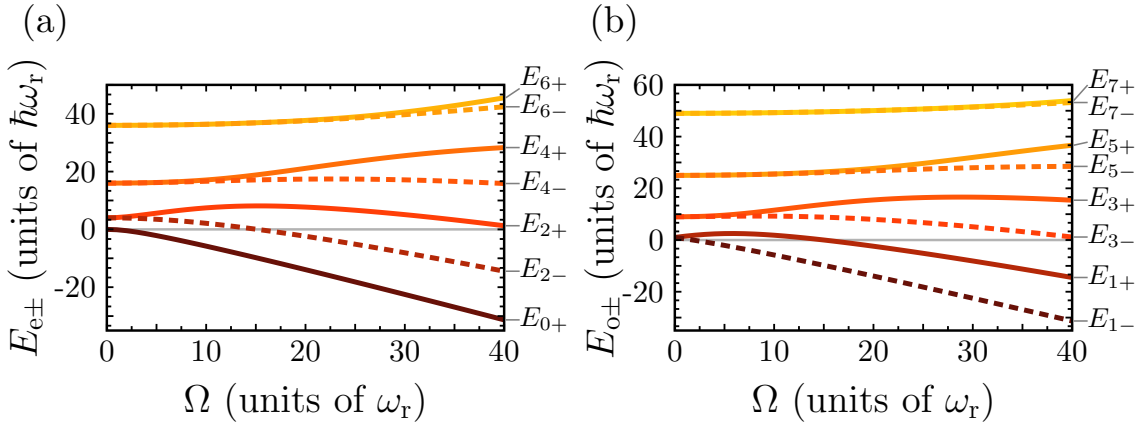


Figure 2.3: **Eigenenergies of the Bragg Hamiltonian.** Spectra of the lowest-energy eigenstates of the Hamiltonians in the (anti)symmetric subspaces vs constant Rabi frequencies Ω in (a) the even subspace, $H_{e\pm}$ in Eq. (2.55a), and (b) the odd subspace, $H_{o\pm}$ in Eq. (2.55b), with truncations $m_{\max,e} = 8$ and $m_{\max,o} = 11$, respectively. The range for Ω includes Rabi frequencies required for high-fidelity quasi-Bragg pulses up to order $n = 5$, which will be shown in Sec. 2.6. Figure adapted from *J.-N. Siemss et al., Phys. Rev. A* **102**, 033709 (2020), Copyright 2022, American Physical Society (Ref. [120]).

The adiabatic theorem states that for an infinitely slow tuning, that is, for an infinitely long pulse $\tau \rightarrow \infty$, no transitions among the energy eigenstates of $H_\alpha(t)$ occur. Thus, the ideal adiabatic solution to Eq. (2.59) is

$$U_{\alpha\pm}(t, t_0) = \sum_{m \in \mathbb{N}_\alpha} e^{-i\theta_{m\pm}(t, t_0)} |m, \pm; t\rangle \langle m, \pm; t_0|, \quad (2.72a)$$

with dynamic phases

$$\theta_{m\pm}(t, t_0) = \frac{1}{\hbar} \int_{t_0}^t dt_1 E_{m\pm}(t_1). \quad (2.72b)$$

In the present case, since the Hamiltonian depends on time only through a single parameter $\Omega(t)$, no geometric phase can occur. In the ideal adiabatic regime and to zeroth order in Doppler detuning, Bragg diffraction simply imprints phases on the (anti)symmetric states $|n, \pm\rangle$. With Eqs. (2.72) and (2.71) the limit in Eq. (2.62) yields a unitary scattering matrix S with $\gamma_{n\pm} = 0$ and dynamic scattering phases $\theta_{n\pm} = \theta_{n\pm}^{\text{dyn}}$ with

$$\theta_{n\pm}^{\text{dyn}} = \frac{1}{\hbar} \int_{-\infty}^{\infty} dt \left(E_{n\pm}(t) - \hbar\omega_r n^2 \right). \quad (2.73)$$

From the structure of the Hamiltonians (2.55) it is clear that any differential phase between symmetric and antisymmetric subspace can only arise by coupling the incoming momentum states $|n, \pm\rangle$ to the lowest states in the spectrum of $H_{\alpha\pm}$, since these Hamiltonians differ only there. From the spectrum shown in Fig. 2.3, it is also evident that a suitable energy splitting between the states $|n, \pm\rangle$ for practical Rabi frequencies $\Omega(t)$ is only possible for low orders of Bragg diffraction. While the logic developed here is applicable to arbitrary Bragg orders n , the figure demonstrates the power requirements of higher Bragg diffraction orders. For example, for $\Omega \lesssim 40\omega_r$, one can expect Bragg diffraction to be efficient only up to $n \leq 5$, which we confirm by numerical simulations in Sec. 2.6. S. S. Szigeti et al. [69] showed that Bragg pulses of orders $n > 5$ suffer from substantial atom loss due to spontaneous emission rendering them unsuitable for state-of-the-art light pulse atom interferometers that rely on high-fidelity atom optics. Consequentially, LMT atom interferometry experiments have in the past either employed single Bragg pulses of orders $n \leq 5$ [64, 94, 97, 98, 104, 109, 111] or combined several "low-order" pulses sequentially [64, 94, 96–98]. For these reasons, we restrict our study to the experimentally relevant cases $n \leq 5$. For later purposes, it will be useful to rewrite the dynamic phase as

$$\theta_{n\pm}^{\text{dyn}} = \tau\omega_r x_{n\pm}(\Omega), \quad (2.74)$$

$$x_{n\pm}(\Omega) = \int_{-\infty}^{\infty} d\zeta \left(\frac{E_{n\pm}(\zeta\tau)}{\hbar\omega_r} - n^2 \right), \quad (2.75)$$

where $x_{n\pm}(\Omega)$ is a dimensionless quantity that generally depends on the exact pulse form $\Omega(t)$ and in particular on the peak Rabi frequency $\Omega = \max_{\{t\}} \Omega(t)$, which we display in Fig. 2.4(a)-(d). Moreover, we introduce a dimensionless time $\zeta = t/\tau$ for a characteristic pulse duration τ . We will see that the dynamic phases (2.74) largely capture the physics of the Bragg pulses, but not with the precision we want to achieve here. In the next section we will therefore treat corrections beyond the ideal adiabatic limit.

2.4 Nonadiabatic Corrections and Doppler Detuning

Corrections beyond the ideal adiabatic limit are two-fold. First, nonadiabatic transitions from $|n, \pm\rangle$ to other states in the respective subspace $\mathcal{H}_{\rho\alpha\pm}$ result in losses of population,

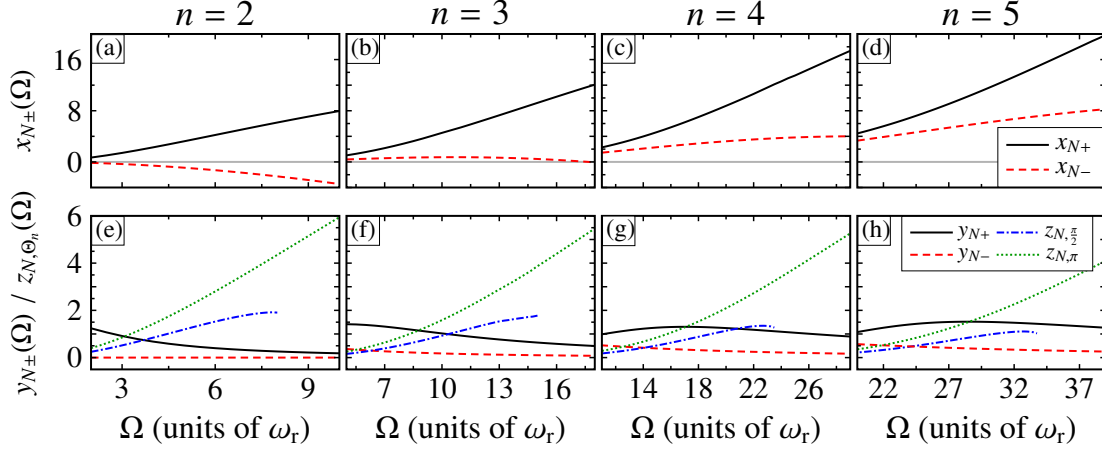


Figure 2.4: **Dimensionless Bragg diffraction parameters.** The parameters are linked to the dynamics phase $x_{n,\pm}$ (2.75) [top row, panels (a)-(d)], the LZ phase $y_{n,\pm}$ (2.90), and the Doppler detuning z_{n,Θ_n} (A.9) [bottom row, panels (e)-(h)] for Bragg orders $n = 2, 3, 4, 5$ (left to right). These are plotted as functions of the peak Rabi frequency Ω and assuming a Gaussian temporal pulse shape. The width of the pulse is fixed by Eq. (2.92). Note that for large values Ω the blue dash-dotted lines representing $z_{n,\frac{\pi}{2}}$ (bottom row) break off as solutions of Eq. (2.92) become imaginary. Such short pulse durations require additional higher-order corrections in τ^{-1} that we do not consider in Eq. (2.89), since this regime is not relevant for high-fidelity beam splitter pulses with Gaussian envelopes, as we will show in Sec. 2.6. Figure adapted from *J.-N. Siemss et al., Phys. Rev. A* **102**, 033709 (2020), Copyright 2022, American Physical Society (Ref. [120]).

$\gamma_{n\pm} \neq 0$. We describe these losses by LZ theory in Sec. 2.4.3. Second, by nonadiabatic off-resonant coupling of the states $|n, \pm\rangle$ to other states within $\mathcal{H}_{p\alpha\pm}$ a further phase is generated, which in addition to the dynamic phase contributes in order τ^{-1} to the net scattering phase of the states $|n, \pm\rangle$. We refer to this contribution as LZ phases $\theta_{n\pm}^{\text{LZ}}$. We will now illustrate how the LZ phases and loss parameters can be calculated, at least approximately, from the Hamiltonians in Eqs. (2.55) and their eigenenergies in Eq. (2.70). As mentioned above, we will focus on Bragg diffraction of order $n \leq 5$ (corresponding to a momentum transfer of at most $10 \hbar k$), and demonstrate that both LZ phases and losses can be understood largely in terms of two-level physics.

2.4.1 Nonadiabatic Corrections: Landau-Zener (LZ) Phases

To cover the LZ phases, we look for a solution of Eq. (2.59) that is nondiagonal in the basis of instantaneous energy eigenstates, i.e.,

$$U_{\alpha\beta}(t, t_0) = \sum_{m,j \in \mathbb{N}_\alpha} e^{-i\theta_{m\beta}(t,t_0)} c_{mj}^\beta(t) |\beta, m, p; t\rangle \langle \beta, j, p; t_0|. \quad (2.76)$$

In the ideal adiabatic limit we have $c_{mj}^\beta(t) = \delta_{mj}$. Beyond the adiabatic limit we are particularly interested in the corrections to the coefficients $c_{mn}^\beta(t)$ as these enter the scattering matrix (2.61). Inserting the ansatz for $U_{\alpha\beta}(t, t_0)$ from Eq. (2.76) into the equation of motion (2.59), using $\partial_t \theta_{l\beta}(t, t_0) = E_{l\beta}(t)/\hbar$, and taking the matrix element $\langle \beta, m, p; t | \dots | \beta, j, p; t_0 \rangle$ one finds

$$\dot{c}_{mj}^\beta(t) = - \sum_{l \in \mathbb{N}_\alpha} e^{-i[\theta_{l\beta}(t, t_0) - \theta_{m\beta}(t, t_0)]} G_{ml}^\beta(t) c_{lj}^\beta(t), \quad (2.77)$$

where $G_{ml}^\beta(t) = \langle \beta, m, p; t | \partial_t | \beta, l, p; t \rangle$. As usual in the analysis of LZ dynamics, it is convenient to impose the gauge condition of parallel transport, where $G_{mm}^\beta(t) = 0$ (see [143]). The set of equations (2.77) should be solved with initial condition $c_{mj}^\beta(0) = \delta_{mj}$. For the relevant coefficient $c_{mn}^\beta(t)$ one finds

$$\dot{c}_{nn}^\beta(t) = - \sum_{\substack{l \in \mathbb{N}_\alpha \\ l \neq n}} e^{-i[\theta_{l\beta}(t, t_0) - \theta_{n\beta}(t, t_0)]} G_{nl}^\beta(t) c_{ln}^\beta(t), \quad (2.78)$$

$$\dot{c}_{ln}^\beta(t) = -e^{-i[\theta_{n\beta}(t, t_0) - \theta_{l\beta}(t, t_0)]} G_{ln}^\beta(t) c_{nn}^\beta(t). \quad (2.79)$$

In the last equation, we kept only the leading term in the sum. The adiabatic solution to the last equation is

$$c_{ln}^\beta(t) = -i\hbar e^{-i[\theta_{n\beta}(t, t_0) - \theta_{l\beta}(t, t_0)]} \frac{G_{ln}^\beta(t)}{E_{n\beta}(t) - E_{l\beta}(t)} c_{nn}^\beta(t). \quad (2.80)$$

Inserting this into Eq. (2.78) and renaming the index $l \rightarrow m$ for consistency yields

$$\dot{c}_{nn}^\beta(t) = i\hbar \sum_{\substack{m \in \mathbb{N}_\alpha \\ m \neq n}} \frac{|G_{mn}^\beta(t)|^2}{E_{n\beta}(t) - E_{m\beta}(t)} c_{nn}^\beta(t). \quad (2.81)$$

Solving the resulting equation and taking the limit for final or initial times to $\pm\infty$, respectively, we obtain $c_{nn}^\beta = \exp(i\theta_{n\beta}^{\text{LZ}})$, where the LZ phase is given by

$$\theta_{n\beta}^{\text{LZ}} = \hbar \int_{-\infty}^{\infty} dt \sum_{\substack{m \in \mathbb{N}_\alpha \\ m \neq n}} \frac{|G_{mn}^\beta(t)|^2}{E_{n\beta}(t) - E_{m\beta}(t)}, \quad (2.82)$$

$$\theta_{n\pm}^{\text{LZ}} = \hbar \int_{-\infty}^{\infty} dt \sum_{\substack{m \in \mathbb{N}_\alpha \\ m \neq n}} \frac{|\langle m, \pm; t | \partial_t | n, \pm; t \rangle|^2}{E_{n\pm}(t) - E_{m\pm}(t)}. \quad (2.83)$$

According to Eq. (2.83), the LZ phases are acquired by the states $|n, \pm\rangle$ due to their off-resonant nonadiabatic coupling to other states in $\mathcal{H}_{p\alpha\pm}$. These phases are given by a rather intuitive expression resulting from a standard application of perturbation theory beyond the adiabatic approximation. The result (2.83) is correct to first order in the adiabaticity

parameter $|\langle m, \pm; t | \partial_t | n, \pm; t \rangle| / (E_{n\pm}(t) - E_{m\pm}(t))$ and is similar in spirit to corrections derived in Ref. [144]. As it stands, the expression for the LZ phases is not very suitable for making quantitative statements. The reason being that the sum runs over all states in $\mathcal{H}_{p\alpha\pm}$ which are different from $|n, \pm\rangle$, and also that it is cumbersome to calculate the matrix elements in the numerator of the integrand.

Two-level Approximation for Bragg Order $n = 2$

Both of these difficulties can be remedied by invoking an appropriate two-level approximation. The idea is to restrict the sum in Eq. (2.83) to its dominant term, which describes the coupling of the state $|n, \pm\rangle$ to the energetically closest state $|n - 2, \pm\rangle$ ³. While the state $|n + 2, \pm\rangle$ also is energetically close, the coupling to it becomes relevant only for Rabi frequencies $\Omega(t)$ that turn out to be prohibitive for high-fidelity Bragg diffraction. We will see later in Sec. 2.6.3 that the Bragg condition can no longer be perfectly satisfied anymore in the case of a Gaussian pulse shape, since nonadiabatic phase contributions occur for these parameters in addition to large losses to other diffraction orders (see also Sec. 2.4.3). If we combine the simplified sum in Eq. (2.83) with a suitable truncation of the Hamiltonian (2.55) to the two-dimensional subspace composed of $|n, \pm\rangle$ and $|n - 2, \pm\rangle$, the matrix element in the numerator on the right-hand side of Eq. (2.83) can be evaluated exactly. In Sec. 2.6.2 we will show that this approximation indeed gives excellent agreement when compared to the numerical results.

In order to explain this idea in more detail, we consider Bragg diffraction of order $n = 2$ as a concrete example. In this case, in the symmetric subspace the level closest to $|2, +\rangle$ is $|0, +\rangle$ [see Hamiltonian (2.57a)]. The coupling of $|2, +\rangle$ to the higher-lying state $|4, +\rangle$ is discarded. The Hamiltonian (2.57a) restricted to the two-level subspace ($|2, +\rangle, |0, +\rangle$) reads

$$H_{e,+}^{(2)}(t) = \hbar\omega_r \begin{pmatrix} 4 & \sqrt{2}w \\ \sqrt{2}w & 0 \end{pmatrix}, \quad (2.84)$$

where we use again $w = \Omega(t)/2\omega_r$. In the antisymmetric subspace the state $|2, -\rangle$ has no lower-lying partner, and its coupling to the higher-lying state $|4, -\rangle$ is of the same order as the coupling already discarded in the symmetric subspace. Thus, the truncated Hamiltonian is trivial, $H_{e,-}^{(2)} = 4\hbar\omega_r$, and the state $|2, -\rangle$ will not acquire a LZ phase in the order considered. For the truncated Hamiltonian (2.84) eigenenergies and state overlaps in Eq. (2.83) can be evaluated analytically. The corresponding LZ phase can then be expressed as a simple time integral which must be evaluated numerically for a given pulse shape $\Omega(t)$.

³This is true for the higher order Bragg diffraction $n \geq 2$. In the case of $n = 1$, the energetically closest states are $|n + 2, \pm\rangle = |3, \pm\rangle$. However, since the two-level Hamiltonians derived in this section are identical, the obtained correction value is the same.

Two-level Approximation for Bragg Orders $n = 3, 4, 5$

Bragg diffraction of higher order can be treated in a similar way with minor complications due to ac Stark shifts. For $n = 3$ one gets from Eq. (2.57b)

$$H_{0,\pm}^{(3)} = \hbar\omega_r \begin{pmatrix} 9 & w \\ w & 1 \pm w \end{pmatrix}. \quad (2.85)$$

For the other relevant cases $n = 4$ and 5 a similar truncation can be performed, but will produce worse results, since now also lower-lying states ($|+, 0, p\rangle$ for $n = 4$, and $|\pm, 1, p\rangle$ for $n = 5$) are neglected, which are of great importance for the spectrum of the Hamiltonians in Eqs. (2.57). This is clearly visible in the avoided crossings in Fig. 2.3. In order to reduce the truncation error it is appropriate to perform a pre-diagonalization of the lower two levels. For $n = 4$ this requires us to diagonalize $H_{e,+}^{(2)}(t)$ in Eq.(2.84) to compute the eigenstates and eigenvalues in the dressed basis. We discard the dressed state with the lower eigenenergy and assume that the second eigenstate and the state corresponding to $n = 4$ form a new effective two-level system. This procedure yields for $n = 4$ and $n = 5$

$$H_{e,\pm}^{(4)} = \hbar\omega_r \begin{pmatrix} 16 & q_{4\pm}w \\ q_{4\pm}w & e_{4\pm}(w) \end{pmatrix}, \quad H_{0,\pm}^{(5)} = \hbar\omega_r \begin{pmatrix} 25 & q_{5\pm}w \\ q_{5\pm}w & e_{5\pm}(w) \end{pmatrix}, \quad (2.86)$$

where $e_{4-} = 4$, $e_{4+}(w) = 2 + \sqrt{4 + 2w^2}$, and $e_{5\pm}(w) = 5 \pm w/2 + \sqrt{16 \mp 4w + 5w^2/4}$ are the larger eigenenergies resulting from the diagonalization of $H_{e,+}^{(2)}(t)$ and $H_{0,\pm}^{(3)}$, respectively. The expressions for e_{4+} and $e_{5\pm}$ correspond to the larger eigenvalues of $H_{e,+}^{(2)}$ and $H_{0,\pm}^{(3)}$, respectively. The off-diagonal elements in the Hamiltonians (2.86) are as well affected by the pre-diagonalization and in principle have a more complicated w dependence. In effect, the coupling will be somewhat smaller than w on average. We account for this by including a parameter $q_{n\beta}$ which we fit to numerical data. Thus, truncated Hamiltonians in all cases

| n | β | $q_{n\beta}$ | $e_{n\beta}(w)$ |
|-----|---------|--------------|-------------------------------------|
| 2 | + | $\sqrt{2}$ | 0 |
| 2 | - | 0 | 0 |
| 3 | + | 1 | $1 + w$ |
| 3 | - | 1 | $1 - w$ |
| 4 | + | 0.58 | $2 + \sqrt{4 + 2w^2}$ |
| 4 | - | 1 | 4 |
| 5 | + | 0.45 | $5 + w/2 + \sqrt{16 - 4w + 5w^2/4}$ |
| 5 | - | 1 | $5 - w/2 + \sqrt{16 + 4w + 5w^2/4}$ |

Table 2.1: Parameters to determine the LZ phases.

$n = 2, 3, 4, 5$ can be written in the form

$$H_{\alpha,\beta}^n = \hbar\omega_r \begin{pmatrix} n^2 & q_{n\beta}w \\ q_{n\beta}w & e_{n\beta}(w) \end{pmatrix}, \quad (2.87)$$

where the parameters $q_{n\beta}$ and functions $e_{n\beta}(w)$ are summarized in Table 2.1. Let the normalized eigenvectors and eigenvalues of this matrix be $|v_j\rangle$ and E_j for $j = 1, 2$. One can check that ($E_1 > E_2$)

$$\hbar\omega_r \frac{|\langle v_1 | \partial_w | v_2 \rangle|^2}{E_1 - E_2} = \frac{q_{n\beta}^2 [n^2 - e_{n\beta}(w) + w\partial_w e_{n\beta}(w)]^2}{\left\{ [n^2 - e_{n\beta}(w)]^2 + 4q_{n\beta}^2 w^2 \right\}^{5/2}}. \quad (2.88)$$

The second ratio on the right-hand side tends to $q^2/64(n-1)^3$ for $w \rightarrow 0$, and vanishes (not necessarily monotonically) for $w \rightarrow \infty$.

Effective Two-level LZ Phases

Using this general result and substituting it into Eq. (2.83), the effective LZ phases in all cases $n \leq 5$ can be expressed as

$$\theta_{n\pm}^{\text{LZ}} = \frac{1}{\omega_r} \int_{-\infty}^{\infty} dt \left(\frac{dw(t)}{dt} \right)^2 \frac{|\langle v_1 | \partial_w | v_2 \rangle|^2}{E_1 - E_2} = \frac{y_{n\pm}(\Omega)}{256(n-1)^3} \frac{\Omega^2}{\omega_r^3 \tau}, \quad (2.89)$$

where

$$y_{n\pm}(\Omega) = \int_{-\infty}^{\infty} d\zeta \left(\frac{\partial_\zeta \Omega(\zeta)}{\Omega} \right)^2 \frac{64q_{n\pm}^2 (n-1)^3 [n^2 - e_{n\pm}(w) + w\partial_w e_{n\pm}(w)]^2}{\left\{ [(n^2 - e_{n\pm}(w))]^2 + 4q_{n\pm}^2 w^2 \right\}^{5/2}}. \quad (2.90)$$

Here, $w(\zeta) = \Omega(\zeta)/2\omega_r$ and $\zeta = t/\tau$ is a dimensionless time scaled to the (effective) pulse duration τ and $\Omega = \max_{\{\zeta\}} \Omega(\zeta)$ is the peak Rabi frequency. The parameter $y_{n\beta}$ is dimensionless as well, absorbs the time integral in Eq. (2.89), and is constructed to be of order one. For the particular example of a Gaussian pulse, we present the dependence on n , \pm and the peak Rabi frequency Ω in Fig. 2.4(e)-(h). Eq. (2.89) clearly depicts that the LZ phase is a first-order correction in τ^{-1} , the weight of which relative to the dynamic phase will become more important for short pulses. As we will see, this approximation gives excellent results for all relevant orders of Bragg diffraction with Gaussian pulses. In summary, the net scattering phase of the state $|n, \pm\rangle$ entering Eq. (2.65) is

$$\theta_{n\pm} = \theta_{n\pm}^{\text{dyn}} + \theta_{n\pm}^{\text{LZ}}. \quad (2.91)$$

The dynamic phase is given by Eq. (2.74) and the correction due to the LZ phase is given by Eq. (2.89). Generally, both can be evaluated numerically for any given pulse form $\Omega(t)$ by means of the time integrals in Eqs. (2.75) and (2.90) for $x_{n\pm}(\Omega)$ and $y_{n\pm}(\Omega)$, respectively.

2.4.2 Bragg Pulse Area Condition

It is important to note that the findings in the previous section provide a (quasi)analytic expression for the condition on the Bragg pulse area linking the pulse duration τ and the peak Rabi frequency Ω . With the help of the now known dependence of the dynamic and LZ phases on the peak Rabi frequency and pulse duration we can determine for a given Ω the pulse duration τ necessary to attain a desired differential phase Θ_n (such as $\Theta_n = \pi/2$ or π). Computing the total scattering phases in Eq. (2.91) by means of the dynamic phases in Eq. (2.74) as well as the LZ phases in Eq. (2.89), and inserting the result into the first of Eqs. (2.65), yields a quadratic equation for τ . The physically relevant solution is the one corresponding to a longer pulse duration, and is given by

$$\tau(\Theta_n, \Omega) = \frac{\Theta_n}{2x_n(\Omega)\omega_r} \left(1 + \sqrt{1 - \frac{x_n(\Omega)y_n(\Omega)\Omega^2}{64(n-1)^3\Theta_n^2\omega_r^2}} \right), \quad (2.92)$$

where $x_n(\Omega) = x_{n+}(\Omega) - x_{n-}(\Omega)$ and $y_n(\Omega) = y_{n+}(\Omega) - y_{n-}(\Omega)$. In this solution the dynamic phase makes the dominant contribution, while the LZ phase is a correction that becomes relevant only for large peak Rabi frequency and, correspondingly, short pulses. In the other (formal) solution for τ this relation is inverted and the LZ phase makes the dominant contribution. In this regime, however, higher-order corrections to Eq. (2.83) as well as LZ losses become significant and impede high-quality Bragg pulses.

In the following, we will use Eq.(2.92) to predict Gaussian pulse parameters that enable Bragg operations with high efficiencies. We denote the resulting beam splitter parameters according to $\Omega_{\text{BS}}, \tau_{\text{BS}} := \Omega, \tau(\pi/2, \Omega)$ and write $\Omega_{\text{M}}, \tau_{\text{M}} := \Omega, \tau(\pi, \Omega)$ in case of a Bragg mirror pulse and will test their validity in Sec. 2.6.

2.4.3 Nonadiabatic Corrections: LZ Losses

The second kind of nonadiabatic corrections we consider are LZ losses from the states $|n, \pm\rangle$ to other states in their respective subspace $\mathcal{H}_{p\alpha\pm}$. As with the LZ phase, it is to be expected that the dominant loss can again be attributed to the state closest in energy. With the same logic and approximations applied in Sec. 2.4.1 the problem is thus reduced to the determination of LZ losses in a two-level system. For the simplest case of $n = 2$ the coupling in the symmetric subspace of $|2, +\rangle$ to $|0, +\rangle$ is still given by the truncated Hamiltonian in Eq. (2.84). Now, in principle LZ theory can be used to determine for a certain pulse form $\Omega(t)$ the population loss from level $|2, +\rangle$ to $|0, +\rangle$. For the particular Hamiltonian (2.84) and Gaussian pulses as in Eq. (2.9) *G. S. Vasilev and N. V. Vitanov [145]* derived an approximate analytic formula for the LZ loss, which reads in our notation

$$\tilde{\gamma}_{2+} = -\frac{1}{2} \ln \left(1 - 2 \frac{\sin(a_{\Theta_n}(\Omega, \tau))^2}{\cosh(b_{\Theta_n}(\Omega, \tau))^2} \right). \quad (2.93)$$

Here, $a_{\Theta_n}(\Omega, \tau)$ and $b_{\Theta_n}(\Omega, \tau)$ are analytical functions of the peak Rabi frequency and pulse duration the explicit form of which is rather cumbersome and therefore included in Appendix A.1 [see Eqs. (A.1)]. In Appendix A.1 the Θ_n -dependence of these functions is explained as well, which we drop for $\tilde{\gamma}_{2+}$ (2.93) in the interest of readability. We neglect the LZ loss in the antisymmetric subspace, i.e., $\gamma_{2-} = 0$, in analogy to the two-level approximation we have performed in the context of the LZ phases in Sec. 2.4.1 for $n = 2$. In Sec. 2.6.3, we will see that these expressions match very well with the numerical results. Most notably, the harmonic modulation of the LZ losses due to the sine function in the numerator on the right-hand side of Eq. (2.93) will be clearly visible. For higher orders of Bragg diffraction $n = 3, 4, 5$ the problem of LZ losses can still be reduced to two-level physics. However, the relevant truncated Hamiltonians given in Sec. 2.4.1 involve time-dependent ac Stark shifts not covered by the work of *G. S. Vasilev and N. V. Vitanov* in Ref. [145]. The same authors reported an extension of their work to account for a linear sweep in time of energy levels [146], but this is still very different from the present case, where the relevant ac Stark shift is proportional to $\Omega(t)^2$. An extension of LZ theory to this case would be very desirable, but is beyond the scope of this thesis. From the numerical results presented in Sec. 2.6.3 for the cases $n = 3, 4, 5$, it will become clear that the relevant physics still corresponds to LZ dynamics in a two-level system, and that one can expect that a formula very similar to Eq. (2.93) also holds for loss parameters $\gamma_{n\pm}$ in higher-order Bragg diffraction.

Determination of LZ Parameters from Population Data

Despite the lack of an analytical formula similar to Eq. (2.93) for higher-order Bragg pulses, we can nevertheless show that also for these orders LZ losses are dominated by two-level dynamics. To see this we infer values for $\gamma_{2,+}$ and $\gamma_{n,\pm}$, for orders $n = 3, 4, 5$ from the numerical solution of the Schrödinger equation in an equivalent two-level approximation (cf. Sec 2.4.1). We omit the tilde to distinguish the numerically inferred quantities $\gamma_{n,\pm}$ from the analytical result $\tilde{\gamma}_{2,+}$ and numerically calculate the LZ populations in zeroth order of the quasi-momentum p via

$$N_{m,\pm}^{\text{num}} = |\langle m, \pm | \psi_{\text{num}}^{\text{out}} \rangle|^2. \quad (2.94)$$

The state $|\psi_{\text{num}}^{\text{out}}\rangle$ is obtained by numerically solving the Schrödinger equation for Hamiltonians (2.55) in the (anti)symmetric basis using

$$|\psi^{\text{in}}\rangle = |-n \hbar k\rangle = \frac{1}{\sqrt{2}} e^{in\phi_L} (|n, +\rangle - |n, -\rangle) \quad (2.95)$$

as the initial condition (see Sec. 2.3.2). We focus on the states $|n - 2, \pm\rangle$, that are energetically closest to the main modes $|n, \pm\rangle$ (for $n = 2$, only $|0, +\rangle$) with $N_{0,+}^{\text{num}}$ turns out to be

relevant). In accordance with the two-level approximation we assume the amplitude loss parameters to be defined entirely by these populations:

$$\gamma_{2,+} = -\frac{1}{2} \ln(1 - 2N_{0,+}^{\text{num}}), \quad (2.96a)$$

$$\gamma_{3,\pm} = -\frac{1}{2} \ln(1 - 2N_{1,\pm}^{\text{num}}). \quad (2.96b)$$

We remark that, as pointed out in Sec. 2.4.1 in the context of the LZ phase, the spectra of the Hamiltonians make it necessary in the cases of $n = 4$ and 5 to include the coupling to the states $|n - 4, \pm\rangle$

$$\gamma_{n,\pm} = -\frac{1}{2} \ln(1 - 2(N_{n-2,\pm}^{\text{num}} + N_{n-4,\pm}^{\text{num}})). \quad (2.96c)$$

We evaluate these quantities for pulse parameters enabling high-fidelity Bragg beam splitter and mirror operations using Gaussian pulse shapes in Sec. 2.6.3.

2.4.4 Doppler Detuning

As a last step, we will further generalize the shape of the scattering matrix (2.64) by also taking into account the effect of first-order Doppler detuning. To this end, we have to consider the Hamiltonian $\mathcal{H}_\alpha(p)$ in Eq. (2.43), which contains the Doppler shift term V_α from Eq. (2.44b). In contrast to Eq. (2.59), we now need to construct a solution of Eq. (2.41) on the subspace $\mathcal{H}_{p\alpha}$, which is valid to first order in the Doppler detuning. In particular, we aim to solve

$$i\hbar \frac{d}{dt} \mathcal{V}_\alpha(p, t, t_0) = (H_\alpha(t) + \epsilon(p)V_\alpha(t)) \mathcal{V}_\alpha(p, t, t_0), \quad (2.97)$$

to first order in $\epsilon(p)$. Using the fact that $U_\alpha(t, t_0)$ in Eq. (2.72a) solves Eq. (2.59) one finds

$$\mathcal{V}_\alpha(p, t, t_0) = U_\alpha(t, t_0) (1 - i\epsilon(p)Z_\alpha(t, t_0)), \quad (2.98a)$$

$$Z_\alpha(t, t_0) = \frac{1}{\hbar} \int_{t_0}^t dt_1 U_\alpha^\dagger(t_1, t_0) V_\alpha(t_1) U_\alpha(t_1, t_0). \quad (2.98b)$$

We can now take the limit

$$\lim_{\substack{t \rightarrow \infty \\ t_0 \rightarrow -\infty}} \exp(i\mathcal{L}_\alpha(t - t_0)/\hbar) \mathcal{V}_\alpha(p, t, t_0) = \mathcal{S}_\alpha(1 - i\epsilon(p)Z_\alpha), \quad (2.99)$$

recalling the zeroth-order scattering matrix \mathcal{S}_α (2.60). With respect to the first-order correction Z_α , it is simplest to consider directly the relevant matrix elements in the (anti)symmetric basis $|n, \pm\rangle$ from Eq. (2.98b). This is consistent with the statement made in Sec. 2.3.3, where we also focus on the action of the Bragg pulse within the two-dimensional subspace spanned by $|n, \pm\rangle$. We show in Appendix A.2 that the diagonal elements vanish,

$\langle n, \pm | Z_\alpha | n, \pm \rangle = 0$, and the off-diagonal elements $\langle n, - | Z_\alpha | n, + \rangle = \langle n, + | Z_\alpha | n, - \rangle^*$ are nonzero. This reflects the fact that Doppler detuning breaks the decoupling of symmetric and antisymmetric subspace. One finds

$$\langle n, + | Z_\alpha | n, - \rangle = 2n\tau^2 \omega_r^2 e^{i\Theta_n/2} z_{n,\Theta_n}(\Omega), \quad (2.100)$$

where Θ_n is the differential phase from Eq. (2.65) and $z_{n,\Theta_n}(\Omega)$ is a positive real parameter of order unity given in Eq. (A.9). It absorbs a time integral of overlaps of instantaneous energy eigenstates and is shown in Fig. 2.4(e)-(h) up to order $n \leq 5$. Overall, we find that the scattering matrix, projected into the subspace $|\pm n \hbar k + p\rangle$ and written in the basis of (anti)symmetric states $(|p, n, +\rangle, |p, n, -\rangle)$ is

$$S(p) = \begin{pmatrix} e^{-i\theta_{n+}-\gamma_{n+}} & 0 \\ 0 & e^{-i\theta_{n-}-\gamma_{n-}} \end{pmatrix} \begin{pmatrix} 1 & i\eta(p)e^{i\Theta_n/2} \\ i\eta(p)e^{-i\Theta_n/2} & 1 \end{pmatrix}. \quad (2.101)$$

From here on we explicitly write again the dependence on the (quasi)momentum p and have introduced in Eq. (2.101) the dimensionless Doppler parameter

$$\eta(p) = -2n\tau^2 \omega_r^2 z_{n,\Theta_n}(\Omega) \frac{p}{\hbar k}. \quad (2.102)$$

Eq. (2.101) incorporates Doppler detuning to first order and therefore generalizes Eq. (2.61). Thus, we have seen that the Doppler detuning causes a mixing of the (anti)symmetric states $|p, n, \pm\rangle$, but no real loss out of this subspace unlike the LZ losses. As it stands, the projected scattering matrix is nonunitary due to the two effects of Doppler detuning and LZ losses, since

$$\text{tr}(S^\dagger(p)S(p)) = (1 + \eta(p)^2)(e^{-2\gamma_{n+}} + e^{-2\gamma_{n-}}). \quad (2.103)$$

However, the nonunitarity due to the Doppler effect is an artifact of the perturbation series expansion adopted here. Whereas, the nonuniformity due to LZ losses is due to actual losses from the relevant subspace. It is important to make this distinction by renormalizing the scattering matrix in order to remove the artificial nonunitarity due to the Doppler shift. This can be achieved by exchanging $S(p) \rightarrow S(p)/\sqrt{1 + \eta(p)^2}$. Finally, the transformation of the scattering matrix (2.101) from the (anti)symmetric basis to the basis of momentum eigenstates $|\pm n \hbar k + p\rangle$ is again achieved by means of T in Eq. (2.63) and $B(p) = T^\dagger S(p)T$. The result is given in the next section in Eq. (2.104b).

2.5 Two-mode Bragg Scattering Matrix

In the previous section, we have formulated a comprehensive and relatively simple analytic model of single Bragg diffraction based on the application of the adiabatic theorem.

We have identified nonadiabatic corrections like LZ phases and LZ losses, as well as corrections due to Doppler detuning, which play an important role for the dynamics of the Bragg pulse. Together, these quantities determine the scattering matrix for n th-order Bragg diffraction:

$$\mathcal{S}(\Omega, \tau, \phi_L) = \int_{-\hbar k/2}^{\hbar k/2} dp \sum_{s,s'=\mp} [B(p, \Omega, \tau)]_{ss'} |s n \hbar k + p\rangle \langle s' n \hbar k + p|, \quad (2.104a)$$

where

$$\begin{aligned} B(p, \Omega, \tau, \phi_L) &= \frac{\exp(-i\frac{\Phi_n - i\Gamma}{2})}{\sqrt{1 + \eta(p)^2}} \begin{pmatrix} \cos\left(\frac{\Theta_n - i\gamma}{2}\right) & -ie^{-i2n\phi_L} \sin\left(\frac{\Theta_n - i\gamma}{2}\right) \\ -ie^{i2n\phi_L} \sin\left(\frac{\Theta_n - i\gamma}{2}\right) & \cos\left(\frac{\Theta_n - i\gamma}{2}\right) \end{pmatrix} \\ &\times \begin{pmatrix} 1 + i\eta(p) \cos\left(\frac{\Theta_n}{2}\right) & e^{-i2n\phi_L} \eta(p) \sin\left(\frac{\Theta_n}{2}\right) \\ -e^{i2n\phi_L} \eta(p) \sin\left(\frac{\Theta_n}{2}\right) & 1 - i\eta(p) \cos\left(\frac{\Theta_n}{2}\right) \end{pmatrix} \\ &:= \begin{pmatrix} B_{--} & B_{-+} \\ B_{+-} & B_{++} \end{pmatrix}. \end{aligned} \quad (2.104b)$$

The scattering matrix for single Bragg diffraction links the products of this elastic-scattering process and the experimental parameters of the Bragg pulse via intuitive analytical expressions for any order n . Table 2.2 summarizes all parameters that enter Eq. (2.104b). We also provide references to their respective definitions, linking them to the Rabi frequency $\Omega(t)$ and, for the special case of a Gaussian pulse, to the peak Rabi frequency Ω and the pulse width τ . The general structure of the scattering matrix (2.104b) holds for arbitrary pulse forms $\Omega(t)$ and accounts for Doppler detuning (to first order in $|p|/\hbar k \ll 1$) as well as for population loss out of the subspace ($|n \hbar k + p\rangle, |-n \hbar k + p\rangle$). The formulas presented in Table 2.2 assume an adiabatic tuning of $\Omega(t)$, and include the dominant nonadiabatic corrections due to LZ processes. For Gaussian pulses we will see in the next section that high-quality quasi-Bragg pulses do indeed always fall within this regime.

In the hypothetical case of vanishing LZ losses ($\Gamma = \gamma = 0$), vanishing Doppler detuning ($\eta(p) = 0$), and zero global phase ($\Phi_n = 0$) the scattering matrix in Eq. (2.104b) assumes familiar forms if the pulse $\Omega(t)$ is tuned in such a way that the differential phase Θ_n takes on specific values: Choosing $\Theta_n = \pi/2$ provides a beam splitter operation, whereas $\Theta_n = \pi$ yields a mirror pulse as given in Eqs. (2.68). The scattering matrix (2.104b) provides a systematic generalization to account for nonideal phases Θ_n as well as unavoidable global phases, population losses, and Doppler shifts. Our model gives a microscopic explanation and analytic characterization for all of these effects in leading order (except for LZ losses in Bragg diffraction of higher order $n > 2$). The approach taken here provides also a systematic framework for deriving higher-order corrections. An important insight that can be gained from our analytic characterization of the differential phase concerns the so-called Bragg

| Parameter | Symbol | defined by | Equation |
|------------------------------------|------------------------------|--|---------------|
| Global phase | Φ | $\Phi = \theta_{n+} + \theta_{n-}$ | (2.65) |
| Global LZ loss | Γ | $\Gamma = \gamma_{n+} + \gamma_{n-}$ | (2.66) |
| Differential phase | Θ_n | $\Theta_n = \theta_{n+} - \theta_{n-}$ | (2.65) |
| Differential LZ loss | γ | $\gamma = \gamma_{n+} - \gamma_{n-}$ | (2.66) |
| Doppler shift | $\eta(p)$ | | (2.102) |
| Laser phase | ϕ_L | | (2.11) |
| Total phase of $ p, n, \pm\rangle$ | $\theta_{n\pm}$ | $\theta_{n\pm} = \theta_{n\pm}^{\text{dyn}} + \theta_{n\pm}^{\text{LZ}}$ | (2.91) |
| Dynamic phase | $\theta_{n\pm}^{\text{dyn}}$ | | (2.74) |
| LZ phase | $\theta_{n\pm}^{\text{LZ}}$ | | (2.89) |
| LZ loss from $ p, n, \pm\rangle$ | $\gamma_{n\pm}$ | | (2.93),(2.96) |

Table 2.2: **Bragg scattering matrix parameters**, [see Eq. (2.104)].

condition: For a Gaussian pulse the requirement to achieve a desired phase Θ_n links Ω to τ . Thus, the pulse duration $\tau(\Theta_n, \Omega)$ can be expressed as a function of the peak Rabi frequency for a given differential phase [see Eq. (2.92)]. For a desired operation, such as a beam splitter ($\Theta_n = \pi/2$) or a mirror ($\Theta_n = \pi$) pulse, this leaves a single free parameter, Ω , which fully determines the scattering matrix (2.104). What is left is to choose the peak Rabi frequency to balance the dominant imperfections: LZ losses will become large for short pulses, i.e., for a large Rabi frequency. The effects of Doppler detuning will be stronger for long, spectrally narrow pulses with correspondingly small Rabi frequencies. We demonstrate in Sec. 2.6.3 that the trade-off implied by this is very well covered by our analytic model.

2.6 Comparison to Numerical Simulations

In this section, we gauge the accuracy of our analytical model. With this purpose in mind, we employ the notion of pulse fidelities to compare the predictions of our model with numerical solutions of the Schrödinger equation given the full Bragg Hamiltonian in Eq. (2.11). As explained in Sec. 2.3.3, the loss of atoms by spontaneous emission provides an effective limit to the Rabi frequency, which imposes a certain threshold above which losses cannot be tolerated [69]. For this reason, we restrict our study to the experimentally relevant cases $n \leq 5$. Furthermore, in the following we consider pulses with Gaussian temporal pulse shapes $\Omega(t)$ (2.9) characterized by peak Rabi frequencies Ω and widths τ . Details of the numerical treatment are given in Appendix A.3 and the *MATHEMATICA* code at the basis of the comparisons presented in this section is available [120].

2.6.1 Quality of Bragg Operations

For the concrete case of an incoming atomic wave packet with average momentum $-n\hbar k$ and a narrow Gaussian envelope of width $\sigma_p \ll \hbar k$ centered at $p = 0$,

$$|\psi^{\text{in}}\rangle = \int_{-\hbar k/2}^{\hbar k/2} dp g(p, \sigma_p) |-n\hbar k + p\rangle, \quad (2.105)$$

with

$$g(p, \sigma_p) = (2\pi\sigma_p^2)^{-1/4} e^{-\frac{p^2}{4\sigma_p^2}}, \quad (2.106)$$

the ideal outgoing state is accordingly $|\psi_{\text{ideal}, \Theta_n}^{\text{out}}\rangle = \mathcal{S}_{\text{ideal}, \Theta_n} |\psi^{\text{in}}\rangle$. The true outgoing state is $|\psi^{\text{out}}\rangle = \mathcal{S}(\Omega, \tau) |\psi^{\text{in}}\rangle$ while the general scattering matrix $\mathcal{S}(\Omega, \tau)$ denotes the limit in Eq. (2.26) for the given pulse shape. Here, we set $\phi_L = 0$ and therefore omit the formal dependence on the phase of the laser for the moment. We quantify the quality of a Θ_n -Bragg pulse by the fidelity between the ideal state and the true output state

$$F_{\Theta_n, \sigma_p}(\Omega, \tau) = |\langle \psi_{\text{ideal}, \Theta_n}^{\text{out}} | \psi^{\text{out}} \rangle|^2. \quad (2.107a)$$

In the limit of an infinitely narrow atomic wave packet,

$$F_{\Theta_n, 0}(\Omega, \tau) = \lim_{\sigma_p \rightarrow 0} F_{\Theta_n, \sigma_p}(\Omega, \tau), \quad (2.107b)$$

we can infer the fidelity for the central momentum component $p = 0$. Ultimately, the analytic approximation for the scattering matrix $\mathcal{S}(\Omega, \tau, \phi_L)$ derived in Secs. 2.3 and 2.4 will be gauged by comparing the corresponding analytic predictions for the fidelities (2.107) to the values $F_{\Theta_n, \sigma_p}^{\text{num}}(\Omega, \tau)$ and $F_{\Theta_n, 0}^{\text{num}}(\Omega, \tau)$ inferred from numerical integration of the Schrödinger equation. We display in anticipation the numerically determined fidelity $F_{\Theta_n, 0}^{\text{num}}(\Omega, \tau)$ for beam splitter ($\Theta_n = \pi/2$) [Fig. 2.5(a)-(d)] and mirror ($\Theta_n = \pi$) [Fig. 2.5(e)-(h)] pulses for the Bragg orders $n = 2, 3, 4, 5$ in Fig. 2.5. We will see that the landscapes depicted in Fig. 2.5 can be very well explained by our analytical model and their dependence on the pulse parameters can be readily understood by means of the quantities summarized in the previous section. We emphasize that the fidelity is only used here as a figure of merit to demonstrate the quality of our approximation for the Bragg scattering matrix, and will turn to a discussion of signals of Bragg atom interferometers in Chapter 3.

Analytical Fidelities

With the analytic form of the scattering matrix in Eq. (2.104) we can evaluate the fidelity from Eq. (2.107a) to

$$F_{\Theta_n, \sigma_p}(\Omega, \tau) = |\langle \psi_{\text{ideal}, \Theta_n}^{\text{out}} | \psi^{\text{out}}(\Omega, \tau) \rangle|^2 = \int_{-\hbar k/2}^{\hbar k/2} dp |g(p, \sigma_p)|^2 \left| \left[B_{\Theta_n}^\dagger B(p, \Omega, \tau) \right]_{11} \right|^2. \quad (2.108)$$

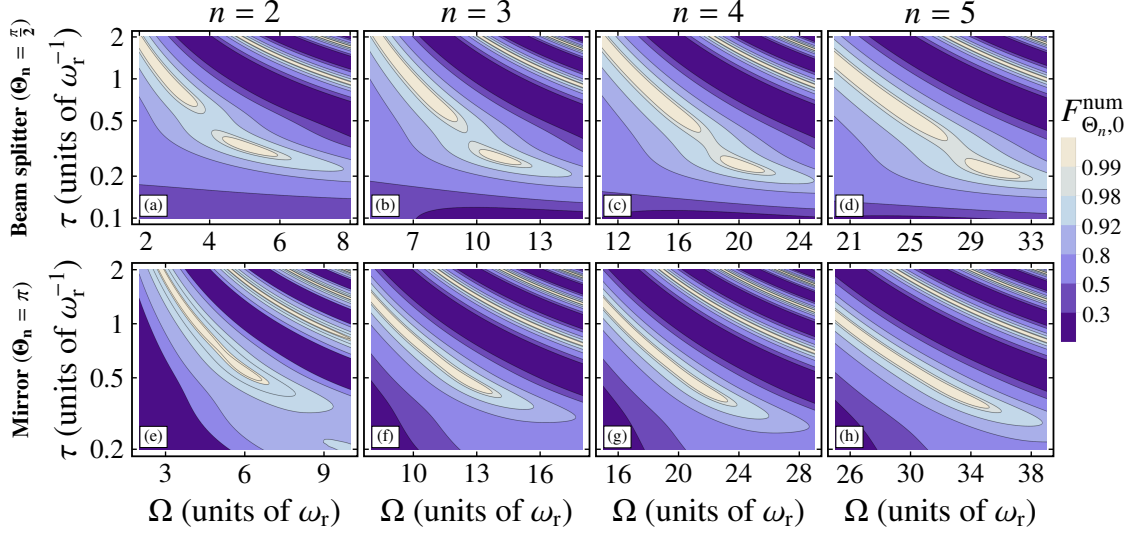


Figure 2.5: **Nonnormalized Bragg diffraction fidelities.** Numerically determined fidelities according to Eq. (2.107b) of a single Gaussian quasi-Bragg pulse (2.9) in case of a wave packet with vanishing momentum spread as a function of the peak Rabi frequency Ω and the temporal pulse width τ . Fidelities are depicted for beam splitters [top row, panels (a)-(d)] and mirrors [bottom row, panels (e)-(h)] of order $n = 2, 3, 4, 5$ (from left to right). Orders $n > 5$ are not suitable for high-fidelity Bragg diffraction due to atom loss, as mentioned in the main text. The parameters (Ω, τ) have been chosen to optimize the plot range for the pulse fidelities while maintaining experimentally relevant pulse durations for atomic clouds with finite momentum spread (see Sec. 2.6.3). Quasi-Bragg beam splitting pulses feature a rich phenomenology that can be explained by LZ physics as we show in Sec. 2.6.3. For the mirror pulses with longer pulse durations, such features are less visible. Figure adapted from *J.-N. Siemss et al., Phys. Rev. A* **102**, 033709 (2020), Copyright 2022, American Physical Society (Ref. [120]).

We can express the squared modulus of the top-left element of the matrix $B_{\Theta_n}^\dagger B(p, \Omega, \tau)$ explicitly assuming $\Theta_n = \pi/2$

$$\begin{aligned} \left| \left[B_{\frac{\pi}{2}}^\dagger B(p, \Omega, \tau) \right]_{11} \right|^2 &= \frac{e^{-\Gamma}}{2[1 + \eta^2(p)]} \left\{ 1 + [1 + \eta^2(p)] \cosh(\gamma) + \sqrt{2}\eta(p) \sinh(\gamma) \right\} \\ &\simeq \frac{e^{-\Gamma}}{2} \left[1 + \cosh(\gamma) - \eta_{0,\frac{\pi}{2}}^2 \left(\frac{p}{\hbar k} \right)^2 + \sqrt{2}\eta_{0,\frac{\pi}{2}} \frac{p}{\hbar k} \sinh(\gamma) \right] \end{aligned} \quad (2.109)$$

or $\Theta_n = \pi$

$$\begin{aligned} \left| \left[B_{\pi}^\dagger B(p, \Omega, \tau) \right]_{11} \right|^2 &= \frac{e^{-\Gamma}}{2[1 + \eta^2(p)]} \left\{ 1 - \eta^2(p) + [1 + \eta^2(p)] \cosh(\gamma) + 2\eta(p) \sinh(\gamma) \right\} \\ &\simeq \frac{e^{-\Gamma}}{2} \left[1 + \cosh(\gamma) - 2\eta_{0,\pi}^2 \left(\frac{p}{\hbar k} \right)^2 + 2\eta_{0,\pi} \frac{p}{\hbar k} \sinh(\gamma) \right]. \end{aligned} \quad (2.110)$$

To obtain the last lines in these two equations we introduced the dimensionless parameter

$$\eta_{0,\Theta_n} := -2n\tau^2\omega_1^2 z_{n,\Theta_n}(\Omega), \quad (2.111)$$

and performed an expansion up to order $O[p]^3$. Assuming an atomic wave packet with a Gaussian momentum distribution $g(p, \sigma_p)$, we can immediately execute the integration in Eq. (2.108) giving us the averaged beam splitter

$$F_{\pi/2, \sigma_p}(\Omega, \tau) \simeq \frac{e^{-\Gamma}}{2} \left\{ \frac{\eta_{0,\pi/2}^2 \sigma_p}{\sqrt{2\pi\hbar k}} e^{-\frac{1}{8} \left(\frac{\sigma_p}{\hbar k}\right)^{-2}} + \left[1 + \cosh(\gamma) - \eta_{0,\pi/2}^2 \left(\frac{\sigma_p}{\hbar k}\right)^2 \right] \operatorname{erf} \left(\frac{1}{2\sqrt{2}} \left(\frac{\sigma_p}{\hbar k}\right)^{-1} \right) \right\} \quad (2.112a)$$

and mirror fidelity

$$F_{\pi, \sigma_p}(\Omega, \tau) \simeq e^{-\Gamma} \left\{ \frac{\eta_{0,\pi}^2 \sigma_p}{\sqrt{2\pi\hbar k}} e^{-\frac{1}{8} \left(\frac{\sigma_p}{\hbar k}\right)^{-2}} + \left[\frac{1}{2} [1 + \cosh(\gamma)] - \eta_{0,\pi}^2 \left(\frac{\sigma_p}{\hbar k}\right)^2 \right] \operatorname{erf} \left(\frac{1}{2\sqrt{2}} \left(\frac{\sigma_p}{\hbar k}\right)^{-1} \right) \right\}. \quad (2.112b)$$

It is useful to also consider the fidelity (2.107b) for the hypothetical situation of an infinitely narrow atomic wave packet with no Doppler effects:

$$F_{\Theta_n, 0}(\Omega, \tau) = \lim_{\sigma_p \rightarrow 0} F_{\Theta_n, \sigma_p}(\Omega, \tau) = \left| \left[B_{\Theta_n}^\dagger B(0, \Omega, \tau) \right]_{11} \right|^2 = \frac{e^{-\Gamma}}{2} (1 + \cosh(\gamma)). \quad (2.112c)$$

This can also be considered as the fidelity achieved for the center component with momentum $p = 0$ of a finite atomic wave packet, or equivalently as the fidelity attained within each subspace ($|-n\hbar k + p\rangle, |n\hbar k + p\rangle$) in zeroth order of the Doppler detuning.

Numerical Fidelities

These approximate analytic expressions for the fidelities can be compared to the fidelities inferred from the numerical solution of the Schrödinger equation $|\psi_{\text{num}}^{\text{out}}(\Omega, \tau)\rangle$ for given pulse parameters. We denote the numerical fidelities that we will be comparing to the ones in Eqs. (2.112) by

$$F_{\Theta_n, \sigma_p}^{\text{num}}(\Omega, \tau) = \left| \langle \psi_{\text{ideal}, \Theta_n}^{\text{out}} | \psi_{\text{num}}^{\text{out}}(\Omega, \tau) \rangle \right|^2, \quad (2.113a)$$

$$F_{\Theta_n, 0}^{\text{num}}(\Omega, \tau) = \lim_{\sigma_p \rightarrow 0} F_{\Theta_n, \sigma_p}^{\text{num}}(\Omega, \tau). \quad (2.113b)$$

The fidelity (2.113b) is shown in Fig. 2.5 for beam splitter ($\Theta_n = \pi/2$) [Fig. 2.5(a)-(d)] and mirror ($\Theta_n = \pi$) [Fig. 2.5(e)-(h)] pulses of Bragg diffraction orders $n = 2, 3, 4, 5$, corresponding to momentum transfers of $4\hbar k, 6\hbar k, 8\hbar k, 10\hbar k$, respectively. One last figure of merit that will be useful in the following discussion is a fidelity where both the Doppler effect and the LZ losses are masked out. This can be achieved by considering the fidelity

for the central $p = 0$ momentum component of the wave packet from Eq. (2.112c) but calculating it with respect to the normalized state $|\psi_{\text{num}}^{\text{out}}(\Omega, \tau)\rangle / \|\psi_{\text{num}}^{\text{out}}(\Omega, \tau)\rangle\|$. This vector describes the state of atoms conditioned on the fact that they actually remain in the correct ($\pm n \hbar k$)-subspace. When Doppler effect and LZ losses are ignored in this way, the conditional fidelity for the conditional, normalized state is

$$\mathcal{F}_{\Theta_n, 0}^{\text{num}}(\Omega, \tau) = \frac{F_{\Theta_n, 0}^{\text{num}}(\Omega, \tau)}{\|\psi_{\text{num}}^{\text{out}}(\Omega, \tau)\rangle\|}. \quad (2.114)$$

It will be reduced below 1 only if the pulse parameters (Ω, τ) do not yield the desired differential phase Θ_n . Thus, $\mathcal{F}_{\Theta_n, 0}^{\text{num}}(\Omega, \tau)$ is an appropriate figure of merit to benchmark the analytic formula for the prediction of the pulse duration (2.92) $\tau(\Theta_n, \Omega)$ required to achieve a desired differential phase Θ_n .

2.6.2 Bragg Pulse Area Condition

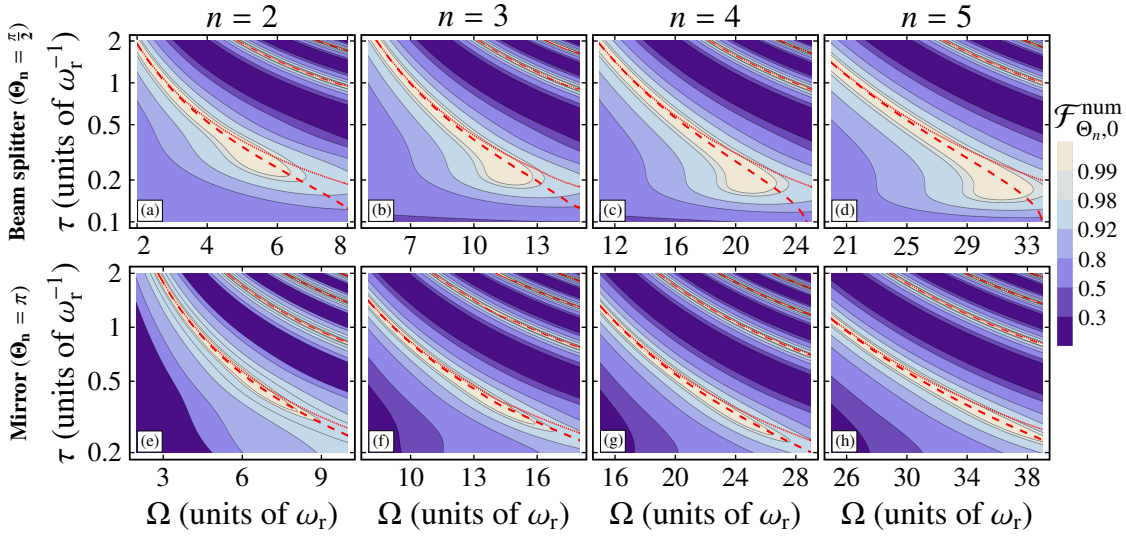


Figure 2.6: **Normalized Bragg diffraction fidelities.** Similar to Fig. 2.5. Here, we plot the normalized beam splitter [top row, panels (a)-(d)] and mirror [bottom row, panels (e)-(h)] fidelities (2.114) of a single Gaussian quasi-Bragg pulse in case of a wave packet with vanishing momentum spread. The results are shown as functions of the peak Rabi frequency Ω and the temporal pulse width τ for diffraction orders $n = 2, 3, 4, 5$ (from left to right). The red lines represent the calculated temporal pulse width $\tau(\Theta_n, \Omega)$ in Eq. (2.92) with (dashed) and without (dotted) the phase contribution from LZ physics. In contrast to Fig. 2.5(a)-(d), beam splitter fidelities possess a simplified structure as LZ losses from the subspace $|\pm n \hbar k\rangle$ are blanked out in the conditional fidelity $\mathcal{F}_{\Theta_n, 0}^{\text{num}}$. Figure adapted from *J.-N. Siemss et al., Phys. Rev. A* **102**, 033709 (2020), Copyright 2022, American Physical Society (Ref. [120]).

Figure 2.6 shows the conditional fidelity $\mathcal{F}_{\Theta_n,0}^{\text{num}}(\Omega, \tau)$ introduced in Eq. (2.114) for Bragg beam splitters and mirrors. These plots are similar to the ones shown in Fig. 2.5 but blank out the effects of LZ losses. We immediately observe that the rich fidelity landscapes showcased in Fig. 2.5 simplify considerably when evaluating this fidelity instead of the unconditional fidelity $F_{\Theta_n,0}^{\text{num}}(\Omega, \tau)$ (2.113b). Considering first the numerical data represented by the shaded regions in Fig. 2.6, one clearly recognizes the condition on the Bragg pulse area (cf. Eqs. (2.20) and Sec. 2.4.2): The shorter the temporal width τ of the pulse is, the stronger its coupling must be to achieve Bragg operations of decent quality. It is also visible, that for sufficiently large parameters (Ω, τ) one can realize an efficient beam splitter (mirror) with a differential phase of $\Theta_n = \pi/2 + m 2\pi$ ($\Theta_n = \pi + m 2\pi$) with $m \in \mathbb{N}$. More importantly, the numerical data highlight the fact that for all Bragg orders depicted, even when disregarding LZ losses, there exists a minimal temporal pulse width beyond which fidelities degrade quickly. Rising nonadiabatic couplings such as the LZ phase introduced in Sec. 2.4.1 and higher-order corrections to the adiabatic theorem make it impossible to perfectly match the Bragg condition with Gaussian pulses featuring pulse widths shorter than that.

This condition on the Bragg pulse parameters can now be compared to the predictions our analytic model provides regarding the pulse timings $\tau(\Theta_n, \Omega)$ (2.92). We show the pulse timings including (red dashed line) and excluding (red dotted line) the contribution of the LZ phase to the differential phase, i.e., with and without the second term under the square root in Eq. (2.92), respectively. Clearly, Eq. (2.92) provides an excellent approximation for the necessary pulse duration in all regimes, where it is even possible to perform a high-quality operation. Thus, for Gaussian pulses adiabaticity is indeed a necessary and sufficient condition for performing efficient Bragg diffraction. From Fig. 2.6 it is also evident that the LZ phase delivers a significant contribution to the Bragg pulse evolution even if the LZ losses themselves have been re-normalized. Naturally, these corrections are less important when operating with small peak Rabi frequencies and accordingly long pulse durations, i.e., for more adiabatic pulses. Following the same logic, it is easy to see that the corrections to the differential phase due to LZ physics are suppressed in the case of a mirror pulse compared to a beam splitting pulse: For the same value of Ω the latter operates with half the temporal width of the former. That is why for Bragg mirror operations the mismatch in differential phase when considering only the dynamic phase is reduced, which is visible in Fig. 2.6(e)-(h). Nonetheless, the figure makes it fairly obvious that using the full Eq. (2.92) instead of just the dynamic phase contribution considerably improves predictions for both operations and especially in the case of a beam splitter.

In fact, from the weight of the LZ-phase term in Eq. (2.92) we can deduce the adiabaticity of the Bragg diffraction process for a given Rabi frequency. This is considerably more

accurate⁴ than the usual adiabaticity criterion derived from the separation of the n -th and $(n-1)$ -th energy levels mentioned in Secs. 2.2.2 and 2.2.3, as well as the estimations done in Sec. V A of [130]. The discrepancy between the numerically determined pulse parameters (Ω, τ) maximizing the fidelity and the results of the full Eq. (2.92) for values $\tau\omega_r < 0.2$ is a consequence of the rising nonadiabaticity and the limitation of perturbation theory developed in Sec. 2.4.1. Since Bragg pulses implemented in state-of-the-art atom interferometry experiments typically aim at efficiencies approaching unity [96–98], this regime can be, however, considered unsuitable for high-performance quasi-Bragg beam splitters and mirrors as fidelities quickly degrade. In the following section we return to the unconditional fidelities in Eqs. (2.113), which include losses from the subspace $|\pm n \hbar k + p\rangle$, and identify them as product of LZ processes that give rise to the features observed in Fig. 2.5.

2.6.3 Bragg Beam Splitters and Mirrors

Gaussian Beam Splitter Pulses

We start by discussing the Bragg beam splitter pulse ($\Theta_n = \pi/2$) in Fig. 2.7 for diffraction orders $n = 2, 3, 4, 5$. We consider first the lowest order $n = 2$. In Fig. 2.7(a) we present the result of our approximate analytic formula for $\tau(\Theta_n, \Omega)$ in Eq. (2.92) on top of the numerically inferred fidelities Eq. (2.113b) in the (Ω, τ) -plane assuming a vanishing momentum width. The figure shows good agreement between our model and the peak fidelities over the relevant range of peak Rabi frequencies. In addition, it illustrates that pulse parameters generating a differential phase $\Theta_n = \pi/2$ between the states $|\pm n \hbar k\rangle$ (red dashed line, cf. Fig. 2.6) are subject to losses with an intricate dependency on the peak Rabi frequency Ω . To demonstrate that this dependency can be understood applying LZ theory, Fig. 2.7(e) depicts the fidelity loss for pulse parameters $\Omega_{\text{BS}}, \tau_{\text{BS}}$ highlighted by the dashed red line in Fig. 2.7(a). The blue circles are obtained evaluating Eq. (2.113b) numerically. The corresponding analytic fidelity (2.112c) is a function of the LZ loss parameters Γ and γ (see Table 2.2) that we derived in Sec. 2.4.3. Within our approximation both are entirely determined by $\tilde{\gamma}_{2,+}$, the loss of amplitude from the symmetric state $|0, 2, +\rangle$, hence the superscript $F_{\Theta_n,0}^{\tilde{\gamma}_{2,+}}$. We insert $\tilde{\gamma}_{2,+}$ (2.93) into Eq. (2.112c) and plot the dashed blue line in Fig. 2.7(e). The analytic results exactly mirror the functional dependence of the numerical data on Ω . Both analytics and numerics show an exponential increase of losses towards large values of Ω that is harmonically modulated as showcased in Eq. (2.93). On top of that, we find good quantitative agreement up to Rabi frequencies of $\Omega < 5\omega_r$. Towards larger Ω , time-dependent ac Stark shifts proportional to $\Omega^2(t)$ become increasingly significant. These are

⁴This statement refers to the fact that the adiabaticity criterion for the temporal slopes of the pulse, $\tau \gg [4(n-1)\omega_r]^{-1}$, provides at best a rough estimate with varying quality depending on the Bragg order n . Moreover, the considerations done in Sec. V A of Ref. [130] underestimate the losses by at least one order of magnitude.

not taken into account in the LZ rates defined in Appendix A.1. Still, for relevant values of the Rabi frequency, formula (2.93) gives remarkably good results in light of the fact that it is based on a simple two-level approximation accounting for losses to the energetically closest-lying level only. Unfortunately, we lack equivalent expressions for the higher-order

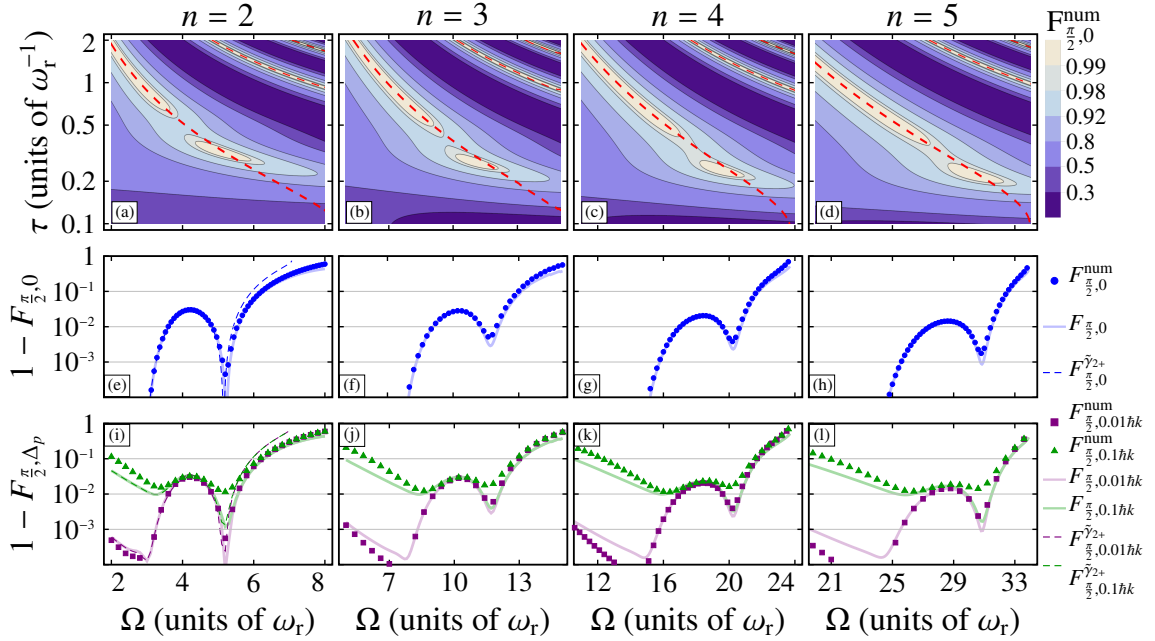


Figure 2.7: **Bragg beam splitter fidelity.** Top row: Pulse duration (2.92) (red dashed line) on top of the numerically determined beam splitter fidelities (2.113b) introduced in Fig. 2.5(a)-(d). Middle row: Fidelity loss as a function of peak Rabi frequency Ω and pulse durations computed via Eq. (2.92). Beam splitter fidelities were determined numerically (blue disks), via Eq. (2.112c) with values (2.96) (solid line). The dashed line in panel (e) for $n = 2$ is obtained by inserting $\tilde{\gamma}_{2,+}$ (2.93) into Eq. (2.112c) and denoted $F_{\frac{\pi}{2},0}^{\tilde{\gamma}_{2,+}}$ in the legend on the right. Bottom row: Fidelity loss extracted from numerics (squares & triangles) is again compared to analytic results (solid & dashed lines) similar to the middle row. Fidelities (2.113a) are now averaged over a wave packet with finite momentum width $\sigma_p = 0.01 \hbar k$ (purple squares and lines) and $\sigma_p = 0.1 \hbar k$ (green triangles and lines). The values for $\gamma_{n,\pm}$ were obtained via Eq. (2.96) (solid lines) or for $\tilde{\gamma}_{2,+}$ using Eq. (2.93) (dashed lines) in the panel (i). Figure adapted from *J.-N. Siemss et al., Phys. Rev. A* **102**, 033709 (2020), Copyright 2022, American Physical Society (Ref. [120]).

Bragg pulses, since this would require an adaptation of the LZ theory in Ref. [145] as outlined in Sec. 2.4.3, which is beyond the scope of this thesis. Nevertheless, Fig. 2.7(e)-(h) makes it clear that the dominant loss from the subspace $|\pm n \hbar k\rangle$ can be associated with two-level dynamics for all Bragg orders treated here. The solid blue lines representing the fidelity loss $1 - F_{\Theta_n,0}$ [see Eq. (2.112c)] in Fig. 2.7(e)-(h) and Fig. 2.8(e)-(h) are in excellent agreement with the numerically determined loss of fidelity based on Eq. (2.113b). Note,

that we evaluate Eq. (2.112c) with the values $\gamma_{n,\pm}$ (2.96) for $n = 2, 3, 4, 5$ based on numerically determined population data and therefore have no superscript to differentiate them from the solutions of $F_{\Theta_n,0}^{\tilde{\gamma}_{2,+}}$ using $\tilde{\gamma}_{2,+}$ (2.93).

In Fig. 2.7(i), we extend our discussion of the pulse parameters indicated by the dashed red line in Fig. 2.7(a) to the experimentally more relevant case of an atomic wave packet with finite momentum width. Here, we contrast the results of Eq. (2.113a) (squares and triangles) with our analytic fidelity (2.108) assuming a Gaussian momentum distribution with widths $\sigma_p = 0.01 \hbar k$ and $0.1 \hbar k$. Again, we find good agreement between numerics and analytics using either the numerically extracted LZ loss [solid lines, see Eq. (2.96a)] and the fully analytic expression [dashed lines, see Eq. (2.93)]. The Doppler detuning drives transitions between the (anti)symmetric states $|p, n, \pm\rangle$, which affects the fidelity in Fig. 2.7(i) compared to Fig. 2.7(e). Thus, in the limiting case of small Ω and long pulse durations, the fidelity is reduced by the velocity filter effect due to the Doppler detuning determined by parameter $\eta(p) \propto \tau^2$ [see Eq. (2.102)]. As expected, the velocity filter effect decreases rapidly toward shorter pulse widths, especially for the $\sigma_p = 0.01 \hbar k$ wave packet. Considering values $\Omega \gtrsim 3\omega_r$, the LZ physics we have already discussed for $p = 0$ visibly dominates the pulse fidelities. Nevertheless, it becomes also clear that averaging over a larger uncertainty in momentum $\sigma_p = 0.1 \hbar k$ blurs the LZ features considerably. The remaining panels of Fig. 2.7 confirm that our analytic model equally applies to Gaussian Bragg pulses of orders $n = 3, 4, 5$. As before, we select the pulse parameters represented by the red dashed lines in Fig. 2.7(b)-(d) for pulses investigated in Fig. 2.7(f)-(h) and 2.7(j)-(l). Figure 2.7(f)-(h) shows that also for these higher orders the fidelity is reduced due to transitions to the closest state in energy $|n - 2, \pm\rangle$ (hybridized level of $|n - 2, \pm\rangle$ and $|n - 4, \pm\rangle$ for $n = 4, 5$). Despite the fact that our perturbative model for the Doppler detuning underestimates the magnitude of the velocity filter for $\sigma_p = 0.1 \hbar k$ and overestimates it for $\sigma_p = 0.01 \hbar k$ in case of a finite momentum width, we still find good qualitative agreement in Fig. 2.7(j)-(l) with regards to the numerics.

Gaussian Mirror Pulses

In the case of Bragg mirrors ($\Theta_n = \pi$) for diffraction orders $n = 2, 3, 4, 5$, corresponding to momentum transfers of $4 \hbar k, 6 \hbar k, 8 \hbar k, 10 \hbar k$, respectively, Fig. 2.8 paints a picture very similar to the discussion of the beam splitter. Yet, Fig. 2.8(e)-(h) shows that unlike the beam-splitter case, the longer pulse widths for Ω_M, τ_M (for the same peak Rabi frequency, $\Omega_{BS} = \Omega_M$) suppress nonadiabatic losses. For the same reason, the fidelity loss in Fig. 2.8(e)-(h) is significantly lower in direct comparison with Fig. 2.7(e)-(h). Still, following the same logic as before, the results confirm that LZ transitions to the closest state in energy are responsible for losses in amplitude during the Bragg mirror process. Moreover, it can be seen in Fig. 2.8(i)-(l) that our perturbative treatment of the Doppler

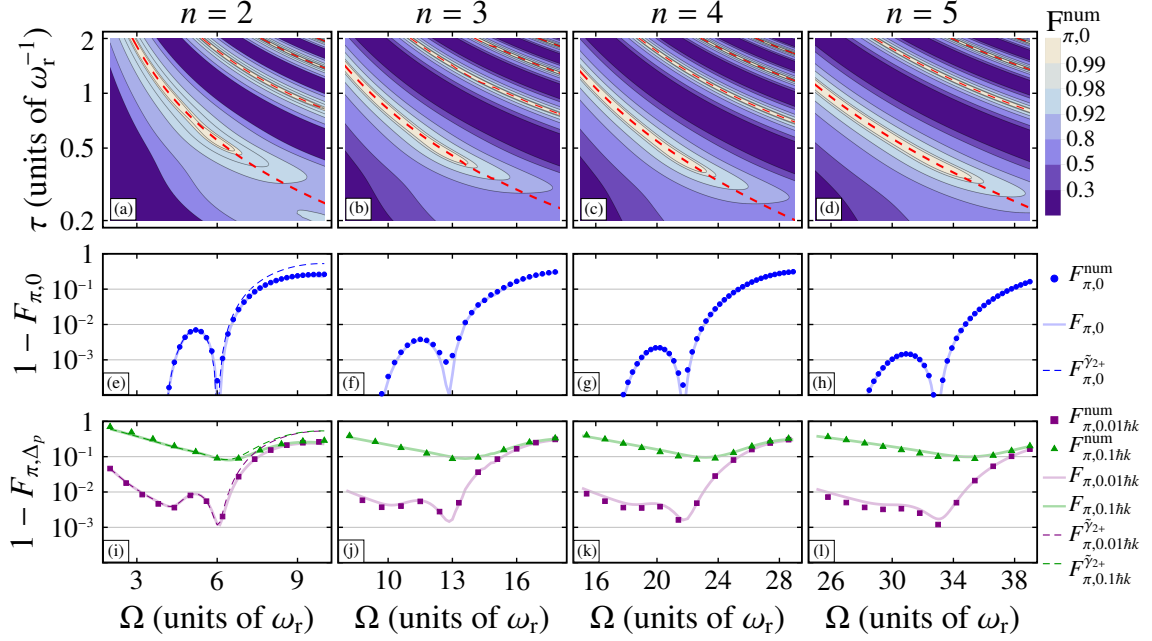


Figure 2.8: **Bragg mirror fidelity.** Top row: Pulse duration (2.92) (red dashed line) on top of the numerically determined mirror fidelities (2.113b) introduced in Fig. 2.5(e)-(h). Middle row: Fidelity loss as a function of peak Rabi frequency Ω and pulse durations computed via Eq. (2.92). Mirror fidelity loss was determined numerically (blue disks), via Eq. (2.112c) with values (2.96) (solid line). The dashed line in panel (e) for $n = 2$ is obtained by inserting $\tilde{\gamma}_{2,+}$ (2.93) into Eq. (2.112c) and denoted $F_{\pi,0}^{\tilde{\gamma}_{2,+}}$ in the legend on the right. Bottom row: Fidelity loss extracted from numerical calculations (squares & triangles) is again compared to analytic results (solid & dashed lines) similar to the middle row. Fidelities (2.113a) are now averaged over a wave packet with finite momentum width $\sigma_p = 0.01 \hbar k$ (purple squares and lines) and $\sigma_p = 0.1 \hbar k$ (green triangles and lines). The values for $\gamma_{n,\pm}$ were obtained again via Eq. (2.96) (solid lines) or for $\tilde{\gamma}_{2,+}$ using Eq. (2.93) (dashed lines) in the panel (i). Figure adapted from *J.-N. Siemss et al., Phys. Rev. A* **102**, 033709 (2020), Copyright 2022, American Physical Society (Ref. [120]).

detuning accurately models the velocity filtering properties of a Bragg mirror on a quantitative level for all orders considered here. Due to the fact that temporal mirror pulse widths are about twice the ones for beam splitters for the same Ω , the acceptance is reduced for off-resonant momentum classes visible in Fig. 2.8(i)-(l), which exhibit fidelity losses in the limit of small peak Rabi frequencies near unity. Indeed, when performing a Gaussian quasi-Bragg pulse of order $n = 2, 3, 4, 5$ for wave packets with finite momentum widths, the results demonstrate that there are optimal combinations of parameters Ω, τ for Bragg beam splitting pulses [see Fig. 2.7(i)-(l)] and mirror pulses [see Fig. 2.8(i)-(l)] that minimize nonadiabatic losses as well as the impact of the velocity filter.

2.7 Four-mode Bragg Scattering Matrix

Comparison with numerical calculations in the previous section emphasizes the accuracy of our model in describing the main diffraction order of Bragg beam splitters and mirror pulses. Nevertheless, there is experimental evidence of parasitic interferometry paths affecting the metrological properties of atom interferometers, and which are populated by scattering to additional states [118, 135, 147]. However, the inclusion of these states in our model requires the expansion of the scattering matrix in Eq. (2.104). To this end, and in anticipation of the discussion of the role played by the multi-port aspects of Bragg diffraction in atom interferometers in the next chapter, we include the dominant parasitic diffraction order arising from the LZ losses by extending the state space in this section as follows. According to Sec. 2.4.1, the (anti)symmetric states we need to consider are

$$\begin{aligned} |s_j(p)\rangle &\in \{|p, 2, \pm\rangle, |p, 0, +\rangle\} & (n = 2), \\ |s_j(p)\rangle &\in \{|p, n, \pm\rangle, |p, n - 2, \pm\rangle\} & (n \geq 3), \end{aligned} \quad (2.115a)$$

and similarly in the momentum eigenbasis we find

$$\begin{aligned} |q_j(p)\rangle &\in \{|\pm 2 \hbar k + p\rangle, |p\rangle\} & (n = 2), \\ |q_j(p)\rangle &\in \{|\pm n \hbar k + p\rangle, |\pm(n - 2) \hbar k + p\rangle\} & (n \geq 3). \end{aligned} \quad (2.115b)$$

Interestingly, the state spaces for first-order and third-order Bragg diffraction are identical. Therefore, for the discussion of $n = 1$, one can simply use the latter case with minor modifications.⁵ Thus, all the following formulas assume $n \geq 3$, as we reproduce the relevant expressions for the unique case $n = 2$ with only a single LZ state $|p\rangle$ in the Appendix A.4. The objective of this section is to derive a transfer matrix coupling the states in Eq. (2.115b),

$$B(p, \Omega, \tau, \phi_L) = \begin{pmatrix} B_{-n,-n} & B_{-n,-(n-2)} & B_{-n,+(n-2)} & B_{-n,+n} \\ B_{-(n-2),-n} & B_{-(n-2),-(n-2)} & B_{-(n-2),+(n-2)} & B_{-(n-2),+n} \\ B_{+(n-2),-n} & B_{+(n-2),-(n-2)} & B_{+(n-2),+(n-2)} & B_{+(n-2),+n} \\ B_{+n,-n} & B_{+n,-(n-2)} & B_{+n,+(n-2)} & B_{+n,+n} \end{pmatrix}. \quad (2.116)$$

We indicate the sub-blocks of the transfer matrix related to the main diffraction order (denoted by black symbols) and parasitic order (blue symbols). As before, the matrix elements $B_{j,l}$ are functions of the pulse parameters Ω, τ as well as the (quasi)momentum p and include the phase of the laser ϕ_L . To derive analytic expressions for these functions, we first generalize the projection of the scattering matrix in the (anti)symmetric basis, \mathcal{S}_α (2.61). We find

$$\mathcal{S}_\alpha = \sum_{j,l} S_{jl} |s_j\rangle \langle s_l|, \quad (2.117)$$

⁵To apply the analytical expressions derived for $n = 3$ to the case of $n = 1$, one must substitute $n \rightarrow n + 2$ and $n - 2 \rightarrow n$.

where we define S as the product matrix

$$S = S_{\text{LZ}} \cdot S_{\text{ad}}, \quad (2.118a)$$

composed of

$$S_{\text{ad}} = \begin{pmatrix} e^{-i\theta_{n+}} & 0 & 0 & 0 \\ 0 & e^{-i\theta_{(n-2)+}} & 0 & 0 \\ 0 & 0 & e^{-i\theta_{(n-2)-}} & 0 \\ 0 & 0 & 0 & e^{-i\theta_{n-}} \end{pmatrix}, \quad (2.118b)$$

and

$$S_{\text{LZ}} = \begin{pmatrix} e^{-\gamma_{n+}} & -e^{i\xi_+} \sqrt{1 - e^{-2\gamma_{n+}}} & 0 & 0 \\ e^{-i\xi_+} \sqrt{1 - e^{-2\gamma_{n+}}} & e^{-\gamma_{n+}} & 0 & 0 \\ 0 & 0 & e^{-\gamma_{n-}} & e^{-i\xi_-} \sqrt{1 - e^{-2\gamma_{n-}}} \\ 0 & 0 & -e^{i\xi_-} \sqrt{1 - e^{-2\gamma_{n-}}} & e^{-\gamma_{n-}} \end{pmatrix}. \quad (2.118c)$$

The entries of the product matrix S are again matrix elements of the time evolution operator in the asymptotic limit, $\lim_{\substack{t \rightarrow \infty \\ t_0 \rightarrow -\infty}} U_{\alpha\pm}(t, t_0)$, analogous to Eq. (2.62) and, as expected, S retains its block-diagonal structure in zeroth order of p . Furthermore, the generalized S contains new transition elements such as $\langle n, \pm | S_{\alpha\pm} | n - 2, \pm \rangle$. It is important to emphasize at this point, that unlike Eq. (2.61), we have defined S (2.118) to be unitary with single parameters $\gamma_{n\pm} \geq 0$ coupling the subspaces $|n, \pm\rangle \leftrightarrow |n - 2, \pm\rangle$ respectively. This not only yields simple off-diagonal elements of S_{LZ} , but is also useful in describing complete interferometer sequences, as we will see in the next chapter. At the same time, requiring $SS^\dagger = S^\dagger S = \mathbb{1}$ does not uniquely determine the order of the matrix multiplication in Eq. (2.118a). Below we explain, how we confirm the order using numerical solutions of the Schrödinger equation and how we use the same numerics to extract the newly introduced LZ transition phases ξ_\pm . Meanwhile, we reintroduce the perturbative effects of a nonvanishing (quasi)momentum p mixing symmetric and antisymmetric subspaces only for the main diffraction order,

$$S(p) = S \cdot \frac{1}{\sqrt{1 + \eta^2(p)}} \begin{pmatrix} 1 & 0 & 0 & i\eta(p)e^{i\Theta_n/2} \\ 0 & \sqrt{1 + \eta^2(p)} & 0 & 0 \\ 0 & 0 & \sqrt{1 + \eta^2(p)} & 0 \\ i\eta(p)e^{-i\Theta_n/2} & 0 & 0 & 1 \end{pmatrix}. \quad (2.119)$$

$S(p)$ represents a generalized version of the scattering matrix defined in Eq. (2.101), but does not incorporate corrections to the dynamics of the $|n - 2, \pm\rangle$ states with respect to p . We recall the assumption $p/\hbar k \ll 1$, which is at the core of our perturbative treatment of the (quasi)momentum and, as we have demonstrated in previous sections, justified when

describing wave packets with momentum widths $\sigma_p < 0.1 \hbar k$. Accordingly, we ignore terms of order $O[\frac{p}{\hbar k} \gamma_{n\pm}]$, which is also motivated by the observation that the LZ parameters $\gamma_{n\pm}$ grow for intense and short Bragg pulses, whereas the Doppler detuning effects are strongest towards long pulse durations. The transformation to the basis of momentum eigenstates is straightforward using

$$T = \frac{1}{\sqrt{2}} \begin{pmatrix} e^{in\phi_L} & 0 & 0 & e^{-in\phi_L} \\ 0 & e^{i(n-2)\phi_L} & e^{-i(n-2)\phi_L} & 0 \\ 0 & e^{i(n-2)\phi_L} & -e^{-i(n-2)\phi_L} & 0 \\ e^{in\phi_L} & 0 & 0 & -e^{-in\phi_L} \end{pmatrix}, \quad (2.120)$$

which provides us with the analytic transfer matrix for the extended state space in Eq. (2.115b),

$$B(p, \Omega, \tau, \phi_L) := T^\dagger S(p) T = \mathcal{M}(\Omega, \tau, \phi_L) \cdot \mathcal{N}(p, \Omega, \tau, \phi_L). \quad (2.121a)$$

Here, we have exploited the product form of $S(p)$ as well as the property $TT^\dagger = \mathbb{1}$. In zeroth order of the (quasi)momentum p , the dynamics of the momentum eigenstates in Eq. (2.115b) that are coupled by Bragg diffraction is described by the matrix $\mathcal{M}(\Omega, \tau, \phi_L)$ asymptotically. Meanwhile, $\mathcal{N}(p, \Omega, \tau, \phi_L)$ accounts for its first-order correction due to Doppler effects for the main diffraction order n . In addition to the entries in each corner being the same as in the case of the two-mode scattering matrix, the former,

$$\mathcal{M}(\Omega, \tau, \phi_L) = \begin{pmatrix} e^{\frac{-i}{2}(\Phi_n - i\Gamma)} \cos\left(\frac{\Theta_n - i\gamma}{2}\right) & \frac{-1}{2} e^{\frac{-i}{2}(\Theta_{n-2} + \Phi_{n-2} + 4\phi_L)} \times \\ & (e^{i\xi_+} h_1(\Gamma, \gamma) + e^{i(\Theta_{n-2} + \xi_-)} h_2(\Gamma, \gamma)) & \frac{-1}{2} e^{\frac{-i}{2}(\Theta_{n-2} + \Phi_{n-2} + 4(n-1)\phi_L)} \times \\ & (e^{i\xi_+} h_1(\Gamma, \gamma) - e^{i(\Theta_{n-2} + \xi_-)} h_2(\Gamma, \gamma)) & -ie^{-i2n\phi_L} e^{\frac{-i}{2}(\Phi_n - i\Gamma)} \sin\left(\frac{\Theta_n - i\gamma}{2}\right) \\ \frac{1}{2} e^{\frac{-i}{2}(\Theta_n + 2(\xi_- + \xi_+) + \Phi_n - 4\phi_L)} \times \\ (e^{i\xi_-} h_1(\Gamma, \gamma) + e^{i(\Theta_n + \xi_+)} h_2(\Gamma, \gamma)) & e^{\frac{-i}{2}(\Phi_{n-2} - i\Gamma)} \cos\left(\frac{\Theta_{n-2} - i\gamma}{2}\right) & -ie^{-i2(n-2)\phi_L} e^{\frac{-i}{2}(\Phi_{n-2} - i\Gamma)} \sin\left(\frac{\Theta_{n-2} - i\gamma}{2}\right) & \frac{1}{2} e^{\frac{-i}{2}(\Theta_n + 2(\xi_- + \xi_+) + \Phi_n + 4(n-1)\phi_L)} \times \\ & & & (e^{i\xi_-} h_1(\Gamma, \gamma) - e^{i(\Theta_n + \xi_+)} h_2(\Gamma, \gamma)) \\ \frac{1}{2} e^{\frac{-i}{2}(\Theta_n + 2(\xi_- + \xi_+) + \Phi_n - 4(n-1)\phi_L)} \times \\ (e^{i\xi_-} h_1(\Gamma, \gamma) - e^{i(\Theta_n + \xi_+)} h_2(\Gamma, \gamma)) & -ie^{i2(n-2)\phi_L} e^{\frac{-i}{2}(\Phi_{n-2} - i\Gamma)} \sin\left(\frac{\Theta_{n-2} - i\gamma}{2}\right) & e^{\frac{-i}{2}(\Phi_{n-2} - i\Gamma)} \cos\left(\frac{\Theta_{n-2} - i\gamma}{2}\right) & \frac{1}{2} e^{\frac{-i}{2}(\Theta_n + 2(\xi_- + \xi_+) + \Phi_n + 4\phi_L)} \times \\ & & & (e^{i\xi_-} h_1(\Gamma, \gamma) + e^{i(\Theta_n + \xi_+)} h_2(\Gamma, \gamma)) \\ -ie^{i2n\phi_L} e^{\frac{-i}{2}(\Phi_n - i\Gamma)} \sin\left(\frac{\Theta_n - i\gamma}{2}\right) & \frac{-1}{2} e^{\frac{-i}{2}(\Theta_{n-2} + \Phi_{n-2} - 4(n-1)\phi_L)} \times \\ & (e^{i\xi_+} h_1(\Gamma, \gamma) - e^{i(\Theta_{n-2} + \xi_-)} h_2(\Gamma, \gamma)) & \frac{-1}{2} e^{\frac{-i}{2}(\Theta_{n-2} + \Phi_{n-2} - 4\phi_L)} \times \\ & (e^{i\xi_+} h_1(\Gamma, \gamma) + e^{i(\Theta_{n-2} + \xi_-)} h_2(\Gamma, \gamma)) & e^{\frac{-i}{2}(\Phi_n - i\Gamma)} \cos\left(\frac{\Theta_n - i\gamma}{2}\right) \end{pmatrix}, \quad (2.121b)$$

contains a very similar (2×2) -submatrix in its center describing the dynamics in the $|\pm(n-2)\hbar k\rangle$ -subspace. The matrix elements in blue at the edges couple both diffraction orders. In order to keep the notation clean, we have defined the functions $h_2(\Gamma, \gamma) := \sqrt{1 - e^{(\gamma - \Gamma)}}$ and $h_1(\Gamma, \gamma) := \sqrt{1 - \cosh(\gamma + \Gamma) + \sinh(\gamma + \Gamma)}$. As a result of neglecting the influence of the (quasi)momentum beyond the main diffraction order, the resulting corrections are the same as in the two-mode case,

$$\mathcal{N}(p, \Omega, \tau, \phi_L) = \begin{pmatrix} \frac{1+i\eta(p) \cos(\Theta_n/2)}{\sqrt{1+\eta^2(p)}} & \mathbf{0} & ie^{-i2n\phi_L} \frac{i\eta(p) \sin(\Theta_n/2)}{\sqrt{1+\eta^2(p)}} \\ \mathbf{0} & \mathbb{1} & \mathbf{0} \\ -ie^{i2n\phi_L} \frac{i\eta(p) \sin(\Theta_n/2)}{\sqrt{1+\eta^2(p)}} & \mathbf{0} & \frac{1-i\eta(p) \cos(\Theta_n/2)}{\sqrt{1+\eta^2(p)}} \end{pmatrix}. \quad (2.121c)$$

In the following chapter, we apply our perturbative description of the (quasi)momentum to study its effects on Bragg mirrors in the context of atom interferometer sequences. At the same time, we neglect effects of finite velocity effects during beam splitting for the following investigation, i.e., we set $\mathcal{N}(p, \Omega_{\text{BS}}, \tau_{\text{BS}}) = \mathbb{1}$. This avoids possible artifacts arising from the fact that our perturbative description of the (quasi)momentum overestimates the strength of velocity filters in the case of Bragg beam splitters. This concerns in particular higher Bragg orders as we show in Fig. 2.7. Furthermore, velocity filtering is generally stronger during the mirror pulse due to the longer interaction times (see Fig. 2.6), whereas the more dominant role of LZ losses during beam splitter results mainly in terms of the order $\mathcal{O}[\frac{p}{\hbar k} \gamma_{n\pm}]$, which we discard as explained above.

Equations (2.121) represent the building blocks of the scattering matrix that describes n th-order Bragg diffraction including the coherent coupling to the dominant LZ states,

$$\mathcal{S}(\Omega, \tau, \phi_L) = \int_{-\hbar k/2}^{\hbar k/2} dp \sum_{j,l} [B(p, \Omega, \tau, \phi_L)]_{jl} |q_j(p)\rangle \langle q_l(p)|, \quad (2.122)$$

where $|q_j(p)\rangle$ are elements of the state space defined in Eq. (2.115b). Except for the laser phase ϕ_L , the choice of Bragg pulse parameters Ω, τ in the experiment determines all quantities in the transfer matrix $B(p, \Omega, \tau, \phi_L)$, most of which have already been introduced in previous sections and can be found in Tab. 2.2. At this stage, it is certainly useful to recall the idealized lossless case [cf. Eqs. (2.68)], in which the perfect choice of pulse parameters yields

$$B_{\text{BS}}^{\text{ideal}} = \begin{pmatrix} 1/\sqrt{2} & \mathbf{0} & -ie^{-i2n\phi_L}/\sqrt{2} \\ \mathbf{0} & \mathbf{B}_{\pm(n-2)} & \mathbf{0} \\ -ie^{+i2n\phi_L}/\sqrt{2} & \mathbf{0} & 1/\sqrt{2} \end{pmatrix}, \quad B_{\text{M}}^{\text{ideal}} = \begin{pmatrix} 0 & \mathbf{0} & -ie^{-i2n\phi_L} \\ \mathbf{0} & \mathbf{B}_{\pm(n-2)} & \mathbf{0} \\ -ie^{+i2n\phi_L} & \mathbf{0} & 0 \end{pmatrix}. \quad (2.123)$$

These matrices represent, respectively, perfect beam splitter and mirror operations for a wave packet initially prepared with mean momentum $-n\hbar k$ or $n\hbar k$ in the limit of a vanishing velocity width. In this idealized two-mode limit the parasitic diffraction orders decouple from the main ones. In the following, we point out some novel aspects regarding the parameters of the four-mode Bragg scattering matrix before discussing the newly introduced transition phases ξ_{\pm} and verifying the assumptions we made for the construction of the scattering matrix. For this purpose, we compare our analytical model with numerical solutions of the Schrödinger equation.

2.7.1 LZ Loss Parameters: γ, Γ

We have seen that γ, Γ represent corrections to the adiabatic dynamics of the Bragg pulse by characterizing the global and differential LZ losses from the main states $|\pm n \hbar k + p\rangle$. In addition, they now determine the transition amplitudes between those and the LZ states $|\pm(n-2) \hbar k + p\rangle$. Similarly, $\gamma_{n\pm}$ couple the corresponding states in the even(+) and odd(-) subspaces, as the form of S_{LZ} (2.118c) makes clear, where we recall the relations $\Gamma = \gamma_{n+} + \gamma_{n-}$ and $\gamma = \gamma_{n+} - \gamma_{n-}$ (see Tab. 2.2). Thus, the fact that the transition matrix $B(p, \Omega, \tau, \phi_{\text{L}})$ (2.121) is unitary by design ultimately requires that all atoms lost from the main diffraction order n are transferred to the $(n-2)$ -subspace. Yet, this is at odds with some of the observations we made in Sec. 2.4.3. There, we argued that, e.g., in the cases of $n = 4, 5$ for some parameters Ω, τ it is necessary to consider also losses to states $|\pm(n-4) \hbar k + p\rangle$. One way to correct this inconsistency would be to introduce two sets of parameters that describe transitions within the extended state spaces (2.115) and losses to other states separately. This would of course mean that $B(p, \Omega, \tau, \phi_{\text{L}})$ is no longer unitary. Alternatively, one could further generalize the scattering matrix (2.117) to include all states populated by the Bragg pulse. Both approaches would significantly complicate the form of the scattering matrices and our analytical model as a whole, and are therefore beyond the scope of this thesis. Furthermore, we demonstrate in the next chapter that the model in Eq. (2.118) provides accurate and valuable insights into the workings of Bragg atom interferometers.

In the remainder of this section, we instead explain how to navigate the intricacies of our model and how to avoid potential errors resulting from its assumptions. In Sec. 2.4.3, we state that in the absence of analytical formulas for $n > 3$, the parameters γ and Γ must be inferred from population data after numerically solving the Schrödinger equation. Assuming there are no LZ losses outside of the four-mode state space, we find [cf. Eqs. (2.96)]

$$\gamma_{n,\pm} = -\frac{1}{2} \ln \left(1 - 2N_{n-2,\pm}^{\text{num}} \right). \quad (2.124)$$

In this way, accurate coupling strengths to the parasitic states $|n-2, \pm\rangle$ are obtained via Eq. (2.118c) and to $|\pm(n-2) \hbar k\rangle$ via Eq. (2.121b), but at the same time this may underestimate the losses from the main diffraction modes, especially for Bragg orders $n > 3$. Alternatively, we can account for losses from the main diffraction order n to all other relevant states,

$$\gamma_{n,\pm} = -\frac{1}{2} \ln \left(1 - 2(N_{n-2,\pm}^{\text{num}} + N_{n-4,\pm}^{\text{num}} + N_{n+2,\pm}^{\text{num}}) \right), \quad (2.125)$$

which overestimate the population transferred to the $(n-2)$ -subspace, when inserted into the scattering matrices. Note, that compared to Eq. (2.96c) we have also included the population of the energetically higher-lying states $|\pm(n+2) \hbar k\rangle$. Indeed, Fig. 2.9(a) illustrates

that population is dominantly lost to the modes $|\pm 3 \hbar k\rangle$ in the case of a fifth-order Gaussian Bragg beam splitting pulse. Assuming the input state in Eq. (2.105) we evaluate and plot

$$N_{-m \hbar k}^{\text{num}} + N_{m \hbar k}^{\text{num}} = \lim_{\sigma_p \rightarrow 0} \int_{-\hbar k/2}^{\hbar k/2} dp \left(\left| \langle -m \hbar k + p | \psi_{\text{num}}^{\text{out}} \rangle \right|^2 + \left| \langle +m \hbar k + p | \psi_{\text{num}}^{\text{out}} \rangle \right|^2 \right), \quad (2.126)$$

after numerically solving the Schrödinger equation with respect to the Hamiltonian in Eq. (2.44a) for parameters $\Omega_{\text{BS}}, \tau_{\text{BS}}$ [see Eq. (2.92)]. The results confirm that the scattering process also couples states $|\pm 1 \hbar k\rangle (= |\pm(n-4) \hbar k\rangle)$. Interestingly, however, in proximity of the LZ minimum the population of the energetically higher-lying states, $|\pm 7 \hbar k\rangle (= |\pm(n+2) \hbar k\rangle)$, is in fact comparable to $|\pm 3 \hbar k\rangle$. For the same Bragg pulse parameters Fig. 2.9(b) illustrates the quantitative difference in the global and differential LZ parameters γ, Γ , when taking into account different numbers of modes. It is evident, that the number of modes especially affects γ and that states $|\pm(n+2) \hbar k\rangle$ play an important role as well due to the intriguing property of the LZ minimum. We can verify that Eq. (2.125) includes all relevant modes if we extract $\gamma_{n,\pm}$ directly from population data obtained on the basis of momentum eigenstates as opposed to the (anti)symmetric basis. For this purpose, we need to numerically solve the dynamics generated by the momentum eigenstate Hamiltonian (2.44a) with different initial conditions,

$$|\psi_{\pm}^{\text{in}}\rangle = \int_{-\hbar k/2}^{\hbar k/2} dp \frac{g(p, \sigma_p)}{\sqrt{2}} (|-n \hbar k + p\rangle \pm |n \hbar k + p\rangle). \quad (2.127)$$

The application of either the scattering matrix in Eq. (2.104) or its generalized version in Eq. (2.122) gives the output state, $|\psi_{\pm}^{\text{out}}(\Omega, \tau, \phi_L)\rangle = \mathcal{S}(\Omega, \tau, \phi_L) |\psi_{\pm}^{\text{in}}\rangle$, which in combination with the assumption $\phi_L = (2c+1)\pi/2$ for $c \in \mathbb{Z}^6$, we can directly connect $\gamma_{n\pm}$ to the output population of a Bragg beam splitter,

$$\begin{aligned} N_{-n \hbar k} + N_{n \hbar k} &= \lim_{\sigma_p \rightarrow 0} \int_{-\hbar k/2}^{\hbar k/2} dp \left(\left| \langle -n \hbar k + p | \psi_{\pm}^{\text{out}}(\Omega, \tau, \phi_L) \rangle \right|^2 + \left| \langle +n \hbar k + p | \psi_{\pm}^{\text{out}}(\Omega, \tau, \phi_L) \rangle \right|^2 \right) \\ &= e^{-2\gamma_{n,\pm}}. \end{aligned} \quad (2.128)$$

Inserting numerical population data $N_{\pm n \hbar k}^{\text{num}}$ and solving this equation for $\gamma_{n\pm}$ ($0 < \gamma_{n\pm} < 1$) allows us to find perfect agreement with the results based on Eq. (2.125), which becomes clear from Fig. 2.9(b). We will see in the next chapter that in the context of the full Bragg atom interferometer sequences, the differential loss from the main states $|\pm n \hbar k + p\rangle$ and the resulting LZ loss parameters play a major role and therefore must be determined accurately. In this context, it is hence necessary to use Eq. (2.125).

⁶We note that Eq. (2.128) also holds in case $\phi_L = c\pi$ with $c \in \mathbb{Z}$ if we make the substitution $\gamma_{\pm} \rightarrow \gamma_{\mp}$.

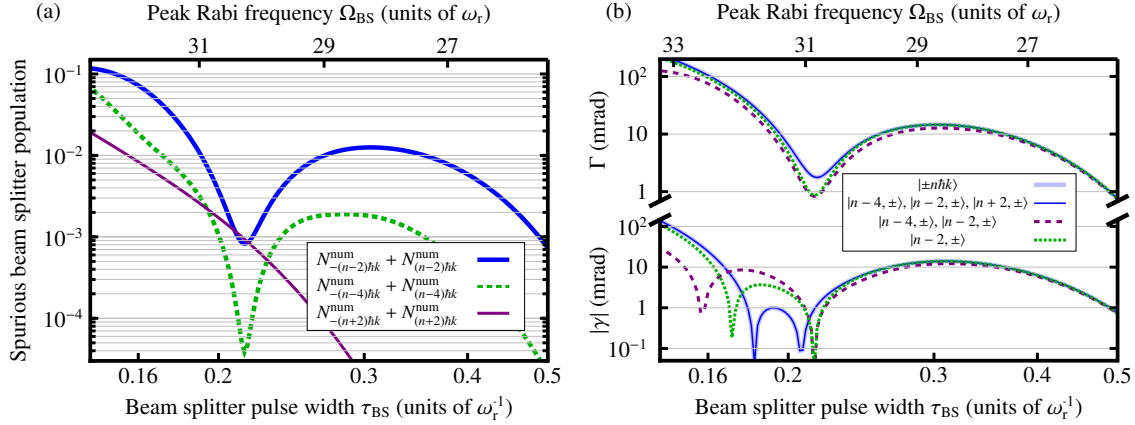


Figure 2.9: **Spurious beam splitter population and LZ amplitudes for Bragg order $n = 5$.** (a) We determine the population of the LZ states using Eq. (2.126). Although population is mainly lost to states $|\pm(n-2)\hbar k\rangle$ (thick blue line), the data highlight that for some parameters Ω_{BS}, τ_{BS} their population is comparable to the one of $|\pm(n+2)\hbar k\rangle$ (thin violet line) because of the existence of the LZ minimum. (b) The global (upper panel) and differential (lower panel) LZ parameters clearly depends on the truncation of state space. Comparison with the results from Eq. (2.128) (thick light blue line) shows that for the parameters considered here the truncation made in Eq. (2.125) is sufficient for fifth-order Bragg diffraction beam splitters at the μrad -level.

2.7.2 Phases

Energetic Phases: $\Theta_n, \Theta_{n-2}, \Phi_n, \Phi_{n-2}$

As a result of the adiabatic theory of Bragg diffraction derived in this section, we have seen that $\Theta_n, \Theta_{n-2}, \Phi_n, \Phi_{n-2}$ are determined by energetic phases acquired during adiabatic dynamics plus their nonadiabatic corrections [see Eq. (2.65) and Eq. (2.91)]. The phase Θ_{n-2} plays a role analogous to that of Θ_n , but within the subspace of parasitic states $|\pm(n-2)\hbar k + p\rangle$. We will demonstrate in the next chapter, how the insight into the Bragg pulse dynamics within both subspaces can be used in Bragg atom interferometers to manipulate undesired interferometry paths. Φ_n as well as Φ_{n-2} denote phases imprinted on the different modes during the Bragg pulse.

Landau-Zener Transition Phases: ξ_+, ξ_-

Apart from the coupling strength to the LZ states $|n, \pm\rangle$, the off-diagonal matrix elements of the scattering matrix (2.118c) also include transition phases ξ_+, ξ_- . Those phases affect the matrix elements of $B(p, \Omega, \tau, \phi_L)$, which couple the $(n-2)$ -states to the main Bragg order n and vice versa, and will therefore be important for the understanding of atom interferometers including parasitic trajectories. Comparison with numerical solutions of the Schrödinger equation in this case not only allows us to extract the numerical values for

ξ_+, ξ_- , but in addition gives us the opportunity to verify the form of the scattering matrices in Eq. (2.118a) and in Eq. (2.121b). We can determine the transition phases for given pulse parameters Ω, τ by solving the time evolution either in the (anti)symmetric basis or in the basis of momentum eigenstates. First, we consider

$$|\psi^{\text{in}}\rangle = \lim_{\sigma_p \rightarrow 0} \int_{-\hbar k/2}^{\hbar k/2} dp \frac{g(p, \sigma_p)}{\sqrt{2}} (|n \hbar k + p\rangle) = \frac{1}{\sqrt{2}} (|n, +\rangle + |n, -\rangle) \quad (2.129)$$

as the initial condition for the dynamics in the (anti)symmetric basis, where the use of $|n \hbar k + p\rangle$ instead of $|-n \hbar k + p\rangle$ simply avoids a phase shift of π in the following calculation. Applying the scattering matrix S to this state in the (anti)symmetric basis representation, we find an analytic expression for the diffracted state,

$$\begin{aligned} |\psi^{\text{out}}(\Omega, \tau)\rangle &= S(\Omega, \tau) |\psi^{\text{in}}\rangle \\ &= \frac{1}{\sqrt{2}} \left\{ e^{-\gamma_+ - i\theta_{n+}}, e^{-i(\theta_{n+} + \xi_+)} \sqrt{1 - e^{-\gamma_+}}, e^{-i(\theta_{n-} + \xi_-)} \sqrt{1 - e^{-\gamma_-}}, e^{-\gamma_- - i\theta_{n-}} \right\}^T. \end{aligned} \quad (2.130)$$

We can now compare this result with the complex amplitudes of numerically determined output states and confirm that the form of S (2.118a) is indeed correct, as well as obtain ξ_+, ξ_- this way, i.e., $|\psi_{\text{num}}^{\text{out}}(\Omega, \tau)\rangle \stackrel{!}{=} S(\Omega, \tau) |\psi^{\text{in}}\rangle$. While we recall that the energetic phases $\theta_{n\pm}$ can be obtained using Eq. (2.91), to remain self-consistent and as an initial step we extract the energetic phases from the numerics⁷ writing $\theta_{n\pm} \stackrel{!}{=} -\text{Im}\{\ln(\langle \pm, n | \psi_{\text{out}}^{\text{num}}(\Omega, \tau) \rangle)\}$. In the same manner, we extract the combined phases $\theta_{n\pm} + \xi_{\pm}$ and find

$$\xi_{\pm} = -\text{Im}\{\ln \langle \pm, n - 2 | \psi_{\text{num}}^{\text{out}}(\Omega, \tau) \rangle\} + \text{Im}\{\ln \langle \pm, n | \psi_{\text{num}}^{\text{out}}(\Omega, \tau) \rangle\}. \quad (2.131)$$

To check if this is indeed correct, we can exploit the analytic form of the scattering matrix (2.122) for momentum eigenstates, this time using the input state in Eq. (2.105). We find an analytical expression for the diffracted LZ populations of a n th-order Bragg pulse via $|\psi^{\text{out}}(\Omega, \tau, \phi_L)\rangle = \mathcal{S}(\Omega, \tau, \phi_L) |\psi^{\text{in}}\rangle$, which reads in the limit for vanishing velocity width,

$$\begin{aligned} N_{\mp(n-2)\hbar k} &= \lim_{\sigma_p \rightarrow 0} \int_{-\hbar k/2}^{\hbar k/2} dp \left| \langle \mp(n-2)\hbar k + p | \psi^{\text{out}}(\Omega, \tau, \phi_L) \rangle \right|^2 \\ &= \frac{1}{2} e^{-\Gamma} \left(e^{\Gamma} - \cosh(\gamma) \pm \cos(\Theta_n + \xi_+ - \xi_-) \sqrt{1 + e^{2\Gamma} - 2e^{\Gamma} \cosh(\gamma)} \right). \end{aligned} \quad (2.132)$$

Inserting the phases ξ_+, ξ_- from above in addition to Γ, γ , which we extract on the basis of Eq. (2.124) to avoid overestimating the population of these states as explained before, we can compare this result to numerical solutions of the Schrödinger equation $N_{\mp(n-2)\hbar k}^{\text{num}}$ [cf. Eq. (2.126)]. We give an example with Fig. 2.10, where we depict the population

⁷Extracting the correct phases from numerically determined states $|\psi_{\text{out}}^{\text{num}}(\Omega, \tau)\rangle$ requires solving the Schrödinger equation in interaction picture introduced in Eq. (2.39). Otherwise, it is necessary to account for phase evolution due to the kinetic energy.

of the parasitic diffraction order $n - 2 = 3$ that is dominantly coupled by the fifth-order beam splitting pulse, again assuming parameters $\Omega_{\text{BS}}, \tau_{\text{BS}}$ (see Sec. (2.4.2)). The perfect agreement between the numerical data and Eq. (2.132) demonstrates that the extended transfer matrix $B(\Omega, \tau, \phi_{\text{L}})$ accurately describes the dynamics of the dominant diffraction orders $|\pm(n - 2)\hbar k + p\rangle$, at least in zeroth order of the (quasi)momentum p . We recall that terms of order $O[\gamma \frac{p}{\hbar k}]$ will be small and are therefore neglected in our description. Note, that agreement is conditional on using Eq. (2.124) to calculate the values for Γ and γ , which we plug into Eq. (2.132). Interestingly, Fig. 2.10 provides further evidence of higher-order corrections to the differential energetic phase of the main diffraction order, Θ_n . Examining $N_{+(n-2)\hbar k}$, one clearly recognizes, that the assumption $\Theta_n = \pi/2$ toward shorter pulse durations breaks down due to corrections not included in $\tau(\pi/2, \Omega)$ (2.92). Instead, for given $\Omega_{\text{BS}}, \tau_{\text{BS}}$ we determine $N_{\mp n\hbar k}^{\text{num}}$ and solve

$$N_{\mp n\hbar k} = \lim_{\sigma_p \rightarrow 0} \int_{-\hbar k/2}^{\hbar k/2} dp \left| \langle \mp n\hbar k + p | \psi^{\text{out}}(\Omega, \tau, \phi_{\text{L}}) \rangle \right|^2 = \frac{1}{2} e^{-\Gamma} (\cosh(\gamma) \pm \cos(\Theta_n)) \quad (2.133)$$

for the exact value of Θ_n . But to obtain accurate results, we need to use Eq. (2.125) in this context to avoid underestimating the losses from the main diffraction orders n . As mentioned earlier, this is an artifact of our definition of $B(p, \Omega, \tau, \phi_{\text{L}})$. Furthermore, Fig. 2.10 confirms our accurate knowledge of the phases ξ_+ and ξ_- inserted in Eq. (2.132).

It is worth mentioning that Eq. (2.133) provides a second way to extract the phase difference $\xi_+ - \xi_-$. Still, it is much simpler to use Eq. (2.131) to extract the individual transition phases on the basis of numerical population data. Although it would certainly be of interest to derive analytical expressions for these transition phases in analogy to the nonadiabatic corrections to the energetic phase evolution discussed in Sec. 2.4.1, this is beyond the scope of this work. Moreover, as the main result of this section, we would like to highlight the analytical form of the transfer matrix $B(\Omega, \tau, \phi_{\text{L}})$, which accurately describes the coherent coupling to the dominant perturbative diffraction orders. This result serves as the foundation for the following discussions of complete Bragg atom interferometers.

2.8 Conclusion and Comparison to Existing Theory

The comprehensive comparison with numerical calculations in the previous section demonstrates that our scattering matrix accurately describes the dynamics of Gaussian Bragg pulses in the so-called quasi-Bragg regime. The general form of the Bragg scattering matrix applies to adiabatic but otherwise arbitrary pulses of any order with constant laser phase. We would like to emphasize that the logic developed in this chapter also covers Bragg orders $n > 5$. Note, though, that losses due to spontaneous emission are not included in our analysis, although, as mentioned earlier, these losses significantly limit the range of Rabi

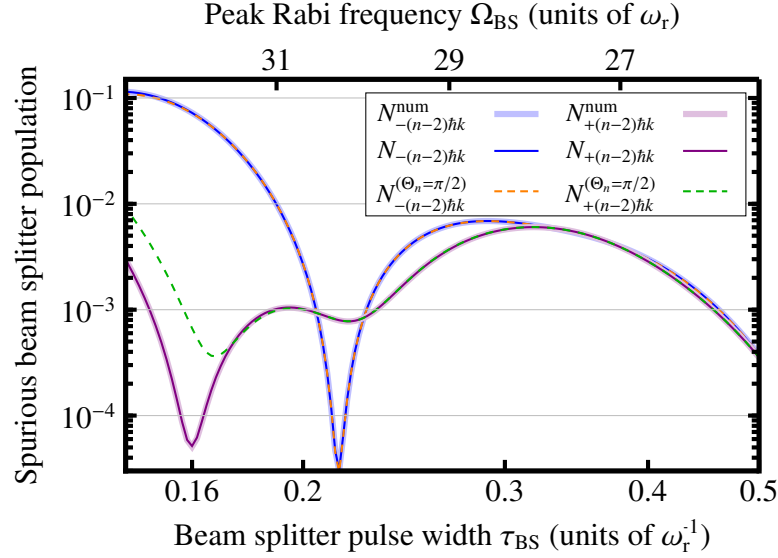


Figure 2.10: **Dominant spurious beam splitter population for Bragg order $n = 5$.** In comparison to Fig. (2.9)(a), we plot the occupation numbers for both dominant parasitic states, $|\pm(n-2)\hbar k\rangle (= |\pm 3\hbar k\rangle)$, separately to highlight their differences. The predictions using Eq. (2.132) (thin lines) are in perfect agreement with the numerical data (thick lines), which validates our result for the four-mode scattering matrix and Eq. (2.131). The dashed lines assume an ideal differential Bragg phase, $\Theta_n = \pi/2$, for all pulse parameters Ω_{BS} , τ_{BS} , leading to visible deviations for $|(n-2)\hbar k\rangle (= |+3\hbar k\rangle)$ from the numerics. Our model does not include the next-order nonadiabatic corrections to Θ_n that become increasingly important for very short pulses, which explains the visible differences in the population.

frequencies useful for performing high-fidelity Bragg pulses. In their study, *S. S. Szigeti et al.* [69] conclude that for the example of ^{87}Rb atoms, viable Bragg orders are limited to $n \leq 5$ due to the effects of spontaneous emission, justifying our focus on this range.

The Bragg scattering matrix (2.58) depends on dynamic (energetic) phases and non-adiabatic first-order (in inverse pulse duration) corrections corresponding to LZ losses and LZ phases. First-order Doppler shifts are included systematically in terms of perturbation theory to account for finite momentum widths of atom wave packets. We provide simple formulas highlighting the analytic dependence of these quantities on the parameters of the Bragg pulse such as its peak intensity, duration and envelope [see Table (2.2)]. Although, with regards to the LZ losses we only give such a formula for the diffraction order $n = 2$, our analysis leaves little doubt that the logic of nonadiabatic losses within a two-level system can be extended to diffraction orders $n > 2$. A suitable adaptation of theoretical treatments as in [145, 146, 148, 149] may therefore give good analytic descriptions for more general cases.

In summary, the theory of Bragg scattering developed in the previous sections allows for exciting perspectives on Bragg pulses that serve as a basis for analytic models of complete

interferometry sequences. This foundation promises significant insights when investigating systematic effects related to the shortcomings of the diffraction process. In the next chapter, we therefore proceed by extending our analytical treatment and investigate how the properties of the Bragg pulses operating in the quasi-Bragg regime affect the characteristics of atom interferometers, as this will have immediate practical implications for the design and operation of such devices. We remark that the fidelities introduced in Sec. 2.6.1 for benchmarking our analytic theory against the numerical integration of the Schrödinger equation are indeed of limited value for experiments because it is not easy to derive statements, e.g., about the metrological performance of a Bragg interferometer. Before proceeding to a discussion of the signal of atom interferometers, however, we put our model in a clear context with the preceding theory, which we seek to complement.

2.8.1 Diabatic Dynamics Described by an Effective Hamiltonian

As outlined in Sec. 2.2, the majority of existing descriptions aim at transferring the concept of a two-level system being diabatically coupled by a Rabi frequency, which is valid in the limit of asymptotically long pulse durations, i.e., in the deep-Bragg regime, to quasi-Bragg pulses. We would like to emphasize once again the conceptual differences between the application of the adiabatic theorem in our model and the adiabatic elimination of off-resonant states. Specifically, our findings are based on the realization that it is far more useful to understand the evolution of the atom interacting with the pulsed optical lattice in terms of the adiabatic theorem, rather than assuming diabatic transitions in between the levels of an effective two-level system. This allows the formulation of a comprehensive and relatively simple analytic model that accurately captures the dynamics of single Bragg diffraction. In doing so, we have successfully applied the adiabatic theorem to describe single Bragg diffraction of arbitrary order n with smooth temporal pulse shapes. As a result, we arrive at intuitive analytical expressions linking the products of this elastic scattering process and the experimental parameters of the Bragg pulse. In particular, our formulas for dynamic and LZ phases provide simple expressions for the so-called Bragg condition on the pulse area (i.e., the combination of pulse duration and peak intensity) in the quasi-Bragg regime. In our formalism, this replaces the concept of the effective Rabi frequency, which has been used in earlier descriptions to formulate this condition on the Bragg pulse parameters [101, 102, 125, 130].

In this context, we stress foremost the efficiency of our approach when increasing the Bragg order n . Since our formalism only requires us to calculate eigenenergies of finite-dimensional Hamiltonians to obtain the phases in Eq. (2.104b), taking into account more states does not significantly increase the complexity of computing the quantities in Table 2.2, whereas the adiabatic elimination of additional states that become relevant when increasing the Bragg order n is more complicated. In direct comparison to Ref. [130], our

solution for the differential dynamic phase (2.73) can be also expanded in orders of $\Omega(t)$ and $\dot{\Omega}(t)$, and we expect to be able to reproduce Eq. (48) in [130] with similar or even higher accuracy. This is conceivable since our formalism allows us to obtain the necessary eigenvalues by diagonalizing finite-dimensional matrices, which can be achieved by efficient and accurate numerical routines even for high truncation orders. Furthermore, our model for smooth Bragg pulses applies to atoms with velocity distributions that are narrow on the scale of the photon recoil of the Bragg lattice as we include linear Doppler shifts via perturbation theory up to first order. The reduction in transfer efficiencies due to velocity selectivity was primarily modeled using numerical simulations [69, 135], but the authors *E. Giese* et al. [132] provided an analytical description for the case, where wave packets featuring a narrow momentum spread, $\sigma_p \ll \hbar k$, interact with double Bragg pulses with rectangular pulse shapes.

2.8.2 Bloch-band Picture

In Sec. 2.2.3 we argue that the concept of describing Bragg diffraction as adiabatic dynamics is closely related to the Bloch-band picture. We hope to have convinced the reader that all the important observations that can be derived from this picture are fully confirmed by our analytic model and complemented by further insights. It is certain that *Gochbauer* et al. anticipated the application of the adiabatic theorem to Bragg diffraction in their work [119]. Figure 2.11 highlights the relationship between the Bloch bands and the spectra of the Hamiltonians derived in this thesis for Bragg scattering of even and odd order, as shown in Fig. 2.3. They correspond exactly to cuts through the Bloch spectra for a fixed constant quasimomentum, $q_B = \pm k$ and $= 0$ (see Fig. 2.11(a) and 2.11(c) and their connection to Fig. 2.11(b) indicated by the vertical dashed grey lines). Thus, instead of solving the entire Bloch-band structure for arbitrary Rabi frequencies and all possible (quasi)momenta p , we reduce the problem to diagonalization of low-dimensional Hamiltonians only for $p=0$. The decomposition of the Hamiltonians into their symmetric and antisymmetric components allows us to determine the energy gap very accurately already for low truncation orders, and avoids the need to numerically determine Bloch spectra for variable potential depths. Our procedure leads to analytical expressions such as Eq. (2.73), which are both instructive and efficient, giving us excellent agreement with the numerical calculations in the experimentally most relevant regime of quasi-Bragg pulses with Gaussian envelopes [130, 131]. In our formalism, a nonvanishing (quasi)momentum p couples the (in zeroth order of p) disjoint (anti)symmetric Hilbert spaces $\mathcal{H}_{p\alpha\pm}$ [see Eq. (2.46)]. According to the theory presented here, this coupling influences the differential phase (2.65), corresponding to an effectively reduced Rabi frequency, and results in a velocity filter that depends on the (quasi)momentum p . Our expression for the net differential dynamic phase $\Theta^{\text{dyn}} = \theta_{n+}^{\text{dyn}} - \theta_{n-}^{\text{dyn}}$, with $\theta_{n\pm}^{\text{dyn}}$ given in Eq. (2.73), is of course nothing else

than what *Gochmauer* et al. refer to as the integrated effective Rabi frequency. It should be evident by now that it is much more economical and appropriate to consider this phase as a differential dynamic phase in terms of the adiabatic theorem. After all, it is this interpretation of the phase that allows us to systematically determine corrections beyond the ideal adiabatic limit. The application of the adiabatic theorem to Bragg diffraction together with the first-order corrections for the LZ phases, LZ losses, and Doppler shifts yields, in fact, an exhaustive analytical description of all high-quality Bragg pulses.

In the next chapter we illuminate the impact the diffraction processes have on the signal of atom interferometers. A better understanding of the so-called diffraction phases [116] is paramount to facilitate the development of new as well as the improvement of existing mitigation strategies [98, 117–119, 150]. A comprehensive study of these phenomena requires the inclusion of realistic three-dimensional light pulses considering as well the effects of the profile of the laser beam. Even though such efforts are beyond the scope of this thesis and though we have restricted ourselves to the case of one-dimensional scattering, the introduction of a position dependence into the amplitude and phase of the laser will allow for a systematic discussion of diffraction processes with realistic optical lattices on a microscopic level.

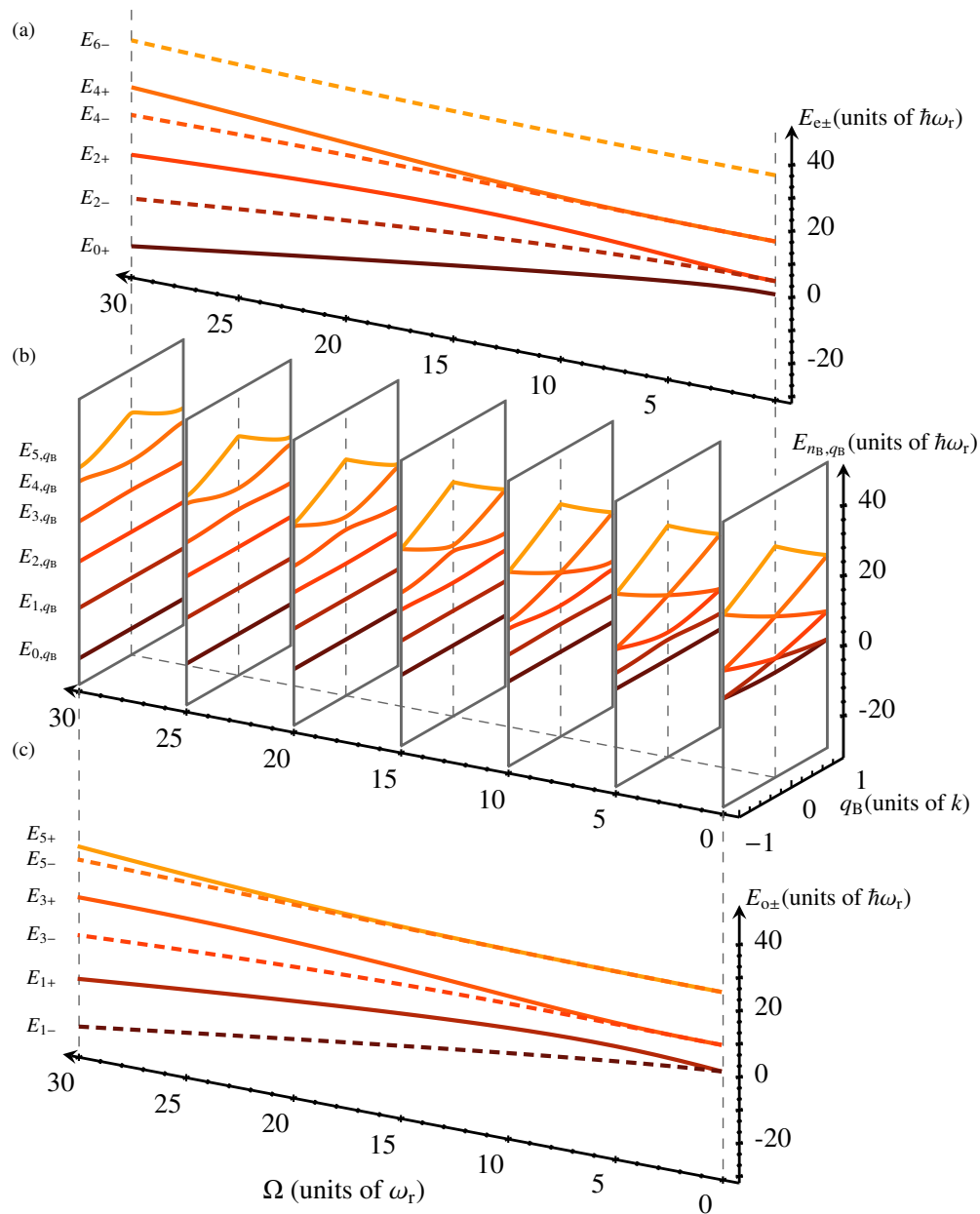


Figure 2.11: **Bloch energy bands and eigenenergies of the Bragg Hamiltonian.** (b) is identical to Fig. 2.2. (a,c) show cuts along the Ω axis at the edge ($q_B = -1k$) and the center ($q_B = 0$) of the Brillouin zone, respectively. The energies of the Bloch spectrum in (a) [(c)] are identical to the spectra of the Bragg Hamiltonians in Eqs. (2.55) displayed in Fig. 2.3(a) [Fig. 2.3(b)]. Figure adapted from *J.-N. Siemss et al.*, Phys. Rev. A **102**, 033709 (2020), Copyright 2022, American Physical Society (Ref. [120]).

3

LMT Bragg Atom Interferometers with μrad -Accuracy

3.1 Motivation and Research Question

At the time of writing this thesis, all atom interferometers demonstrating metrological gain from LMT separations [23, 32, 112, 113] use beam splitters based on the elastic scattering of atoms from time-dependent optical lattice potentials, i.e., Bragg diffraction [101, 151]. Yet, a comprehensive analytical model of Bragg interferometers is still missing.

We have seen in the previous chapter how higher-order Bragg pulses with Gaussian temporal envelopes can be used to realize efficient matter wave beam splitters and mirrors. Light-pulse atom interferometry combines several of those atom optics elements to create and recombine spatial atomic superpositions [125].

Bragg pulses can be used to generate and recombine multiple copies of different momenta from a single incoming wave packet, as we show in Fig. 3.1(a), where a mirror pulse in between two identical beam splitters forms a MZ interferometer [9]. For these devices, the interrogation time T between the pulses is typically much larger than the duration of the individual pulse.

Using the example of an inertial sensor, we have explained in Sec. 1.1 that any force coupling to the atomic degrees of freedom during that time may cause a differential phase evolution between the components of the atomic superposition due to their spatial separation. In particular, atom interferometers are uniquely sensitive to inertial effects such as local accelerations and rotations because of the inertia of the atomic test masses [54]. Since the laser interactions track the relative motion between the atoms and the wavefronts of the light field, the acceleration of the atoms by the force, which depends on the trajectory, can in principle be detected via a differential Doppler shift. The resulting relative phase ϕ is a linear function of the light phases that are transferred onto the diffracted parts of

the superposition during each pulse [e.g., see Eqs. (2.104)]. In the case of a MZ interferometer realized by n th-order Bragg pulses and assuming linear gravity g acting along the propagation direction of the optical lattice, the phase shift is given by [55, 56]

$$n\phi = 2n (kgT^2 + \phi_{L,1,BS} - 2\phi_{L,M} + \phi_{L,2,BS}). \quad (3.1)$$

Here, the ϕ_L are the Bragg laser phases that we have defined in the previous chapter and the scaling with $2n$ results from multiple pairs of photons being absorbed and emitted during each pulse. The relative phase ϕ must then be inferred indirectly from measurements of the interferometer signal that are performed after the final beam splitter. A common method to record the signal is counting atoms in the output ports of the atom interferometer. In some experiments, though, the information about the phase is obtained via spatial interference images by resolving the local density distribution of the atomic ensemble [98, 152]. In both cases, detection is typically achieved either through fluorescence detection [153] or absorption imaging [154].

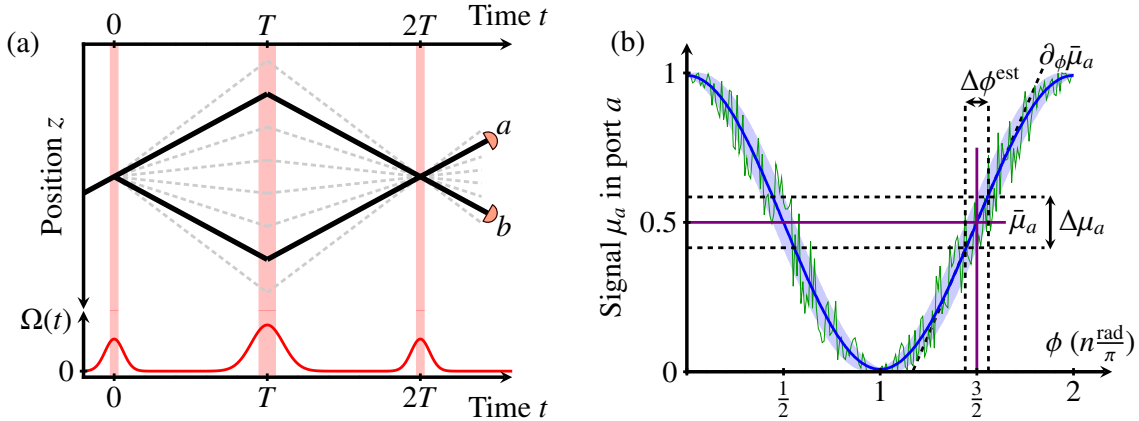


Figure 3.1: Space-time diagram of a three-pulse MZ interferometer and sample interference signal. (a) Three Gaussian n th-order Bragg pulses separated by the time T realize the interferometer. The resulting trajectories are shown in the inertial frame of the optical lattice. Typically, beam splitters and mirrors are considered two-mode operations populating the two main trajectories (solid black lines) that are detected in ports a and b . Scattering to undesired diffraction orders causes spurious trajectories and output ports (dashed grey lines). We study their implications for the phase measurement, which we illustrate in (b) based on the MZ signal (3.2) with $P_0 = \frac{1}{2} = A$ in port a at mid-fringe $P_a(\phi) \approx 0.5$. The noisy signal (assuming Gaussian noise, thin green line) represents statistically distributed measurement outcomes μ_a at particular ϕ with a mean $\bar{\mu}_a$ (solid blue line) and variance $(\Delta\mu_a)^2$ (shaded blue region). The phase sensitivity $\Delta\phi^{\text{est}}$ can be obtained via error propagation (see main text). If $\Delta\mu_a$ does not depend on the phase, $\Delta\phi^{\text{est}}$ is minimal at those positions, where the signal slope $\partial_\phi \bar{\mu}_a$ is maximized.

In this work, we consider atom counting. The two detectors a and b in Fig. 3.1(a) record the number of atoms exiting the interferometer, N_a and N_b , to calculate the transition

probabilities $\mu_{a(b)} := N_{a(b)}/(N_a + N_b)$. In atom interferometry, the measurement of relative populations $\mu_{a(b)}$ ideally suppresses the statistical fluctuations of the atom number entering the interferometer between realizations. Since $\mu_{a(b)} = \mu_{a(b)}(\phi)$, it is possible to infer the value of the phase ϕ from the measurement results and thus, e.g., the magnitude of the gravitational acceleration g in Eq. (3.1). Before we discuss in the next section the concepts of parameter estimation theory that provide us with the tools to estimate ϕ , let us briefly outline the known basics of how ϕ is measured in an atom interferometer.

For any two-mode interferometer, the functional relationship between the measurement results $\mu_{a(b)}(\phi)$ and ϕ can be described by a simple model in terms of a finite Fourier series,

$$P_{a(b)}(\phi) = P_0 \pm A \cos(n\phi). \quad (3.2)$$

The amplitudes are defined as $0 \leq P_0, A \leq \frac{1}{2}$, so that probability is conserved and in the ideal case $P_a(\phi) + P_b(\phi) = 1$. We see that $P_{a(b)}(\phi)$ depends on the relative phase $n\phi$ accumulated between the two arms of the interferometer during the complete interrogation time $2T$. The standard two-mode model in Eq. (3.2) enables efficient phase estimation based on the collective properties of the measurement statistics in many experiments, making it a powerful tool. In Fig. 3.1(b), we give an example for the signal measured in port a of the MZ interferometer as we show in Fig. 3.1(a). Assuming normally distributed phase-fluctuations, we also indicate the first statistical moments of measurement data, namely the average values $\bar{\mu}_a(\phi)$ and the variances $\Delta\mu_a(\phi)$. To do so, the analytical function $P_a(\phi)$ must be calibrated using a series of measurements for different values of ϕ , which can be scanned via the Bragg laser phases ϕ_L according to Eq. (3.1). Fitting $P_a(\phi)$ to the statistical averages of the recorded data $\bar{\mu}_a(\phi)$ determines the amplitudes P_0 and A so that $\bar{\mu}_a(\phi) = P_a(\phi)$. Subsequently, inverting the calibrated function yields the estimate

$$\phi^{\text{est}} \equiv P_a^{-1}(\bar{\mu}_a|_{\phi_0}), \quad (3.3a)$$

which ideally corresponds to the true value of ϕ_0 that would produce the measured average value $\bar{\mu}_a$. Here, ϕ_0 corresponds to a value of the phase for which the inversion of $P_a(\phi)$ exists. It is worth noting that this, in combination with Eq. (3.1) and the fact that the wave number k and the interrogation time T can be controlled with high accuracy and stability in modern experiments [54], allows absolute measurements of inertial forces such as g . The statistical uncertainty of the phase estimate, which is typically inferred via error propagation, is also determined via $P_a(\phi)$ and the measurement statistics,

$$\Delta\phi^{\text{est}}(\phi_0) = \frac{1}{\sqrt{N_{\text{atoms}}}} \frac{\Delta\mu_a(\phi_0)}{|\partial_\phi \bar{\mu}_a|_{\phi_0}} = \frac{1}{\sqrt{N_{\text{atoms}}}} \frac{\Delta\mu_a(\phi_0)}{|\partial_\phi P_a(\phi)|_{\phi_0}}. \quad (3.3b)$$

Thus, the statistical uncertainty of the phase estimate scales inversely with the slope of the signal and therefore with the Bragg order n according to Eq. (3.2). The subsequent gain in

sensitivity towards variations of ϕ motivates the use of higher-order Bragg pulses and other LMT techniques. Assuming uncorrelated atoms, the uncertainty also scales inversely with the square root of the number of atoms, N_{atoms} , contributing to the signal of the atom interferometer in a single realization. Finally, the nominator of $\Delta\phi^{\text{est}}(\phi_0)$ is determined by the uncertainty in the measurement data $\Delta\mu_a(\phi_0)$, which generally comprises technical noise as well as quantum fluctuations. Since the estimation strategy characterized by Eqs. (3.3) is determined by the first and second moments of the distribution of measurement outcomes, it is often referred to as the "method of moments" [155].

From the above summary, it is clear that both the accuracy and the statistical uncertainty of the phase measurement hinge on the quality of the model $P_a(\phi)$. However, we have seen in the previous chapter that efficient higher-order Bragg processes must be operated in the quasi-Bragg regime and will as a result coherently populate undesired diffraction orders in contrast to idealized two-mode atom optics. It is therefore unsurprising that the physics of Bragg atom interferometers can deviate significantly from the standard two-mode interferometer picture in Eq. (3.2). For instance, parasitic couplings not taken into account in Eq. (3.3a) have been known to cause systematic uncertainties on the mrad-level referred to as diffraction phases [54,60,98,116,117]. Thus, the objective of the following sections is to derive a generalized model $P_a(\phi)$ that takes into account the multipoint as well as multipath physics of Bragg diffraction. By extending the scattering matrix formalism that we have introduced in the previous chapter, we aim to accurately describe the metrological properties of Bragg atom interferometers. Moreover, our goal is to formulate an efficient phase estimation strategy that is, ideally, as practical to implement experimentally as Eq. (3.2).

With that in mind, we begin this chapter with a review of the basic concepts of parameter-estimation theory in Sec. 3.2, which we have only briefly outlined so far. In this context, we formally introduce the method of moments and justify the usefulness of this strategy, although it is not necessarily optimal. Optimal estimation strategies feature a minimal statistical phase uncertainty and thus saturate the Cramér-Rao bound (CRB) [156–158]. We introduce the CRB and the more general quantum Cramér-Rao bound (QCRB) [159], which represent the fundamental limits to the sensitivity of any interferometric measurement and hence are key results of parameter-estimation theory. Nonetheless, and despite the fact that they modify the standard-quantum limit, neither has been determined for Bragg atom interferometers at the time of writing. In Secs. 3.3 and 3.4, we extend the scattering matrix formalism for elementary Bragg operations from the previous chapter to entire interferometer sequences. Using the popular MZ geometry as an example, we develop a scattering matrix for higher-order Bragg atom interferometers including the population of dominant parasitic paths and ports. The result is an analytical expression for the signal of such interferometers, which yields unique insight into its dependence on the individual Bragg pulse parameters. In particular, this reveals that spurious contributions to the interferometric

phase shift up to several mrad are determined by the LZ parameter γ introduced previously, since they originate from the multiport nature of the Bragg beam splitters [117, 118]. Moreover, in Sec. 3.5 we generalize the two-mode model (3.2) and quantify the accuracy of our adapted estimation strategy using simulations of the MZ interferometer realized by fifth-order Bragg diffraction pulses in numerical experiments in Sec. 3.6. Based on these results, we present a conceptually straightforward way to suppress the systematic error of the phase estimate also known as diffraction phase below the mrad-level simply by identifying a suitable choice of parameters for the Bragg mirror pulse. In addition to the discussion of systematic effects, we also study the implications parasitic diffraction orders have on the statistical uncertainty of the measurement in Sec. 3.7. Based on our scattering matrix description we calculate the (Q)CRB and show that it exhibits a nontrivial dependence on the inevitable atom loss associated with Bragg diffraction. Moreover, we demonstrate that the phase estimation strategies we present in this work allow saturation of these fundamental bounds. Finally, we give an overview of future possibilities offered by our analytical theory for Bragg atom interferometers.

3.2 Review: Concepts of Phase Estimation

The purpose of this section is to embed the rough description of phase measurements in atom interferometry given above, and in particular models such as Eq. (3.2), into the proper framework provided by classical parameter estimation theory. In addition, we rely on methods from quantum theory of phase estimation to make general statements about the metrological properties of the quantum state at the output of the interferometer. For instance, they enable us to formulate fundamental bounds on the minimal uncertainty when measuring the phase. For a detailed overview of these concepts, we recommend the reader the work of *L. Pezzè et al.* in Ref. [155], on which we base in this section, or to a review focused on interferometry with photons by *R. Demkowicz-Dobrzański et al.* [160].

3.2.1 Generalized Measurements

In interferometry, phase shifts are inferred indirectly from measurements of quantum mechanical observables. Here, we consider the detection of relative number of atoms, e.g., recorded at the output port a of the MZ interferometer Fig. 3.1(a), which we describe by the corresponding operator

$$\hat{P}_a = \frac{\hat{a}^\dagger \hat{a}}{\hat{a}^\dagger \hat{a} + \hat{b}^\dagger \hat{b}}. \quad (3.4)$$

To simplify the notation in this chapter, the operators and functions associated with the output port a of the interferometer are representative of those that apply to port b , unless stated

otherwise. The relative number operator in Eq. (3.4) is defined by the annihilation and creation operators in each port, and its average value $\langle \hat{P}_a \rangle(\phi)$ and its variance $(\Delta \hat{P}_a)^2(\phi)$ are functions of the phase ϕ . This is due to the quantum state at the output of the interferometer $\rho^{\text{out}}(\phi)$ being ϕ -dependent. For now, we continue our discussion considering single particle states, so that $\rho^{\text{out}}(\phi) = |\psi^{\text{out}}(\phi)\rangle\langle\psi^{\text{out}}(\phi)|$ represents the density operator of a pure state $|\psi^{\text{out}}(\phi)\rangle$ after the final beam splitter.

In general, estimation of an a priori unknown phase shift ϕ requires performing a series of independent measurements of \hat{P}_a with probabilistic outcomes $\mu_a := \{\mu_a^1, \mu_a^2, \dots, \mu_a^m\}$. Generally, the conditional probabilities associated with the j th outcome can be calculated evaluating

$$\mathcal{P}^{(j)}(\mu_a^j|\phi) = \text{tr}\{\hat{P}_a^{(j)} \rho_{(j)}^{\text{out}}(\phi)\}, \quad (3.5)$$

where $\hat{P}_a^{(j)}$ describes the j th measurement operation and $\rho_{(j)}^{\text{out}}(\phi)$ represents the density operator of the j th subsystem, so that in the case of independent measurements

$$\rho^{\text{out}}(\phi) = \rho_{(1)}^{\text{out}}(\phi) \otimes \rho_{(2)}^{\text{out}}(\phi) \otimes \dots \otimes \rho_{(m)}^{\text{out}}(\phi). \quad (3.6)$$

The measurement statistics is determined by the combined probability distribution, the so-called "likelihood",

$$\mathcal{P}(\mu_a|\phi) = \prod_{j=1}^m \mathcal{P}^{(j)}(\mu_a^j|\phi) = \text{tr}\{\hat{P}_a \rho^{\text{out}}(\phi)\}, \quad (3.7)$$

with $\hat{P}_a = \hat{P}_a^{(1)} \otimes \hat{P}_a^{(2)} \otimes \dots \otimes \hat{P}_a^{(m)}$, representing the statistically independent measurements. The likelihood, $\mathcal{P}(\mu_a|\phi)$, is unique for a given experimental realization and generally includes, e.g., the effects of any technical noise processes, which we do not consider in this work. In contrast, we illustrate in Fig. 3.1(b) that the expression in Eq. (3.2) is a simple model for the functional relationship between the average values of the measured data, $\bar{\mu}_a = (1/m) \sum_{j=1}^m \mu_a^j$, and the phase ϕ in two-mode atom interferometers. As for the estimation of the phase based on the measured data, in principle any function, $\phi^{\text{est}} : \mu \rightarrow \phi$, i.e., $\phi^{\text{est}} = \phi^{\text{est}}(\mu)$, associating the measurement outcome μ with a phase value ϕ can be considered as an estimator. Since such a map is defined on sets of the probabilistic outcomes (of measurements $\mu_{a(b)}$ in ports a and b) the estimator itself is a statistical quantity with a mean

$$\bar{\phi}^{\text{est}} = \sum_{l=a,b} \mathcal{P}(\mu_l|\phi) \phi^{\text{est}}(\mu_l) \quad (3.8a)$$

and a variance

$$(\Delta \phi^{\text{est}})^2 = \sum_{l=a,b} \mathcal{P}(\mu_l|\phi) (\phi^{\text{est}}(\mu_l) - \bar{\phi}^{\text{est}})^2. \quad (3.8b)$$

For metrological application, it is desirable that the mean of the estimator approaches the true value of ϕ for sufficiently large samples sizes, $m \gg 1$, and that its statistical uncertainty is minimal. Hence, a useful estimator needs to be at least locally unbiased, i.e., $\bar{\phi}^{\text{est}} = \phi$ and $\partial \bar{\phi}^{\text{est}} / \partial \phi = 1$. If an estimator in addition features a minimal variance it is considered optimal. However, without knowledge of the full probability distributions $\mathcal{P}(\mu_{a(b)}|\phi)$ specific to the experiment, it is not clear what the optimal estimator looks like for a given type of measurement. Furthermore, extracting $\mathcal{P}(\mu_{a(b)}|\phi)$ is often challenging as it requires comprehensive theoretical modelling including imperfections or extensive calibration of the experiment.

Method of Moments

Instead, it is often more economical to use an estimation strategy that requires the knowledge of only the first and the second moments of the measured data. This is referred to as the method of moments, which is based on two central ideas. First, not only the individual measurement outcomes but also their collective properties such as the mean $\bar{\mu}_a$ depend on ϕ , see Fig. 3.1(b). Second, according to the law of large numbers, the sample mean $\bar{\mu}_a$ converges to the mean of the underlying probability distribution, i.e., $\bar{\mu}_a = \langle \hat{P}_a \rangle(\phi)$ in the limit $m \rightarrow \infty$. In addition, in this limit, the probability distribution for the sample average, $\mathcal{P}(\bar{\mu}_a|\phi)$, is described by a normal distribution with a mean $\langle \hat{P}_a \rangle(\phi)$ and a variance $(\Delta \hat{P}_a)^2(\phi)$, which provides a constructive way to find an estimator that is unbiased [161]. It requires formulating a function $P_a(\phi)$ that satisfies $\bar{\mu}_a = P_a(\phi)$. For phases $\phi = \phi_0$, for which the function $P_a(\phi)$ is a bijection and can therefore be inverted, $P_a^{-1}(\phi_0)$, we obtain

$$\phi^{\text{est}} = P_a^{-1}(\bar{\mu}_a|\phi_0). \quad (3.9a)$$

This is Eq. (3.3a) from above and explains the utility of the standard two-mode model (3.2) for interferometry experiments. Instead of retrieving the probability distribution of the single measurement results, it allows the estimation of ϕ_0 via the collective properties of the measurement samples. Moreover, the uncertainty of this estimator can be calculated directly via error propagation

$$\Delta \phi^{\text{est}}(\phi_0) = \frac{\Delta \hat{P}_a(\phi_0)}{\sqrt{N_{\text{atoms}}} |\partial_\phi \langle \hat{P}_a \rangle|_{\phi_0}} = \frac{1}{\sqrt{N_{\text{atoms}}}} \frac{\Delta \mu_a(\phi_0)}{|\partial_\phi P_a(\phi)|_{\phi_0}}, \quad (3.9b)$$

which is identical to Eq. (3.3b). Here, we have substituted the number of independent samples m with the number of uncorrelated particles N_{atoms} contributing to the signal of the interferometer in a single shot. If the uncertainty of the measurement statistics is independent of the phase, $\Delta \mu_a(\phi_0) = \Delta \mu_a$, the sensitivity of the phase estimate can be optimized by maximizing the slope $|\partial_\phi P_a(\phi)|_{\phi_0}$. With respect to the two-mode model in Eq. (3.2), this is the case at the so-called mid-fringe position, i.e., $P_a(\phi_0) = 0.5$, where $\phi_0 = (2m+1) \cdot \pi / (2n)$

with $m \in \mathbb{Z}$. At these operating points, and considering the measurement is only subject to quantum projection noise, we obtain the standard quantum limit for an ideal two-mode MZ Bragg interferometer

$$\Delta\phi^{\text{est}}(\phi_0) = \frac{\sqrt{P_0(1-P_0)}}{n A \sqrt{N_{\text{atoms}}}}, \quad (3.10)$$

where P_0, A are defined as in Eq. (3.2) and where the favorable scaling with n^{-1} due to the implementation of higher-order Bragg pulses is immediately visible.

In Sec. 3.5, we formulate estimation strategies $P_a(\phi)$ describing realistic Bragg atom interferometers including spurious paths and ports indicated as in Fig. 3.1(a). We evaluate their performance via Eqs. (3.9), when applied to numerical experiments, which mimics their application in the real-world and gives us absolute control over the true value of ϕ_0 to test the accuracy of ϕ^{est} . In this context, the result in Eq. (3.10) serves as an important benchmark.

3.2.2 Cramér-Rao Bound (CRB)

The CRB [156–158] serves as a lower bound on the statistical uncertainty of any unbiased estimator and therefore represents another important benchmark for the phase uncertainty $\Delta\phi^{\text{est}}$,

$$\Delta\phi^{\text{est}} \geq \Delta\phi_{\text{CRB}} = \frac{1}{\sqrt{N_{\text{atoms}}}} \frac{1}{\sqrt{F(\phi)}}. \quad (3.11)$$

The CRB is determined by the Fisher information [74],

$$F(\phi) = \sum_{l=a,b} \frac{(\partial_\phi \mathcal{P}(\mu_l|\phi))^2}{\mathcal{P}(\mu_l|\phi)} \geq \frac{1}{(\Delta\mu_{a(b)}(\phi_0))^2} \left(\left. \frac{d\bar{\mu}_{a(b)}}{d\phi} \right|_{\phi_0} \right)^2, \quad (3.12)$$

which quantifies how sensitive the conditional probabilities $\mathcal{P}(\mu_{a(b)}|\phi)$ are to variations of the parameter ϕ . In consequence, the Fisher information is larger or equal to the rate of change of the first moments of these distributions with ϕ (because the full probability distribution contains potentially more information), which gives rise to the inequalities in Eqs. (3.11) and (3.12). In other words, if an estimator satisfies the CRB it means that its statistical uncertainty is as low as possible given the chosen observable, in our case \hat{P}_a .

3.2.3 Quantum Cramér-Rao Bound (QCRB)

Quantum estimation theory provides the tools to answer an even more fundamental question: What is the best possible sensitivity (lowest uncertainty) for a given quantum state $\rho^{\text{out}}(\phi)$? The answer to this question is provided by the QCRB. Its definition requires the

notion of a positive-operator-valued measure (POVM), describing a complete set of positive Hermitian measurement operators $\{\hat{E}(\mu)\}$ parameterized by the outcomes μ . POVMs include the most general measurement operations, and the observable \hat{P}_a discussed in this work represents only one element in the class of the well-known projective von Neumann measurements. Operators $\{\hat{E}(\mu)\}$ must have the properties $\hat{E}(\mu) \geq 0$ and $\sum_{\mu} \hat{E}(\mu) = \mathbb{1}$ so that $\mathcal{P}(\mu|\phi) \geq 0$ as well as $\sum_{\mu} \mathcal{P}(\mu|\phi) = 1$. The QCRB is formally obtained by maximizing the Fisher information over all elements of the POVM, $F_Q[\rho^{\text{out}}(\phi)] = \max_{\hat{E}} F(\phi)$ and as such represents the ultimate lower bound for the statistical uncertainty of any unbiased phase estimator,

$$\Delta\phi^{\text{est}} \geq \Delta\phi_{\text{CRB}} \geq \Delta\phi_{\text{QCRB}} = \frac{1}{\sqrt{N_{\text{atoms}}}} \frac{1}{\sqrt{F_Q}}. \quad (3.13)$$

Therefore, while the attainable sensitivity when estimating ϕ for a particular measurement choice is limited by the CRB, the QCRB generalizes this limit by optimizing over all possible measurements. Unfortunately, the definition of neither bound is constructive in the sense that it does not provide practical means to construct an estimator capable of reaching it¹. Nevertheless, in the following we calculate the analytical CRB and QCRB to compare them to the local sensitivity $\Delta\phi^{\text{est}}$. We obtain the latter by applying the method of moments to relative atom number measurements of numerically simulated Bragg atom interferometers. Here, we take advantage of the fact that computing the quantum Fisher information F_Q is straightforward when $\rho^{\text{out}}(\phi)$ is a pure state [155],

$$F_Q = 4 \left(\langle \dot{\psi}^{\text{out}} | \dot{\psi}^{\text{out}} \rangle - |\langle \dot{\psi}^{\text{out}} | \psi^{\text{out}} \rangle|^2 \right), \text{ where } |\dot{\psi}^{\text{out}} \rangle \equiv \frac{d|\psi^{\text{out}} \rangle}{d\phi}. \quad (3.14)$$

Since the quantum Fisher information is fully determined by the final state $\rho^{\text{out}}(\phi)$, it can also be used to quantify the precision enhancements offered by non-classical states [155, 160]. Our detailed study of the atomic projection noise of efficient Bragg interferometers in Sec. 3.7 considers tensor product states suitable to describe, e.g., a BEC (see Sec. 4.2) and thus crucially establishes important design criteria for operating these devices at or below the standard quantum limit [141, 162–164].

3.3 Scattering Matrix for Bragg Interferometers

In this section, we extend the formalism for Bragg pulses to study Bragg atom interferometers potentially including multiple paths and ports. Experiments have shown that their

¹Note that least asymptotically, i.e., in the limit $m \rightarrow \infty$, the CRB can always be saturated by the so-called maximal likelihood estimator. However, the definition of this unbiased estimator requires full knowledge of $\mathcal{P}(\mu|\phi)$, e.g., see Sec. B.5 in Ref. [155], which is not feasible in many cases.

contributions to the interferometer signal can be significant [117, 118, 135, 147]. Our objective is to find an analytic expression for the interferometer signal that provides crucial insight into its structural dependence on the Bragg operations. This includes the role of the individual pulse parameters as well as that of the momentum width of the atomic wave packet. These findings serve as the basis for generalizing the two-mode model in Eq. (3.2) to account for both multiport and multipath features of Bragg diffraction. As already mentioned at the beginning of this chapter, in Bragg interferometry a matter wave is brought into spatial superposition of at least two different momenta following separate trajectories. In the MZ geometry depicted in Fig. 3.1(a), the different momentum modes are coupled by the atom-light interaction at three distinct moments in time, which we model via the Bragg transfer matrices defined in Sec. 2.5 and Sec. 2.7. Before we define a scattering matrix describing complete interferometer sequences, we first need to outline two key assumptions.

First, we remind the reader that the scattering matrix \mathcal{S} is the asymptotic limit of the time evolution operator, see Eq. (2.26). It maps the input state incoming from the very distant past ($t = -\infty$) to the output state of the Bragg scattering event in the very distant future ($t = +\infty$). In the case of a Gaussian pulse, the relevant time scale is set by the temporal width τ . Consequently, we consider pulse durations to be much shorter than the time scale of the interferometer given by the pulse separation time, $\tau \ll T$. In this limit, the effects of finite pulse durations on the phase evolution can be neglected [165]. Second, we require that the assignment of momentum modes to different spatial trajectories in Fig. (3.1)(a) is unambiguous. Thus, we can define every interferometer on a finite basis of unique trajectories with associated momentum modes $|q_{j=1,2,\dots,r}\rangle$ [in analogy to Eq. (2.115b)]. Here, r represents the total number of trajectories, which depends on both the dimensionality of the Bragg transfer matrices and the geometry of the interferometer. This second assumption is readily fulfilled using ultra-cold atomic ensembles with momentum widths $\sigma_p \ll \hbar k$ that lead to comparatively small expansion velocities [64, 65]. As a result, trajectories separated by $2\hbar k$ or more can be measured individually after a sufficiently long time of flight. Under this assumption and without loss of generality, we assign the incoming wave packet with average momentum $-n\hbar k$ the trajectory $|q_1\rangle = |q_1(p)\rangle$,

$$|\psi^{\text{in}}(\sigma_p)\rangle = \int_{-\hbar k/2}^{\hbar k/2} dp c_1(p) |q_1(p)\rangle_{\text{in},1} = \int_{-\hbar k/2}^{\hbar k/2} dp g(p, \sigma_p) | -n\hbar k + p \rangle. \quad (3.15)$$

As before, it is characterized by a Gaussian momentum distribution $g(p, \sigma_p)$ [see Eq. (2.105)] featuring a momentum width well below the lattice recoil $\sigma_p \ll \hbar k$. We remark that $|\psi^{\text{in}}(\sigma_p)\rangle$ represents a single-particle state, which is sufficient at this point to describe the dynamics of Bragg interferometers, especially since we are not considering particle-particle interactions. Later in Sec. 3.7.2, we discuss the implications of the input state consisting of many

uncorrelated atoms following a Poissonian distribution of the total atom number. The scattering matrix that describes the action of arbitrary Bragg interferometer sequences on the input state can also be expanded in the basis of modes $|q_j\rangle$,

$$\mathcal{S} = \int_{-\hbar k/2}^{\hbar k/2} dp \sum_{j,l=1}^r [\mathcal{I}(p)]_{jl} |q_j\rangle_{\text{out},j} \langle q_l|. \quad (3.16)$$

The matrix $\mathcal{I}(p)$ is unique to a particular interferometer scheme. It is composed of several transfer matrices that account for the diffraction operations as well as for the free propagation in between. In addition to the pulse parameters, the scattering matrix in Eq. (3.16) also depends on a metrological phase ϕ to be measured. We will define $\mathcal{I}(p)$ for the concrete example of the MZ geometry in the next section and calculate the corresponding output state,

$$|\psi^{\text{out}}\rangle = \mathcal{S} |\psi^{\text{in}}(\sigma_p)\rangle = \int_{-\hbar k/2}^{\hbar k/2} dp g(p, \sigma_p) \sum_{j=1}^r [\mathcal{I}(p)]_{j1} |q_j\rangle_{\text{out},j}. \quad (3.17)$$

3.4 Mach-Zehnder (MZ) interferometer

In the MZ interferometer, several undesired diffraction orders coupled by higher-order Bragg pulses can populate parasitic interferometer paths and open output ports to varying degrees depending on the pulse parameters. We show some of these spurious paths and ports in Fig. 3.1(a) and include the dominant ones populated by n th-order Bragg pulses focusing on $n \geq 3$. Therefore, each Bragg operation is described by a transfer matrix $B(p, \Omega, \tau, \phi_L)$ acting on the four-dimensional subspace of momentum states that we have introduced in Sec. 2.7,

$$|q_j(p)\rangle \in \{ |\pm n \hbar k + p\rangle, |\pm(n-2) \hbar k + p\rangle \} \quad (n \geq 3). \quad (3.18)$$

Regarding the cases $n = 1, 2$, we refer the reader to Sec. 2.7 for further information, since they can be treated analogously with adjusted state spaces, $\{ |\pm 1 \hbar k + p\rangle, |\pm 3 \hbar k + p\rangle \}$ and $\{ |\pm 2 \hbar k + p\rangle, |p\rangle \}$. In the following, we will suppress the explicit dependence of $|q_j\rangle$ on the (quasi)momentum p for the sake of clarity and reintroduce it when appropriate.

3.4.1 MZ Scattering Matrix

With this in mind, Fig. 3.2 depicts all trajectories in a MZ interferometer that are populated by fifth-order Bragg beam splitters and mirrors. The total number of trajectories, $r = 36$, is representative for Bragg orders $n > 3$ considering our truncation. We note that in reality, diffraction beyond the truncated state space in Eq. (3.18) may result in additional, less strongly populated parasitic interferometers, which we neglect in our description. However,

if the state space includes all unwanted diffraction orders that are smaller than the targeted Bragg order, $m \leq n$, this number is determined by the more general relation $r = d \cdot (2d - 1)$. It is a product of the dimensionality of the state space d , which determines the number of output ports per interaction, and the number of unique intersections zones $(2d - 1)$ at time $t = 2T$, which results from the symmetry of the MZ geometry. Thus, assuming $n = 3$ and including the dominant parasitic modes $|\pm 1 \hbar k + p\rangle$ yields $r = 28$.

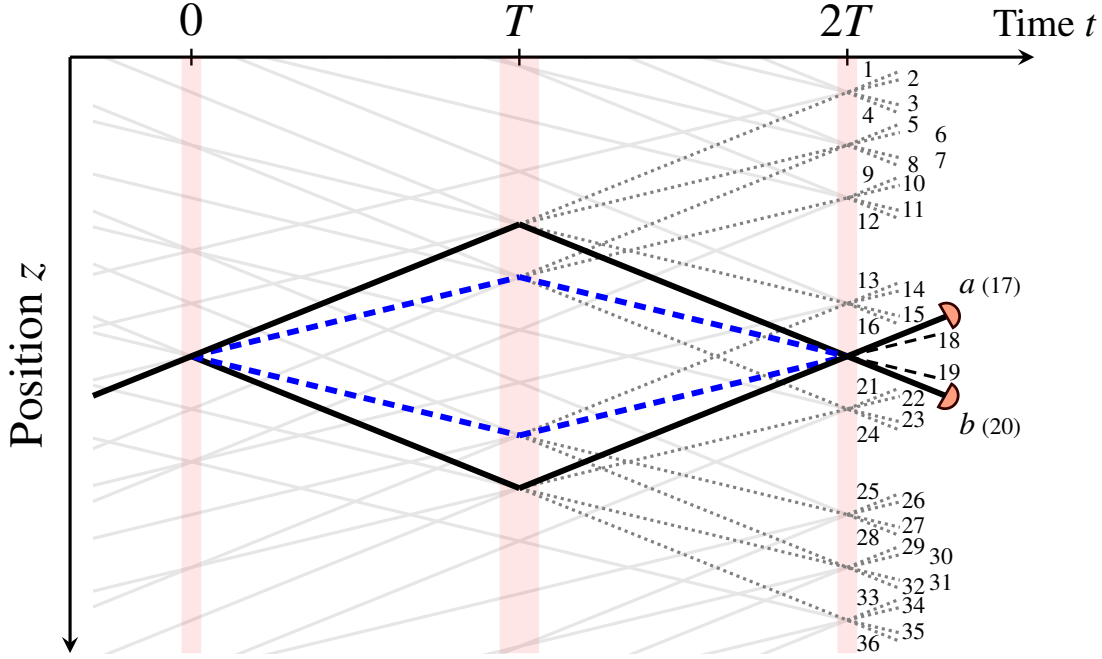


Figure 3.2: **Space-time diagram of the MZ geometry showing dominant parasitic paths of Bragg orders $n \geq 3$.** Besides the main (solid black lines) and the parasitic (dashed blue lines) interferometry paths loss, channels coupled by the mirror and final beam splitter interaction are displayed as well (dotted gray lines). The definition of the scattering matrix in Eq. (3.16) includes the 36 trajectories for all times t even if they are unpopulated (solid light-gray lines) using the initial state $|\psi^{\text{in}}\rangle = c_1 |q_1\rangle_{\text{in},1}$ defined in Eq. (3.15). We regard coupling to output ports other than $a(17)$, 18, 19, and $b(20)$ as incoherent atom losses. Furthermore, we neglect the visual deformation of the trajectories due to the gravitational potential (see main text).

Formally, one can construct the scattering matrix for the interferometer by composing $\mathcal{I}(p)$ in Eq. (3.16) from individual transfer matrices representing the different elements of the sequence

$$\mathcal{I}_{\text{MZ}}(p) = \mathcal{B}_{2.\text{BS}} \cdot \mathcal{U}(T) \cdot \mathcal{B}_{\text{M}} \cdot \mathcal{U}(T) \cdot \mathcal{B}_{1.\text{BS}}. \quad (3.19)$$

The Bragg matrices $\mathcal{B}_{\Lambda} \equiv \mathcal{B}(p, \Omega_{\Lambda}, \tau_{\Lambda}, \phi_{\text{L},\Lambda})$ describe the coupling of individual trajectories due to the atom-light interaction during the two beam splitters and the mirror pulse. The

subscript $\Lambda = 1.\text{BS}, 2.\text{BS}, \text{M}$ denotes the different choices of pulse parameters $\Omega_\Lambda, \tau_\Lambda$ and laser phase $\phi_{L,\Lambda}$. Figure 3.2 shows that more than half of the trajectories are populated only after the final beam splitter when a single input path is considered, which is why we define these matrices as sparse,

$$\mathcal{B}_\Lambda = [\mathcal{B}_\Lambda]_{j,l=1,\dots,36} = \begin{cases} [B_\Lambda]_{v_1,v_2}, & \text{if } j = [L_\Lambda]_{s,v_1} \text{ and } l = [L_\Lambda]_{s,v_2} \\ 1, & \text{if } j = l \notin L_\Lambda \\ 0, & \text{otherwise} \end{cases} \quad (3.20)$$

with non-zero entries $[B_\Lambda]_{v_1,v_2}$ being elements of the transfer matrices defined in Eqs. (2.121). The L_Λ are two-dimensional index lists of trajectories $|q_j\rangle_j$ being coupled as a result of the diffraction processes. Looking at Fig. 3.2 one finds (for $n > 3$)

$$\begin{aligned} L_{1.\text{BS}} &= [L_{1.\text{BS}}]_{\substack{s=1,\dots,4 \\ v=1,\dots,4}} = \begin{cases} 9 \cdot v, & \text{if } v > 2 \\ 9 \cdot v - 8, & \text{otherwise.} \end{cases} = \{\{1, 10, 27, 36\}\}, \\ L_{\text{M}} &= [L_{\text{M}}]_{\substack{s=1,\dots,4 \\ v=1,\dots,4}} = v + 4(v + s - 2) + \begin{cases} 0, & \text{if } s, v \leq 2 \\ 8, & \text{if } s, v > 2 \\ 4, & \text{otherwise.} \end{cases} \\ &= \{\{1, 6, 15, 20\}, \{5, 10, 19, 24\}, \dots, \{17, 22, 31, 36\}\}, \\ L_{2.\text{BS}} &= [L_{2.\text{BS}}]_{\substack{s=1,\dots,9 \\ v=1,\dots,4}} = v + 4(s - 1) = \{\{1, 2, 3, 4\}, \{5, 6, 7, 8\}, \dots, \{33, 34, 35, 36\}\}. \end{aligned} \quad (3.21)$$

Up to this point, we have only considered the interaction of the atom with the optical lattice based on the analytical description developed in Chapter 2. Since we regard this interaction as instantaneous, the phase evolution takes place during the free propagation time T and is described by the matrices $\mathcal{U}(T)$ in Eq. (3.19). Most importantly, their action on the quantum state gives rise to the metrological phase ϕ . For simplicity, we assume that the phase evolution is caused by a potential $V = Mg_{\text{Lab}}\hat{z}$ due to a linear gravitational acceleration in the laboratory frame g_{Lab} . Naturally, the linear acceleration caused by the gravitational potential will affect the atomic trajectories when the atom interferometer is operated in free fall. This is not considered in Fig. 3.2 because to avoid detrimental Doppler effects in experiments, the frequencies of the laser light fields are typically adjusted by introducing a tunable frequency difference $\delta = \delta(t)$ [see Eqs. (2.8) and (2.10)] to accelerate the optical lattice. When the optical lattice is almost comoving with the free-falling atoms, experiments measure the effective acceleration $g := g_{\text{Lab}} - a_{\text{L}}$ with $|g| \ll \hbar k/(MT)$ and $a_{\text{L}} = \frac{1}{k} \frac{d\delta(t)}{dt}$.

To find the explicit form of the matrix $\mathcal{U}(T)$, we follow Ref. [166], and describe the evolution of the quantum state $|\psi(t)\rangle = \hat{U}(t)|\psi\rangle$ via the time evolution operator

$$\hat{U}(t) = \exp\left[-\frac{it}{\hbar}\left(\frac{\hat{\mathbf{p}}^2}{2M} + Mg\hat{z}\right)\right], \quad (3.22)$$

featuring the kinetic energy term and a linear potential. Ideally, we expect this operator to give rise to a relative phase of the form in Eq. (3.1). The state evolving according to $\mathcal{U}(T)$ during free propagation can be readily calculated (see Appendix B):

$$|\psi(T)\rangle = \mathcal{U}(T) \sum_{j=1}^{36} c_j(p) |q_j\rangle_j = \sum_{j=1}^{36} c_j(p) e^{i\vartheta(g,T,q_j)} |q_j - MgT\rangle_j. \quad (3.23)$$

Given that the change in momentum caused by the gravitational acceleration is small, we neglect its visual representation, e.g., in Fig. 3.2. Most importantly, the time evolution described by the scattering matrix \mathcal{U} imprints a path-dependent propagation phase

$$\vartheta(g, T, q_j) = M \frac{g^2 T^3}{3\hbar} - \frac{gT^2}{2\hbar} q_j - \frac{T}{2M\hbar} (q_j - MgT)^2. \quad (3.24)$$

Here, we assume that the effective wave vector of the light fields is aligned parallel to the z direction and use the fact that $|q_j\rangle_j$ are eigenstates of the momentum operator. Expanded in this basis, the scattering matrix \mathcal{U} in Eq. (3.25) is hence diagonal,

$$\mathcal{U}(T) = [\mathcal{U}(T)]_{j,l=1,\dots,36} = \begin{cases} e^{i\vartheta(g,T,q_j)}, & \text{if } j = l, \\ 0, & \text{otherwise.} \end{cases} \quad (3.25)$$

Finally, by substituting $\mathcal{I}(p)$ into \mathcal{S} , we are able to compute the output state $|\psi^{\text{out}}\rangle$ in Eq. (3.17) for the MZ interferometer sequence depicted in Fig. 3.2.

3.4.2 Atom Number Signals

Using the Bragg scattering matrix developed in the previous section, we arrive at an analytical expression for the quantum state after the final beam splitter interaction of the MZ interferometer²

$$|\psi^{\text{out}}(\phi, T, \Omega_{\text{BS}}, \tau_{\text{BS}}, \Omega_{\text{M}}, \tau_{\text{M}}, \sigma_p)\rangle = \mathcal{S}_{\text{MZ}} |\psi^{\text{in}}(\sigma_p)\rangle = \int_{-\hbar k/2}^{\hbar k/2} dp g(p, \sigma_p) \sum_{j=1}^{36} [\mathcal{I}_{\text{MZ}}(p)]_{j1} |q_j\rangle_{\text{out},j}. \quad (3.26)$$

We note that we are primarily considering the use of identical parameters $\Omega_{\text{BS}}, \tau_{\text{BS}}$ for both beam splitters and comment below on the primary effects of possible asymmetry on the interferometer signal. Furthermore, we absorb the Bragg lasers phase in ϕ , which we define in analogy to Eq. (3.1) for the remainder of this chapter as

$$\phi := 2(kgT^2 + \phi_{\text{L},1,\text{BS}} - 2\phi_{\text{L},\text{M}} + \phi_{\text{L},2,\text{BS}}). \quad (3.27)$$

²Strictly speaking, the momenta of the individual trajectories are as well affected by gravity, i.e., one should expect $|q_j\rangle_{\text{out},j} = |q_j - 2MgT\rangle_{\text{in},j}$. Since we assume this change to be negligible on the scale of the photon recoil, we omit it here.

The knowledge of $|\psi^{\text{out}}\rangle$ enables us to derive analytical expressions for the interferometer signal, $P_a(\phi) = N_a(\phi) / (N_a(\phi) + N_b(\phi))$ [analogous for port b (see Fig. 3.2)], which is recorded in terms of relative atom numbers in the detected ports. Nevertheless, it is instructive to first discuss the absolute atom numbers recorded at the individual output ports,

$$N_j(\phi) := N_j(\phi, T, \Omega_{\text{BS}}, \tau_{\text{BS}}, \Omega_{\text{M}}, \tau_{\text{M}}, \sigma_p) = N_{\text{atoms}} \int_{-\hbar k/2}^{\hbar k/2} dp |\langle \psi^{\text{out}} | q_j \rangle_j|^2. \quad (3.28)$$

As Eq. (3.17) describes only a single-particle output state, we have included the number of atoms entering the interferometer N_{atoms} in the definition of $N_j(\phi)$ assuming uncorrelated atoms and no interparticle interactions. A more nuanced discussion of Poissonian statistics in the initial atom number and its implications will be given in Sec. 3.7.2. Including the dominant undesired diffraction order for the MZ interferometer, we obtain the following absolute atom numbers in the main output ports

$$N_a(\phi) = P_{a,0} + A_{a,1} \cos(\phi + \varphi_{a,1}) + A_{a,2} \cos((n-2)\phi + \varphi_{a,2}) + A_{a,3} \cos((n-1)\phi + \varphi_{a,3}) + A_{a,4} \cos(n\phi + \varphi_{a,4}), \quad (3.29a)$$

$$N_b(\phi) = P_{0,b} + A_{b,1} \cos(\phi + \varphi_{b,1}) + A_{b,2} \cos((n-2)\phi + \varphi_{b,2}) + A_{b,3} \cos((n-1)\phi + \varphi_{b,3}) + A_{b,4} \cos(n\phi + \varphi_{b,4}), \quad (3.29b)$$

represented as Fourier series of the phase ϕ in their amplitude-phase form. This is consistent with the existing experimental evidence of undesired additional Fourier components contributing to the signal found in Refs. [118, 135, 147]. By definition, the amplitudes and phases in Eqs. (3.29) are functions of the parameters in Eqs. (2.121), which characterize the beam splitter and mirror interactions. However, stating their explicit forms is not useful at this point as they are too unwieldy. Nevertheless, it is still worthwhile to discuss the phenomenology of these expressions, which consists of sums of interference terms that can be identified with the trajectories that spatially overlap at the time of the final beam splitter $t = 2T$ (17, 18, 19, and 20 in the case of Fig. 3.2), since we can map the different Fourier components to pairs of trajectories via their separation in momentum in the inertial frame of the optical lattice. Meanwhile, the amplitude offset $P_{0,a(b)}$ collects the self-interference terms and is therefore independent of ϕ . In the case of third-order Bragg diffraction ($n = 3$), Eqs. (3.29) will contain only three Fourier components, namely ϕ , 2ϕ and 3ϕ .

As expected, the main interferometer arms represented by the solid black lines in Fig. 3.2 yield the largest Fourier component $n\phi$. Therefore, in the idealized two-mode limit we find $\lim_{\gamma, \Gamma, \sigma_p \rightarrow 0} N_{a(b)}(\phi) = N_{\text{atoms}} (\frac{1}{2} \pm \frac{1}{2} \cos(n\phi))$. In particular, this limit requires perfect 50/50 beam splitting ratios ($\Theta_{\text{BS},n} = \pi/2$) and a lossless mirror pulse ($\Theta_{\text{M},n} = \pi$), meaning in turn that the diffraction angles $\Theta_{\text{BS}/\text{M}}$ have a direct influence on the amplitudes $P_{0,a(b)}$ and $A_{4,a(b)}$ even in the absence of LZ losses. We have seen in Sec. 2.6.3 that velocity-dependent

detunings reduce the beam splitting ratio as well as the reflectivity of the Bragg mirror pulses. Thus, a finite momentum width σ_p has a very similar effect on the amplitude of this principal Fourier component as the Bragg diffraction angles. As pointed out in Sec. 2.7, in this study we restrict the finite velocity effects to the Bragg mirrors, which contributes to the loss of atoms from the main trajectories. As a result, velocity filtering reduces all amplitudes except $A_{2,a(b)}$, which depends only on the parasitic trajectories represented by the blue dashed lines in Fig. 3.2. Most notably, the main Fourier component features an asymmetric phase shift $\varphi_{4,a(b)}$, when comparing the signals in ports a and b . While there is no shift in port a , in port b it is a function of the γ -parameter that describes the differential LZ loss in the (anti)symmetric subspaces during the beam splitting process (see Tab. 2.2),

$$\begin{aligned}\varphi_{a,4} &= 0, \\ \varphi_{b,4} &= -\pi + 2\gamma + \mathcal{O}[\gamma]^3.\end{aligned}\tag{3.30}$$

It is a spurious phase shift caused by the multiport physics of the Bragg beam splitters, which vanishes for the signal in the output port with the same average momentum $-n\hbar k$ as the input port (see Fig. 3.2) due to the symmetry of the MZ geometry, cf. Ref. [117]. If we were to assume two sets of generic beam splitter parameters $\Omega_{1,\text{BS}}, \tau_{1,\text{BS}}$ and $\Omega_{2,\text{BS}}, \tau_{2,\text{BS}}$, we would obtain the more general expressions

$$\begin{aligned}\varphi_{a,4} &= \gamma_{1,\text{BS}} - \gamma_{2,\text{BS}} + \mathcal{O}[\gamma_{1,\text{BS}}/2,\gamma_{2,\text{BS}}]^3, \\ \varphi_{b,4} &= -\pi + \gamma_{1,\text{BS}} + \gamma_{2,\text{BS}} + \mathcal{O}[\gamma_{1,\text{BS}}/2,\gamma_{2,\text{BS}}]^3.\end{aligned}$$

Despite the fact that the use of different beam splitting pulses will reduce the amplitudes of the main Fourier components and thus negatively affects signal contrast, it is certainly interesting to investigate such asymmetries further in the future. We focus on the discussion of the phases in Eq. (3.30) and show below that it leads to a phase-dependent total atom number $N_a(\phi) + N_b(\phi)$.

In the MZ geometry, LZ losses during the initial beam splitting pulse also give rise to a second MZ interferometer with reduced Bragg order $(n - 2)$ (see blue dashed lines in Fig. 3.2) and to two more contributions due to interference with the main trajectories. These describe interferometers with smaller space-time areas. For sufficiently adiabatic pulse parameters, the relative weight of these terms is comparatively small, i.e., $A_{j,a(b)} < A_{4,a(b)}$, with $j = 1, 2, 3$. Nevertheless, we will show in the following sections that they can cause phase estimation errors in the order of several mrad if ignored. In doing so, we are going to exploit the fact that the absolute atom numbers as well as the signal of a multipath MZ interferometer are functions of the pulse separation time T . In their MZ interferometer, *Altin et al.* [147] observed that contrast was lost due to destructive interference of multiple interferometry paths but saw a periodic reappearing of the fringe visibility separated by intervals of $\delta T \approx \pi/(4\omega_r)$. The severity of the effect in this experiment can be linked

to the choice of non-adiabatic Bragg beam splitting pulses featuring large LZ populations leading to many competing Fourier components contributing to the signal as a result. This was done in part to account for the fact that the atomic source was a thermal cloud of ^{87}Rb atoms with a relatively large momentum width $\sigma_p \approx 1 \hbar k$, placing this particular experiment outside the parameter range considered in our calculations. Nevertheless, our analytical description confirms that the Fourier components can interfere constructively, if the kinematic propagation phases of all trajectories

$$\phi_r := 8\omega_r T \cdot l = \frac{4 \hbar k^2}{M} T \cdot l \quad \text{with } l \in \mathbb{N}, \quad (3.31)$$

are multiples of 2π . Phases ϕ_r arise from the term in Eq. (3.24) that is quadratic in momentum q_j . In the context of the asymmetric Ramsey-Bordé atom interferometer, they allow the most precise measurements of the recoil frequency ω_r at the time of writing [23, 24]. Meanwhile, their contributions to the MZ signal typically vanish due to the symmetry of the momentum transfer. Still, the spurious amplitudes and phases ($A_{1,a(b)}$, $\varphi_{1,a(b)}$) as well as $A_{3,a(b)}$, $\varphi_{3,a(b)}$) in Eqs. (3.29) depend on ϕ_r and thereby on T because they arise from the interference between the main and the parasitic interferometer arms featuring different kinetic energies (see Fig. 3.2). Specifically, we find that these quantities are periodic functions of the phase difference $\delta\phi_r = (n-1)\omega_r T$ as a result of our analytical calculation, which is consistent with the predictions based on Eq. (4) in Ref. [147]. In a later part of this study, we will be confirming this by comparison with numerical simulations of the MZ atom interferometer.

In summary, the detected atom numbers $N_{a(b)}(\phi)$ are complex functions of the phase ϕ , the pulse separation time T , and the parameters of the Bragg pulses because of the multipath, multiport properties of the MZ interferometer. Looking at Fig. 3.2, the mirror pulse plays a unique role in this context. Not only does it ensure that the main trajectories overlap spatially at time $t = 2T$, but is also responsible for the LZ losses during the initial beam splitting pulse forming parasitic interferometers. In consequence, the amplitudes and phases of all spurious Fourier components in Eqs. (3.29) depend on the diffraction angle $\Theta_{M,n-2}$ via $\sin(\Theta_{M,n-2}/2)$, originating from the matrix elements $B_{\mp(n-2),\pm(n-2)}$ in Eq. (2.121). In Sec. 3.4.4, we demonstrate by the example of fifth-order Bragg diffraction that this allows for a simple way to efficiently suppress interference with the dominant parasitic paths in the MZ geometry by finding pulse parameters Ω_M, τ_M providing $\Theta_{M,n-2} = m \cdot 2\pi$, with $m \in \mathbb{Z}$ while we ensure $\Theta_{M,n} = \pi$.

Suppression of Parasitic Interferometers

Before confirming our ability to suppress parasitic interferometers using the mirror pulse in numerical experiments, we first assess the impact of this adapted mirror pulse on the

interferometer signal. To do that, we assume the mirror pulse is transparent with respect to the undesired diffraction orders, and therefore set $\Theta_{M,n-2} = 0$ in our analytical model. This leaves the absolute atom numbers in the main ports with only a single Fourier component stemming from interference of the main interferometer arms,

$$N_a(\phi) = P_{a,0} + A_{a,4} \cos(n\phi), \quad (3.32a)$$

$$N_b(\phi) = P_{0,b} + A_{b,4} \cos(n\phi - \pi + 2\gamma + \mathcal{O}[\gamma]^3). \quad (3.32b)$$

We note that the amplitudes in these equations are generally different from the ones in Eqs. (3.29), but emphasize that the asymmetric phase shift that is a function of the LZ parameters γ remains unchanged. Since it is a result of spurious phases imprinted by the multiport Bragg beam splitters, it renders the combined atom number in the detected ports a and b phase-dependent, $N_a(\phi) + N_b(\phi) = N_{\text{atoms}} - N_{\text{open}}(\phi)$, even in the absence of any parasitic interferometers. Here, $N_{\text{open}}(\phi)$ denotes the population of all undetected (open) output ports, see Fig. 3.2. Accordingly, the relative atom numbers $P_{a(b)}(\phi)$ will always be a ratio of ϕ -dependent functions. We show this explicitly in the limit of vanishing momentum width assuming $\Theta_{BS,n} = \pi/2$ and $\Theta_{M,n} = \pi$, and by suppressing the parasitic interference terms ($\Theta_{M,n-2} = 0$), which yields

$$\lim_{\sigma_p \rightarrow 0} N_{\text{open}}(\phi) = N_{\text{atoms}} (\gamma^2 + 2(\Gamma - 1)\Gamma + \gamma^2 \cos(n\phi) + (\gamma - 2\gamma\Gamma) \sin(n\phi)) + \mathcal{O}[\gamma, \Gamma]^3. \quad (3.33)$$

This expression depends on the LZ parameters of the Bragg beam splitters γ, Γ (we neglect LZ losses for the mirror pulse as they are largely suppressed by the generally longer interaction times, see Sec. 2.6.3), and can be separated into two different contributions. The first one accounts for the atoms scattered to the dominant undesired diffraction orders during the initial beam splitting. It is independent of ϕ because at time $t = 2T$ there is no spatial overlap with the main interferometers arms if $\sin(\frac{\Theta_{M,n-2}}{2}) = 0$. Secondly, the final beam splitting pulse coherently populates additional output ports as we show in Fig. 3.2. Because LZ populations are relatively small and therefore typically go undetected (cf. [118, 135, 147]), they cause phase-dependent contribution to $N_{\text{open}}(\phi)$. Using Eqs. (3.32) and (3.33), we can study the relative atom numbers in the main ports, $\mu_{a(b)}(\phi) = N_{a(b)}(\phi)/(N_{\text{atoms}} - N_{\text{open}}(\phi))$, predicted by our analytical model (making the same assumptions as before)

$$\begin{aligned} \mu_{a(b)}(\phi) \approx & \frac{1}{2} \pm \frac{1}{8}(4 - \gamma^2) \sin\left(n\phi + \gamma + \frac{\pi}{2}\right) \pm \frac{\gamma}{4} \sin\left(2\left(n\phi + \gamma + \frac{\pi}{2}\right)\right) \\ & \pm \frac{\gamma^2}{8} \sin\left(3\left(n\phi + \gamma + \frac{\pi}{2}\right)\right) + \mathcal{O}[\gamma]^3. \end{aligned} \quad (3.34)$$

In general, $\mu_{a(b)}(\phi)$ are complicated functions of ϕ that must be represented by infinite Fourier series, however, as we are interested in highly efficient LMT Bragg atom interferometers with small off-resonant population ($|\gamma| < 0.1$), we interpret $\mu_{a(b)}(\phi)$ as a series

expansions in the open-port population $N_{\text{open}}(\phi)$. Equation (3.34) demonstrates that the resulting MZ signal is determined by a single Fourier component and its harmonics, when suppressing the parasitic interferometers³. It is independent of the global LZ loss parameter Γ and the velocity filtering effects of the mirror pulses describing the population loss outside of the interferometer trajectories, as one would expect due to the normalization. Yet, all harmonics feature a common phase shift determined by the differential LZ parameter γ , which exclusively depends on the beam splitter parameters $\Omega_{\text{BS}}, \tau_{\text{BS}}$. We conclude that the physics of the MZ interferometer realized by multiport Bragg beam splitter and mirror pulses deviates substantially from the simple two-mode picture in Eq. (3.2). It is therefore obvious that our scattering matrix description provides valuable insight into the different contributions to the signal of interferometers. Specifically, we have seen that it features several different Fourier components and their harmonics, potentially causing significant deviations from the idealized sinusoidal signal in Bragg atom interferometry previously referred to as signal distortions [118, 135, 147].

3.4.3 Tensorial Signal Calculus

In the following, we will briefly explain the principles of a tensorial approach for calculating the signals of atom interferometers based on our scattering matrix formalism. It was developed in collaboration with *R. Bösche and K. Hammerer*, and is reported in the Master thesis of *R. Bösche* [167].

We have seen in the previous section, that the absolute atom numbers $N_j(\phi)$ in Eq. (3.28) can be expressed as a finite Fourier series of the relative phases between the interferometer arms, as one would expect based on the superposition principle. Therefore, in the most general case of \mathcal{N} Fourier components contributing to the signal of the interferometer, we can write

$$N_j(\phi) = N_{\text{atoms}} \int_{-\hbar k/2}^{\hbar k/2} dp |\langle \psi^{\text{out}} | q_j \rangle_j|^2 = P_{j,0} + \sum_{l=1}^{\mathcal{N}} A_{j,l} \cos(l\phi + \varphi_{j,l}). \quad (3.35)$$

This result implies that it is also possible to express the quantum state at the end of the interferometer as a finite Fourier series, i.e., $|\psi^{\text{out}}\rangle$ in Eq. (3.26) takes the form

$$|\psi^{\text{out}}\rangle \stackrel{!}{=} \sum_{j=1}^r \sum_{l=-\mathcal{N}}^{\mathcal{N}} [C]_{j,l} e^{il\phi}. \quad (3.36)$$

In the case of the MZ interferometer discussed in this work, where $N_j(\phi)$ is a Fourier series of a single component ϕ , $C := C_{j,l}(T, \Omega_{\text{BS}}, \tau_{\text{BS}}, \Omega_{\text{M}}, \tau_{\text{M}}, \sigma_p)$ with $C \in \mathbb{C}^{r \times (2\mathcal{N}+1)}$ is a tensor of order two. Generally, depending on the interferometer topology, the interferometer signal

³Note, that our analytical model does not include noise processes, resulting in $\bar{\mu}_{a(b)}(\phi) = \mu_{a(b)}(\phi)$.

can be significantly more complex and C can be of higher order. In any case, we have seen that when calculating $|\psi^{\text{out}}\rangle$ as prescribed in the previous section [cf. Eq. (3.26)], finding manageable expressions in the forms of Eqs. (3.35) and (3.36) is rather challenging and tedious. This is true even in the case of the MZ interferometer, which includes only the dominant spurious interferometry paths. Therefore, it is preferable to directly evaluate the action of the atom interferometer on the input state ψ^{in} in the form of Eq. (3.36). However, this requires prior knowledge of the relevant basis elements of the Fourier series, e.g., by calculating the relative phase of the interferometer using standard methods [55–57].

The main idea of the tensorial approach is to write the input state of the interferometer as

$$|\psi^{\text{in}}\rangle = \sum_{j=1}^r \sum_{l=-N}^N [C]_{j,l} e^{il\phi} = C \cdot \hat{\mathbf{e}}_\phi, \quad (3.37)$$

where we have introduced the basis vector containing the Fourier components,

$$\hat{\mathbf{e}}_\phi = (e^{-iN\phi}, e^{-i(N-1)\phi}, \dots, 1, \dots, e^{i(N-1)\phi}, e^{iN\phi})^T. \quad (3.38)$$

In case of the input state in Eq. (3.15), the only nonvanishing component of the tensor C is

$$[C]_{1,0} = \int_{-\hbar k/2}^{\hbar k/2} dp g(p, \sigma_p) | -n\hbar k + p \rangle. \quad (3.39)$$

Our goal is to propagate $|\psi^{\text{in}}\rangle$ preserving its form in Eq. (3.37), which will immediately produce the desired result. Unfortunately, in this case, the effect of the scattering matrix of the atom interferometer, $|\psi^{\text{out}}\rangle = \mathcal{S}|\psi^{\text{in}}\rangle$, can no longer be described by a simple matrix multiplication [cf. Eq. (3.19)]. We will illustrate this using the previous example of the Mach-Zehnder interferometer, for which the matrix representation of the interferometer is composed of the same matrices describing the atom-light interaction as well as the free propagation as previously outlined,

$$\mathcal{I}_{\text{MZ}} = \mathcal{B}_{2,\text{BS}} \mathcal{U}(T) \mathcal{B}_{\text{M}} \mathcal{U}(T) \mathcal{B}_{1,\text{BS}}. \quad (3.40)$$

Let us briefly explain, how to propagate a general state $|\psi^{\text{in}}\rangle$ of the form in Eq. (3.37) step by step. First, we describe the actions of the Bragg matrices,

$$|\psi^{\text{out}}\rangle = \mathcal{B}_\Lambda |\psi^{\text{in}}\rangle = \mathcal{B}_\Lambda \cdot C \cdot \hat{\mathbf{e}}_\phi =: \tilde{C}_\Lambda \cdot \hat{\mathbf{e}}_\phi, \quad (3.41)$$

through a straightforward matrix multiplication, $\tilde{C}_\Lambda = \mathcal{B}_\Lambda \cdot C$. Here, the different Bragg operations in Eq. (3.40) are again denoted by the index $\Lambda = 1,\text{BS}, 2,\text{BS}, \text{M}$ as before. Accounting for the free propagation, on the other hand, is more complicated. Let us first recall,

that according to Appendix B, the matrix $\mathcal{U}(T)$ is diagonal in the basis of the individual trajectories,

$$\mathcal{U}(T) = \sum_{j=1}^r \exp(i(\theta_j + m_j\phi)) |q_j - MgT\rangle_{j,l} \langle q_l|. \quad (3.42)$$

Furthermore, this equation shows that free propagation imprints a multiple of the phase $m_j\phi$, where the value of $m_j \in \mathbb{Z}$ depends on q_j , as we demonstrate in the appendix. Using the result in Eq. (3.42), we can solve the free propagation by writing

$$\begin{aligned} |\psi^{\text{out}}\rangle &= \mathcal{U}(T) |\psi^{\text{in}}\rangle = \sum_{j=1}^r \sum_{l=-N}^N \underbrace{e^{i\theta_j} [C]_{j,l}}_{[\tilde{C}]_{j,l}} e^{i(l+m_j)\phi} \\ &= \sum_{j=1}^r \sum_{\nu=-N}^N [\tilde{C}]_{j,\nu-m_j} e^{i\nu\phi} =: \tilde{C}(T) \cdot \hat{\mathbf{e}}_\phi, \end{aligned} \quad (3.43)$$

where, in the second line, we introduce the index $\nu = l + m_j$ and use the fact that we can choose N large enough, so that $N + m_j \approx N$. Moreover, we have performed an index shift in the second line of Eq. (3.43) that is only well defined if N is sufficiently large, such that the coefficients at the edges of the interval vanish, i.e., $[\tilde{C}]_{j,\pm N} = 0 \forall j$.

Performing these two operations according to the sequence of the atom interferometer [see, e.g. Eq. (3.40)] we can obtain the output state

$$|\psi^{\text{out}}\rangle = \sum_{j=1}^r \sum_{l=-N}^N [C]_{j,l} e^{il\phi}, \quad \text{with } C = C_{j,l}(T, \Omega_{\text{BS}}, \tau_{\text{BS}}, \Omega_{\text{M}}, \tau_{\text{M}}, \sigma_p). \quad (3.44)$$

To derive the absolute number of atoms in the j th port in its amplitude-phase form as in Eq.(3.35), we must transform the expression

$$N_j(\phi) = \sum_{l=-N}^N \sum_{l'=-N}^N [C]_{j,l} [C]_{j,l'}^* e^{i(l-l')\phi}. \quad (3.45)$$

To rewrite this equation as a Fourier series, we perform the substitution $L := l - l'$. This permits us to write

$$N_j(\phi) = \sum_{L=-2N}^{2N} \underbrace{\sum_{l'=-N}^N [C]_{j,L+l'} [C]_{j,l'}^*}_{\tilde{C}_{j,L}} e^{iL\phi} = \sum_{L=-2N}^{2N} \tilde{C}_{j,L} e^{iL\phi}, \quad (3.46)$$

where we have used the assumption that effectively $N \rightarrow \infty$, meaning we can treat the sums in this equation as infinite sums. Finally, having expressed the absolute atom numbers

$N_j(\phi)$ in a Fourier series, we can simply find the amplitude-phase form in Eq. (3.35) using the relations

$$A_{j,l} = \sqrt{4[\tilde{C}]_{j,l}[\tilde{C}]_{j,-l}} \quad \text{and} \quad \varphi_{j,l} = \arccos\left(\frac{[\tilde{C}]_{j,l} + [\tilde{C}]_{j,-l}}{A_{j,l}}\right), \quad (3.47)$$

as well as $P_{0,j} = [\tilde{C}]_{j,0}$.

Finally, it is worth noting that the sums in Eq. (3.46) can run over millions of summands depending on the number of trajectories and on the order of the tensor C . However, most of these entries vanish, which is why an efficient implementation of the above steps is paramount. One example of such a program written by *R. Bösche* using *MATHEMATICA* can be found in Appendix C of Ref. [167], where it was successfully used to analyze the signal of the conjugated Ramsey-Bordé interferometer [168]. This implementation demonstrates that the tensorial generalization of the scattering matrix formalism developed in this thesis provides an efficient and versatile approach to describing most atom interferometer topologies based on Bragg diffraction.

3.4.4 Pulse Parameters for Fifth-order Bragg Diffraction

Up to this point, we have analyzed the signals of MZ interferometers without making specific assumptions about the parameters of the Bragg pulses, other than the expectation that the LZ losses of high-fidelity Bragg operations are comparatively small, i.e., $\gamma, \Gamma \leq 0.1$. However, the discussion in the previous section raises the question, particularly with respect to the Bragg mirror, of which pulse parameters achieve good reflectivity while suppressing parasitic interferometers. One of the main results of the previous chapter is the observation that parameters enabling efficient Bragg beam splitter and mirror operations can be predicted analytically using the adiabatic theorem. Figure 3.3(a) shows the selection of parameters for fifth-order Bragg diffraction that we have obtained using Eq. (2.92) and already discussed in the context of Sec. 2.6. As we have explained previously, the experimentally relevant diffraction orders are restricted to $n \leq 5$, mainly due to the increasing power requirements of higher orders and subsequent spontaneous emission losses (cf. [69]). Therefore, we focus on $n = 5$ specifically in the following sections. The tuples $\Omega_{\text{BS}}, \tau_{\text{BS}}$ and $\Omega_{\text{M}}, \tau_{\text{M}}$ shown in Fig. 3.3(a) satisfy the condition on the Bragg pulse area, i.e., $\Theta_{\text{BS},n} = \frac{\pi}{2}$ and $\Theta_{\text{M},n} = \pi$ respectively, and we have restricted their range to balance velocity filtering towards long pulse durations, as well as the diffraction losses of the Bragg beam splitters. In addition, Fig. 3.3(b) shows the analytical and numerical solutions for the reflectivity $|B_{\mp(n-2),\pm(n-2)}|^2$ in Eq. (2.121) for parameters $\Omega_{\text{M}}, \tau_{\text{M}}$ ensuring $\Theta_{\text{M},n} = \pi$ [see light blue line in Fig. 3.3(a)]. Both solutions are in excellent agreement and allow us to systematically identify two minima for the given set, only one of which produces the desired suppression, i.e., ensuring $\sin\left(\frac{\Theta_{\text{M},n-2}}{2}\right) = 0$, while being compatible with atomic

ensembles featuring a finite velocity width [see Fig. 2.8(1)]. We mark this working point $\Omega_M, \tau_M = 31.8 \omega_r, 0.463 \omega_r^{-1}$ for the adapted Bragg mirror pulse via a vertical black bar and furthermore highlight it in the inset of Fig. 3.3(a).

Our following study of phase estimation in the MZ interferometers will involve two configurations in terms of pulse parameter selection: In the first scenario (A) we simply set $\Omega_{BS} = \Omega_M$, whereas in the second scenario (B) we ensure that the Bragg mirror is transparent for the dominant parasitic diffraction order ($\Theta_{M,n-2} = 0$) to suppress the closure of parasitic interferometry paths, while maintaining high reflectivity for the main interferometry paths ($\Theta_{M,n} = \pi$). In general, it is also worth noting that the description of realistic Bragg diffraction pulses requires the truncation of the Gaussian temporal envelopes of the pulses. With regard to our analytical calculation based on the application of the adiabatic theorem, we choose time intervals $t \in [-22, 22] \omega_r^{-1}$ that reflect the asymptotic nature of our scattering theory. On the other hand, in the following sections we will present results from numerical experiments in which we chose Gaussian pulse durations of $t \in [-10, 10] \omega_r^{-1}$ to suppress truncation effects [130].

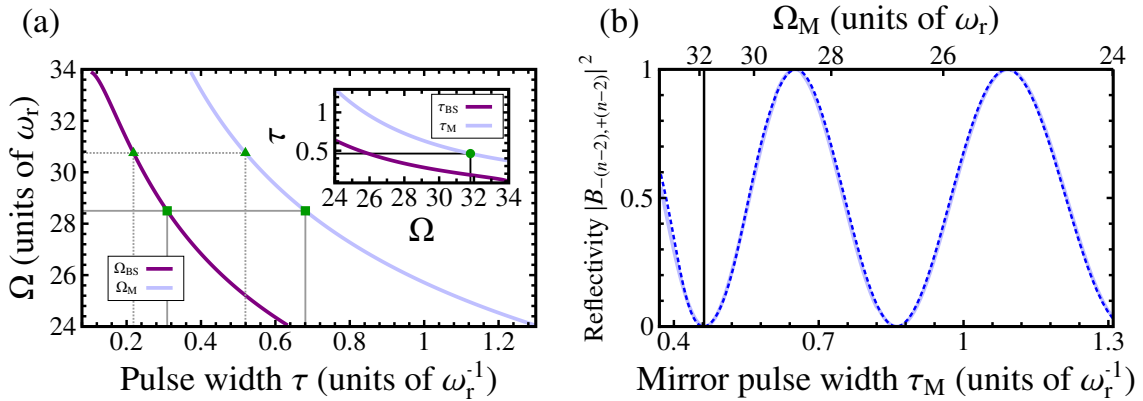


Figure 3.3: **Pulse parameters and mirror reflectivity for Bragg order $n = 5$.** (a) Analytically determined pulse parameters Ω_{BS}, τ_{BS} and Ω_M, τ_M enabling efficient Bragg beam splitter and mirror pulses for Bragg order $n = 5$ via Eq. (2.92) as we have already seen in Sec. 2.6.3. The green triangles (squares) as well as the dashed (solid) lines mark the parameter combinations with $\Omega_{BS} = \Omega_M$, which we discuss in the following. They indicate the local minimum (maximum) of the beam splitter losses in Fig. 3.4. We have interchanged the axes in the inset and highlight the mirror pulse parameters suppressing dominant parasitic interferences for $n = 5$ that we identify in (b). In (b), we compare analytical (solid light blue line) and numerical (dashed blue line) solutions for the reflectivity of the Bragg mirror for the dominant parasitic order as a function of the tuples Ω_M, τ_M from (a). The solid black vertical line highlights the adapted mirror parameters.

Beam Splitter Losses

Our selection of parameters in Fig. 3.3(a) restricts the population scattered to undesired diffraction orders to below 10 %, which we show in Fig. 3.4. We define the losses from the target momentum states $|\pm n \hbar k + p\rangle$ in a single beam splitter as

$$\mathcal{L}_{\text{BS}} = 1 - \lim_{\sigma_p \rightarrow 0} \int_{-\hbar k/2}^{\hbar k/2} dp \left(|\langle -n\hbar k + p | \psi_{\text{BS}}^{\text{out}} \rangle|^2 + |\langle +n\hbar k + p | \psi_{\text{BS}}^{\text{out}} \rangle|^2 \right) \quad (3.48a)$$

$$\stackrel{\Theta_n = \pi/2}{=} 1 - e^{-\Gamma} \cosh(\gamma). \quad (3.48b)$$

Here, $|\psi_{\text{BS}}^{\text{out}}(\Omega_{\text{BS}}, \tau_{\text{BS}}, \sigma_p)\rangle = S(\Omega_{\text{BS}}, \tau_{\text{BS}})|\psi^{\text{in}}(\sigma_p)\rangle$ denotes the quantum state after the beam splitter and $|\psi^{\text{in}}(\sigma_p)\rangle$ represents our usual Gaussian input. Using the scattering matrix in Eq. (2.121b) and assuming $\Theta_{\text{BS},n} = \pi/2$, one finds the identity in Eq. (3.48b), which yields a simple analytic expression for the losses. Note that in order to accurately predict beam splitter losses by means of this result, one must insert LZ parameters that account for all losses, e.g., using Eq. (2.128). In this case, we have calculated the data depicted in Fig. 3.4 by inserting a numerical solution for $|\psi_{\text{BS}}^{\text{out}}\rangle$ into Eq. (3.48a) as we describe, e.g., in Sec. 2.7.1. Unsurprisingly, the losses depend on the beam splitter parameters in a similar way as the corresponding pulse infidelity in Fig. 2.7(h). As a result of the underlying LZ physics discussed in Sec. 2.4.3, the LZ losses increase exponentially towards shorter pulse durations and feature a local minimum. In Sec. 2.6.3 we saw that such minima exist for all orders $n > 1$ and are a feature predicted by LZ theory. However, the corresponding parameters in Fig. 3.4 have been referred to by *R. Parker et al.* [118] as a "magic" Bragg duration, which effectively reduces variation of the diffraction phase with the pulse separation time in the conjugated Ramsey-Bordé interferometer. With this in mind, it will be particularly interesting to investigate the potential of the LZ minimum in suppressing the diffraction related phase shifts in the MZ interferometer.

3.5 Analytical Signals of Bragg Atom Interferometers

The analytical description we have derived for Bragg interferometer signals, including their multipath and multiport characteristics, provides the tools to formulate generalized phase estimation strategies. In particular, we are interested in formulating models $P_{a(b)}(\phi)$ that accurately predict the transition probabilities $\bar{\mu}_{a(b)}$, and that are ideally as practical to use as Eq. (3.2) in experiments. Comparison with simulations of a MZ interferometer realized by fifth-order Bragg pulses in numerical experiments allows us to analyze the performance of a given estimation strategy. Specifically, we investigate the two scenarios (A) and (B) illustrated in Fig. 3.5, where in (A) the undesired diffraction orders populate parasitic interferometers, potentially causing diffraction phases on the mrad-level. In scenario (B), we

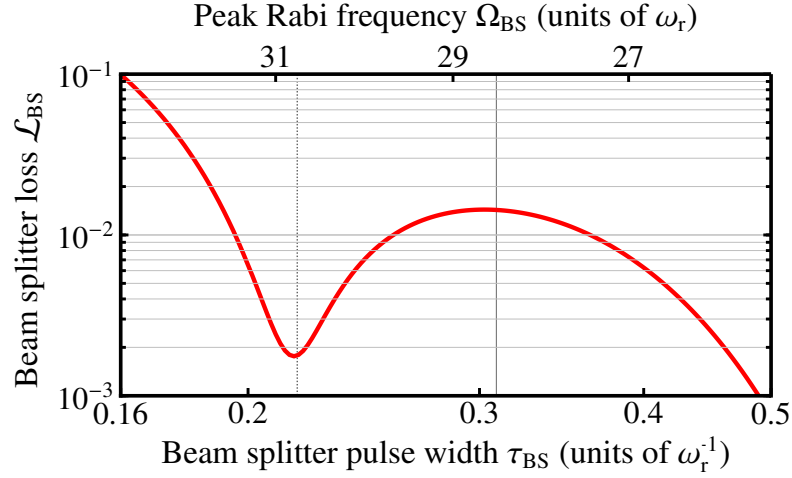


Figure 3.4: **Beam splitter population loss for Bragg order $n = 5$.** We show the numerically calculated population loss from the main diffraction order $|\pm 5 \hbar k\rangle$ after a single beam splitter pulse. Hence, the curve represents the sum of the data shown in Fig. 2.9. The results in Fig. 3.6 (Fig. 3.8) were obtained for parameters corresponding to the visible local maximum (minimum) denoted by the solid (dotted) vertical line with $\Omega_{\text{BS}}, \tau_{\text{BS}} = 28.5 \omega_r, 0.309 \omega_r^{-1}$ ($\Omega_{\text{BS}}, \tau_{\text{BS}} = 30.75 \omega_r, 0.218 \omega_r^{-1}$). Previously, the minimum in the LZ losses has been referred to as the "magic" Bragg duration for $n = 5$ in Ref. [118] (see main text).

apply the tailored combination of laser intensity and duration of the Bragg mirror pulse identified in the previous section, which suppresses the closing of parasitic interferometers, as illustrated in Fig. 3.5(B). We have already discussed in Sec. 3.4.2 that the signal of the MZ interferometer is dramatically simplified as a result, which should affect phase estimation as well.

3.5.1 Interferometer Including Parasitic Paths

Assuming a generic set of parameters $\Omega_{\text{BS}}, \tau_{\text{BS}}, \Omega_{\text{M}}, \tau_{\text{M}}$, the contributions of the parasitic paths and open ports can be significant. In the most general case, the signal of the relative atom number measurements, $\bar{\mu}_a(\phi)$, can be modeled using an infinite Fourier series,

$$P_a^{\text{exact}}(\phi) = P_0 + \sum_{j=1}^{\infty} A_j \cos(j\phi + \varphi_j), \quad (3.49)$$

with amplitudes A_j and phases φ_j that can be calculated as explained in Sec. 3.4.2. We contrast this result with the standard model of an n th-order Bragg MZ interferometer in Eq. (3.2), which is obtained by idealizing the beam splitters and mirror as two-mode operations. Figure 3.6(a,b) demonstrates good agreement between data from numerical simulations and the analytical signal $P_a^{\text{exact}}(\phi)$, when taking into account the dominant parasitic

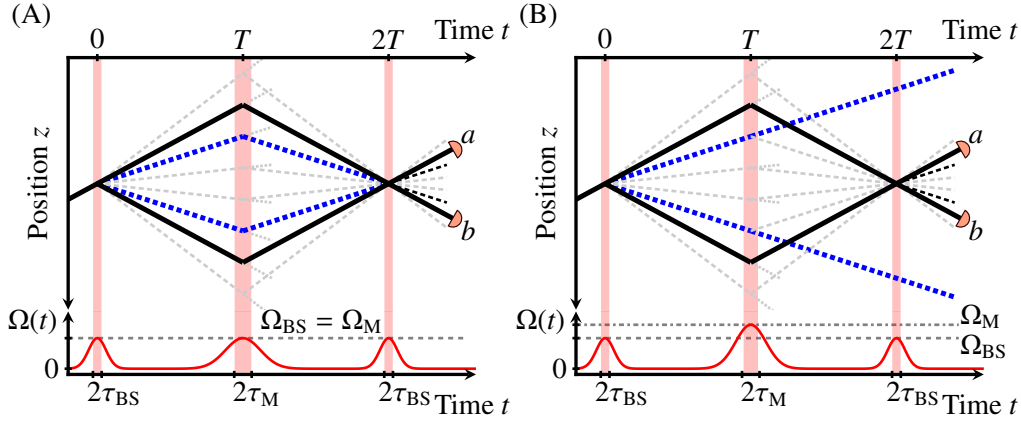


Figure 3.5: **Space-time diagrams of the MZ geometry showing parasitic paths of Bragg order $n = 5$.** The main trajectories (solid lines) are similar to Fig. 3.1(a), but here we also highlight the dominant parasitic paths (thick dashed blue lines) resulting from the Bragg scattering process. Other spurious trajectories (thin dashed gray lines) are not considered in our analytical description. The lower panel on the left demonstrates the locked peak Rabi frequencies in scenario (A), whereas in (B) tailored parameters Ω_M, τ_M [see Fig. 3.3(b)] enable the deflection of undesired paths and thus the suppression of the dominant parasitic interference effect, see main text. In the following, we will refer to the depicted configurations as MZ types (A) and (B).

paths for $n = 5$. The simulations are based on one-dimensional descriptions of the complete matter-wave interferometer in position space as per [169], whereby all diffraction orders and their potential trajectories (see gray dashed paths in Figs. 3.5) are fully accounted for. This is achieved by solving the single-particle Schrödinger equation in one dimension via the split-step method [170].

Because of its widespread application in atom interferometry [54], we assume the use of ^{87}Rb atoms as atomic species for all numerical experiments presented in this thesis. Therefore, the Bragg laser potential addresses the D_2 -line of the alkali atoms with a laser wavelength set to $\lambda = 780 \text{ nm}$ in our simulations, which corresponds to a recoil frequency $\omega_r \approx 2\pi \cdot 3.77 \text{ kHz} \approx 42.2 \mu\text{s}^{-1}$ [100]. To generate the data presented in Fig. 3.6(a,b), we fix the pulse separation time to $T = 10 \text{ ms}$ (ensuring $\tau \ll T$) and scan ϕ via the phase of the final beam splitting pulse, which we control by selecting a value for $\phi_{L,2,BS}$ for each data point while setting $g = 0 = \phi_{L,1,BS} = \phi_{L,M}$ [see Eq. (3.27)]. Here, we consider a set of pulses with identical peak Rabi frequency $\Omega = \Omega_{BS} = \Omega_M$ (A), and choose to operate the beam splitters in the local LZ maximum in Fig. 3.4 with about 1.4% diffraction losses from the main paths per first beam splitting pulse. Already this amount of scattering to undesired diffraction orders results in the MZ signal exhibiting a diffraction phase shift of several mrad with respect to the sinusoidal signal of an ideal two-mode interferometer, as shown in Fig. 3.6(b). The origin of this shift can be understood as follows:

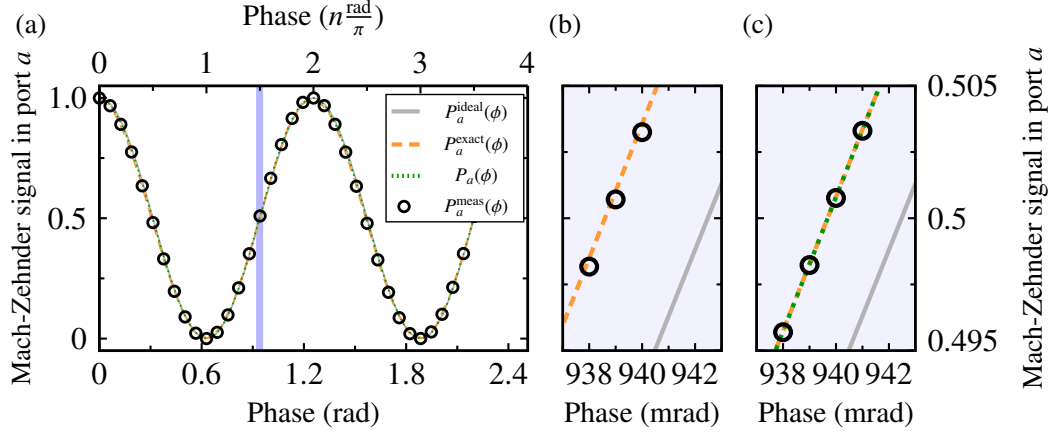


Figure 3.6: **Signal phase scan of the MZ interferometer.** (a,b) Signal of MZ type (A) in port a scanned via the lattice phase $\phi_L(t) = \phi_L$ of the final beam splitter for Bragg order $n = 5$. We compare numerically simulated data $P_a^{\text{meas}}(\phi)$ (circles) to an ideal sinusoidal signal, $P_a^{\text{ideal}}(\phi) \equiv 1/2 \cdot (1 + \cos(n\phi))$ (gray solid line), and the analytical predictions of Eqs. (3.49) (orange dashed line) and Eq. (3.50) (green dotted line). Pulse parameters are $\Omega, \tau_{\text{BS}}, \tau_{\text{M}} = 28.5 \omega_r, 0.309 \omega_r^{-1}, 0.681 \omega_r^{-1}$, with $\omega_r = \hbar k^2/2M$ being the recoil frequency of an atom with mass M . Beam splitter diffraction losses of $\approx 1.4\%$ amplify the signal distortions. (b) shows a bias phase shift of the ideal sinusoidal signal on the mrad-level around mid fringe, i.e., $P_a(\phi_0) \approx 0.5$. In (c) mirror pulse parameters $\Omega_{\text{M}}, \tau_{\text{M}} = 31.8 \omega_r, 0.463 \omega_r^{-1}$ suppress dominant interference effects, as illustrated in Fig. 3.5(B). This provides excellent agreement between the numerics and both analytical models in Eqs. (3.49) and Eq. (3.50).

- (i) As we saw in Sec. (3.4.2), not detecting the spurious output ports of the final beam splitter transforms the relative atom numbers in a Bragg interferometer, $\mu_{a(b)}(\phi)$, into ratios of ϕ -dependent functions. Consequently, the signals generally contain Fourier components of arbitrary order. This is in contrast to an ideal two-mode interferometer, where the denominator simply amounts to the total number of atoms contributing to the signal N_{atoms} .
- (ii) In addition, we have demonstrated that the functional dependence of the absolute atom numbers $N_{a(b)}(\phi)$ [Eq. (3.29)] is also complicated by the occurrence of parasitic interferometers. This causes A_j and φ_j in Eq. (3.49) to depend on the interrogation time T as a result of differential kinematic phases ϕ_r [see Eq. (3.31)]. Notwithstanding its correctness, it will be challenging to apply the waveform in Eq. (3.49) due to the large number of parameters involved and the limited control over them.

3.5.2 Interferometer with Suppressed Parasitic Paths

We have suggested a simple way to efficiently suppress interference with the dominant parasitic paths in the MZ geometry by designing the mirror pulse to be approximately

transparent to them, as illustrated in Fig. 3.5(B). In Fig. 3.3(b), we provided specific combinations Ω_M, τ_M that achieve this for $n = 5$. Meanwhile, they do exist for all relevant higher orders of Bragg diffraction, except $n = 2$. It is straightforward to omit the influence of parasitic paths in our analytical model and consider only the effects of the open ports (point (i) above) following the arguments made in Sec. 3.4.2. This simplifies the signal of the MZ interferometer $\bar{\mu}_{a(b)}(\phi)$, which can then be modeled by

$$P_{a(b)}(\phi) = P_0 \pm \sum_{j=1}^3 A_j \sin\left(j \cdot \left(n\phi + \gamma + \frac{\pi}{2}\right)\right) + O[\gamma^3], \quad (3.50)$$

where $P_b(\phi)$ is shifted by π relative to $P_a(\phi)$ as one would expect. In general, both functions must be represented by infinite Fourier series, however, as we are interested in highly efficient LMT Bragg atom interferometers with small off-resonant populations (see Fig. 3.4), we interpret $P_{a(b)}(\phi)$ as a series expansions in the open-port population $N_{\text{open}}(\phi)$, so that the contributions of A_j decrease with increasing index j . The models $P_{a(b)}(\phi)$ are more general versions of the expressions in Eq. (3.34). As such, they contain only the harmonics of a single Fourier component $n\phi$ in addition to the shift phase shift γ , which unlike Eq. (3.49) applies to all harmonics. For an interferometer with suppressed parasitic paths as in Fig. 3.5(B), both the exact signal in Eq. (3.49) and the much simpler formula in Eq. (3.50) are in excellent agreement with the data from a numerical simulation as Fig. 3.6(c) shows.

3.6 Systematic Error: The Diffraction Phase

We proceed to quantify the diffraction phase [117, 118], i.e., the systematic error of the model in Eq. (3.50) when applied to numerical experiments. Using simulated measurement data for the detected relative atom numbers $\bar{\mu}_a$, we compare MZ interferometers without (A) and with (B) suppression of the dominant parasitic paths. Formally, we define the diffraction phase as the deviation between the true local phase value ϕ_0 and its estimate $\phi^{\text{est}} = P_a^{-1}(\bar{\mu}_a|_{\phi_0})$,

$$\delta\phi = P_a^{-1}(\bar{\mu}_a|_{\phi_0}) - \phi_0 = P_a^{-1}(\bar{\mu}_a|_{\phi_0})\Big|_{\gamma=0} - \frac{\gamma}{n} - \phi_0. \quad (3.51)$$

Here, we emphasize the fact that γ is a shift common to all Fourier components in Eq. (3.50), which we have taken advantage of in the second equation. Therefore, the error $\delta\phi$ is determined by the knowledge of γ as well as the remaining phase, $P_a^{-1}(\bar{\mu}_a|_{\phi_0})\Big|_{\gamma=0}$, which depends on the accuracy of the analytical model $P_a(\phi)$ besides the offset with γ . If γ can be inferred with sufficiently high accuracy for given beam splitter parameters it is the latter contribution which sets the systematic uncertainty. Furthermore, we highlight that both contributions to the diffraction phase in Eq. (3.51) will be linearly suppressed by the order n of the Bragg

pulses as a consequence of the scaling with $n\phi$ in Eq. (3.50). A similar suppression was noted by the authors of Ref. [117] in the case of the asymmetric Ramsey-Bordé interferometer.

3.6.1 Phase Offset γ/n

Before evaluating $\delta\phi$, we discuss the magnitude of the offset γ/n , and analyze how it is affected by intensity fluctuations. Comparison between Fig. 3.4 and Fig. 3.7 confirms the close relationship between the linear phase offset in the MZ signals γ/n in Eq. (3.51) and the LZ losses of the Bragg beam splitters. In particular, the maxima of both curves coincide, but their minima are slightly shifted. This discrepancy, and the fact that γ/n can take on negative values, is explained by the observation that the LZ parameter describes the differential population loss between the symmetric and antisymmetric subspaces, which we explain in Sec. 2.3.3. Most importantly, Fig. 3.7 highlights that even for beam splitter losses of less than 10 %, the magnitude of the spurious phase shift can amount to several mrad, and is therefore larger than the atomic projection noise of an ideal two-mode atom interferometer assuming atom numbers, N_{atoms} , in the order of 10^6 . This implies that sufficient knowledge and suppression of the phase shift γ/n are paramount for accurate phase estimation in MZ interferometers using higher-order Bragg diffraction, even though it is not the only contribution to the diffraction phase in Eq. (3.51).

We have demonstrated in Secs. 2.4.3 and 2.7.1 how to extract the LZ parameters from numerical solutions of the Schrödinger equation both in the (anti)symmetric basis representation and in the basis of momentum eigenstates. In principle, Eq. (2.128) provides a way to calculate those parameters based on experimental measurements of beam splitter output populations. We note that this would require the preparation of the (anti)symmetric input state in Eq. (2.127) as the initial state for the experiment. Therefore, it may prove more practical to determine these parameters indirectly by calibrating a theoretical model of the atom-light interaction to the experimental parameters. In this case, intensity fluctuations in the experiment may limit the accuracy with which γ/n can be determined. To estimate their effect, we introduce a statistically fluctuating error in the peak Rabi frequency of the Bragg beam splitting pulse $\Omega_{\text{BS}} = \Omega_{\text{BS}}(1 + \delta\Omega)$, where $\delta\Omega$ is a random variable following a normal distribution with zero mean and variance $\sigma_{\delta\Omega}^2$,

$$\delta\Omega(\sigma_{\delta\Omega}) = (2\pi\sigma_{\delta\Omega}^2)^{-1/2} \exp\left(-\frac{\delta\Omega^2}{2\sigma_{\delta\Omega}^2}\right). \quad (3.52)$$

The data in Fig. 3.7 illustrate that the mean values $\bar{\gamma}/n$ are largely unaffected by variations in the range of one percent and less, whereas the standard deviations of the data can reach up to one mrad in those cases, where the LZ parameter is comparatively large. Intensity fluctuations of five percent, on the other hand, can lead to errors of several mrad, which are

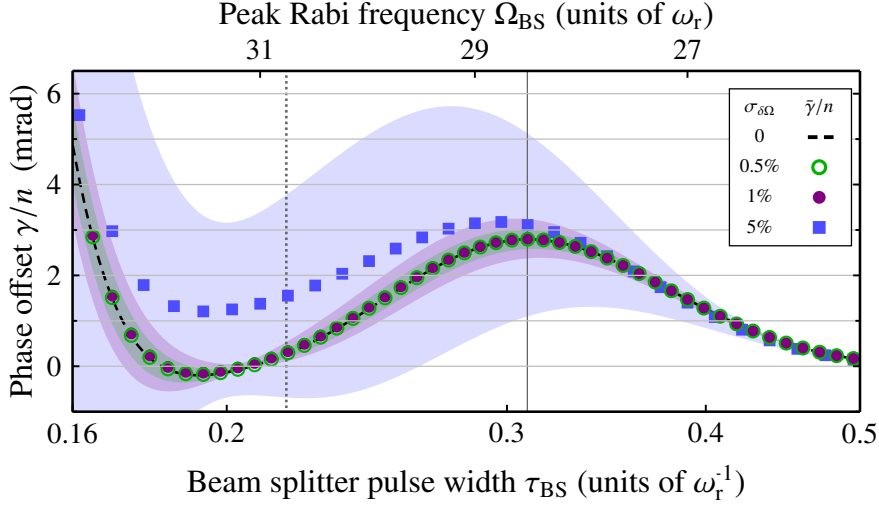


Figure 3.7: **Phase offset γ/n introduced in Eq. (3.51) of the MZ interferometer.** The data for Bragg order $n = 5$ are similar to the lower panel of Fig. 2.9(b) but rescaled by the Bragg order and with a linear y-axis. Additionally, we introduce a normally distributed uncertainty in the peak Rabi frequency with variances $(\sigma_{\delta\Omega})^2$ according to Eq. (3.52). The average spurious phase shifts can be in the order of several mrad and their maximum coincides with the maximum in the beam splitter loss (solid vertical line). The shaded regions represent the standard deviations in the data, which reach several hundred μrad considering fluctuations at the percent level. Larger fluctuations make accurate determination of γ/n impossible, especially close to the LZ minimum (dotted vertical line). Because γ describes the difference in loss between the symmetric and the antisymmetric state (see Tab. 2.2), the offset can become negative.

particularly severe for pulse parameters near the local minimum, where the phase offset is more sensitive to changes of the peak Rabi frequency.

In summary, our observations indicate that the peak Rabi frequency must be stable on the level of one percent to avoid diffraction phases of several mrad for all but long beam splitter pulse durations. Long pulse durations featuring small γ/n are favorable, since they are much less susceptible to fluctuations of the laser intensity. Their impact is especially severe for parameters in and around the LZ minimum. Despite these relevant implications, including the aspect of intensity noise in the following discussion of the diffraction phase is beyond the scope of this thesis. Therefore, we assume perfect control over the peak Rabi frequencies for the remainder of this chapter.

3.6.2 Diffraction Phases for Fifth-order Bragg Diffraction

In this section, we extract the diffraction phase $\delta\phi$ in Eq. (3.51) from MZ signals $\bar{\mu}_a$ generated in numerical realizations of the complete interferometer sequence in position space.

Once converged, we find that the numerical data feature no relevant fluctuations, since we do not consider noise processes in our calculation. Therefore, we can fit the analytical model $P_a(\phi)$ (3.50) directly to single measurement outcomes $\bar{\mu}_a = \mu_a$. Figure 3.8 shows the diffraction phase as a function of the pulse separation time T for interferometers of type (A) and (B). This highlights, in particular, the contributions of the parasitic interference terms to the interferometer signal as they vary with the separation time T and are not included in the model in Eq. (3.50). We again operate at mid-fringe $\phi_0 = \frac{3\pi}{2} \frac{1}{5}$ selected via the laser phase of the final Bragg pulse in our numerical simulations and plot the diffraction phase $\delta\phi$ for different pulse separation times $T \in [10.0, 10.017]$ ms in Fig. 3.8. Despite minimizing beam splitter losses to about 0.18 % by operating the beam splitters in the LZ minimum, spurious MZ interference terms cause visible oscillations on the μrad -level for both configurations of the MZ geometry. We find oscillation frequencies $(5 \pm 1) \cdot 8 \omega_r$ corresponding to ca. $0.88 \mu\text{s}^{-1}$ and $1.32 \mu\text{s}^{-1}$, which can be related to the differences in kinematic phases $\delta\phi_r$ in Eq. (3.31) between the main interferometer arms and the parasitic trajectories, which we have discussed in Sec. 3.4.2. We verify this observation by showing perfect agreement between the data and a suitable fit model

$$f(T) = B_0 + B_1 \cos(4 \cdot 8\omega_r T + \nu_1) + B_2 \cos(6 \cdot 8\omega_r T + \nu_2). \quad (3.53)$$

The recoil frequency is fixed by our choice of laser wavelength $\lambda \approx 780 \text{ nm}$ and atomic species ^{87}Rb , with $\omega_r \approx 42.2 \mu\text{s}^{-1}$. The second phase contribution originates from the interference of the main trajectories with the parasitic paths belonging to momentum modes $|\pm(n-4)\hbar k + p\rangle$ with $\delta\phi_r = (n+1) \cdot 8\omega_r T = 6 \cdot 8\omega_r T$, which according to the state space in Eq. (3.18) we do not consider in our current analytical description⁴.

Since the amplitudes (and phase shifts) in $f(T)$ are free parameters, we can use the fit model to extract the amplitude offset B_0 and the peak-to-peak value PP of the oscillations in the diffraction phase,

$$\text{PP} := |\max_{\nu T} f(T) - \min_{\nu T} f(T)|. \quad (3.54)$$

For the pulse parameters assumed in Fig. 3.8, the offset $B_0 \approx -27 \mu\text{rad}$ is the same for both cases (A) without and (B) with suppression of parasitic paths. This shows that the inclusion of $\gamma/n \approx 280 \mu\text{rad}$ in Eq. (3.51) accounts for most of the T -independent shift. However, PP values of both data sets are very different, lying in the range of $200 \mu\text{rad}$ for (A) and about $40 \mu\text{rad}$ for (B) making them a sensitive measure of the influence of parasitic interferometers. Indeed, reduction achieved by the adapted Bragg mirror is significant

⁴The fact that states $|\pm(n+2)\hbar k + p\rangle$ are irrelevant may seem counter intuitive, when looking only at the LZ beam splitter populations shown for $n = 5$ in Fig. 2.9(a). In this context, it is important to remember that the parasitic trajectories only overlap with the main arms at $t = 2T$ if they are reflected by the mirror pulse. However, for the parameters Ω_M, τ_M in Fig. 3.3(a) the mirror angle $\Theta_{M,n+2} \approx 0$ is essentially zero, which is a result of the increasing power requirements of higher-order Bragg pulses discussed already in Sec. 2.3.4.

because the net diffraction phase shift can be in the order of the PP value due to insufficient control over the separation time T at the μs level or, if T is sampled, due to aliasing effects as pointed out in by *R. Parker* et al. in Ref. [118]. The authors performed a study similar to the one discussed here, but experimentally and in the case of the conjugated Ramsey-Bordé geometry. The results in Fig. 13 of Ref. [118] primarily show that operating the Bragg beam splitters in the LZ minimum (referred to as "magic" Bragg duration in the reference) reduces the oscillations as the amplitudes of parasitic interference terms are suppressed.

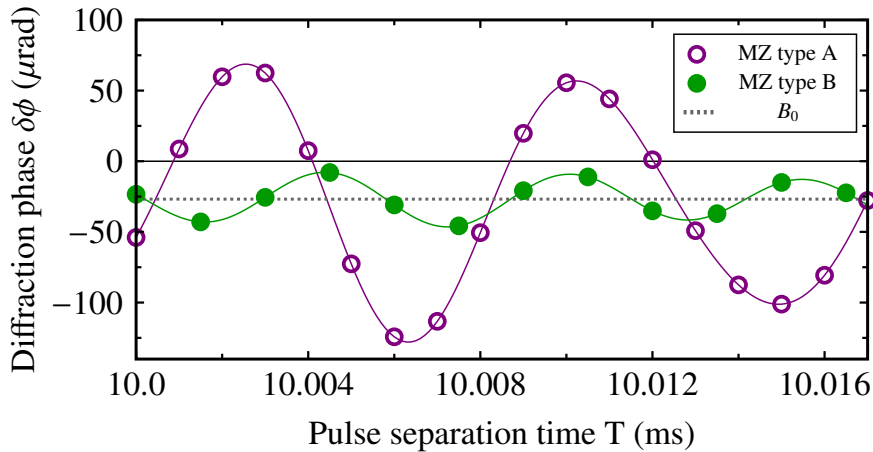


Figure 3.8: **Phase estimation error for different pulse separation times T .** We evaluate the diffraction phase $\delta\phi$ in Eq. (3.51) using numerical simulations of MZ interferometers of types (A) and (B) with $n = 5$. $\delta\phi$ is determined at mid fringe $\phi_0 = \frac{3\pi}{2} \frac{1}{5}$ and beam splitters are chosen to operate at a so-called "magic" Bragg duration, minimizing individual diffraction losses to $\approx 0.18\%$ (see main text). This reduces oscillations in $\delta\phi$ to the μrad -level while scanning the pulse separation time T (cf. [118, 147]). The first data set (open circles) was obtained for parameters $\Omega, \tau_{\text{BS}}, \tau_{\text{M}} = 30.75 \omega_{\text{r}}, 0.218 \omega_{\text{r}}^{-1}, 0.519 \omega_{\text{r}}^{-1}$, where $\omega_{\text{r}} = \hbar k^2/2M$ is the recoil frequency of an atom with mass M . Suppressing dominant parasitic interference effects via $\Omega_{\text{M}}, \tau_{\text{M}} = 31.8 \omega_{\text{r}}, 0.463 \omega_{\text{r}}^{-1}$ [closed circles, case (B)] further reduces the oscillation amplitude by a factor of five to $< 40 \mu\text{rad}$. Solid lines represent fits to the data explained in the main text, the offset of which, $B_0 \approx -27 \mu\text{rad}$ (horizontal dotted line), is identical for both data sets.

In Fig. 3.9, the offset $|B_0|$ and the PP value of the oscillations in the diffraction phase obtained with the same T -interval as before are plotted, but analyzed for the entire parameter range given in Fig. 3.3(a). We again compare both Bragg mirror pulse configurations (A) and (B). Figure 3.9(a) confirms that the inclusion of γ in the model $P_a(\phi)$ in Eq. (3.50) reduces the T -independent contribution to the diffraction phase $\delta\phi$ to at most a few tenths μrad for both Bragg mirror configurations. At the same time, Fig. 3.9(b) highlights that the oscillations of $\delta\phi$ can be in the order of several mrad and are therefore comparable to γ/n , see Fig. 3.7, when considering pulse parameters with relatively strong couplings to

undesired diffraction orders. Comparison with Fig. 3.4 highlights that the behavior of both quantities characterizing $\delta\phi$ is directly related to the losses of the beam splitter operations.

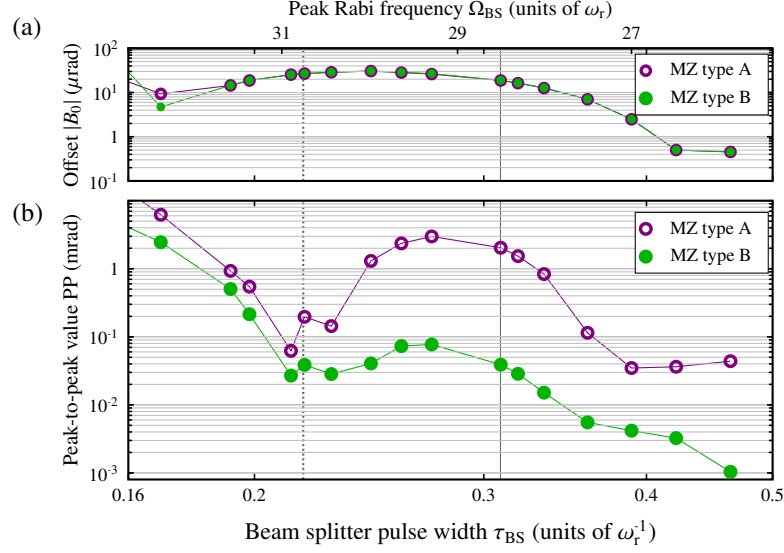


Figure 3.9: **Suppression of the diffraction phases in the MZ geometry at mid fringe**, $\phi_0 = \frac{3\pi}{2} \frac{1}{5}$. Results in (a,b) are obtained from fits to $\delta\phi$ in Eq. (3.51), which has been evaluated for numerical MZ signals recorded over scans of $T \in [10, 10.017]$ ms as shown in Fig. 3.8(a) using pulse parameter in Fig. 3.3 and at $\phi_0 = \frac{3\pi}{2} \frac{1}{5}$. Closed (open) symbols represent data with (w/o) suppression of parasitic paths parameterized via $\Omega = \Omega_{BS}, \tau_{BS}$. (a) We plot absolute values of the residual offset $|B_0| \leq 30 \mu\text{rad}$ (symbols) independent of the mirror pulse. (b) The adapted mirror pulse [case (B)] significantly suppresses PP values for most parameters below 1 mrad and to less than $10 \mu\text{rad}$ for sufficiently long beam splitter pulse durations. Lines connecting the data points serve as guides to the eye. Solid (dotted) vertical line corresponds to the local maximum (minimum) in the beam splitter losses in Fig. 3.4.

We can infer from these results that the diffraction phase of MZ Bragg interferometers with $n = 5$ can be suppressed by means of the Bragg mirror pulse below 1 mrad for most parameters Ω_{BS}, τ_{BS} and even down to a few μrad for sufficiently long beam splitter durations ($\tau_{BS} \approx 0.45 \omega_r^{-1}$). In contrast, without suppression of parasitic paths and without accounting for the diffraction phases (including γ) by means of Eq. (3.50), the accuracy would be limited to more than 0.5 mrad in the same regime, which constitutes an improvement by two orders of magnitude. The remaining diffraction phase is limited by higher-order contributions in γ and the finite efficiency in suppressing parasitic paths. We have focused our discussion around Bragg order $n = 5$, because it is the largest diffraction order that can reasonably be realized in experiments in the presence of spontaneous emission (see related discussion in previous chapter). At the same time, our observations suggest that the adapted Bragg mirror is most effective when applied to third-order Bragg diffraction. In

this case, the mirror pulse suppresses parasitic interferometers associated with the modes $|\pm 1 \hbar k + p\rangle$, while the coupling to other diffraction orders $|\pm(n+2) \hbar k + p\rangle$ with larger kinetic energy is inherently low, as we have seen here. Therefore, a dedicated quantitative study of the performance of the phase estimation strategy in this setup seems certainly fruitful, but is beyond the scope of this thesis.

Concluding this section, we discuss the observation that realistic signals of interferometers using higher-order Bragg diffraction do not feature the same periodicity as the two-mode model in Eq. (3.2). In this work, we focus on analyzing the multiport properties of Bragg atom interferometers in a regime, where the population of undesired diffraction orders is small, unlike, e.g., in Section 5 of Ref. [147]. Hence, the "distortions" [118, 135, 147] caused by the spurious Fourier components are difficult to discern for instance by simply looking at the data in Fig. 3.6. However, they cause the MZ signals in Eq. (3.34) to exhibit different slopes at mid-fringe positions $\phi_0 = (4m+1) \cdot \pi/(2n)$, compared to $\phi_0 = (4m-1) \cdot \pi/(2n)$, with $m \in \mathbb{Z}$, even in the absence of parasitic interferometers. Moreover, we demonstrate in Fig. 3.10 that this asymmetry also affects the diffraction phase and can therefore have significant implications for precision experiments. Here, we evaluate the diffraction phase for the alternative mid-fringe position $\phi_0 = \frac{\pi}{2} \frac{1}{5}$ and demonstrate that the T -independent contributions to $\delta\phi(\phi_0)$ in Eq. (3.51) remain unchanged. While the adapted mirror configuration significantly suppresses the PP values by an order of magnitude for most of the parameters presented, the PP values are increased by about the same amount overall compared to the previous operating point in Fig. 3.9(b). This is attributed to the interferometry signal varying greatly with pulse separation time T , which affects the accuracy of the waveform in Eq. (3.50), mainly because, unlike Eq. (3.49), it does not take into account contributions due to parasitic interferometers. We note that the PP values in Fig. 3.10(b) are sharply reduced for pulse parameters around the LZ minimum, so that they are similar for both mid-fringe positions. This is expected since these parameters strongly suppress LZ couplings to diffraction order $n-2$ and especially $n-4$ [see Fig. 2.9(a)], which is not affected by the adapted Bragg mirror.

In summary, to keep systematic errors on the μrad -level for this alternate mid-fringe position either adiabatic beam splitter pulse parameters or operation in the LZ minimum is required. It should be noted, however, that some of the effects observed here, in particular those contributing to the phase differences between the mean fringe positions, can be attributed to the higher harmonics occurring in the signal of the atom interferometer, see Eq. (3.50). If the phase ϕ is fluctuating, e.g., due to laser phase noise caused by vibrations of the experimental apparatus, the contributions of these higher frequency components potentially average out when recording the data, diminishing their importance (cf. [118]). Apart from this, the role played by the spurious population of the diffraction order $n-4$ in our discussion of $\delta\phi$ suggests that there may be quantitative advantages in controlling

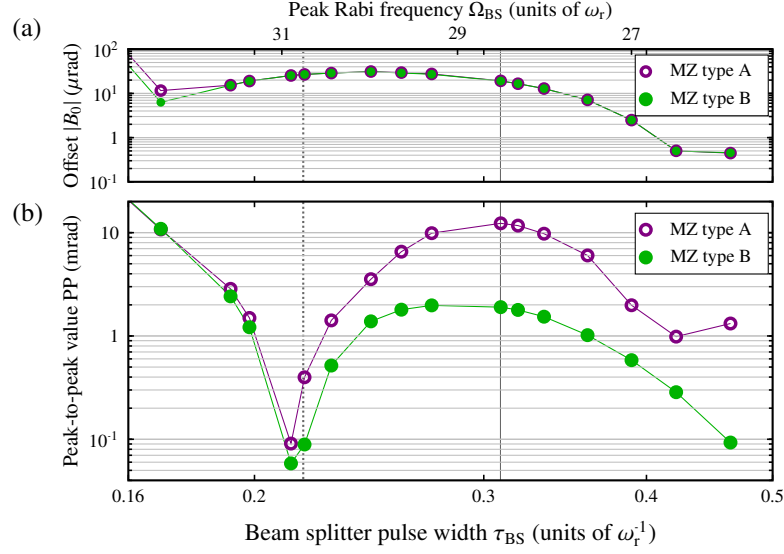


Figure 3.10: **Suppression of the diffraction phases at the alternative mid-fringe position**, $\phi_0 = \frac{\pi}{2} \frac{1}{5}$. The residual offset $|B_0| \leq 30 \mu\text{rad}$ in (a) is the same as in Fig. 3.9(a) since we are using identical pulse parameters. We show in (b) that the adapted mirror pulse [case (B)] still suppresses PP values by about one order of magnitude for most pulse parameters, but suppression below 1 mrad is achieved only for long pulse durations or for parameters close to the LZ minimum. Here, PP values are comparable to Fig. 3.9(b). The local differences in the accuracy of the estimator result from the wave form in Eq. (3.50) not including parasitic interferometer effects, especially because the adapted mirror does not affect modes with diffraction order $n - 4$ in the case of fifth-order Bragg pulses (see main text). Lines connecting the data points serve as guides to the eye.

the diffraction phase if the MZ interferometer is realized with third-order Bragg pulses for which the states $|\pm(n - 4) \hbar k\rangle$ do not exist.

3.7 Statistical Uncertainty: Phase Sensitivity

Besides systematic effects, the complex contributions of parasitic paths and undetected open ports also affect the statistical aspects of phase estimation with Bragg atom interferometers. To complete our analysis of the model in Eq. (3.50), we discuss the statistical uncertainty of the corresponding estimator $\phi^{\text{est}} = P_a^{-1}(\bar{\mu}_a | \phi_0)$ and investigate whether it saturates the projection noise limit set by the CRB and the QCRB, both of which bound the phase sensitivity of an interferometer from below.

3.7.1 Sensitivity Bounds for Uncorrelated Particles

Formulating the (Q)CRB is straightforward based on the analytical expression for the quantum state at the output of the MZ interferometer in Eq. (3.26). We evaluate the CRB for atom number measurements in the main ports a and b of the MZ interferometer. The detection probability $\mathcal{P}(\mu_a|\phi) = N_a(\phi)/N_{\text{atoms}}$ can be derived from our analytical model with the expressions for the absolute atom numbers in Eqs. (3.29). They enable the calculation of the single-particle Fisher information, which in turn defines the CRB according to Eq. (3.11),

$$\Delta\phi_{\text{CRB}} = \frac{1}{\sqrt{N_{\text{atoms}}}} \frac{1}{\sqrt{F(\phi)}} \quad \text{with} \quad F(\phi) = \sum_{j=a,b} \frac{(\partial_\phi N_j(\phi)/N_{\text{atoms}})^2}{N_j(\phi)/N_{\text{atoms}}}. \quad (3.55)$$

Unfortunately, even in the limit of small LZ losses, no simple analytical expression for $F(\phi)$ can be found when assuming otherwise general pulse parameters. This is because the terms in $N_{a(b)}(\phi)$ describing the interference between the main and the parasitic arms depend not only on the separation time T via the kinematic phase ϕ_r , but also on the phases and diffraction angles we discuss in Sec. 2.7. Nevertheless, it is instructive to analyze the Fisher information in the limit of a vanishing momentum width and in the absence of parasitic interferometers, i.e., assuming $\Theta_{M,n-2} = 0$,

$$\lim_{\sigma_p \rightarrow 0} F(\phi) = n^2(1 - 2\Gamma - \gamma \sin(n\phi)) + \mathcal{O}[\gamma, \Gamma]^2. \quad (3.56a)$$

Scaling with the Bragg order n illustrates the increase in sensitivity due to higher-order Bragg diffraction, and at the same time this result also shows that LZ losses primarily reduce the Fisher information [we recall $\gamma \leq \Gamma$; for $n = 5$ see Fig. 2.9(b)]. Moreover, $F(\phi)$ is a function of the phase ϕ , which in particular gives different results for the two types of mid-fringe positions we have identified in Sec. 3.6.2,

$$\lim_{\sigma_p \rightarrow 0} F(\phi) = n^2(1 - 2\Gamma \mp \gamma) + \mathcal{O}[\gamma, \Gamma]^2, \quad \text{if } \phi = (4m \mp 1) \cdot \pi/(2n) \text{ with } m \in \mathbb{Z}. \quad (3.56b)$$

As mentioned previously, the signals in Eq. (3.50) exhibit different slopes for these working points affecting the Fisher information and therefore the CRB. While this difference is proportional to the differential LZ parameter γ , we learn that the Fisher information for atom number measurements restricted to the main output ports and with suppressed parasitic interferometers decreases overall with increasing population of undesired diffraction orders. With respect to the finite velocity distribution of the atomic ensemble, we consider only velocity filtering in the Bragg mirror, which leads to a reduction in the detected atom number. In Sec. 3.7.3, we use the example of $n = 5$ to show how this loss of atoms increases the CRB in a similar way as it reduces the pulse fidelities of the Bragg mirror, which we have discussed in Sec. 2.6.3.

Moreover, we derive the QCRB for Bragg MZ interferometers based on the analytical model developed in this work by calculating the quantum Fisher information in Eq. (3.14) with respect to the quantum state $|\psi^{\text{out}}\rangle$ in Eq. (3.26). In doing so, we restrict measurements to the subspace of the four output ports of the final beam splitter in Fig. 3.2 and treat coupling outside of that due to non-adiabatic transitions or velocity filtering as incoherent atom loss. This limitation is motivated by our goal to study multi-mode effects in the metrologically relevant regime of high diffraction efficiencies, where LZ populations are small and typically go undetected. In this context the QCRB serves, e.g., as a tool to quantify the potential benefits of resolving all the output ports of the final beam splitter. In contrast, multi-mode interferometry featuring multiple trajectories with comparable populations is beyond the scope of the work presented here. As one example, the authors *W. D. Li et al.* [137] proposed the realization of a multipath atom interferometer via elastic scattering in the Raman-Nath regime (see Sec. 2.2.2) and predict substantial sensitivity enhancements due to the multi-mode character of such a setup. In our case, we proceed by formally conditioning the output state $|\psi^{\text{out}}\rangle$ on those trajectories, which spatially overlap with the main interferometer arms at $t = 2T$. A suitable projection on the respective subspace $D := \{a(17), 18, 19, b(20)\}$ is given by

$$|\tilde{\psi}_D^{\text{out}}\rangle = \mathbb{P}_D |\psi^{\text{out}}\rangle \quad , \quad \text{where} \quad \mathbb{P}_D = \int_{-\hbar k/2}^{\hbar k/2} dp \sum_{j \in D} |q_j\rangle_j \langle q_j|. \quad (3.57)$$

After renormalizing the result, $|\psi_D^{\text{out}}\rangle := |\tilde{\psi}_D^{\text{out}}\rangle / \|\tilde{\psi}_D^{\text{out}}\|$, we obtain the single particle quantum Fisher information with respect to the pure state,

$$F_Q := 4 \|\tilde{\psi}_D^{\text{out}}\|^2 \left(\langle \tilde{\psi}_D^{\text{out}} | \dot{\tilde{\psi}}_D^{\text{out}} \rangle - |\langle \tilde{\psi}_D^{\text{out}} | \psi_D^{\text{out}} \rangle|^2 \right) , \quad \text{where} \quad |\dot{\psi}_D^{\text{out}}\rangle \equiv \frac{d|\psi_D^{\text{out}}\rangle}{d\phi}. \quad (3.58)$$

Here, we account for the loss of information due to transitions outside of the trajectories contained in subspace D via the norm $\|\tilde{\psi}_D^{\text{out}}\| \leq 1$. Calculating the QCRB in analogy to Eq. (3.13), we make use of the additivity of F_Q for uncorrelated particles,

$$\Delta\phi_{\text{QCRB}} = \frac{1}{\sqrt{N_{\text{atoms}}}} \frac{1}{\sqrt{F_Q}}. \quad (3.59)$$

In the limit of vanishing momentum width, we find a simple analytical expression for the quantum Fisher information

$$\lim_{\sigma_p \rightarrow 0} F_Q = n^2 \left[1 - \frac{\Gamma}{2}(1 + \cos(\Theta_{M,n-2})) \right] - 2\Gamma(n-1)(1 - \cos(\Theta_{M,n-2})) + \mathcal{O}[\gamma^2, \Gamma^2], \quad (3.60)$$

where we have suppressed higher-order LZ terms. Although this result shows that the QFI depends on the reflectivity of the mirror pulse for the spurious Bragg order, since the second term in Eq. (3.60) arises due to inferences with the parasitic arms in case of

$\Theta_{M,n-2} \in [0, 2\pi)$, modest LZ losses still lead to a decrease in phase sensitivity, regardless of the chosen measurement type or the working point, ϕ_0 . This is in contrast to related statements made in Ref. [147], where the authors suggested that a locally increased signal slope compared to the two-mode case in Eq. (3.2) could result in a net benefit for phase estimation. Finite velocity effects, on the other hand, affect the QCRB in the same way as they affect the CRB via a reduction of the norm $\|\tilde{\psi}_D^{\text{out}}\|$.

3.7.2 Statistical Uncertainty $\Delta\phi^{\text{est}}$

We proceed with the derivation of the phase estimation uncertainty $\Delta\phi^{\text{est}}(\phi_0)$. Because we rely on the method of moments to infer the phase ϕ_0 from changes in the statistical properties of the relative atom number measurements, following Eq.(3.9b), we must evaluate

$$\Delta\phi^{\text{est}}(\phi_0) = \frac{\Delta\hat{P}_a(\phi_0)}{\sqrt{N_{\text{atoms}}} |\partial_\phi \langle \hat{P}_a \rangle|_{\phi_0}} = \frac{\sqrt{\langle \hat{P}_a^2 \rangle(\phi_0) - \langle \hat{P}_a \rangle^2(\phi_0)}}{\sqrt{N_{\text{atoms}}} |\partial_\phi \langle \hat{P}_a \rangle|_{\phi_0}}. \quad (3.61)$$

We restrict the operator \hat{P}_a defined in Eq. (3.4) to measurements of states with non-vanishing occupation numbers in ports a and b respectively. We have explained in Sec. 3.2.1 that the phase uncertainty is proportional to $N_{\text{atoms}}^{-1/2}$, but in experiments the number of uncorrelated particles entering the interferometer is fluctuating from shot to shot [171]. When the atom numbers N_{atoms} are statistically distributed, losses to modes $|q_j\rangle_j$ not being detected after the final beam splitter will affect the uncertainty $\Delta\hat{P}_a$. We model this by assuming that the initial state prepared on the input trajectory, $j = 1$, as shown in Fig. 3.2, is in a Poissonian mixture of number states $|l\rangle$,

$$\rho^{\text{in}} = e^{-N_{\text{atoms}}} \sum_{l=0}^{\infty} \frac{(N_{\text{atoms}})^l}{l!} |l\rangle\langle l|_{\text{in},1} = \frac{1}{2\pi} \int_0^{2\pi} d\theta |\sqrt{N_{\text{atoms}}} e^{i\theta}\rangle \langle \sqrt{N_{\text{atoms}}} e^{i\theta}|_{\text{in},1}. \quad (3.62)$$

Here, we have suppressed all other input modes that are assumed to be vacuum modes and interpret N_{atoms} for the remainder of this chapter as the mean number of atoms entering the interferometer. In the second equation we have exploited the fact that ρ^{in} can also be written as a phase averaged mixture of coherent states, following the work of *S. Haine and M. T. Johnsson* in Ref. [172]. The states $|\sqrt{N_{\text{atoms}}} e^{i\theta}\rangle$ in Eq. (3.62) are Glauber coherent states [173], $|\alpha\rangle \equiv e^{-|\alpha|^2} \sum_l \frac{\alpha^l}{\sqrt{l!}} |l\rangle$, with amplitude $\alpha = \sqrt{N_{\text{atoms}}} e^{i\theta}$.

We remark that when evaluating the statistics of the relative atom number measurement in Eq. (3.61), the effects of finite velocity detuning must be taken into consideration and that the experimentally determined atom numbers are averages over the finite Gaussian momentum spread $g(p, \sigma_p)$ of the initial state $|\psi^{\text{in}}\rangle$ given in Eq. (3.15). We do this by

expanding the annihilation and creation operators of the input modes in their respective mode functions depending on the (quasi)-momentum p ,

$$\hat{a}_{\text{in},1} = \int_{-\hbar k/2}^{\hbar k/2} dp g(p, \sigma_p) \hat{\Psi}_{\text{in},1}(p), \quad (3.63)$$

where $[\hat{\Psi}_{\text{in},1}(p), \hat{\Psi}_{\text{in},1}^\dagger(\bar{p})] = \delta(p - \bar{p})$ and $[\hat{a}_{\text{in},1}, \hat{a}_{\text{in},1}^\dagger] = 1$. We can describe the action of the transfer matrix in Eq. (3.19) on this state by first denoting the input-to-output relation of the operators in Eq. (3.63),

$$\hat{\Psi}_{\text{out},j}(p) = [\mathcal{I}_{\text{MZ}}(p)]_{j,1} \hat{\Psi}_{\text{in},1}(p), \quad (3.64)$$

which allows us to describe the unitary evolution of the MZ interferometer in the Heisenberg picture. Here, we again neglect all unoccupied input modes on the right-hand side of Eq. (3.64) as they will not contribute to a measurement of the occupation numbers in the output ports of the interferometer. The propagated and normalized annihilation operator for measurements in the main output port a then becomes

$$\hat{a}_j \equiv \hat{a}_{\text{out},j} = \frac{1}{\nu_j} \int_{-\hbar k/2}^{\hbar k/2} dp g(p, \sigma_p) [\mathcal{I}_{\text{MZ}}(p)]_{j,1} \hat{\Psi}_{\text{in},1}(p), \quad (3.65)$$

with a normalization factor

$$\nu_j(\phi) := \left(\int_{-\hbar k/2}^{\hbar k/2} dp |g(p, \sigma_p)|^2 |[\mathcal{I}_{\text{MZ}}(p)]_{j,1}|^2 \right)^{\frac{1}{2}}. \quad (3.66)$$

In reference to Eq. (3.61) we continue to use the shorthand notation $\hat{a}^{(\dagger)} \equiv \hat{a}_{\text{out},17}^{(\dagger)}$ and $\hat{b}^{(\dagger)} \equiv \hat{a}_{\text{out},20}^{(\dagger)}$, when referring to measurements in the main ports a and b as labeled in Fig. 3.2. With the help of the input-output relation in Eq. (3.65), we obtain the output density operator for the input in Eqs. (3.62),

$$\rho^{\text{out}} = \mathcal{S}_{\text{MZ}} \rho^{\text{in}} \mathcal{S}_{\text{MZ}}^\dagger = \frac{1}{2\pi} \int_0^{2\pi} d\theta \bigotimes_{j=1}^{36} |\nu_j(\phi)\sqrt{N_{\text{atoms}}}e^{i\theta}\rangle_{\text{out},j} \langle \nu_j(\phi)\sqrt{N_{\text{atoms}}}e^{i\theta}|_{\text{out},j}, \quad (3.67)$$

where the normalizations $\nu_j(\phi) \equiv \nu_j(\phi, T, \Omega_{\text{BS}}, \tau_{\text{BS}}, \Omega_{\text{M}}, \tau_{\text{M}}, \sigma_p)$ crucially depend on the matrix representation of the MZ interferometer in Eq. (3.19), since they contain dependencies of the output on the experimental parameters and in particular the interferometric phase ϕ . We calculate the statistics of the relative atom number measurements in the main ports according to Eq. (3.65) with respect to this output state by reformulating \hat{P}_a in Eq. (3.4) in the limit of non-vanishing occupation numbers

$$\hat{P}_a = \frac{\hat{a}^\dagger \hat{a}}{\hat{a}^\dagger \hat{a} + \hat{b}^\dagger \hat{b}} = \int_0^1 dx \left[\frac{\partial}{\partial x} x^{\hat{a}^\dagger \hat{a}} \right] \otimes [x^{\hat{b}^\dagger \hat{b}}], \quad (3.68)$$

and similarly for port b . With this and Eq. (3.67) we find

$$\begin{aligned} \langle \hat{P}_a \rangle (\phi) &= \text{tr}\{\rho^{\text{out}}(\phi) \hat{P}_a\} \\ &= \int_0^1 dx \left(\frac{\partial}{\partial x} \langle \nu_a(\phi) \sqrt{N_{\text{atoms}}} |x^{\hat{a}^\dagger \hat{a}} \nu_a(\phi) \sqrt{N_{\text{atoms}}}\rangle \right) \langle \nu_b(\phi) \sqrt{N_{\text{atoms}}} |x^{\hat{b}^\dagger \hat{b}} \nu_b(\phi) \sqrt{N_{\text{atoms}}}\rangle \\ &= N_{\text{atoms}} |\nu_a(\phi)|^2 e^{-N_{\text{atoms}} (|\nu_a(\phi)|^2 + |\nu_b(\phi)|^2)} \int_0^1 dx \left(e^{x N_{\text{atoms}} (|\nu_a(\phi)|^2 + |\nu_b(\phi)|^2)} \right), \end{aligned} \quad (3.69)$$

where we have made use of the relations $|\langle \alpha|0\rangle|^2 = e^{-|\alpha|^2}$ as well as $\langle \alpha|x^{\hat{a}^\dagger \hat{a}}|\alpha\rangle = e^{-|\alpha|^2} e^{x|\alpha|^2}$ in the last line. Identifying the absolute atom numbers as defined in Eq. (3.28),

$$N_j(\phi) = N_{\text{atoms}} |\nu_j(\phi)|^2 = N_{\text{atoms}} \int_{-\hbar k/2}^{\hbar k/2} dp |g(p, \sigma_p)|^2 |[\mathcal{I}_{\text{MZ}}^*(p)]_{j,1}|^2, \quad (3.70)$$

and taking the limits $N_{\text{atoms}} |\nu_a(\phi)|^2, N_{\text{atoms}} |\nu_b(\phi)|^2 \gg 1$, the statistical quantities with respect to \hat{P}_a in Eq. (3.63) simplify to

$$\langle \hat{P}_a \rangle (\phi) \approx \frac{N_a(\phi)}{N_a(\phi) + N_b(\phi)} = P_a(\phi), \quad (3.71a)$$

$$\langle \hat{P}_a^2 \rangle (\phi) \approx P_a^2(\phi) + \frac{P_a(\phi) \cdot P_b(\phi)}{N_a(\phi) + N_b(\phi)}. \quad (3.71b)$$

Inserting both results into Eq. (3.61) we arrive at an expression for the statistical uncertainty of phase estimates performed in port a ,

$$\Delta\phi^{\text{est}}(\phi_0) = \frac{\sqrt{\langle \hat{P}_a^2 \rangle (\phi_0) - \langle \hat{P}_a \rangle^2 (\phi_0)}}{|\partial_\phi \langle \hat{P}_a \rangle|_{\phi_0}} = \sqrt{\frac{P_a(\phi_0) \cdot P_b(\phi_0)}{N_a(\phi_0) + N_b(\phi_0)}} \frac{1}{|\partial_\phi P_a(\phi)|_{\phi_0}}. \quad (3.72)$$

We emphasize that, in general, this result differs significantly from the projection noise of an ideal two-mode MZ Bragg interferometer. However, as expected, it approaches this case in the adiabatic limit $\gamma, \Gamma \rightarrow 0$.

3.7.3 Phase Uncertainty for Fifth-order Bragg Diffraction

To complete our study of the model for $P_a(\phi)$ in Eq. (3.50), we benchmark the statistical uncertainty in Eq. (3.72) comparing it against the CRB and the QCRB. We determine $\Delta\phi^{\text{est}}(\phi_0)$ by first calibrating the waveform $P_a(\phi)$ as before to numerical simulations of the MZ interferometer, and extract the total atom numbers $N_a(\phi) + N_b(\phi)$ from the numerical data. It is important to remember that both the phase uncertainty as well as the CRB (3.55) are local quantities. Therefore, we select the mid-fringe working point $\phi_0 = \frac{3\pi}{2} \frac{1}{5}$ to optimize performance when we plot both quantities for the MZ interferometer of type (B) in

Fig. 3.11, while in the inset we show the same information for type (A). For both scenarios we assume the same range of beam splitter parameters already considered in Fig. 3.9.

First of all, we observe that the phase uncertainty of our model agrees well with the CRB and the QCRB. The visible deviations are on a level to be expected due to our perturbative treatment of finite velocity effects, cf. the corresponding discussion in Sec. 2.7. We show the phase sensitivity in Fig. 3.11 scaled to $n\sqrt{N_{\text{atoms}}}$, i.e., the shot noise limit given by the CRB of an ideal two-mode interferometer with $P_0 = A = 1/2$ [see Eq. (3.10)]. This reveals that the projection noise limit for a Bragg interferometer lies a few percent above this value as already hinted at by Eqs. (3.56a) and (3.60). The increase of the CRB with growing momentum spread σ_p is caused by atom losses due to velocity selectivity of the scattering process, which become stronger for longer pulse durations, as we have already seen in Sec. 2.6.3. In addition, as revealed by our two choices of velocity width, velocity selectivity is reduced for case (B) because of the comparatively short mirror pulse duration [see the inset of Fig. 3.3(a)]. The loss of sensitivity at shorter beam splitter pulse durations is due to the increasing non-adiabaticity of Bragg diffraction and the associated diffraction losses as we show in Fig. 3.4. Interestingly, there is no discernible difference in performance between either configuration in this regime despite deliberately deflecting atoms out of the interferometer in scenario (B), see Fig. 3.5(B). The reason being that Bragg diffraction losses primarily populate parasitic interferometers with scale factors smaller than the main diffraction order $n = 5$ in this case. In consequence, their contributions effectively decrease the space-time area and thus increase the statistical uncertainty of the phase measurement, which is ultimately confirmed by the quantum Fisher information in Eq. (3.60). Overall, best sensitivity is achieved at the local minimum of beam splitting losses from the main diffraction orders $\pm 5\hbar k$, cf. Fig. 3.9(c). This sets the fundamental projection noise limit of a Bragg atom interferometer.

Figure 3.11(b) depicts the same quantities as before but for the alternative mid-fringe position $\phi_0 = \frac{\pi}{2} \frac{1}{5}$. We have already seen that for $\phi_0 = (4m + 1) \cdot \pi/(2n)$ with $m \in \mathbb{Z}$ there is a difference in signal slope, which directly effects the phase sensitivity of the atom number measurement according to Eqs. (3.56b) and (3.72). This is confirmed by the results in Fig. 3.11(b), which show that both the phase uncertainty and the CRB perform worse by several percent, especially near the LZ maximum. Therefore, and in contrast to the two-mode case (3.10) in the presence of non-negligible scattering to spurious diffraction orders, the projection noise and the projection noise limit are increased for those mid-fringe positions. As mentioned before, we remark that this effect is dominated by the appearance of the higher harmonics in the signal $P_a(\phi)$ defined in Eq. (3.50). Thus, it could be less apparent if the signal ϕ is subject to fluctuations such as phase noise of the Bragg lasers, e.g., caused to vibrations of a retro-reflecting mirror [94].

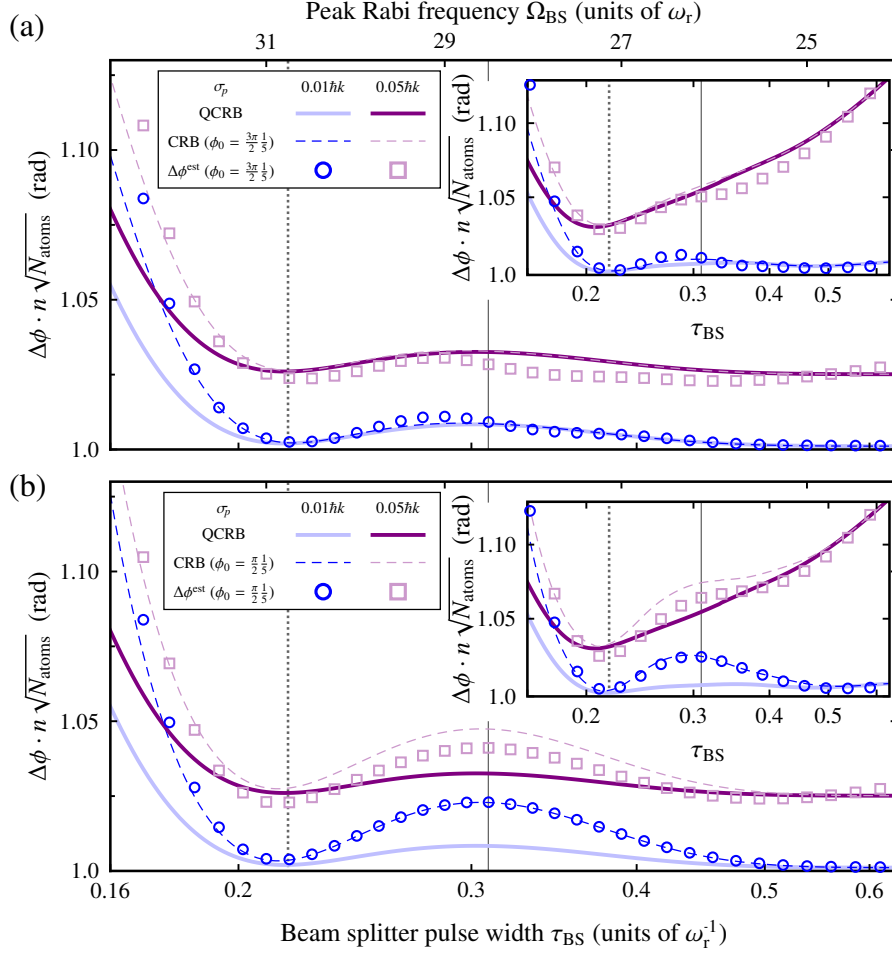


Figure 3.11: **Sensitivity bound of multiport Bragg interferometers with uncorrelated particles.** We show the QCRB (solid lines), the CRB (dashed lines), as well as the statistical uncertainty $\Delta\phi^{\text{est}}(\phi_0)$ based on Eq. (3.50) applied to numerical simulations (symbols) for configuration (B) of a fifth-order Bragg MZ interferometer. Configuration (A) is shown in both insets respectively. Both the CRB and $\Delta\phi^{\text{est}}(\phi_0)$ assume mid-fringe positions (a) $\phi_0 = \frac{3\pi}{5}$ and (b) $\phi_0 = \frac{\pi}{5}$. Upon scanning $\Omega_{\text{BS}}, \tau_{\text{BS}}$ we suppress the dominant parasitic interferometry paths using the pulse parameters $\Omega_{\text{M}}, \tau_{\text{M}} = 31.8 \omega_r, 0.463 \omega_r^{-1}$. Both bounds are shown for the momentum spread $\sigma_p = 0.01 \hbar k$ ($0.05 \hbar k$) in blue (purple) and multiplied by the inverse of the projection noise limit of an ideal two-mode MZ, $n\sqrt{N_{\text{atoms}}}$. We fix the time $T = 10$ ms and we set $\phi_0 = \frac{3\pi}{5}$ in (a) for both the CRB and for $\Delta\phi^{\text{est}}$. Choosing $\Omega_{\text{BS}} = \Omega_{\text{M}}$ [case (A)] suffers from increased finite-velocity Doppler effects. In (b) the CRB and $\Delta\phi^{\text{est}}(\phi_0)$ demonstrate significant deviations from the phase-independent QCRB. Notably, for the parameters around the LZ maximum, the reduced signal slope increases projection noise (see main text).

3.8 Conclusion and Outlook

In summary, we have presented an analytical model for LMT atom interferometers based on Bragg diffraction, which permits a thorough understanding of their systematic and statistical uncertainties and their fundamental sensitivity bounds. Our model provides design criteria for reaching these bounds and paves the way towards accuracies in the μrad -range using higher-order Bragg diffraction in combination with ultra-cold atomic sources [64,65]. The operation of LMT interferometers at or near the limit of quantum projection noise is a critical requirement if they are to be combined with entangled sources [163, 164]. The methods and techniques developed in this chapter are general and can be applied also to other interferometer topologies, such as the conjugated Ramsey-Bordé interferometer in Ref. [23].

Our work contributes to the development of high-precision quantum sensors for fundamental tests and towards atom interferometers that benefit from improvements in momentum separation (scale factor) and, on the other hand, meet the size, weight, and power (SWaP) requirements of modern real-world applications [54,60], especially in combination with resonator-enhanced light fields [174].

4

Atom Interferometry in a Twin Lattice

4.1 Motivation

The work presented in the previous two chapters is dedicated to developing a deeper understanding of the unique properties of atom interferometers employing higher-order single Bragg diffraction. These and related analyses (cf., e.g., Ref. [135] or Ref. [136] for the case of a double Bragg interferometer) are essential to convert the advantage in phase sensitivity over the much more common standard Raman interferometers [54] into an actual metrological gain. At the same time, our study of the spectrum of the Bragg Hamiltonian (cf. Fig. 2.3 and the surrounding text) provides an intuitive explanation for the increasing demands on the laser power of multiphoton Bragg diffraction [130]. It is one of the main reasons why interferometers using this technique have been limited to a momentum separation of $24 \hbar k$ [103], which is far from the ambitious goals of future LMT interferometer designs featuring separations of one thousand photon recoils or more [37, 38, 40, 175].

While we have explained, that sequential Bragg pulse sequences have successfully overcome this hurdle allowing for separations in the order of $100 \hbar k$ [97, 98], their scalability is limited in three key areas: Duration of the momentum transfer, efficiency of the transfer and susceptibility to noise due to an asymmetric momentum transfer. The maximum separation of $102 \hbar k$ achieved by *S.-w. Chiow* et al. [97] was limited by a loss of $\sim 90\%$ of the initial number of atoms despite transferring $\sim 99\%$ of the atoms per recoil simply due to the large number of pulses. The authors *B. Plotkin-Swing* et al. [98] even achieved a separation of $112 \hbar k$ in a three-path contrast interferometer, but their results highlight the increasing demands on the stability of the laser intensity in asymmetric geometries due to the detrimental role of diffraction phases caused by intensity fluctuations [98, 116, 119]. In theory, double diffraction techniques seem to offer an obvious solution to those challenges, since addressing both arms of the interferometer simultaneously not only doubles the momentum transfer, but ideally also makes the device more robust against temporal fluctuations of the light fields. That said, current implementations of double Bragg [94, 105, 132] and double

Raman diffraction [176, 177] have been limited to separations of eight photon recoils. In particular, scalability of double Bragg diffraction (DBD) appears to be hampered by couplings to undesired diffraction orders and finite velocity effects, as we have discussed in the previous two chapters, but to a greater extent than for the single-Bragg implementation [132, 136]. This places stringent requirements on the atomic source.

Bloch oscillations (BO) [106–108] on the other hand have shown to transfer more than $\sim 1000 \hbar k$ in interferometers used for state-of-the-art metrology experiments [24], reporting efficiencies beyond 99.9 % per recoil with laser-cooled sources [178, 179]. Instead of pulsing an optical lattice potential moving at a constant velocity relative to the atoms, the comoving optical potential is first slowly ramped up to trap the atoms and then adiabatically accelerated. In proof-of-principle experiments where BO were used to levitate a superposition of atoms against gravity, successful transfer of tens of thousands of photons has been achieved before coherence was lost in a cavity environment of small volume [87, 88]. Symmetric acceleration of both interferometry arms, of course, mitigates this problem to a considerable extent [180], so that the above and other experiments [23, 85, 86, 109, 181, 182] have been able to take advantage of BO albeit without increasing the separation between the arms. At the time of writing, the achievable momentum separation with an asymmetric LMT beam splitter combining BO with an initial Bragg pulse has been limited to $80 \hbar k$ [111]. In summary, BO clearly provide scalability for future LMT applications, but long interaction times with the optical potentials needed for efficient pulse transfer place even greater demands on the control of differential light shifts [88, 110].

Combining BO with the robustness against temporal laser intensity fluctuations and phase noise inherent to the double diffraction geometries mentioned above, recent realizations of dual-lattice interferometry promise to solve this challenge for next-generation LMT beam splitting. *Z. Pagel* et al. [142] demonstrated a pure Bloch-based interferometer featuring coherent momentum splittings of up to $240 \hbar k$ via two independently controlled optical lattices. It is particularly intriguing how the authors exploit the momentum parity symmetry of the dual-lattice Hamiltonian¹ to successfully split and recombine matter waves via adiabatic BO. State-of-the-art momentum separation of up to $408 \hbar k$ was recently achieved in the QUANTUS-1 experiment using twin-lattice interferometry. This achievement was made possible by three key components [96]: (i) A combination of DBD and BO that enables efficient transfer of hundreds of photon recoils. (ii) A "twin-lattice" setup with two identical optical lattice potentials, which counterpropagate horizontally (here in the y -direction) and whose symmetry ideally suppresses many of the systematic effects mentioned earlier. (iii) The use of well-collimated BEC sources [65] improving the efficiency of the Bragg pulses. All of these factors contribute to a high contrast and improve the signal

¹The formalism used in Ref. [142] to understand the time evolution in a dual lattice is closely related to the symmetric and antisymmetric states introduced in Chapter 2 of this work.

to noise ratio of the LMT atom interferometer [79, 89, 183]. The purpose of this chapter is to provide insight into the current limitations of the experiment, an understanding of which is critical to assessing the scalability of this technique to momentum separations in the order of one thousand photon recoils and beyond. In this sense, our results serve to promote a deeper understanding of coherence loss in dual-lattice interferometry in general and are already partially contained in Ref. [96]. The theoretical work presented here serves as a complement to the experimental efforts within the QUANTUS project.

We begin this chapter with an overview of the basic properties of BECs that are used as an atomic source in the QUANTUS-1 experiment. Then, in Sec. 4.3, we derive the twin-lattice potential assuming an idealized retroreflective geometry and briefly review the key beam-splitting techniques, namely DBD and BO, both of which are implemented using the same optical potential. In this context, we introduce non-adiabatic LZ transitions and spontaneous emission as the main sources of atom loss during adiabatic acceleration of atoms in moving optical lattices. Before analyzing the experimental data, we take a quick look at the realization of the interferometer in the QUANTUS-1 apparatus in Sec. 4.4, which will give us valuable insight into the potential experimental imperfections affecting the results. In Sec. 4.4.2, we commence our analysis by modeling the measured acceleration efficiencies recorded at the beginning of the beam-splitting sequence, which show significant deviations compared to the predictions of LZ theory for a single lattice. We find that the reason is not the second lattice, but a spurious standing lattice potential caused by an error in the polarization of the light fields. By comparing the measurements to numerical solutions of the Gross-Pitaevskii equation (GPE), we confirm this and determine the magnitude of the error, which is in line with independent experimental observations. Furthermore, we show that the generation of a larger initial momentum separation via sequential double Bragg pulses is an effective mitigation strategy.

After an introduction to the full twin lattice sequence in Sec. 4.4.3 and an assessment of the potential sensitivity to inertial forces offered by this scheme, we then turn to the main topic of this chapter: The experimentally observed decay of the interferometric contrast in Sec. 4.4.4, which is a measure of the loss of coherence with increasing momentum separations. Our findings, which are the result of theoretical modeling of the contrast decay in Secs. 4.5 and 4.6, provide strong evidence that its origin is a two-fold one: On the one hand, contrast is lost due to inefficiencies in the DBD, resulting in the detection of an incoherent fraction of atoms in the output ports of the interferometer. On the other hand, local intensity fluctuations, most likely originating from diffraction of the twin-lattice beam, affect the trajectories of the atoms via the dipole force, causing the interferometer to not properly close and leading to a dephasing of the ensemble. In Sec. 4.7, our analysis shows good agreement with the experimental results, suggesting that the scalability of the twin-lattice interferometer is primarily limited by the imperfection of the light field in the

current implementation. Therefore, we conclude in Sec. 4.7 that twin-lattice interferometry is a suitable technology for beyond state-of-the-art atom interferometry separating BECs, potentially by more than one thousand photon recoils.

4.2 Bose-Einstein Condensates

Before presenting the twin-lattice beam splitter sequence in the next section, it is useful to take a closer look at the atomic sources whose properties enable higher sensitivities via LMT or very long interrogation times or both. So far, we have only assumed that the momentum spread of the atoms in the direction of the optical lattice is small compared to the photon recoil, $\sigma_p \ll \hbar k$, to ensure efficient Bragg operations (cf. Sec. 2). In fact, however, a small velocity width and the associated low expansion rates offer a number of advantages, especially when considering realistic three-dimensional laser beams with finite radii and limited laser power. They range from the ability to perform efficient atom optics even after seconds of interrogation time [88, 184] to reduced susceptibility to many systematic effects [89], some of which are due to inhomogeneities of the optical potentials [85, 86, 88, 179].

In recent years, in addition to the development of improved atomic sources based on laser-cooled atoms [71, 77], efforts have been made to exploit the special properties of BECs for atom interferometry [79, 80, 185]. The potential of BECs lies in the fact that they represent a coherent quantum state of matter that can be described by a single-particle wave function (see below). Along with their coherence properties [186, 187] comes the ability to generate ensembles with extremely low momentum widths and small sizes, especially when combined with lensing techniques such as delta-kick collimation [64, 65, 80, 188]. Moreover, BECs provide the unique opportunity to increase the interferometry sensitivity by preparing and manipulating non-classical input states [72, 73] to overcome the standard quantum limit, which scales with the number of uncorrelated atoms $N_{\text{atoms}}^{-1/2}$ due to atomic projection noise. However, both the generally lower flux of state-of-the-art condensed sources [63] and the effect of interparticle interactions [79, 185] have so far prevented widespread adaptation of BECs for atom interferometry (see Tab. I in Ref. [54]). Nonetheless, BECs play a central role in the development of next-generation atom interferometers both on Earth [189] and in space [47]. On top of that, the QUANTUS-1 experiment, which we present in more detail in Sec. 4.4, enabled the first realization of BECs in microgravity during a free fall in a drop tower [93]. With the objective of this chapter in mind, to understand the current limitations of twin-lattice interferometry realized in the QUANTUS-1 experiment, it is therefore appropriate to first give a brief overview of BECs and their mathematical description. For a detailed account of the first realizations of BECs

and their description, we kindly refer the reader to Refs. [154, 190]. In particular, we follow the work done by *C. J. Pethick and H. Smith* in their textbook [190].

Bose-Einstein condensation describes the macroscopic occupation of the ground state of a system that is composed of massive particles with integer spin, also known as bosons. They are named after the physicist *S. Bose*, who together with *A. Einstein*, predicted the existence of this previously unknown state of matter derived from statistical arguments [19, 20]. Heuristically speaking, this phenomenon occurs in the so-called regime of "quantum degeneracy", when the temperature T of the thermal ensemble is low enough so that the de Broglie wavelength,

$$\lambda_{\text{dB}} := \sqrt{\frac{2\pi\hbar^2}{Mk_{\text{B}}T}}, \quad (4.1)$$

of the particles with mass M , which also depends on the Boltzmann constant k_{B} , approaches the length scale set by the mean distance between the particles in the atomic gas. In this regime, the localized wave packets start to spatially overlap and interfere to a single wave function describing the entire condensate.

Einstein argued that the lowest energy state of a gas consisting of N noninteracting bosons becomes macroscopically occupied as soon as the temperature T falls below a critical value T_{C} . His observation was based on the fact that the corresponding average occupation number, $\langle n_0 \rangle$, is determined by the Bose statistics [190],

$$\langle n_j \rangle = \frac{1}{e^{(E_j - \mu)/k_{\text{B}}T} - 1}, \quad (4.2)$$

where E_j denotes the energy of the j th state and μ is the chemical potential. In free space (and in the thermodynamic limit $N \rightarrow \infty$) this is marked by a sudden phase transition, whereas the coherent fraction increases smoothly for trapped ensembles. In addition, both the occupation numbers $\langle n_j \rangle$ and the critical temperature T_{C} are functions of the trapping potential as they depend on the density of states of the system.

Beyond Einstein's arguments for an ideal gas, condensation also occurs in trapped ensembles and in the presence of interparticle interactions. In the case of a three-dimensional harmonic trapping potential

$$V(\mathbf{x}) = \frac{M}{2}(\omega_x^2 x^2 + \omega_y^2 y^2 + \omega_z^2 z^2) \quad (4.3)$$

with trap frequencies ω_{x_j} , where $x_j = x, y, z$, the ground state occupation scales like [190]

$$\langle n_0 \rangle = N \left[1 - \left(\frac{T}{T_{\text{C}}} \right)^3 \right], \quad \text{with} \quad T_{\text{C}} \approx 0.94 \frac{\hbar \bar{\omega}}{k_{\text{B}}} N^{1/3}. \quad (4.4)$$

The second equation shows that T_{C} is a function of the geometric mean of the trapping frequencies $\bar{\omega} = (\omega_x \omega_y \omega_z)^{1/3}$.

A complete theoretical description of BECs is obtained through the language of quantum field theory, to which, e.g., Ref. [191] provides a good introduction. However, introducing this framework is beyond the scope of this thesis, in particular because in many cases it is sufficient to approximate the correlations between the particles by a mean-field theory and neglect fluctuations of the bosonic field [12].

4.2.1 Gross-Pitaevskii Equation (GPE)

The description via a mean-field theory is particularly useful in the limit of a low particle density ρ , where we have $\rho|a_s|^3 \ll 1$, with the s-wave scattering length a_s [12]. In this regime, the average distance between particles is typically much larger than the range of their effective interaction potential characterized by a_s . As a result, the interaction between two particles can be interpreted as two hard spheres scattering off of each other and their potential becomes contact-like at this point

$$V_{int}(\mathbf{x}, \mathbf{x}') = g_{scat} \delta(\mathbf{x} - \mathbf{x}'). \quad (4.5)$$

Here, $\delta(\mathbf{x} - \mathbf{x}')$ denotes the delta-distribution and the interaction strength between the non-distinguishable bosons is defined according to $g_{scat} = 4\pi\hbar^2 a_s / M$. The Hamiltonian of the system including $V_{int}(\mathbf{x}, \mathbf{x}')$ reads

$$H = \sum_{j=1}^N \left[-\frac{\hbar^2}{2M} (\nabla^2)_{\mathbf{x}_j} + V(\mathbf{x}_j) \right] + g_{scat} \sum_{j<l} \delta(\mathbf{x}_j - \mathbf{x}_l), \quad (4.6)$$

with the differential operator $\nabla = (\partial_x, \partial_y, \partial_z)$ and an additional trapping potential $V(\mathbf{x}_j)$. To find the state vector solving the Schrödinger equation with respect to this Hamiltonian, we perform the Hartree-Fock approximation, which is motivated by the observation that ideally all atoms in the BEC occupy the ground state of the system [12]. In this sense, we write the N-particle state in position representation as the product of identical single-particle wave functions,

$$\Psi(\mathbf{x}_1, \mathbf{x}_2, \dots, \mathbf{x}_N) = \prod_{i=1}^N \varphi(\mathbf{x}_i) \quad \text{with} \quad \int d^3\mathbf{x} |\varphi(\mathbf{x})|^2 = 1, \quad (4.7)$$

where we have abbreviated $d^3\mathbf{x} = dx dy dz$. After introducing the condensate wave function $\psi(\mathbf{x}) = \sqrt{N}\varphi(\mathbf{x})$ with $\int d^3\mathbf{x} |\psi(\mathbf{x})|^2 = N$, one can find the time-independent non-linear Schrödinger equation via minimization of the energy $E(\Psi) = \langle \Psi | H | \Psi \rangle / \langle \Psi | \Psi \rangle$ with respect to the state in Eq. (4.7) [192],

$$\mu\psi(\mathbf{x}) = \left(-\frac{\hbar^2}{2M} \nabla^2 + V(\mathbf{x}) + g_{scat} |\psi(\mathbf{x})|^2 \right) \psi(\mathbf{x}). \quad (4.8)$$

On the left-hand side of this equation is the chemical potential μ of the system, and the interaction term on the right-hand side is proportional to the density of the condensate wave function, $g_{\text{scat}} |\psi(\mathbf{x})|^2$, thus providing the coupling to the mean-field potential. Generally, Eq. (4.8) is known as the time-independent Gross-Pitaevskii equation (GPE) and determines the stationary state of the condensed ensemble. The time evolution of the BEC, on the other hand, is determined by the time-dependent GPE

$$i\hbar \frac{\partial \psi(\mathbf{x}, t)}{\partial t} = \left(-\frac{\hbar^2}{2M} \nabla^2 + V(\mathbf{x}, t) + g_{\text{scat}} |\psi(\mathbf{x}, t)|^2 \right) \psi(\mathbf{x}, t). \quad (4.9)$$

In case of time-independent Hamiltonians, it is possible to obtain the time-independent GPE from Eq. (4.9) by making the separation ansatz,

$$\psi(\mathbf{x}, t) = \psi(\mathbf{x}) e^{-i\mu t/\hbar}. \quad (4.10)$$

Finding solutions $\psi(\mathbf{x}, t)$ that solve the GPE and determining the ground state of the BEC in a given potential via Eq. (4.8) typically requires numerical calculus in form of the split-operator method [170] and imaginary time propagation. The former is the same method we have employed to solve the one-dimensional Schrödinger equation with respect to the Bragg Hamiltonian in Eq. (2.8) for non-interacting particles following Ref. [169] in the previous chapter.

4.2.2 Effective One-dimensional GPE

However, solving the time-dependent GPE in Eq. (4.9) in three dimensions can quickly become computationally too expensive. This is especially true when interparticle interactions are important and or if fine spatial structures like the wells of an optical lattice potential (in the order of the laser wavelength λ_L) must be resolved (cf. Tab. 1 in Ref. [169]). In Sec. 4.4.2, we will compare numerical solutions of the dynamics of a BEC being accelerated in a twin-lattice potential to the implementation in the QUANTUS-1 experiment. Since in this context we are primarily interested in the dynamics of the system in the axial direction of the twin-lattice laser beam, we resort to an effective one-dimensional description [193]. Additionally, this significantly relaxes the computational complexity of the problem. This method implies that the time scales dominating the dynamics of the problem differ substantially between the axial and radial directions. This applies, e.g., in the case of cylindrical traps,

$$V(\mathbf{x}) = V(y, t) + \frac{M}{2} (\omega_x^2(t)x^2 + \omega_z^2(t)z^2), \quad (4.11)$$

when the harmonic confinement in the radial directions characterized by the trap frequencies ω_x, ω_z differs significantly from the potential in the y -direction. To exploit the resulting

asymmetry one can make the following separation ansatz for the wave function in three dimensions,

$$\psi(\mathbf{x}, t) = \varphi(y, t) G(x, t; \sigma_x(y, t)) G(z, t; \sigma_z(y, t)). \quad (4.12)$$

Here, the $G(x_j, t; \sigma_{x_j}(y, t))$, with $x_j = x, z$, represent normalized Gaussian functions whose width depends on their axial position

$$G(x_j, t; \sigma_{x_j}(y, t)) = \frac{1}{\sqrt{2\pi}\sigma_{x_j}} e^{-x_j^2/2\sigma_{x_j}^2(y, t)}. \quad (4.13)$$

Usually, this method is applied in situations, where the radial confinement due to the potential in Eq. (4.11) is much stronger in the radial than in the axial direction (cigar-shaped trapping potentials). Nonetheless, we find good agreement between the experimental data and our numerical results using this ansatz in Sec. 4.4.2. It is reasonable to assume, that this is due to the relatively short interaction times paired with the low expansion rates of the BEC and the very weak radial confinement provided by the laser beam. Instead of computing three-dimensional solutions to the time-dependent GPE in Eq. (4.9), we solve a system of three coupled differential equations. For the axial direction we find an effective one-dimensional time-dependent GPE [193]

$$i\hbar \frac{\partial \varphi(y, t)}{\partial t} = \left[-\frac{\hbar^2}{2M} \frac{\partial^2}{\partial y^2} + V(y, t) + \frac{g_{\text{scat}}}{2\pi} \sigma_x^{-1}(y, t) \sigma_z^{-1}(y, t) |\varphi(y, t)|^2 + \frac{\hbar^2}{4M} (\sigma_x^{-2}(y, t) + \sigma_z^{-2}(y, t)) + \frac{M}{4} (\omega_x^2(y, t) \sigma_x^2(y, t) + \omega_z^2(y, t) \sigma_z^2(y, t)) \right] \varphi(y, t), \quad (4.14a)$$

while the transverse widths are determined by differential equations coupled via the density, $|\varphi(y, t)|^2$, with $\int dy |\varphi(y, t)|^2 = N$,

$$0 = \frac{\hbar^2}{2M} - \frac{M}{2} \omega_x^2(y, t) \sigma_x^4(y, t) + \frac{g_{\text{scat}}}{4\pi} \frac{\sigma_x(y, t)}{\sigma_z(y, t)} |\varphi(y, t)|^2, \quad (4.14b)$$

$$0 = \frac{\hbar^2}{2M} - \frac{M}{2} \omega_z^2(y, t) \sigma_z^4(y, t) + \frac{g_{\text{scat}}}{4\pi} \frac{\sigma_z(y, t)}{\sigma_x(y, t)} |\varphi(y, t)|^2. \quad (4.14c)$$

The initial conditions required to solve these coupled differential equations can be derived for a three-dimensional wave function $\psi(\mathbf{x}, t_0)$, e.g., describing the ground state of a trapped ensemble that is subsequently transferred into a potential of the form in Eq. (4.11). The Gaussian widths at the start of the effective dynamics $t = t_0$ are then linked to the spatial variances of the wave function in the radial directions so that $\sigma_{x_j}(y, t_0) = \sigma_{x_j}(t_0)$, where

$$\sigma_x(t_0) = \sqrt{\langle x^2 \rangle - \langle x \rangle^2} = \left(\int d^3\mathbf{x} x^2 |\psi(\mathbf{x}, t_0)|^2 - \left(\int d^3\mathbf{x} x |\psi(\mathbf{x}, t_0)|^2 \right)^2 \right)^{1/2}, \quad (4.15a)$$

$$\sigma_z(t_0) = \sqrt{\langle z^2 \rangle - \langle z \rangle^2} = \left(\int d^3\mathbf{x} z^2 |\psi(\mathbf{x}, t_0)|^2 - \left(\int d^3\mathbf{x} z |\psi(\mathbf{x}, t_0)|^2 \right)^2 \right)^{1/2}. \quad (4.15b)$$

Similarly, the real-valued wave function in the axial direction is the solution of the integral

$$\varphi(y, t_0) = \left(\int dx dz |\psi(\mathbf{x}, t_0)|^2 \right)^{1/2}. \quad (4.16)$$

4.2.3 Thomas-Fermi Approximation

In general, also the ground state wave function of a BEC in a trap satisfying the time-independent GPE (4.8) must be calculated numerically, e.g., via imaginary time evolution. Nevertheless, it is possible to find analytical solutions for the ground state of the BEC that satisfy Eq. (4.8) in certain limits with regards to the interaction term $g_{\text{scat}}|\psi(\mathbf{x})|^2$, when assuming quadratic potentials (4.3). In the weakly-interacting regime, interactions can be neglected and the GPE simply transforms into the linear time-independent Schrödinger equation, the ground state of which is given by the solutions of the three-dimensional harmonic oscillator. At the other extreme there is a situation where the ensemble is thus localized due to the trapping potential that the interparticle distance is much smaller than the characteristic length scale defined by the length of the harmonic oscillator $a_{\text{HO}} = \sqrt{\hbar/M\bar{\omega}}$. This is the case if

$$\frac{N |a_s|^3}{a_{\text{HO}}^3} \gg 1, \quad (4.17)$$

and motivates neglecting the kinetic energy in Eq. (4.8) as it is overpowered by the interaction term

$$\mu\psi(\mathbf{x}) \approx \left(V(\mathbf{x}) + g_{\text{scat}} |\psi(\mathbf{x})|^2 \right) \psi(\mathbf{x}). \quad (4.18)$$

This is the Thomas-Fermi approximation, which provides an algebraic expression for the spatial density distribution of the BEC,

$$|\psi(\mathbf{x})|^2 = \begin{cases} (\mu - V(\mathbf{x})) / g_{\text{scat}} & \text{if } \mu \geq V(\mathbf{x}), \\ 0 & \text{else.} \end{cases} \quad (4.19)$$

For the harmonic potential (4.3) the density has the shape of an inverted parabola

$$|\psi(\mathbf{x})|^2 = \max \left\{ \frac{\mu}{g_{\text{scat}}} \left(1 - \frac{x^2}{R_{x,TF}^2} - \frac{y^2}{R_{y,TF}^2} - \frac{z^2}{R_{z,TF}^2} \right), 0 \right\}, \quad (4.20)$$

where the TF Radii define the distances from the center of the condensate at which the density vanishes. Thus, they can be expressed as

$$R_{x_j,TF} = \sqrt{\frac{2\mu}{M\omega_{x_j}^2}}. \quad (4.21)$$

Moreover, the normalization condition on the condensate wave function $\psi(\mathbf{x})$ lets us find an analytical relationship between the chemical potential μ and the number of particles in the condensate N

$$\mu = \frac{1}{2} \hbar \bar{\omega} \left(\frac{15Na_s}{a_{\text{HO}}} \right)^{2/5}. \quad (4.22)$$

4.3 Twin-lattice Beam Splitting

In Sec. 2.2.1, we have derived the Hamiltonian for single Bragg diffraction (2.8) assuming two counterpropagating light fields [cf. Eq. (2.1)]. However, many sensors based on light-pulse atom interferometry rely on two copropagating laser fields and retroreflection to realize Bragg or Raman pulses [54, 114, 152]. Deriving the two incident light fields from the same laser so that they share a common beam path can help to make the system more robust against temporal fluctuations and spatial inhomogeneities of the laser phase fronts. On top of that, any relative movement between the atoms and the mirror will be imprinted during the atom-light interaction, making the mirror the inertial reference. Thus, many experimental setups exploit the advantages provided by a retroreflective setup as the one sketched in Fig. 4.1(a).

4.3.1 Ideal Twin-lattice Potential

To form two counterpropagating optical lattices in the retroreflected geometry the incident laser light must be composed of at least two frequency components, $2\omega_{\text{L}} \approx \omega_1 + \omega_2$, whose sum can be assumed to be constant in time. If we assume similar but now generally time-dependent detunings as discussed at the start of Chapter 2, i.e., $2\delta(t) = \omega_1(t) - \omega_2(t)$ and $k \equiv k_1 \approx k_2$, we can express the incident and reflected electric fields as

$$\begin{aligned} \mathbf{E}_{\text{in}}(\mathbf{x}, t) &= E_0(\mathbf{x}, t) [\boldsymbol{\varepsilon}_1 \cos(ky - \theta_1(t)) + \boldsymbol{\varepsilon}_2 \cos(ky - \theta_2(t))], \\ \mathbf{E}_{\text{retro}}(\mathbf{x}, t) &= E_0(\mathbf{x}, t) [\boldsymbol{\varepsilon}_2 \cos(-ky - \theta_1(t)) + \boldsymbol{\varepsilon}_1 \cos(-ky - \theta_2(t))]. \end{aligned} \quad (4.23)$$

For simplicity, we have assumed identical electric field amplitudes $E_0(\mathbf{x}, t)$ but allow for general polarization vectors $\boldsymbol{\varepsilon}_1, \boldsymbol{\varepsilon}_2$. The phases of the two running lasers are now determined via time-integrals $\theta_j(t) = \int_0^t dt' \omega_j(t')$ and accumulate the difference

$$\delta\theta(t) := \frac{\theta_1(t) - \theta_2(t)}{2} = \int_0^t dt' \delta(t'). \quad (4.24)$$

Note that the reflected electric field has switched polarizations because the light passes twice through the quarter-wave plate shown in Fig. 4.1(a). The total electric field then

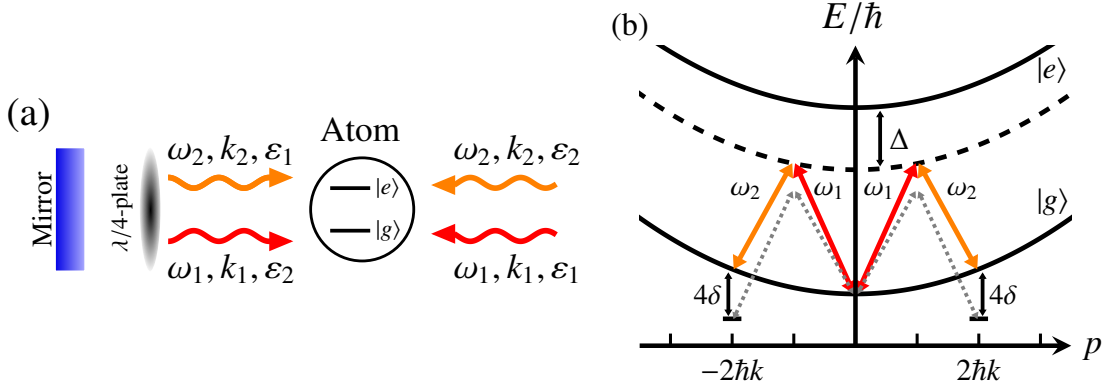


Figure 4.1: **Double Bragg diffraction (DBD) setup.** (a) A two-level atom exposed to two laser frequencies $\omega_1(t)$ and $\omega_2(t)$ and wave numbers $k \equiv k_1 \approx k_2$ in a retroreflective setup. Ideally, the choice of linear polarization and with orthogonal alignment of $\boldsymbol{\varepsilon}_1$ and $\boldsymbol{\varepsilon}_2$ in combination with the $\lambda/4$ -plate (quarter-wave plate) results in two optical lattices propagating in opposite directions. By controlling the lattice power and the frequency difference, $2\delta(t) = \omega_1(t) - \omega_2(t)$, this setup can be used for either DBD or BO. (b) Dispersion for first-order DBD with fixed $\delta(t) = 2\omega_r$ shown in the inertial frame comoving with the optical lattice. Compared to the single-Bragg case in Fig. 2.1(b), the atom-light interaction is ideally described as a three-level system. Outside of the deep-Bragg regime, finite pulse durations give rise to off-resonant couplings modifying the transition probabilities of DBD [94, 132].

reads

$$\begin{aligned} \mathbf{E}(\mathbf{x}, t) &= \mathbf{E}_{\text{in}}(\mathbf{x}, t) + \mathbf{E}_{\text{retro}}(\mathbf{x}, t) \\ &= 2E_0(\mathbf{x}, t) \cos(\omega_L t) [\boldsymbol{\varepsilon}_1 \cos(ky - \delta\theta(t)) + \boldsymbol{\varepsilon}_2 \cos(ky + \delta\theta(t))]. \end{aligned} \quad (4.25)$$

In addition, we again move to a frame corotating with the laser frequency ω_L and perform the rotating wave approximation with respect to fast oscillating terms $\propto \exp(\pm 2i\omega_L t)$. This provides us with an effective dipole potential seen by the atom that is proportional to the resulting intensity of the light field,

$$\begin{aligned} \tilde{I}(\mathbf{x}, t) = |\tilde{\mathbf{E}}(\mathbf{x}, t)|^2 &= |E_0(\mathbf{x}, t)|^2 \left[|\boldsymbol{\varepsilon}_1|^2 \cos^2(ky - \delta\theta(t)) + |\boldsymbol{\varepsilon}_2|^2 \cos^2(ky + \delta\theta(t)) \right. \\ &\quad \left. + 2|\boldsymbol{\varepsilon}_1^* \cdot \boldsymbol{\varepsilon}_2| \cos(ky - \delta\theta(t)) \cos(ky + \delta\theta(t)) \right], \end{aligned} \quad (4.26)$$

where the effective field in the corresponding interaction picture is²

$$\tilde{\mathbf{E}}(\mathbf{x}, t) = E_0(\mathbf{x}, t) [\boldsymbol{\varepsilon}_1 \cos(ky - \delta\theta(t)) + \boldsymbol{\varepsilon}_2 \cos(ky + \delta\theta(t))]. \quad (4.27)$$

Ideally, the normalized polarization vectors of both frequency components are orthogonal, i.e., $|\boldsymbol{\varepsilon}_1^* \cdot \boldsymbol{\varepsilon}_2| = 0 = |\boldsymbol{\varepsilon}_2^* \cdot \boldsymbol{\varepsilon}_1|$, which immediately yields the twin-lattice potential

$$V^{\text{twin}}(\mathbf{x}, t) = 2\hbar\Omega(\mathbf{x}, t) \left[\cos^2(k(y - y_L(t))) + \cos^2(k(y + y_L(t))) \right]. \quad (4.28)$$

²The factor 2 in Eq. (4.25) cancels performing the rotating wave approximation, cf. Eq. (2.7).

Here, we have introduced the time-dependent shift in position

$$y_L(t) = \int_0^t dt' v_L(t') = \delta\theta(t)/k, \quad (4.29a)$$

so that we can write in turn

$$v_L(t) = \dot{y}_L(t) = \frac{(\delta\dot{\theta})(t)}{k} = \frac{\delta(t)}{k}, \quad (4.29b)$$

using the notation $\dot{f}(t) = df(t)/dt$. From Eq. (4.26) it is clear that the alignment of the polarization vectors of the light fields plays a crucial role in the effective potential in the experiment, and we will discuss how imperfect polarization can affect the beam-splitting sequence in Sec. 4.4.1. Meanwhile, the depth of the optical lattice is a function of the two-photon Rabi frequency $\Omega(\mathbf{x}, t) = \Omega_{\text{eg}}^2(\mathbf{x}, t)/2\Delta$, which in turn depends on the detuning from the atomic resonance as well as the electric field strength $E_0(\mathbf{x}, t)$, see Eq. (2.4). Although the setup in Fig. 4.1(a) gives rise to a twin lattice, it is also generally used in experiments to perform single diffraction, which is enabled by a suitable constant relative velocity between atoms and the optical lattices. When the atoms are in free fall in a fountain experiment [95, 114, 152] and possess a velocity v_0 ³, the Bragg condition with respect to the relative velocities [cf. Eq. (2.10)], $|v_0 - \delta/k| = n\hbar k/M$, is only fulfilled for one of the lattices. This lattice thus drives the n th-order Bragg pulse, as we explain in Chapter 2, while the Doppler shift for the other one is too large to play a role for the momentum transfer. Nonetheless, it is possible to realize symmetric momentum transfer with both lattices if the relative velocity between the atoms and the retroreflective mirror vanishes in the direction of the lattice beams. This can be achieved, e.g., in a microgravity environment, in horizontal setups on Earth with gravity acting perpendicularly to the direction of the wave vectors of the light fields or by adding additional frequency components to the light field (see, e.g., Refs. [142, 177]). The latter is the situation we are going to analyze in the following sections in the context of the QUANTUS-1 experiment. But first, we give an overview of the beam splitting techniques employed in the experimental sequence using the twin-lattice potential in Eq. (4.28), namely DBD and BO.

4.3.2 Brief Review of Double Bragg Diffraction (DBD)

Both single Bragg and double Bragg pulses diffract atoms from time-dependent optical lattices via multiphoton transitions without changing their internal state. Hence, these methods share many advantageous characteristics such as a reduced sensitivity to external field fluctuations. Unlike single diffraction, however, a double diffraction pulse can

³In this case the setup in Fig. 4.1 is aligned vertically via rotation by $\pm 90^\circ$.

drive simultaneous transitions between the initial state and two momentum states in opposite directions, as we show in Fig. 4.1(b). In the context of an atom interferometer, this allows, first, a doubling of the achievable momentum separation per pulse. Second, the inherent symmetry of the diffraction process ideally makes this method more robust against laser phase noise. DBD has first been realized in 2016 [94, 105] and an in-depth analysis of the related studies performed in the QUANTUS-1 experiment can be found in Ref. [194]. In addition, the authors *E. Giese* et al. [132] were the first to provide a comprehensive analytical description of the atom-light interaction in their work of which we briefly report some results in the following.

In contrast to the adiabatic two-level dynamics of single Bragg pulse discussed in Chapter 2, the time evolution of DBD is characterized by diabatic transitions between at least three momentum eigenstates. We illustrate in Fig. 4.1(b) that a double Bragg pulse dominantly couples those states forming a three-level system. Due to additional off-resonant transitions this picture is only exact in the deep-Bragg regime, where long pulse durations lead to sharp resonance conditions. Importantly, the nature of the three-level system changes the roles of beam splitters and mirrors compared to the single-diffraction case. We illustrate this briefly for the example of a first-order double Bragg pulse acting on an atom at rest (in the lab frame) with vanishing momentum width: First, we express the state vector $|\psi(t)\rangle$ in the three-level system as a linear combination of states $|0\rangle$, $|\pm 2\hbar k\rangle$,

$$|\psi(t)\rangle = c_{-2\hbar k}(t) |-2\hbar k\rangle + c_0(t) |0\rangle + c_{2\hbar k}(t) |2\hbar k\rangle. \quad (4.30)$$

Assuming the twin-lattice potential (4.28) is switched on instantaneously with a constant Rabi frequency $\Omega(\mathbf{x}, t) = \Omega$ at $t = 0$ and a fixed suitable detuning $\delta(t) = 2\omega_r$ is selected, the coefficients in Eq. (4.30) obey the equation

$$\begin{pmatrix} c_{-2\hbar k}(t) \\ c_0(t) \\ c_{2\hbar k}(t) \end{pmatrix} = \Lambda_{\text{DBD}}(\Omega, t) \begin{pmatrix} c_{-2\hbar k}(0) \\ c_0(0) \\ c_{2\hbar k}(0) \end{pmatrix}. \quad (4.31)$$

Accordingly, the time evolution in the deep-Bragg regime is described by the matrix⁴

$$\begin{aligned} \Lambda_{\text{DBD}}(\Omega, t) = & \cos\left(\frac{\sqrt{2}\Omega t}{2}\right) \mathbb{1} + \frac{1}{2} \left[1 - \cos\left(\frac{\sqrt{2}\Omega t}{2}\right) \right] \begin{pmatrix} 1 & 0 & -1 \\ 0 & 0 & 0 \\ -1 & 0 & 1 \end{pmatrix} \\ & + \frac{i}{\sqrt{2}} \sin\left(\frac{\sqrt{2}\Omega t}{2}\right) \begin{pmatrix} 0 & e^{i2\phi_L} & 0 \\ e^{-i2\phi_L} & 0 & e^{-i2\phi_L} \\ 0 & e^{i2\phi_L} & 0 \end{pmatrix}. \end{aligned} \quad (4.32)$$

⁴The matrix takes this form in a suitable interaction picture that includes the kinetic energy $\hat{\mathbf{p}}^2/2M$. For reference see Eq. (31) in Ref. [132], where we note the different definitions of Ω : We define $\Omega = \Omega_{\text{eg}}^2/2\Delta$ compared to $\Omega = \Omega_{\text{eg}}^2/4\Delta$. The phase ϕ_L is included in the result given in Eq. (2.27) in Ref. [195], where $\Omega_{\text{DB}} = \sqrt{2}\Omega$ (assuming $\Omega_{\text{eg}} \in \mathbb{R}$).

At first glance, one sees that the effective Rabi frequency is enhanced by a factor of $\sqrt{2}$ when comparing the arguments of the trigonometric functions with those of the Pendellösung for a first-order single-Bragg pulse in Eq. (2.20). Nevertheless, the duration of double Bragg pulses is not shorter, but even longer for beam splitters (t_{BS}) and mirrors (t_{M}) than in the single Bragg case at the same Rabi frequency Ω . This becomes clear when considering the corresponding forms of the matrix in Eq. (4.32) for these two cases,

$$\Lambda_{\text{DBD}}(\Omega, t_{\text{BS}} = \frac{\pi}{\sqrt{2}\Omega}) = \begin{pmatrix} \frac{1}{2} & \frac{i}{\sqrt{2}}e^{i2\phi_{\text{L}}} & -\frac{1}{2} \\ \frac{i}{\sqrt{2}}e^{-i2\phi_{\text{L}}} & 0 & \frac{i}{\sqrt{2}}e^{-i2\phi_{\text{L}}} \\ -\frac{1}{2} & \frac{i}{\sqrt{2}}e^{i2\phi_{\text{L}}} & \frac{1}{2} \end{pmatrix}, \quad (4.33a)$$

$$\Lambda_{\text{DBD}}(\Omega, t_{\text{M}} = \frac{2\pi}{\sqrt{2}\Omega}) = \begin{pmatrix} 0 & 0 & -1 \\ 0 & -1 & 0 \\ -1 & 0 & 0 \end{pmatrix}. \quad (4.33b)$$

Assuming the atom is initially at rest, $|\psi(0)\rangle = |0\rangle$, Eq. (4.33a) shows that in the three-level system a beam splitter ideally depopulates the state $|0\rangle$,

$$|0 \hbar k\rangle \rightarrow \frac{i}{\sqrt{2}}e^{i2\phi_{\text{L}}} (|-2 \hbar k\rangle + |2 \hbar k\rangle). \quad (4.34)$$

Thus, in contrast to the single-Bragg equivalent (cf., e.g., Eq. (2.20) with $t_{\text{BS}} = \pi/(2\Omega)$ for $n = 1$), the interaction time actually increases by $\sqrt{2}$ according to Eq. (4.33a). The same is true for mirror pulses, making DBD inherently more susceptible to detrimental Doppler detunings, the effects of which can be inferred from the preceding discussion of finite velocity widths. In addition, DBD leads to off-resonant couplings of momentum states, as shown in Fig. 4.1(b). In consequence, the Rabi oscillations exhibit a spurious modulation at a frequency of 4δ , which can be attributed to the presence of the respective off-resonant optical lattice, which is not included in the deep-Bragg solution in Eq. (4.32) (see Ref. [132] for more details). The magnitude of both these off-resonant transitions as well as the spurious couplings to other momentum states increases when operating in the experimentally more useful quasi-Bragg regime, since the pulse durations are shorter. The consequences of both effects on the signal of a double Bragg MZ interferometer were recently quantified numerically by *J. Jenewein* et al. [136] in an analysis similar to that presented in Chapter 3 of this thesis.

Despite these potential complications, double Bragg pulses still provide twice the momentum separation compared to single diffraction, and do so symmetrically, suppressing important systematic effects, as shown by the imprint of the laser phase ϕ_{L} on both output ports of an ideal beam splitter in Eq. (4.34). This makes this technique not only desirable for microgravity environments [81], which naturally provide a vanishing atomic velocity in the direction of the laser beams. Successful implementation on the ground in a horizontal

configuration [94], with gravitational acceleration acting perpendicularly to the direction of the Bragg beams, has demonstrated the potential of this technique for LMT atom interferometry. In the following sections, we will see that the momentum separations reached with DBD can be dramatically increased, when combined with BO in accelerated optical lattices.

4.3.3 Coherent Acceleration via Bloch Oscillations (BO)

The key to achieving unprecedented momentum separations in the twin-lattice interferometer is to combine DBD with BO in accelerated optical lattices [106–108] to transfer hundreds of photon recoils with high efficiencies. Before analyzing the implementation of such a setup in the QUANTUS-1 experiment, it is therefore crucial to introduce the fundamental aspects of BO. We will therefore reproduce the most important results of the pioneering work done by the authors of Refs. [106, 108] in this section considering only a single one-dimensional lattice potential

$$V(\hat{y}, t) = V_0 \cos^2(k(\hat{y} - y_L(t))). \quad (4.35)$$

For the sake of clarity we use position and momentum operators in this section, and for simplicity we consider a one-dimensional optical lattice whose depth is the function of a constant two-photon Rabi frequency, $V_0 = 2\hbar\Omega$ [see Eq. (4.28)]. Assuming a single lattice is also justified because the initial momentum separation generated by the DBD sequence ideally serves to make the optical lattice sequences in each interferometer arm ideally independent of each other. Perturbative effects due to the respective off-resonant lattice in the actual experiment are discussed below in Sec. 4.4.2.

Atoms in Optical Lattice Potentials

For now, let us consider a static lattice by setting $\delta = 0$, so that the Hamiltonian describing the motion of an atom with mass M in the periodic potential $V(\hat{y} + d) = V(\hat{y})$ becomes time-independent

$$H_0 = \frac{\hat{p}^2}{2M} + V_0 \cos^2(k\hat{y}). \quad (4.36)$$

The periodicity of the optical potential is determined by the wave number or respectively the wavelength of the laser $d = \pi/k = \lambda_L/2$. Defining the one-dimensional translation operator in position space

$$\hat{T}_d = \exp(i\hat{p}d/\hbar), \quad \text{with} \quad \hat{T}_d f(\hat{y}) = f(\hat{y} + d), \quad (4.37)$$

and using the form of the momentum operator in position representation, $\hat{p} = -i\hbar\partial_y$, we find that there exists a common eigenbasis between \hat{T}_d and the Hamiltonian in Eq. (4.36) as their commutator vanishes

$$[H_0, \hat{T}_d] = 0. \quad (4.38)$$

This observation is at the heart of Bloch's theorem [196, 197], which states that the eigenstates $|n_B, q_B\rangle$ and eigenenergies $E_{n_B}(q_B)$ that solve the time-independent Schrödinger equation,

$$H_0 |n_B, q_B\rangle = E_{n_B}(q_B) |n_B, q_B\rangle, \quad (4.39)$$

are labeled by a continuous index q_B and a discrete band index n_B . The former is usually referred to as the quasimomentum. Both $|n_B, q_B\rangle$ and $E_{n_B}(q_B)$ are $2\pi/d$ -periodic, i.e., $E_{n_B}(q_B + 2\pi/d) = E_{n_B}(q_B + 2k) = E_{n_B}(q_B)$. The periodicity of the system in Eq. (4.36) motivates dividing configuration space into so-called Brillouin zones. The discussion of the dynamics of BO is usually restricted to the first Brillouin zone, which corresponds to the quasimomentum being confined to the interval $q_B \in]-\pi/d, \pi/d] =]-k, k]$ [196, 197]. The quasimomentum is therefore closely related to the (quasi)momentum $p \in [-\hbar k/2, \hbar k/2]$ we have introduced in Chapter 2. We show the first five energy bands for a shallow lattice potential and a considerably deeper one in Fig. 4.2(a) and (b) within the first Brillouin zone. Except for the ac Stark shift in energy and the factor of 2 between V_0 and Ω , these plots correspond to the individual panels in Figs. 2.2 and 2.11(b). As we have already discussed, they show that the higher the laser intensity, the more the energy bands deviate from the dispersion relation of a free particle, as band gaps appear and the bands become increasingly flat. In particular, the band gaps at the edges of the Brillouin zone ($q_B = \pm k$), shown in the lower panel of Fig. 4.2(c), are a crucial factor for the fidelity for the BO. We will see below that in the regime of modest lattice depths ($V_0 < 20 E_r$) the non-adiabatic loss processes are dominated by LZ transitions between effective two-level systems, and therefore the associated energy differences for BO play a role similar to the energy differences in the Bragg spectra depicted in Fig. 2.3 and Figs. 2.11(a,b) [cf. Eq. (2.83)]. In position representation, the eigenstates in Eq. (4.39) take the form of delocalized Bloch waves

$$\psi_{n_B, q_B}(y) = \langle y | n_B, q_B \rangle = e^{iq_B y} u_{n_B, q_B}(y) \quad \text{with} \quad u_{n_B, q_B}(y + d) = u_{n_B, q_B}(y). \quad (4.40)$$

Using the relations

$$\hat{p}(e^{iq_B y} u_{n_B, q_B}(y)) = \hat{p}(e^{iq_B y}) u_{n_B, q_B}(y) + (e^{iq_B y} \hat{p} u_{n_B, q_B}(y)) = e^{iq_B y} (\hat{p} + \hbar q_B) u_{n_B, q_B}(y), \quad (4.41)$$

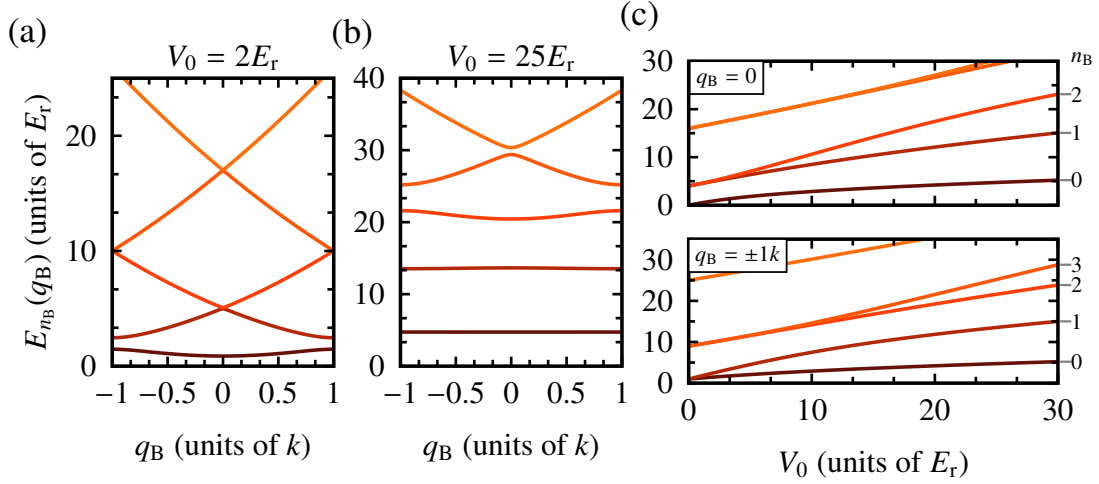


Figure 4.2: **Spectra of the Bloch Hamiltonian.** Bloch band energies of the optical lattice Hamiltonian H_0 according to Eq. (4.39) depicted in the first Brillouin zone for depths $V_0 = 2 E_r$ (a) and $V_0 = 25 E_r$ (b). In (c) we show the energies as a function of V_0 fixing the quasimomentum to the center (upper panel, $q_B = 0$) or the edge (lower panel, $q_B = \pm k$) of the Brillouin zone. The Bloch energies differ from the eigenenergies of the Bragg Hamiltonian in Eq. (2.11) by an ac Stark shift and are otherwise identical to the ones shown in Figs. 2.2, 2.3 and 2.11.

we can derive a Schrödinger equation for the Bloch functions $u_{n_B, q_B}(y)$ and the associated states $|u_{n_B, q_B}\rangle$. We find via the position representation of Eq. (4.39) (substituting $|n_B, q_B\rangle \rightarrow \langle y|n_B, q_B\rangle$) that

$$\left[\frac{\hat{p}^2}{2M} + V(\hat{y}) \right] e^{iq_B y} u_{n_B, q_B}(y) = e^{iq_B y} \left[\frac{(\hat{p} + \hbar q_B)^2}{2M} + V(\hat{y}) \right] u_{n_B, q_B}(y) \quad (4.42)$$

yielding

$$H_{q_B} u_{n_B, q_B}(y) = E_{n_B}(q_B) u_{n_B, q_B}(y), \quad (4.43)$$

where H_{q_B} is defined according to

$$H_{q_B} = \left[\frac{(\hat{p} + \hbar q_B)^2}{2M} + V(\hat{y}) \right]. \quad (4.44)$$

Atoms in an Accelerated Optical Lattice Potential

To accelerate the atoms trapped in the lattice potential via BO the optical potential must be set in motion resulting in a time-dependent Hamiltonian in the laboratory frame

$$H^{\text{LF}} = \frac{\hat{p}^2}{2M} + V_0 \cos^2(k(\hat{y} - y_L(t))). \quad (4.45)$$

According to Eq. (4.29a) the position of the lattice can experimentally be controlled via the frequency difference between the light fields. The dynamics of BO is usually derived in the inertial frame comoving with the optical lattice and the corresponding Hamiltonian can be found applying a suitable unitary transformation as we have done in Sec. (2.2.1), $H^{\text{MF}} = i\hbar\dot{\mathcal{G}}\mathcal{G}^\dagger + \mathcal{G}H^{\text{LF}}\mathcal{G}^\dagger$. Since the moving frame is accelerated in this case, the unitary operator assuming that the atom is initially at rest is given by

$$\mathcal{G}(t) = \exp(-i(\hat{y} - \hat{p}t/M)Mv_L(t)/\hbar + i\Phi_{\mathcal{G}}(t)), \quad (4.46a)$$

which yields after some calculation using the Baker–Campbell–Hausdorff formula and the commutation relation $[\hat{y}, \hat{p}] = i\hbar$ (cf. App. B)

$$i\hbar\dot{\mathcal{G}}\mathcal{G}^\dagger = Ma_L(t)\hat{y} - v_L(t)\hat{p} - \hbar\dot{\Phi}_{\mathcal{G}}(t), \quad (4.46b)$$

$$\mathcal{G}H^{\text{LF}}\mathcal{G}^\dagger = H_0 + v_L(t)\hat{p} + \frac{M}{2}v_L^2(t). \quad (4.46c)$$

At this point, we have introduced the lattice acceleration $a_L(t) = \dot{v}_L(t)$, and if we choose $\dot{\Phi}_{\mathcal{G}}(t) = Mv_L^2(t)/2\hbar$, we obtain the standard Hamiltonian in the accelerated frame [108]

$$H^{\text{MF}} = \frac{\hat{p}^2}{2M} + V_0 \cos^2(k\hat{y}) + Ma_L(t)\hat{y}. \quad (4.47)$$

This result implies that the motion of the atoms in the lab frame results in a net inertial force $F = Ma_L(t)$ in the comoving frame. We note that the experimental realization of the transition from a static lattice in Eq. (4.36) to a moving one in Eq. (4.45), i.e., the temporal shape of the function $a_L(t)$, has a significant impact on the dynamics of the atoms and refer the interested reader, e.g., to Ref. [198] for more information.

While the Bloch states $|n_B, q_B\rangle$ are no longer energy eigenstates of H^{MF} (those are the Wannier-Stark states [199]), one can show that the eigenstates of the new Hamiltonian retain the form in Eq. (4.40). In order to see this, we must first boost H^{MF} to a third frame referred to as the "solid-state physics" point of view in Ref. [108] via another transformation $H^{\text{SSP}} = i\hbar\dot{\tilde{\mathcal{G}}}\tilde{\mathcal{G}}^\dagger + \tilde{\mathcal{G}}H^{\text{MF}}\tilde{\mathcal{G}}^\dagger$ using the unitary $\tilde{\mathcal{G}}(t) = \exp(i\hat{y}Mv_L(t)/\hbar)$, which leads to

$$H^{\text{SSP}} = \frac{(\hat{p} - Mv_L(t))^2}{2M} + V_0 \cos^2(k\hat{y}). \quad (4.48)$$

The translation operator also commutes with this Hamiltonian, $[H^{\text{SSP}}, \hat{T}_d] = 0$, and thus both have the same set of time-dependent eigenfunctions

$$\psi(\hat{y}, t) = e^{iq_B\hat{y}}u(\hat{y}, t) \quad \text{with} \quad u(\hat{y} + d, t) = u(\hat{y}, t). \quad (4.49)$$

Using again Eq. (4.41) we can rewrite the Schrödinger equation

$$i\hbar\frac{d\psi(\hat{y}, t)}{dt} = H^{\text{SSP}}\psi(\hat{y}, t), \quad (4.50)$$

and find that the periodic function $u(\hat{y}, t)$ solves the differential equation

$$i\hbar \frac{du(\hat{y}, t)}{dt} = \left[\frac{(\hat{p} + \hbar q_B(t))^2}{2M} + V_0 \cos^2(ky) \right] u(\hat{y}, t) =: H_{q_B(t)} u(\hat{y}, t). \quad (4.51)$$

Here, we have introduced the time-dependent quasimomentum

$$q_B(t) := q_B(0) - \frac{M}{\hbar} v_L(t) = q_B(0) - \frac{M}{\hbar} \int_0^t dt' a_L(t'). \quad (4.52)$$

Therefore, we can find the solutions of

$$i\hbar \frac{d\Psi(\hat{y}, t)}{dt} = H^{MF} \Psi(\hat{y}, t) \quad (4.53)$$

via the transformation with $\tilde{\mathcal{G}}^\dagger(t)$ giving

$$\Psi(\hat{y}, t) = \tilde{\mathcal{G}}^\dagger(t) \psi(\hat{y}, t) = e^{iq_B(t)y} u(\hat{y}, t), \quad (4.54)$$

with a periodic part that evolves according to the Schrödinger equation with respect to the Hamiltonian in Eq. (4.51),

$$i\hbar \frac{d}{dt} |u(t)\rangle = H_{q_B(t)} |u(t)\rangle. \quad (4.55)$$

Assuming that atoms are initially loaded⁵ into the lowest Bloch band $n_B = 0$ and considering a weak-enough acceleration starting at $t = 0$ so that transitions to higher bands are negligible, we can give an explicit solution for $|u(t)\rangle$,

$$|u(t)\rangle = \exp\left(-i \int_0^t dt' \frac{E_0(q_B(t'))}{\hbar}\right) |0, q_B(t)\rangle. \quad (4.56)$$

This single-band approximation is based on the assumption of an adiabatic time evolution, so that the eigenstate of the accelerated system can be expressed as the former Bloch state $|0, q_B(t)\rangle$ plus an accumulated phase. The phase must be obtained via the time integral over the corresponding eigenenergy $E_0(q_B(t))$ of $H_{q_B(t)}$ due to the change in quasimomentum $q_B(t)$.

The criterion for the adiabatic approximation we have cited here is very similar to the one we formulated in our adiabatic theory for the single-Bragg description [cf. Eq. (2.83)].

⁵Loading atoms into the lattice requires increasing the lattice depth $V_0(t) = 2\hbar\Omega(t)$. The loading ramp and the relative velocity between lattice and atom determine, whether an atom is loaded into a single band (adiabatic) or a superposition of bands (nonadiabatic). The criterion to load into the fundamental band reads $|\langle 1, q_B | \partial_t H_0 | 0, q_B \rangle| \ll (E_1(q_B) - E_0(q_B))^2 / \hbar$ [200], and for sufficiently narrow momentum widths of the atomic cloud $\sigma_p \ll \hbar k$ it is even possible to target specific quasimomenta q_B . For further reference we suggest, e.g., Refs. [150, 200, 201].

In this case, we require that the energy gap $\Delta E_{n'_B, n_B}(q_B) := E_{n'_B}(q_B) - E_{n_B}(q_B)$ between bands $n \neq n'$ is much larger than the overlap of the corresponding Bloch states, i.e.,

$$|\langle n_B, q_B | \frac{d}{dt} | n'_B, q_B \rangle| \ll |\Delta E_{n'_B, n_B}(q_B)| / \hbar. \quad (4.57)$$

In the limit of a shallow optical lattice $V_0 \leq 10 E_r$, the band gap between the fundamental and the first excited band is proportional to the depth of the optical lattice, $\Delta E_{1,0}(q_B) \propto V_0$. Assuming Eq. (4.57) imposes an upper bound for the constant force, $F = Ma_L$, to avoid transitions to higher bands one can derive the relation [108],

$$|F|d \ll \frac{\pi V_0^2}{8 E_r}. \quad (4.58)$$

This result assumes $q_B = \pm k$ because the band gap $\Delta E_{1,0}(q_B)$ is narrowest at the edges of the Brillouin zone due to the curvature of the bands (compare, e.g., Fig. 4.2(a) to (b) for $q_B = \pm k$). Now that we have found an approximate solution for the time evolution in the accelerated frame in Eq. (4.56), the name "Bloch oscillations" becomes apparent: The mean velocity of a particle in a Bloch state $|n_B, q_B\rangle$ is determined by

$$\langle v \rangle_{n_B}(q_B) = \frac{1}{\hbar} \frac{dE_{n_B}(q_B)}{dq_B}. \quad (4.59)$$

Here, we recall the periodicity $d = \pi/k = \lambda_L/2$ of the optical lattice potential, e.g., in Eq. (4.45). Since the eigenenergies $E_{n_B}(q_B)$ are periodic in the quasimomentum, so is $\langle v \rangle_{n_B}(q_B)$ making it an oscillating function with average zero. Again assuming a constant force F , the period of one oscillation is determined by the periodicity of $q_B(t) = q_B - Ft/\hbar$ and is called the "Bloch period",

$$T_B = \frac{2\pi\hbar}{|F|d}. \quad (4.60)$$

Figure 4.3 illustrates the dynamics in the inertial frame comoving with the optical lattice. Here we represent the wave packets as individual points moving through the dispersion relation of the periodic potential, which is justified in the case of a narrow momentum width ($\sigma_p \ll 2\hbar k$). As soon as the lattice starts moving, the atoms experience a force in opposite direction due to their inertia [cf. Eq. (4.47)]. At the edge of the Brillouin zone, the atoms either transition to a higher band meaning that they do not adiabatically follow the motion of the lattice, the velocity of which is steadily increasing at a rate $|a_L| = \frac{2\hbar k}{MT_B}$, or they remain in the same band. In case of the latter, after one *Bloch period*, $t = T_B$, the system is back in its initial state. In the lab frame the atoms undergo a two-photon transition gaining $2\hbar k$ in momentum once they reach the edge of the Brillouin zone [108]. In the next section, we will briefly outline, how to quantify the losses to higher bands using LZ theory.

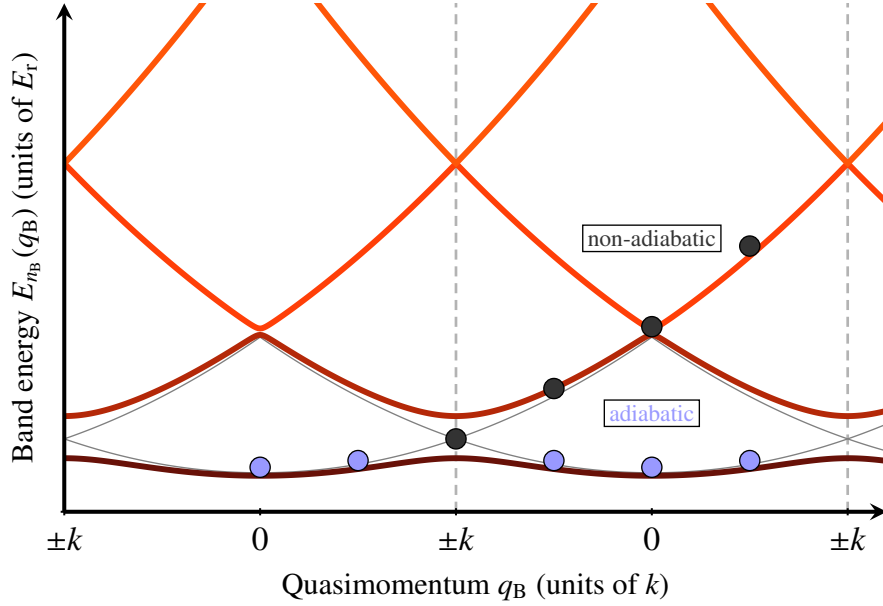


Figure 4.3: **Bloch oscillations in the Bloch-band picture.** The figure shows the unfolded Bloch band structure for the lowest energy bands of two neighboring Brillouin zones. Provided an atom with a narrow momentum width, $\sigma_p \ll \hbar k$, has been loaded in the fundamental band, its quasimomentum $q_B(t)$ evolves according to Eq. (4.52) represented by the blue dots. At the edge of the Brillouin zone interband transitions can occur meaning that the atom is no longer comoving with the accelerated optical lattice. For sufficiently large band curvatures (requiring $V_0 \lesssim 20 E_r$) LZ theory accurately predicts the transition probabilities, see Eq. (4.61).

4.3.4 Lattice Transport Fidelity

To analyze the experimental results presented in the following section, a basic understanding of the principal loss mechanism in the twin-lattice interferometer is required. We have already briefly touched on potential shortcomings of DBD in Sec. 4.3.2, but considering the majority of the photon recoils are transferred via BO, it is very probable that the overall loss accumulated during the much longer Bloch sequences will impact the signal of the interferometer much more significantly. Thus, we give a short introduction into the corrections to the adiabatic dynamics of BO and discuss the aspect of spontaneous emission.

Non-adiabatic LZ Transitions

Beyond the single-band approximation in Eq. (4.56), while the atoms undergo periodic BO and the quasimomentum $q_B(t)$ scans the Brillouin zone, transitions to higher bands occur with finite probability [202], which we illustrate in Fig. 4.3. As previously mentioned, for sufficiently shallow lattices, $V_0 \leq 20 E_r$, the curvature of the bands $E_{nB}(q_B)$ for different

q_B shown in the figure justifies focusing on a single point in the Brillouin zone, where the band gap $\Delta E_{n'_B, n_B}(q_B)$ is smallest. With respect to the fundamental and the first excited band, $\Delta E_{1,0}(q_B)$, this is the case at the edges $q_B = \pm k$. Using LZ theory one can quantify the transition probability [108, 202],

$$\mathcal{L}_{n'_B, n_B} = \exp\left(-\frac{\pi}{4\delta(t)}\left(\frac{\Delta E_{n'_B, n_B}}{\hbar}\right)^2\right), \quad (4.61)$$

which depends on the band gap $\Delta E_{n'_B, n_B}(q_B = k)$ as well as on the force $F = M\dot{\delta}(t)/k$ that is controlled by the change in detuning, $2\delta(t) = \omega_1(t) - \omega_2(t)$, between the light fields. During our study of the spectra of the Bragg Hamiltonians and their connection to the Bloch bands shown in Fig. 2.11, we have already seen that $\Delta E_{n'_B, n_B}$ decreases for higher band indices at a given lattice depth V_0 . This is also clearly visible in both panels of Fig. 4.2(c). According to Eq. (4.61) this means that once an atom has transitioned from the fundamental to the first excited band it is most likely to continue to tunnel to higher bands until it is no longer bound by the optical lattice due to the increasing velocity of the atom in the inertial frame comoving with the optical lattice. However, it is also possible for atoms to remain in one of the higher energy bands, which has been demonstrated experimentally by performing what is called "Stückelberg interferometry" with ultracold atoms in optical lattices [203, 204].

Leaving aside this interference effect, the LZ formula can be used, at least theoretically, to estimate the fidelity of LMT sequences that transfer $2N_B$ photon recoils, with $N_B \in \mathbb{N}$. Assuming that consecutive BO are uncorrelated events, one can simply take the product of the fidelity of a single BO $\mathcal{F}_{\text{LMT}} = (\mathcal{F}_{0,0})^{N_B} := (1 - \mathcal{L}_{1,0})^{N_B}$. However, as mentioned above, this is only true for moderate lattice depths ($V_0 \leq 20 E_r$). In practice, LMT sequences that rely on efficient transfer in the order of a thousand or more photon recoils operate in the tight-binding limit [24, 175], where the single-band approximation and therefore the LZ formalism fails as the energy bands become essentially flat [see Fig. 4.2(b)]. Thus the Bloch picture presented above does prove to be suboptimal in those cases [198]. Instead, working in a representation of the Wannier-Stark ladders, which are the eigenstates of the Hamiltonian in Eq. (4.45), provides a more natural description of BO in this regime [199, 205] that can also explain, e.g., the phenomenon of resonantly enhanced tunneling seen in optical lattice experiments [206]. Despite its potential, a dedicated study of BO from this perspective is outside of the scope of this thesis.

In Sec. 4.4.2, we compare the prediction of the LZ formula (4.61) with the experimentally measured transfer fidelities for at the beginning of the twin-lattice interferometer sequence assuming modest $V_0 < 10 E_r$. This will help us to better understand the effect of the off-resonant lattice on the momentum transfer, which is not considered in Eq. (4.36).

Spontaneous Emission Losses

In the context of single Bragg diffraction, we have not explicitly treated spontaneous emission. However, in our discussions in the previous two chapters, we have considered Bragg orders $n \leq 5$, mainly because of the increasing demands on the laser power at higher diffraction order leading to detrimental losses due to spontaneous scattering (cf. Ref. [69]). In comparison, many experiments realizing LMT via BO require much higher lattice depths, $\sim 70 E_r$, for longer durations of several ms [24, 179, 207], since the acceleration fidelity improves at deeper optical potential and for longer acceleration times [corresponding to a reduced force, cf. (4.61)]. Thus, we have to take into account losses due to random scattering during BO.

For our analysis of the twin-lattice interferometer, we simply assume spontaneous emission to reduce the number of atoms coherently contributing to the signal (cf. Sec. 5.2 in Ref [208]). In this sense, the surviving fraction decays exponentially as a function of the interaction time with the optical potential and the rate of spontaneous emission Γ_{sp} ,

$$\mathcal{F}_{\text{sp}} = \exp(-\Gamma_{\text{sp}} \cdot t_{\text{int}}). \quad (4.62)$$

The rate Γ_{sp} depends on the natural properties of the atomic transition as well as the effective potential seen by the atom [209],

$$\Gamma_{\text{sp}} = \frac{\Gamma_{\text{nat}} \langle V(\hat{y}) \rangle}{|\Delta| \hbar}. \quad (4.63)$$

Here, Γ_{nat} denotes the natural line width of the atomic transition and as before Δ is the detuning of the laser from the resonance frequency. To estimate Γ_{sp} , one must evaluate $\langle V(\hat{y}) \rangle$ with respect to the atomic state. In the case of an atom trapped in the fundamental band of a deep optical lattice potential $V(\hat{y}) \propto \cos^2(k\hat{y})$, one can assume that the atom is well described by the Bloch state in Eq. (4.56) corresponding to the lowest energy band as described in Ref. [179]. Depending on the sign of the detuning Δ of the light field, two different rates are obtained when the harmonic approximation of the trapping potential is performed for the case of an atom that is well localized in the wells of the optical potential. In the case of a red detuned lattice, $\Delta < 0$, the atoms are primarily confined to the anti-nodes of the optical lattice, where the intensity is highest [209]. Thus they experience a decay rate,

$$\Gamma_{\text{sp,red}} = \frac{\Gamma_{\text{nat}} V_0}{|\Delta| \hbar} \left[1 - \frac{1}{2\sqrt{V_0/E_r}} \right], \quad (4.64)$$

that is enhanced compared to a blue detuning

$$\Gamma_{\text{sp,blue}} = \frac{\Gamma_{\text{nat}} V_0}{|\Delta| \hbar} \frac{1}{2\sqrt{V_0/E_r}}. \quad (4.65)$$

Therefore, using a blue detuned potential can have a significant positive impact on the spontaneous emission losses. Later, in Sec. (4.5), we will modify Eq. (4.65) slightly to estimate the spontaneous emission losses in the QUANTUS-1 experiment. In this context, we will account for the imperfections of the experimental realization of the twin-lattice potential.

4.4 Realization in the QUANTUS-1 experiment

QUANTUS-1 is the product of a longstanding collaboration between several German universities funded by the German Aerospace Center (DLR, Deutsches Zentrum für Luft- und Raumfahrt [92]). It represents a first-generation platform for experiments with ultra-cold atomic gases in microgravity. To perform autonomous experiments in harsh environments such as planes [52], drop towers [63, 65, 80, 93], sounding rockets [81, 90] or space [47, 83, 210] it is necessary to drive the transition from lab based apparatuses to robust quantum sensors that are deployable in real-world scenarios. The QUANTUS-1 experiment demonstrated the first realization of a BEC in free fall in 2007 [93] and showcased the successful manipulation of the atomic ensemble towards atom interferometry with long interrogation times [80]. For more details about the experimental apparatus and earlier works we refer the reader to Refs. [194, 211–213]. Not only do these efforts represent important milestones on the path to discover new physics with atom optics experiments in weightlessness [82, 83, 210], but also proved vital in progressing the development of inertial sensors based on light-pulse atom interferometry with condensed matter waves [94, 95].

In the following, we present a theoretical analysis of the contrast loss of the twin-lattice interferometer realized in the QUANTUS-1 experiment. By accelerating ensembles of ^{87}Rb atoms via moving optical lattices a MZ-type geometry is realized featuring differential momenta between the arms of up to 408 photon recoils. For more details about the twin-lattice setup, we kindly refer the reader to the PhD thesis of *M. Gebbe* [96, 208], who performed most of these experiments.

The main ingredients of the experimental setup are depicted in Fig. 4.4. At the top it features a so-called "atom chip" that is aligned perpendicularly to gravity (here acting in positive z -direction). This device provides the required magnetic potentials for the generation of BECs consisting of up to $1.5 \cdot 10^4$ ^{87}Rb atoms [93]. After the atoms reach their condensed quantum state and before the start of the interferometry sequence, the ensemble is released from the magnetic trap undergoing a vital preparation stage for ≈ 15 ms. During that time, the cloud first freely expands and undergoes an adiabatic rapid passage for state preparation before the magnetic potential is briefly switched on again. This "re-trapping" (also referred to as "delta-kick collimation" (DKC) or "lensing") acts as a collimating lens for the atomic source minimizing its momentum width [65, 188] along the interferometry

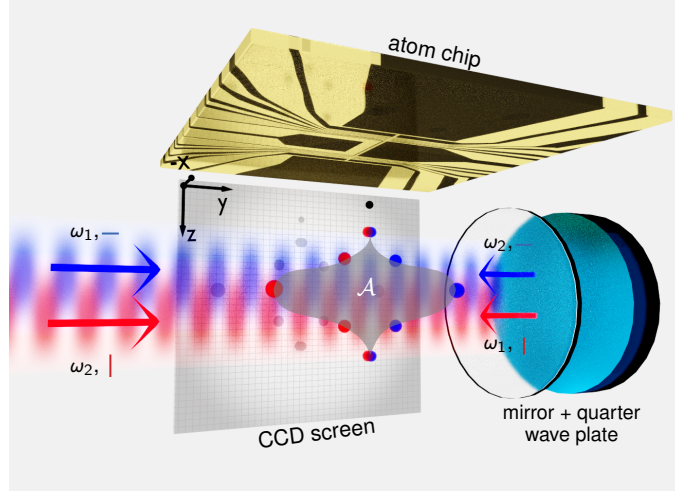


Figure 4.4: **Experimental twin-lattice setup.** The twin lattice is formed by retroreflecting light using two frequencies, ideally with linear orthogonal polarization. A quarter-wave plate in front of the retroreflector alters the polarization to generate two counterpropagating lattices (indicated in red and blue). After release from the atom chip trap and state preparation, the BEC is symmetrically split and recombined by the lattices driving DBD and BO. In this way, the interferometer arms enclose an area \mathcal{A} (shaded in gray). The interferometer output ports are detected on a CCD chip by absorption imaging. Figure adapted from *M. Gebbe et al.*, Nat. Comm. **12**(1):2544 (Ref. [96]), CC BY 4.0, <https://creativecommons.org/licenses/by/4.0/>.

axis to about $\sigma_p = 0.03 \hbar k$ (or $\sigma_v = 0.18$ mm/s in velocity). This corresponds to an effective temperature of 340 pK in the y -direction and is paramount for efficient Bragg diffraction. For a more exhaustive account of the atomic source preparation, see chapter 4 in Ref. [208].

4.4.1 Twin-lattice Potential

According to Fig. 4.4, the twin-lattice laser beam propagates below and parallel to the surface of the atom chip. It has a beam waist of 3.75 mm and features up to 1.2 W in power with a negative (blue) detuning of $\Delta = (\omega_e - \omega_g) - \omega_L = -100$ GHz⁶. (and two frequency components that will be detuned up to several hundred kHz during the interferometer sequence) from the D_2 -line of the ^{87}Rb atoms. As mentioned above, the twin-lattice potential can be used for the generation of double Bragg pulses as well as for BO after loading the atoms into the lattice. The Bragg pulses considered here use Gaussian temporal shapes, while the intensity during the Bloch sequences is a linear function of time. Furthermore, to accelerate the lattices into opposite directions and perform BO time-dependent frequency ramps are required. For technical reasons in the QUANTUS-1 experiment these ramps

⁶Recall, that the light field contains two laser frequencies for which we can roughly estimate $2\omega_L \approx \omega_1 + \omega_2 \sim 200$ GHz and $2\delta(t) = \omega_1(t) + \omega_2(t) < 1$ MHz.

are linear functions of time (see Sec. 3.3 in Ref. [208]), despite the fact that this translates into instantaneous switching of the acceleration $a_L(t) = \dot{\delta}(t)/k$, which may increase non-adiabatic losses [198].

To understand the measured beam splitter fidelities at the beginning of the experimental sequence it is necessary to take a closer look at the role played by polarization of the incoming laser light in Eq. (4.26): To model imperfect experimental control over the alignment of the polarization vectors, we assume linearly polarized light and allow either frequency component to contain both horizontal and vertical polarization contributions,

$$\boldsymbol{\varepsilon}_1 = (1 - \epsilon) \boldsymbol{\varepsilon}_+ + \epsilon \boldsymbol{\varepsilon}_- \quad \text{and} \quad \boldsymbol{\varepsilon}_2 = \epsilon \boldsymbol{\varepsilon}_+ + (1 - \epsilon) \boldsymbol{\varepsilon}_-. \quad (4.66)$$

In particular, we have introduced the spurious contribution strength $0 \leq \epsilon \leq 0.5$. Using $|\boldsymbol{\varepsilon}_+|^2 = 1 = |\boldsymbol{\varepsilon}_-|^2$ and $\boldsymbol{\varepsilon}_+^* \cdot \boldsymbol{\varepsilon}_- = 0 = \boldsymbol{\varepsilon}_-^* \cdot \boldsymbol{\varepsilon}_+$ this directly translates into an error in the potential by modifying the scalar products in Eq. (4.26),

$$|\boldsymbol{\varepsilon}_{1,2}|^2 = (1 - \epsilon)^2 + \epsilon^2 = 1 - \sigma_{\text{pol}}, \quad (4.67a)$$

$$|\boldsymbol{\varepsilon}_1^* \cdot \boldsymbol{\varepsilon}_2| = 2(\epsilon - \epsilon^2) = \sigma_{\text{pol}}. \quad (4.67b)$$

A non-vanishing polarization error, $\sigma_{\text{pol}} := 2(\epsilon - \epsilon^2)$ with $0 \leq \sigma_{\text{pol}} \leq 0.5$, therefore affects the interference pattern (4.26) by reducing the effective depth of the counterpropagating twin-lattice potentials, $V_0(\mathbf{x}, t) := (1 - \sigma_{\text{pol}})2\hbar\Omega(\mathbf{x}, t)$, and causing an additional parasitic potential term

$$\begin{aligned} V(\mathbf{x}, t) &= V_0(\mathbf{x}, t) \left[\cos^2(k(y - y_L(t))) + \cos^2(k(\hat{y} + y_L(t))) \right. \\ &\quad \left. + \frac{\sigma_{\text{pol}}}{1 - \sigma_{\text{pol}}} 2 \cos(k(\hat{y} - y_L(t))) \cos(k(\hat{y} + y_L(t))) \right] \quad (4.68) \\ &=: V^{\text{twin}}(\mathbf{x}, t) + V^{\text{para}}(\mathbf{x}, t). \end{aligned}$$

We will see in the next section that the occurrence of this additional term can have a significant impact on the beam splitter fidelities in the twin lattice as it acts as a standing lattice potential,

$$V^{\text{para}} \propto \cos(k(\hat{y} - y_L(t))) \cos(k(\hat{y} + y_L(t))) = \cos^2(k\hat{y}) - \sin^2(ky_L(t)). \quad (4.69)$$

The second term on the right-hand side of this equation describes a temporal beat, which therefore has no effect on the momentum transfer via BO, but plays a role in the spontaneous emission losses due to the twin-lattice potential.

4.4.2 Beam Splitter Fidelity

Before discussing the complete interferometer in the next section, we would like to stress the importance of high beam splitter fidelities, when generating symmetric interferometers with large momentum separations. In case of a twin lattice, one lattice may interfere with the dynamics of the other, which would mean transfer amplitudes are more complex than suggested by the LZ formula in Eq. (4.61). Therefore, we study the fidelity of the beam splitters at the beginning of the interferometer separately. First, DBD is used to generate a superposition of two wave packets moving in opposite directions. In comparison to the pure Bloch beam splitter presented in Ref. [142], combining Bragg diffraction with BO reduces the complexity of the time dependent intensity and frequency ramps while maintaining high fidelities. To evaluate the performance of the subsequent Bloch ramps, the atoms are first brought into a superposition of mean momenta $\pm 2 \hbar k$ via the Bragg pulses. The light pulses driving DBD have a Gaussian-shaped temporal envelope of $37.5 \mu\text{s}$ width (corresponding to $\tau \approx 0.89 \omega_r^{-1}$ [100]). Subsequently, the intensity of the copropagating optical lattices is linearly ramped up, and the optical potentials are then accelerated to impart an additional momentum of $\pm 2 \hbar k$ via BO. At the end of the sequence the number of atoms in the final momentum states is measured.

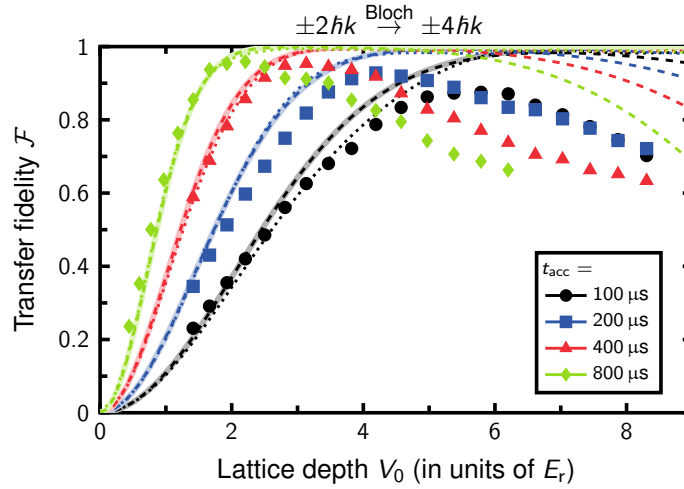


Figure 4.5: **Fidelity of one Bloch oscillation (BO) in the twin lattice.** A superposition of momentum $\pm 2 \hbar k$ (see main text) is loaded into the twin lattice and accelerated for different times t_{acc} to acquire additional momentum of $\pm 2 \hbar k$. The transfer fidelity is evaluated as a function of the lattice depth V_0 . Neither the LZ curves for a single lattice (see Eq. (4.61), solid lines), nor the ones, for which we added the effect of a second hypothetical standing lattice according to Eq. (4.70) (dashed lines) reproduce the features of the experimental data (symbols) toward deeper potentials. The same is true for the fidelities $\mathcal{F}_{\pm 4 \hbar k}^{\text{num}}$ in Eq. (4.71) calculated via our 1D GPE simulation using the ideal twin-lattice potential in Eq. (4.28) (dotted lines), which demonstrates the same scaling as the LZ curves.

In Fig. 4.5, we analyze the experimentally achieved fidelity, when increasing the initial separation from $4\hbar k$ to $8\hbar k$ ($\pm 2\hbar k \xrightarrow{\text{Bloch}} \pm 4\hbar k$). We compare different durations $t_{\text{acc}} = (100, 200, 400, 800)\mu\text{s}$, where shorter times translate into faster accelerations and show the results in dependence of the lattice depth, which can be understood as the effective lattice depth averaged over the atomic ensemble with respect to Eq. (4.68). Experimentally, V_0 has been determined using LZ curves (see Ref. [208] for more information). For shallow lattices ($V_0 \leq 2E_r$), the losses are reduced for more adiabatic timings and hence the measured data mirror the LZ losses in a single lattice (see Sec. 4.3.4). This is confirmed by our addition of the LZ fidelities for BO in the fundamental band calculated according to Eq. (4.61). To explain the differences between the measurements and the LZ model, we first attempt to extend the single-lattice model via the inclusion of a hypothetical second lattice with a momentum offset of $2\hbar k$. This can be achieved by multiplying the probability of staying in the fundamental band of the copropagating lattice $\mathcal{F}_{0,0} = (1 - \mathcal{L}_{1,0})$ (4.61) with the probability of tunneling into higher bands with respect to the lattice that is offset in velocity by $2\hbar k$ as described in Ref. [180],

$$\mathcal{F}_{\text{LZ}} = \mathcal{F}_{0,0}\mathcal{L}_{3,2} = \left[1 - \exp\left(-\frac{\pi}{4} \frac{t_{\text{acc}}\omega_r}{4} \left(\frac{\Delta E_{1,0}}{E_r}\right)^2\right) \right] \cdot \exp\left(-\frac{\pi}{4} \frac{t_{\text{acc}}\omega_r}{4} \left(\frac{\Delta E_{3,2}}{E_r}\right)^2\right). \quad (4.70)$$

Here, we have inserted the constant acceleration $a_L = \dot{\delta}/k = 4\omega_r/kt_{\text{acc}}$ required for a velocity change $\Delta v_L = 2\hbar k/M = 4\omega_r/k$ over a duration t_{acc} , and the band gap $\Delta E_{3,2}$ determines the probability $\mathcal{L}_{3,2}$ that the atom remains unaffected by the hypothetical second lattice. According to Fig. 4.5, the combined LZ fidelities are worse for deeper lattices and even more so for longer acceleration times as the effect of the off-resonant lattice increases, but they still do not explain the features exhibited by the measured data. Moreover, using Eq. (4.70) implicitly assumes a second parasitic lattice with full depth V_0 and a velocity difference of only $2\hbar k$, which is inconsistent with the result in Eq. (4.68).

To explain the momentum transfer measurements we adapt the time-dependent GPE model introduced previously in Secs. 4.2.1 and 4.2.2, taking into account the complete potential in Eq. (4.68). First, we numerically solve the three-dimensional GPE in Eq. (4.9) combining imaginary and real time evolution to compute an initial state for the lattice dynamics, which is calibrated to the experimentally observed free evolution of the atomic wave packet. In particular, we have focused on gauging the expansion velocity in the lattice direction, which we managed by using the simulation parameters provided in the first part of Tab. 4.1. Assuming the dynamics in the two radial directions is essentially static, the resulting three-dimensional wave function is then translated into our effective one-dimensional GPE model in order to simulate the lattice acceleration sequences that are characterized by the parameters given in the lower part of Tab. 4.1. Since we focus on understanding the fidelities of the Bloch sequence, we idealize the double Bragg interaction

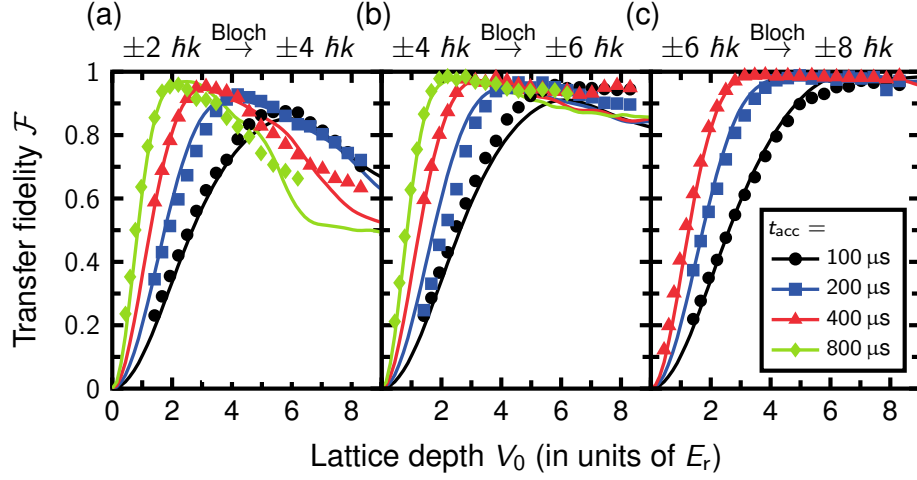


Figure 4.6: **Fidelity of one Bloch oscillation (BO) in the twin lattice for different DBD splittings.** Experimental data (symbols) in (a) are identical to Fig. 4.5. In (b) and (c) the initial DBD sequence produces an initial splitting of $\pm 4 \hbar k$ and $\pm 6 \hbar k$, respectively. The theoretical simulations ($\mathcal{F}_{\pm n \hbar k}^{\text{num}}$ in Eq. (4.71), lines) largely reproduce the measured data, assuming an additional standing lattice of depth $0.37 V_0$ (see Eq. (4.68)) with $\sigma_{\text{pol}} = 0.2688$) due to polarization errors. The losses caused by the imperfections decrease with a larger initial splitting Δp and from (a) to (c) as the detuning from the standing lattice increases. The parameters for the 1D GPE simulations of the Bloch sequence are presented in Tab 4.1. Figure adapted from *M. Gebbe et al.*, Nat. Comm. **12**(1):2544 (Ref. [96]), CC BY 4.0, <https://creativecommons.org/licenses/by/4.0/>.

neglecting effects such as velocity selectivity or off-resonant couplings (see Chapter 2 for single Bragg diffraction or, e.g., Ref. [134] for DBD specifically). In this sense, we describe DBD realizing the initial relative momentum Δp_{DBD} at the start of the sequence by creating an ideal superposition of counterpropagating wave packets in position space. The atomic state is multiplied with the phase factors $\frac{1}{\sqrt{2}} e^{\pm i \varphi_{\text{DBD}}}$ (including normalization) providing the constituents of the superposition, where $\varphi_{\text{DBD}} = \Delta p_{\text{DBD}} \hat{y} / 2 \hbar$.

First of all, the simulated data in Fig. 4.5 show that an ideal twin lattice, i.e., $\sigma_{\text{pol}} = 0$, cannot reproduce the features of the experiment. We obtain the numerical fidelity by integrating the density of the final wave function over the momentum regions of the two output ports,

$$\begin{aligned} \mathcal{F}_{\pm n \hbar k}^{\text{num}} &= |\langle \psi_{\text{ideal}}^{\text{out}} | \psi_{\text{num}}^{\text{out}} \rangle|^2 \\ &= \int_{-\hbar k/2}^{\hbar k/2} dp |\tilde{\psi}_{\text{num}}^{\text{out}}(-n \hbar k + p)|^2 + \int_{-\hbar k/2}^{\hbar k/2} dp |\tilde{\psi}_{\text{num}}^{\text{out}}(n \hbar k + p)|^2, \end{aligned} \quad (4.71)$$

where we have used the Fourier transformation,

$$\tilde{\psi}_{\text{num}}^{\text{out}}(p) = \frac{1}{\sqrt{2\pi\hbar}} \int_{-\infty}^{\infty} dx \exp(-ipx/\hbar) \psi_{\text{num}}^{\text{out}}(x, t_{\text{final}}), \quad (4.72)$$

to obtain the momentum representation of the wave function after the end of the lattice sequence, $\psi_{\text{num}}^{\text{out}}(x, t_{\text{final}})$. In fact, the visible losses are almost identical to the ones of the individual lattices. However, we demonstrate in Fig. 4.6(a) that by adding a standing lattice of $0.37V_0$ depth the simulated curves agree with the experimental data. By effectively changing the relative orientation of the polarization vectors, we have used the strength of the undesired contributions to the dipole potential according to Eq. (4.68) as a fit parameter and obtained the best match with $\sigma_{\text{pol}} = 0.2688$, which is a plausible assumption for the experimental setup. Polarization measurements show that the optical components, in particular the vacuum windows, degrade the polarization quality resulting in an extinction ratio of less than 20dB and a mismatch of several degrees from perfect orthogonality (see Sec. 3 in Ref. [208] for more details). Hence, the losses shown in Fig. 4.6(a) mainly result from an imperfect polarization of the light fields giving rise to a spurious standing lattice potential [cf. Eq. (4.68)].

Fortunately, these losses can be overcome by increasing the initial momentum splitting of the BEC corresponding to a larger detuning to the standing wave. This becomes clear when comparing the results in Fig. 4.6(a) to the other panels, where we have prepared a superposition of symmetric momentum states, $\pm 4 \hbar k$ (b) and $\pm 6 \hbar k$ (c). To this end, the experiment uses an initial first-order DBD pulse and in addition a respective number of consecutive pulses before a momentum of $\pm 2 \hbar k$ is imparted via BO. Our results clearly confirm that the importance of the perturbative potential diminishes for larger initial separations. While the fidelities in Fig. 4.6(b) still feature local optima, in Fig. 4.6(c) they follow the predictions of LZ theory and equal almost a hundred percent for sufficiently deep lattices. In consequence, we start our interferometers with a beam splitter creating a superposition of $\pm 4 \hbar k$ [as in Fig. 4.6(b)], which represents the best trade-off between the losses caused by parasitic standing waves and the lower efficiency of Bragg processes.

4.4.3 Twin-lattice Interferometer

The twin-lattice interferometer scheme realized in the QUANTUS-1 experiment is depicted in Fig. 4.7. Table 4.2 includes the most relevant parameters for all realizations sharing a common total duration of $2T = 12.1$ ms. As the figure illustrates, the temporal sequence of DBD processes and BO is controlled via the power of the lattice laser and the frequency difference $\delta(t)$. Ideally, the center-of-mass motion of the atoms follows the space-time trajectories shown for momentum separations $\Delta p = (24, 128, 208, 408) \hbar k$. After preparing the BEC, the twin lattice is pulsed to induce two successive first-order DBD processes so that the BEC is split into two wave packets with a momentum separation of $\pm 4 \hbar k$. Thanks to the use of delta-kick collimated BECs, the experiment achieves a transfer fidelity of 98.8 % per recoil in these processes. By linearly increasing the lattice depth V_0 within $t_{\text{load}} = 200 \mu\text{s}$ and adjusting $\delta(t)$ to match the mean velocities of the atomic clouds, the

| Parameter | Symbol | Value |
|----------------------------|---|---|
| State preparation | | |
| Atom number | N | $\sim 1.1 \cdot 10^4$ |
| Scattering length (s-wave) | a_{scat} | 5.272 nm |
| Initial trap frequencies | $\omega_x, \omega_y, \omega_z$ | $2\pi (35.1, 185, 184)$ Hz |
| Magnetic lens frequencies | $\omega_x^{\text{DKC}}, \omega_y^{\text{DKC}}, \omega_z^{\text{DKC}}$ | $2\pi (35.1, 112.8, 128.5)$ Hz |
| Free expansion before lens | $t_{\text{free,I}}$ | 6 ms |
| Magnetic lens duration | t_{lens} | 280 μs |
| Free expansion after lens | $t_{\text{free,II}}$ | 10.72 ms |
| Time step (free expansion) | dt_{free} | 10 μs |
| Time step (lens) | dt_{lens} | 1 μs |
| Bloch acceleration | | |
| Laser wavelength | λ_L | 780.2412 nm |
| Harmonic trap frequencies | $\omega_x, \omega_y, \omega_z$ | $2\pi (0.48, 0, 0.48)$ Hz |
| (Un)loading time | $t_{(\text{un})\text{load}}$ | 100 μs |
| Acceleration time | t_{acc} | (100, 200, 400, 800) μs |
| Time of flight | t_{TOF} | 10 μs |
| Time step | dt | $5 \cdot 10^{-3} \cdot \lambda_L / \sqrt{40 E_r / M}$ |

Table 4.1: **Input parameters for the GPE simulation.** The upper part shows the parameters for the three-dimensional simulation of the input state via the GPE in Eq. (4.9), the lower part contains the parameters of the beam splitter sequences using the effective one-dimensional GPE (4.14). The time step dt is chosen to be sufficiently small compared to the frequency of a harmonic oscillator approximating an optical lattice well of depth $V_0 = 20 E_r$. The time-of-flight t_{TOF} after unloading ensures that the lattice potential has vanished when calculating the fidelity.

BECs are efficiently loaded into the optical lattices. Each wave packet is accelerated by its copropagating lattice via BO for $t_{\text{acc}} = 2$ ms and gains additional momentum of up to $200 \hbar k$. For the release from the lattices, the intensity is lowered again linearly within $t_{\text{unload}} = 200 \mu\text{s}$. In this way, fidelities of up to 99.93 % per recoil for BO can be obtained. The accelerated wave packets evolve freely for $t_{\text{free}} = 200 \mu\text{s}$, before their motion is first slowed down via BO to $\pm 4 \hbar k$, then inverted via successive DBD. This marks the transition between the first and the second part of the interferometer and afterwards the atoms are accelerated again via BO in opposite directions as before. After another sequence of free evolution for $200 \mu\text{s}$, the velocities of the wave packets are reduced to $\pm 4 \hbar k$ to recombine them via the last DBD process resulting in three output ports with mean momenta of $\pm 2 \hbar k$ and $0 \hbar k$ (cf. Sec. 4.3.2) as shown by the absorption images at the bottom of Fig. 4.7.

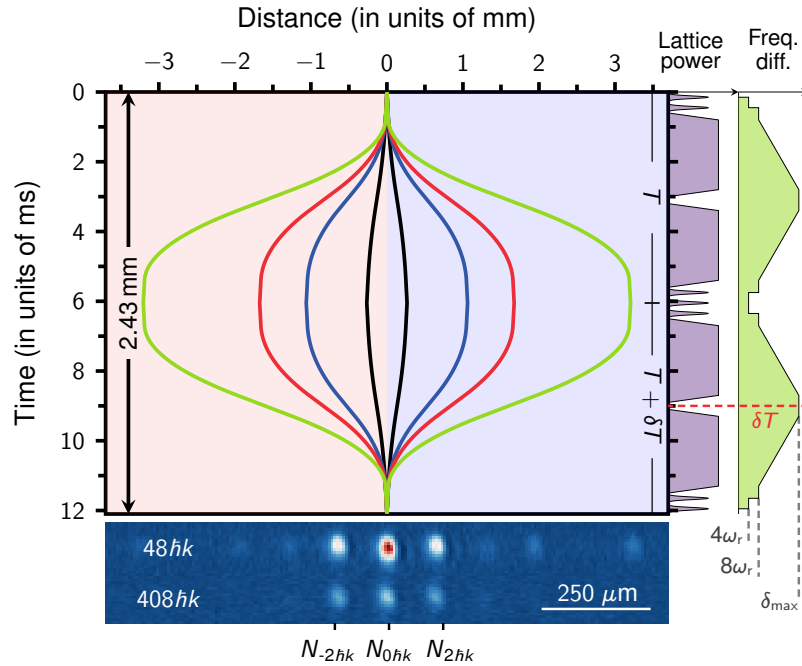


Figure 4.7: **Twin-lattice interferometer scheme.** Space-time trajectories of the wave packets travelling along the interferometer arms depicted for momentum transfers of $\Delta p = (24, 128, 208, 408) \hbar k$ (black, blue, red, green) with distances given relative to the center of the atom chip. Below: Interferometer output ports for $48 \hbar k$ and $408 \hbar k$. Right: Temporal sequence of the twin-lattice laser power and the frequency difference $\delta(t)$ in the interferometer (neither to scale). DBD is driven by Gaussian-shaped pulses and BO use linear frequency ramps of 2 ms (for $\Delta p \geq 128 \hbar k$ the ramps include two steps, see Ref. [96] for details) in between $200 \mu\text{s}$ of loading and unloading time. For the contrast analysis, the free evolution time in the second half is modified by δT with respect to the first half. Figure adapted from *M. Gebbe et al.*, Nat. Comm. **12**(1):2544 (Ref. [96]), CC BY 4.0, <https://creativecommons.org/licenses/by/4.0/>.

The signal of the twin-lattice interferometer is defined as the normalized number of atoms detected in the output ports $\mu_a := N_{0\hbar k}/N$ and $\mu_b := (N_{2\hbar k} + N_{-2\hbar k})/N$, where we have used the notation introduced in Chapter 3. Here, $N := N_{-2\hbar k} + N_{2\hbar k} + N_{0\hbar k}$ is the total number of atoms recorded in the ports with average momenta $\pm 2 \hbar k$ as well as $0 \hbar k$.

Estimated Phase Sensitivity

Before analyzing the measured data in detail to draw conclusions about the coherence properties of the atomic ensemble after it has been subjected to the twin-lattice sequence, it is worth considering the potential sensitivity gains that result from this geometry in terms of a relative phase between the arms ϕ . We have discussed in the previous chapter that the signal of the two-mode MZ interferometer realized by n th-order single-Bragg pulses has a

| Parameter | Symbol | Value |
|---------------------------------|------------------------------|--------------------|
| DBD lattice depth | V_0 | $3-4 E_r$ |
| DBD pulse width | τ | $37.5 \mu\text{s}$ |
| DBD beam splitter sequence | t_{BS} | $600 \mu\text{s}$ |
| DBD mirror sequence | t_{M} | $900 \mu\text{s}$ |
| Bloch lattice depth | $V_0(\Delta p)$ | $0-25.3 E_r$ |
| Lattice (un)loading time | $t_{(\text{un})\text{load}}$ | $200 \mu\text{s}$ |
| Acceleration time | t_{acc} | 2 ms |
| Free propagation time | t_{free} | $200 \mu\text{s}$ |
| Interrogation time | $2T$ | 12.1 ms |
| Time of flight t_{TOF} | 8 ms | |

Table 4.2: **Twin-lattice sequence parameters.** The DBD sequences and timings are identical for all momentum separations $\Delta p = (8, 24, 48, 88, 128, 208, 308, 408) \hbar k$. The laser intensities and thus the Bloch lattice depths $V_0(\Delta p)$ are varied to maintain high BO fidelities as the acceleration is increased. The experimentally determined values for $V_0(\Delta p)$ are plotted in Fig. 4.8(c).

sinusoidal dependence on ϕ [see Eq.(3.2)],

$$P(\phi) = P_0 + A \cos(\phi). \quad (4.73)$$

In this equation, we have absorbed the Bragg order n in the relative phase ϕ . If we assume that the signal is given by linear gravitational acceleration g and neglect effects of finite pulse durations the phase takes the form $\phi = n 2kgT^2$. Consequently, transferring momentum to both arms simultaneously, e.g., via DBD will double the sensitivity,

$$\phi = 2n 2kgT^2. \quad (4.74)$$

The twin-lattice scheme combines sequential DBD with the acceleration in Bloch lattices. Sequential momentum kicks as used in Refs. [97, 98] further increase the momentum separation and thereby the sensitivity of the device. If in a double diffraction scheme a number of n_p (infinitely short) pulses separated by a finite time t_{sep} are used to further increase the separation symmetrically, then the sensitivity scales as [214]

$$\phi = 2n(n_p + 1) 2kgT (T - n_p t_{\text{sep}}). \quad (4.75)$$

Because the mean velocity of the atoms only changes during the (instantaneous) pulses the phase still scales quadratically with the effective interrogation time, which is now modified by the waiting time t_{sep} in between the sequential pulses. However, when Bloch sequences

are included, this is no longer the case [57, 215], since the relative velocity changes linearly with time under the assumption of constant acceleration a_L as in Fig. 4.7, leading to a quadratic separation of the space-time trajectories $\Delta y_L(t)$. Using semi-classical arguments one can show that in this case the relative phase is proportional to the space-time area enclosed by the interferometer arms $\phi \propto \mathcal{A}$, with $\mathcal{A} = \int_0^{2T} \Delta y_L(t) dt$ [57].

While this is not true for an arbitrary time dependence $a_L(t)$ [216], this result enables us to make a statement about the scaling of the phase sensitivity of the twin-lattice interferometer with respect to an external acceleration \mathbf{a}_{ext} ⁷. Assuming that the time in between sequential Bragg pulses is sufficiently small, justifying $T - t_{\text{sep}} \approx T$ (see Tab. 4.2), we find [215]

$$\phi = 2 \left(n + N_B \frac{t_{\text{acc}} + t_{\text{free}}}{T} \right) 2\mathbf{k} \cdot \mathbf{a}_{\text{ext}} T^2. \quad (4.76)$$

In order to see the cubic scaling with T we need to assume a constant acceleration a_L during the time $t_{\text{acc}} = N_B T_B$, which we can divide into N_B intervals with the length of the Bloch period in Eq. (4.60). Inserting N_B into the above equation we obtain, in the limit $t_{(\text{un})\text{load}}, t_{\text{free}} \ll t_{\text{acc}} \rightarrow T/2$, the scaling

$$\phi = 4n\mathbf{k} \cdot \mathbf{a}_{\text{ext}} T^2 + \frac{\mathbf{k} \cdot \mathbf{a}_{\text{ext}} T^3}{2T_B}. \quad (4.77)$$

This shows that the twin-lattice geometry forms a combination of the MZ interferometer and an interferometer with a T^3 scaling as long as T_B is constant (cf. Refs. [215, 216]).

4.4.4 Experimental Contrast Analysis

Atom interferometers featuring wave packet separations of hundreds or even thousands of photon recoils require not just LMT beam splitting techniques, which exhibit very good transfer fidelities per $\hbar k$. A key question is, whether these operations maintain the coherence of the atomic ensemble, which is essential for a phase-sensitive atom interferometer. If, as a result of coherent manipulation by means of atomic optics, the population at the outputs of the interferometer exhibits a functional dependence in the form $P(\phi) = P_0 + A \cos(\phi) = P_0 (1 + C \cos(\phi))$, we can introduce the fringe contrast $C := A/P_0$, which serves as a measure of how well the variation of the signal due to a change in phase ϕ can be distinguished from ϕ -independent noise affecting the measurement. A non-vanishing contrast is therefore direct evidence of the sensitivity of the interferometer to phase shifts. We have seen in Chapter 3, the contrast can be inferred by scanning the phase ϕ in the experiment and recording data $\mu_{a(b)}|_{\phi}$ in order to fit an estimator $P(\phi)$

⁷In contrast to the interferometers discussed in Chapter 3 the horizontal alignment makes the twin-lattice interferometer insensitive to a gravitational acceleration. However, such a setup is sensitive to tilts [94, 217] or can be used as a gyroscope [122, 218].

to the measurement data. However, this is not possible in the presence of phase noise in excess of 2π due to a lack of fringe visibility. If ϕ is subject to shot-to-shot fluctuations, e.g., caused by vibrations of the experimental platform transmitted onto the retroreflective mirror in Fig. 4.1(a) the phase is practically randomized [52]. Fortunately, thanks to the underlying functional dependence of the measurement statistics on ϕ , it is still possible to evaluate the contrast by statistical means [103, 124]. In other words, while the visibility of stable fringes is a sufficient condition for the coherence of the atom interferometer, it is not a necessary one.

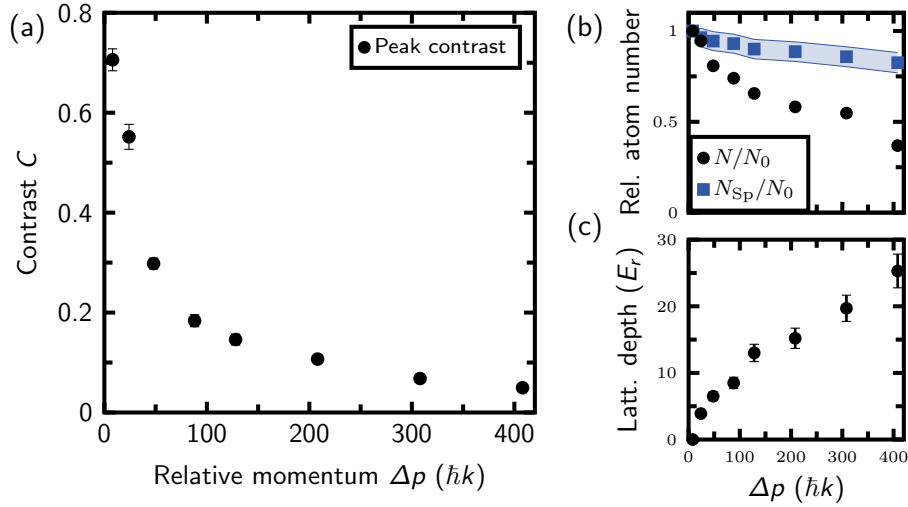


Figure 4.8: **Twin-lattice interferometer contrast data.** (a) Experimental contrast in dependence of momentum transfer Δp for a lattice laser with 3.75 mm beam waist. The analysis of the experimental data is described in Sec. 5 of Ref. [208] including a definition of the error bars that lie below the marker size for most of the data points. (b) Relative atom number N/N_0 measured in the output ports normalized to the DBD interferometer (black circles) with $N_0 := N(\Delta p = 8 \hbar k)$ and considering an absolute error of 0.05. Also, calculated spontaneous emission decay N_{sp}/N_0 (blue squares) with confidence intervals given by the errors in N/N_0 and V_0 . (c) Lattice depth V_0 for different separations Δp with an assumed relative error of 10%. Atom number and lattice depth serve as input parameters for our contrast simulation. Figure adapted from *M. Gebbe et al., Nat. Comm. 12(1):2544 (Ref. [96])*, CC BY 4.0, <https://creativecommons.org/licenses/by/4.0/>.

In the QUANTUS-1 experiment, vibrational noise as large as $10^{-2} \text{ m s}^{-2} \text{ Hz}^{-1/2}$ [219] essentially randomizes the phase even for the smallest interferometer with separation $\Delta p = 8 \hbar k$ [208]. Nonetheless, it is possible to evaluate the contrast if the signal depends on ϕ according to Eq. (4.73). Assuming the phase noise to be uniformly distributed translates into randomized measurement outcomes, the variance of which will depend on C . Specifically, if $\Delta\mu_{a(b)}$ denotes the standard deviation of the measurement data and we assume the offset P_0 to be the same from shot to shot, we can write $C = 2\sqrt{2}\Delta\mu_{a(b)}$ [103, 124, 219]. A more

complete characterization of the coherence of the atom interferometer can be obtained by introducing a shift in time $T + \delta T$ in the second half of the interferometer as we show on the right-hand side of Fig. 4.7. Such an asymmetry introduces a spatial separation between the atomic clouds $\Delta y = \frac{\Delta p}{m} \delta T$, which depends on the timing asymmetry and the differential velocity of the two clouds. As the overlap between the envelopes of the superpositions during the recombination pulse is reduced and the interferometer no longer closes, the fluctuations $\Delta\mu_{a(b)}(\delta T)$ decay and so does the contrast [220], which we will discuss in more detail below in Sec. 4.6.2. To analyze the contrast in the QUANTUS-1 experiment, measurement data $\mu_{a(b)}$ for different values δT are considered, which allow not only to determine the contrast of the closed interferometer $C(\delta T = 0)$ shown in Fig. 4.8(a) as function of the momentum separation Δp , but also to provide information about the coherence length of the BEC source [124, 221]. For more information on the details of the experimental contrast measurement, we kindly refer the reader to Sec. 5 of the dissertation of *M. Gebbe* in Ref. [208], who performed this study as primary researcher.

The following sections are devoted to the question of whether the visible contrast loss towards larger separations Δp in Fig. 4.8(a) is fundamentally connected to the twin-lattice scheme or rather due to the technical limitations of the current experimental setup shown in Fig. 4.4.

4.5 Contrast Model: Atom Loss

Previous experiments suggest that atom loss is one of the main factors limiting the contrast in LMT atom interferometers [97]. Even if the efficiency per photon recoil is high (see Sec. 4.4.3), the losses can be expected to grow exponentially with the number of transitions and the contrast is eventually lost at large momentum separation as the fraction of atoms coherently oscillating with the phase ϕ approaches zero. However, in case of the QUANTUS-1 experiment comparison between the detected total atom number for the Bragg-Bloch interferometers, $N(\Delta p)$, and the DBD interferometer, $N_0 := N(\Delta p = 8 \hbar k)$, in Fig. 4.8(b) demonstrates that at the end of the largest twin-lattice interferometer a fraction of $N(408 \hbar k)/N_0 = 35\%$ remains. Thus, the atom loss is not sufficient to explain the contrast decay in Fig. 4.8(a). In addition, detecting relative atom numbers not only makes the measurement less susceptible to fluctuations of the initial atom number as explained in the previous section, but also makes the contrast more robust to the removal of atoms from the interferometer as long as technical noise can be neglected.

Therefore, it seems most likely that the twin-lattice sequences cause a background of incoherent atoms, N_{incoh} , whose relative fraction increases as the total atom number, $N(\Delta p) = N_{\text{coh}}(\Delta p) + N_{\text{incoh}}(\Delta p)$, decreases according to Fig. 4.8(b). Since all interferometers rely on the same DBD sequence, we conclude that this fraction originates imperfection

of the DBD beam splitters (see Sec. 5.2.1 in Ref. [208]). These initial losses may cause a spurious fraction of atoms with average momentum $0\hbar k$ to overlap with the main interferometer arms at the time of the final pulse without having taken part in the interferometer. If we assume that the final beam splitter distributes the incoherent fraction equally among the output ports, we find for the extreme values with respect to ϕ (here for port a):

$$\mu_{\min} = \min_{\phi \in]0, 2\pi]} \mu_a(\phi) = \frac{N_{\text{incoh}}/2}{N} \quad \text{and} \quad \mu_{\max} = \max_{\phi \in]0, 2\pi]} \mu_a(\phi) = \frac{N_{\text{coh}} + N_{\text{incoh}}/2}{N}. \quad (4.78)$$

Hence, we can express the contrast of the two-mode signal (4.73) as

$$C(\Delta p) = \frac{N_{\text{coh}}(\Delta p)}{N_{\text{coh}}(\Delta p) + N_{\text{incoh}}(\Delta p)} = \frac{N(\Delta p) - N_{\text{incoh}}(\Delta p)}{N(\Delta p)}. \quad (4.79)$$

In this equation we have used that contrast can be expressed in terms of the difference between the maximum and the minimum signal $C = (\mu_{\max} - \mu_{\min})/(\mu_{\max} + \mu_{\min})$. This is justified because the use of first-order DBD pulses suppresses undesired couplings. Accordingly, previous phase-sensitive measurements with an identical beam splitter setup discussed in Ref. [94] did not provide evidence for significant contributions from parasitic interferometry paths to the interferometer signal.

Our goal is to formulate a model that explains that contrast is lost when the Bloch sequences primarily reduce the number of coherent atoms, N_{coh} . To do this, we combine Eq. (4.79) with the experimentally determined atom numbers in Fig. 4.8(b), making the following assumptions:

Assumption (i): Contrast of the DBD Interferometer

The contrast of the DBD interferometer, $C(8\hbar k) = 0.7059 \pm 0.022$ [see Fig. 4.8(a)], is reduced primarily due to the fraction of incoherent atoms, N_{incoh} ⁸. In this case, we can solve Eq. (4.79) for N_{incoh} and insert the experimentally determined values for the contrast $C(8\hbar k)$ and number N_0 in Fig. 4.8,

$$N_{\text{incoh}}(8\hbar k) = N_0[1 - C(8\hbar k)]. \quad (4.80)$$

Assumption (ii): Spontaneous Emission

Spontaneous scattering affects both N_{incoh} and N_{coh} equally and therefore does not impact the contrast according to Eq. (4.79). We justify this assumption by estimating the rate of spontaneous decay for both fractions induced by the twin-lattice laser intensities. Once again, we simplify this de facto three-dimensional problem for the purpose of this calculation by assuming a homogeneous effective lattice depths V_0 as per Fig. 4.8(c) across the

⁸Again, this is only true when the DBD interferometer does not feature parasitic interferometers to a significant degree, which would alter the signal in Eq. (4.73) (see Chapter 3).

cloud based on the large beam waist ~ 3.75 mm compared to the radii of the BEC being in the order of tens of μm . Thus, we only need to adapt the calculations done in Sec. 4.3.4 to account for the potential in Eq. (4.68). First, we evaluate the scattering rate for an atom copropagating with one of the lattices,

$$\begin{aligned} \tilde{V}(\hat{y}, t) = V_0 & \left[\cos^2(k\hat{y}) + \cos^2(k(\hat{y} + 2y_L(t))) \right. \\ & \left. + \frac{\sigma_{\text{pol}}}{1 - \sigma_{\text{pol}}} 2 \cos(k\hat{y}) \cos(k(\hat{y} + 2y_L(t))) \right]. \end{aligned} \quad (4.81)$$

Here, we have introduced a shift in position, $\hat{y} \rightarrow \hat{y} + y_L(t)$, consistent with the center-of-mass velocity of the wave packet, $v_{\text{BEC}}(t) = +v_L(t) = \delta(t)/k$ [cf. Eq. (4.46a)]. In a blue-detuned potential, the first term associated with the copropagating lattice averages to $\langle \cos^2(k\hat{y}) \rangle = \frac{1}{2} \sqrt{E_r/V_0}$ (see Sec. 4.3.4). To evaluate the time-dependent cos-functions we can compare the time scale relevant for the shift in position $y_L(t) = \delta(t)/k$ to the scattering rate $\Gamma_{\text{sp,blue}}$ (4.65), which is much smaller in the QUANTUS-1 experiment because of the 100 GHz detuning from resonance,

$$\Gamma_{\text{sp,blue}} \propto \frac{\Gamma_{\text{nat}}}{|\Delta|} \omega_r \ll \omega_r < \delta(t). \quad (4.82)$$

Hence, the temporal averages for the other terms read

$$\langle \cos^2(k(\hat{y} + 2y_L(t))) \rangle \approx \frac{1}{2} \quad \text{and} \quad \langle \cos(k\hat{y}) \cos(k\hat{y} + 2\delta t) \rangle \approx 0. \quad (4.83)$$

Inserting these results into Eq. (4.63) yields the total emission rate for an atom copropagating with one of the lattices

$$\Gamma_{\text{twin}}(V_0) = \frac{\Gamma_{\text{nat}}}{|\Delta|} \frac{V_0}{\hbar} \left[\frac{1}{2\sqrt{V_0/E_r}} + \frac{1}{2} \right]. \quad (4.84)$$

Using the form of the parasitic term in Eq. (4.69), we find a very similar result for an atom that has been lost during the first beam splitting pulse with $v_{\text{BEC}} = 0 \hbar k$,

$$\Gamma_{0\hbar k}(V_0) = \frac{\Gamma_{\text{nat}}}{|\Delta|} \frac{V_0}{\hbar} \left[1 + 2 \frac{\sigma_{\text{pol}}}{1 - \sigma_{\text{pol}}} \left(\frac{1}{2\sqrt{V_0/E_r}} - \frac{1}{2} \right) \right]. \quad (4.85)$$

Comparing both scattering rates and assuming $\sigma_{\text{pol}}/(1 - \sigma_{\text{pol}}) \approx 0.37$ (see Sec. 4.4.2), we find that both scattering rates differ only by a few percent with $\Gamma_{0\hbar k} \gtrsim \Gamma_{\text{twin}}$, confirming our initial hypothesis that spontaneous emission affects all classes of atoms to a similar extent. Therefore, in the following we consider only a single scattering rate Γ_{twin} for all atoms and insert this rate into Eq. (4.62). The surviving fraction of atoms after being exposed to the twin lattice for a time t_{twin} thereby reads,

$$N_{\text{sp}}(\Delta p) := N_0 \cdot \exp(-\Gamma_{\text{twin}}(V_0) \cdot t_{\text{twin}}). \quad (4.86)$$

We plot the ratio N_{sp}/N_0 in Fig. 4.8(b) including the 10 % uncertainty in the experimentally determined peak lattice depth, V_0 . Assuming $N_{\text{incoh}}(\Delta p)$ is reduced only by spontaneous scattering, we can also use Eq. (4.86) to estimate the incoherent fraction of all other twin lattice interferometers when combined with Eq. (4.80),

$$N_{\text{incoh}}(\Delta p) = N_{\text{incoh}}(8 \hbar k) \cdot \exp(-\Gamma_{\text{twin}}(V_0) \cdot t_{\text{twin}}) = N_{\text{sp}}(\Delta p)[1 - C(8 \hbar k)]. \quad (4.87)$$

Assumption (iii): LZ Losses

Non-adiabatic LZ losses during the Bloch sequences remove coherent atoms from the interferometer and therefore reduce $N_{\text{coh}}(\Delta p)$, resulting in a loss of contrast. Atoms lost through LZ transitions are expected to be spatially well separated from the output ports and thus are unlikely to couple back into the interferometer. Meanwhile, it is reasonable to assume that atoms $N_{\text{incoh}}(\Delta p)$ do not perform BO due to their velocity detuning (see Sec. 4.4.2) and hence are only affected by spontaneous emission as described above. The combination of the above aspects allows us to give the estimated contrast (4.79) for all twin-lattice interferometers,

$$C_A(\Delta p) := \frac{N(\Delta p) - N_{\text{incoh}}(\Delta p)}{N(\Delta p)} = 1 - \frac{1 - C(8 \hbar k)}{N(\Delta p)/N_{\text{sp}}(\Delta p)}. \quad (4.88)$$

To evaluate this expression, one must input the experimentally determined atom numbers, $N(\Delta p)$, the contrast of the DBD interferometer, $C(8 \hbar k)$, and the calculated spontaneous emission losses, $N_{\text{sp}}(\Delta p)$. All of these quantities are plotted in Figs. 4.8(a) and (b).

Looking at the data for the contrast in Fig. 4.8(a) and for N/N_0 it is clear that the model in Eq. (4.88) by itself cannot explain the functional dependence of C on the momentum separation Δp , which features a steep initial decline followed by an almost asymptotic profile for $\Delta p > 88 \hbar k$. Moreover, our model treats spontaneous emission losses in the twin-lattice interferometer as a mere loss channel. This is based on the assumption that the vast majority of spontaneously scattered atoms are separated from the output ports due to the use of delta-kick collimated BECs with momentum widths far below the photon recoil (see Sec. 5.2.1 in Ref. [208]). Nevertheless, it would certainly be fruitful to investigate more thoroughly the consequences of spontaneous emission for the properties of an atom interferometer using BO beyond this simple contrast model. Unfortunately, this is beyond the scope of this thesis.

4.6 Contrast Model: Light Field

A second potential source for a loss of contrast is the light field of the twin-lattice lasers. Previous experiments have demonstrated that realistic electric fields, which deviate from

the idealized case of a homogeneous plane wave, can have significant effects on the performance of atom interferometers [85, 86, 118, 179, 222]. The most convincing evidence for this is, on the one hand, the contrast improvements in LMT atom interferometers with large separations made possible by the implementation of a so-called "ac-Stark compensation" [118, 124]. This technique suppresses absolute light shifts caused by intensity variations that induce local changes to the dipole potential. On the other hand, it is very likely that the recent realization of atomic interferometers with unprecedented coherence times of tens of seconds was made possible in large part by optical mode filtering of the cavity environment [87, 88].

The QUANTUS-1 experiment operates in free space, and the space-time trajectories in Fig. 4.7 show that the larger the momentum separation, the larger the region of the light field probed by the interferometer arms. It can be assumed that this will make the interferometers increasingly susceptible to perturbations of the electric field. At the same time, Fig. 4.8(c) highlights that to suppress LZ losses during the Bloch ramps in the experiment, the average lattice depth V_0 is increased with Δp , which also increases the strength of these perturbations.

According to our explanation in Sec. 3.1, the wave form $P(\phi)$ in Eq. (4.73) typically establishes a functional dependence between ϕ and the first momentum of the measurement statistics $\bar{\mu}$. Consequently, $C := A/P_0 \leq 1$ represents the contrast after averaging over the atomic ensemble during the measurement process. This means that, in principle, contrast is lost in two different ways: First, due to a reduction in the single-particle contrast, e.g., caused by an unbalanced beam splitter (i.e., deviation from a 50/50 ratio), due to spontaneous emission [223] or as a result of an open interferometer [220]. Second, dephasing of the atomic ensemble can decrease the average fringe contrast, which has been attributed in the past to the deformation of realistic laser wavefronts [66–68] as well as distortions of the intensity profile of the laser [85, 86]. Both mechanisms play a crucial role in the formulation of an empirical model for the contrast loss reported for the twin-lattice interferometer realized in the QUANTUS-1 experiment. Before doing so, however, we first establish a more formal framework that captures both contributions to the contrast on atom interferometers.

4.6.1 Single Particle Contrast

Let $|\psi^{\text{out}}\rangle \equiv |\psi^{\text{out}}(t)\rangle$ be the quantum state after the final beam splitter, $t > 2T$, at the output of the interferometer as depicted in Fig. 4.7. In the previous chapter, we have expanded this state in a basis of spatial trajectories corresponding to sets of momentum states, which was instrumental in defining a scattering matrix to describe multi-port, multi-path atom interferometers (cf. Sec. 3.3). In the idealized case of a lossless two-mode interferometer,

it is often useful to express the state $|\psi^{\text{out}}\rangle$ as a superposition of the atomic wave packet exiting the interferometer via the ports a and b ⁹,

$$|\psi^{\text{out}}\rangle = \frac{1}{\sqrt{2}}(|\psi_a^{\text{out}}\rangle + |\psi_b^{\text{out}}\rangle). \quad (4.89)$$

If there are no losses, probability is conserved, $\langle\psi^{\text{out}}|\psi^{\text{out}}\rangle = 1$, and we find

$$1 = \langle\psi^{\text{out}}|\psi^{\text{out}}\rangle = \frac{1}{2}\langle\psi_a^{\text{out}}|\psi_a^{\text{out}}\rangle + \frac{1}{2}\langle\psi_b^{\text{out}}|\psi_b^{\text{out}}\rangle =: \mu_a + \mu_b, \quad (4.90)$$

where we have introduced the probability for a single particle to be detected in ports a and b , $\mu_{a(b)} = \langle\psi_{a(b)}^{\text{out}}|\psi_{a(b)}^{\text{out}}\rangle/2$. It is convenient to interpret the quantum state in either output port as superpositions of wave packets travelling along the different arms of the interferometer (labeled 'left' and 'right'),

$$|\psi_a^{\text{out}}\rangle = \frac{1}{\sqrt{2}}(|\psi_a^{\text{left}}\rangle + |\psi_a^{\text{right}}\rangle). \quad (4.91)$$

This interpretation was successfully applied in the past to study the physics of conjugate Ramsey-Bordé interferometers [118] as well as the features of open interferometers [220]. In Eq. (4.91), we have labeled the two arms depending on whether they propagate in negative ("left") or positive ("right") y -direction as can be seen in Fig. 4.7. Using this convention and assuming $\langle\psi_a^{\text{left}}|\psi_a^{\text{left}}\rangle = 1 = \langle\psi_a^{\text{right}}|\psi_a^{\text{right}}\rangle$, the probability to detect an atom in port a (for any MZ type atom interferometer) becomes

$$\begin{aligned} \mu_a &= \frac{1}{2}\langle\psi_a^{\text{out}}|\psi_a^{\text{out}}\rangle = \frac{1}{4}\langle\psi_a^{\text{right}}|\psi_a^{\text{right}}\rangle + \frac{1}{4}\langle\psi_b^{\text{left}}|\psi_b^{\text{left}}\rangle + \frac{1}{2}\text{Re}\{\langle\psi_a^{\text{left}}|\psi_a^{\text{right}}\rangle\} \\ &= \frac{1}{2}\left(1 + \text{Re}\{\langle\psi_a^{\text{left}}|\psi_a^{\text{right}}\rangle\}\right). \end{aligned} \quad (4.92)$$

The last equation shows that the probability of detecting a single particle in port a is determined by the overlap between the wave packets travelling along the different trajectories. In particular, the overlap is a complex number, $\langle\psi_a^{\text{left}}|\psi_a^{\text{right}}\rangle = \langle\psi_a^{\text{right}}|\psi_a^{\text{left}}\rangle^* \in \mathbb{C}$, which means that we can write

$$\langle\psi_a^{\text{left}}|\psi_a^{\text{right}}\rangle \equiv C_0 e^{i\Phi}. \quad (4.93)$$

Here, we have introduced the single-particle contrast and the relative phase between the two wave packets travelling along the two different arms of the interferometer

$$C_0 \equiv |\langle\psi_a^{\text{left}}|\psi_a^{\text{right}}\rangle|, \quad (4.94a)$$

$$\Phi \equiv \text{Im}\left\{\ln\left(\frac{\langle\psi_a^{\text{left}}|\psi_a^{\text{right}}\rangle}{|\langle\psi_a^{\text{left}}|\psi_a^{\text{right}}\rangle|}\right)\right\}. \quad (4.94b)$$

⁹We remind the reader that due to the fact that the twin-lattice interferometer is fundamentally a double diffraction interferometer, the two ports are composed of a single inner $\mu_a = N_{0\hbar k}/N$ and the two outer ports $\mu_b := (N_{2\hbar k} + N_{-2\hbar k})/N$ shown in Fig. 4.7.

In combination with Eq.(4.92), we can express the probability of a single particle to exit the interferometer in port a in the familiar form

$$\mu_a = \frac{1}{2}(1 + C_0 \cos(\Phi)). \quad (4.95)$$

4.6.2 Contrast Loss in Open Interferometers

Our goal is to analyze the reduction of C_0 in the case of imperfect closure of the interferometer. Contrast may be lost when the trajectories of the interferometer arms do not overlap perfectly in phase space at the time of the last pulse, $t = 2T$. A detailed analysis of open interferometers due to gravity gradients was presented by the authors *A. Roura* et al. [220]. While we only give a brief overview of their main results as part of our contrast model, we recommend the reader to refer to this work and the related PhD thesis of one of the co-authors *W. Zeller* in Ref. [224] for a more detailed account.

Formally, a relative displacement $(\delta\mathbf{x}, \delta\mathbf{p})$ in phase space between the center-of-mass coordinates of two otherwise identical wave packets in port a results in a phase shift potentially reducing C_0 ,

$$C_0 = |\langle \psi_a^{\text{left}} | \psi_a^{\text{right}} \rangle| = |\langle \psi | e^{i(\delta\mathbf{p}\hat{\mathbf{x}} - \delta\mathbf{x}\hat{\mathbf{p}})/\hbar} | \psi \rangle| \leq 1. \quad (4.96)$$

Such a displacement can originate, e.g., due to an asymmetry of the interferometer by introducing a timing delay δT of the final beam splitter. This leads to a position offset, $\delta\mathbf{x} = \Delta\mathbf{v}\delta T$, where $\Delta\mathbf{v}$ is the relative velocity of the wave packets during the time δT . To provide a more intuitive understanding of how C_0 can be affected by the relative phase in Eq. (4.96), it is useful to write the wave packets in position representation:

$$\psi_a^{\text{left}}(\mathbf{x}, t) = \langle \mathbf{x} | \psi_a^{\text{left}} \rangle \quad \text{and} \quad \psi_a^{\text{right}}(\mathbf{x}, t) = \langle \mathbf{x} | \psi_a^{\text{right}} \rangle. \quad (4.97)$$

In this representation, the single-particle contrast takes the form of an integral,

$$C_0 = \left| \int d^3\mathbf{x} \exp\left(\frac{i}{\hbar}\delta\mathbf{p} \cdot \mathbf{x}\right) \psi^*(\mathbf{x} + \delta\mathbf{x}/2, t) \psi(\mathbf{x} - \delta\mathbf{x}/2, t) \right|, \quad (4.98)$$

where we have displaced both wave packets equidistantly from the origin. At first glance, it is obvious that contrast will be lost if the spatial overlap between the wave packets at the time of the last beam splitting pulse vanishes. This effect is exploited in atom interferometry experiments performing contrast measurements in the presence of inertial phase noise greater than 2π , as we have explained in Sec. (4.4.4). Assuming otherwise perfect overlap of the interferometer arms, the delay δT in the second half of the twin-lattice scheme (cf. the right-hand side of Fig. 4.7) causes an offset in the direction of the beam splitter, $\delta y = \Delta p \delta T / M$, the magnitude of which depends on the momentum separation Δp . According to Eq. (4.98), this offset has to be compared to the spatial extent of the wave packets,

which in the case of the QUANTUS-1 experiment is determined by the Thomas-Fermi radii of the BEC (4.21). Varying δT , one can record the controlled decay of C_0 as evidence for the coherence of the ensemble, although it is not possible to observe stable fringes of the form of Eq.(4.95) [124, 221].

However, we focus on relating the contrast loss for increasing Δp and $\delta T = 0$ shown in Fig. 4.8(a) to the phase term in Eq. (4.98). To this end, we study the expression for C_0 after a sufficiently long time of flight after the final beam splitter, t_{TOF} , so that the output ports are spatially well separated and the clouds have freely expanded. In this limit, the expression in Eq. (4.98) simplifies to [220]

$$C_0 \approx \left| \int d^3\mathbf{x} \exp\left(\frac{i}{\hbar} \left(\delta\mathbf{p} - \frac{M}{t_{\text{TOF}}}\delta\mathbf{x}\right)^T \cdot \mathbf{x}\right) |\psi(\mathbf{x}, t_{\text{TOF}})|^2 \right|. \quad (4.99)$$

Thus, a displacement in phase space translates into spatially dependent interference fringes [59] characterized by the wave vector

$$\frac{2\pi}{\lambda_{\text{fr}}} \hat{\mathbf{n}} = \frac{1}{\hbar} (\delta\mathbf{p} - \frac{M}{t_{\text{TOF}}}\delta\mathbf{x}). \quad (4.100)$$

From Eq. (4.99) it can be deduced that contrast is lost when the fringe spacing is significantly smaller than the spatial extent of the atomic cloud. In this case, these fringes usually cannot be resolved during detection, and the contrast is "washed out" as performing the integral averages over the spatial pattern. In the next sections, we examine how intensity fluctuation of the twin-lattice laser can cause the interferometer to fail to close properly at the time of the recombination pulse $t = 2T$, and how C_0 is further reduced as a result of phase variations across the ensemble.

4.6.3 Contrast Loss due to Dephasing

During the discussion of the signal of multi-port MZ interferometers in Sec. 3.4.2, we have already mentioned that fringe visibility is lost when the spurious interferometry arms are sufficiently populated and when their contributions to the signal are out of phase (cf. Sec. 5 in Ref. [147]). Similarly, the contrast of a two-mode interferometer can be lost due to dephasing across the atomic ensemble. Experiments realizing Ramsey-Bordé atom interferometers with BO have shown that interaction with inhomogeneous laser potentials can lead to large phase variations over time, depending on how the atomic cloud moves and expands in the light field [85–88]. Such phases can be caused by light shifts [88], random velocity changes due to spontaneous emission [85, 86, 223], or the effects of speckle patterns on the laser beam [85, 86], and result in a loss of contrast when averaging over the phase space distribution of the cloud during detection.

To model the effect of an inhomogeneous phase evolution on the signal, we simply add a parameter-dependent phase shift to the phase in Eq. (4.95) following Refs. [225, 226],

$$\Phi = \phi + \delta\phi(\lambda). \quad (4.101)$$

In this case, the probability in Eq. (4.95) depends on the parameter, i.e., $\mu_a = \mu_a(\lambda)$, and assuming that the measurement process requires averaging over the (for now) arbitrary probability distribution, $1 = \int \mathcal{P}(\lambda) d\lambda$, we find the average signal using Eqs. (4.92) and (4.93):

$$\begin{aligned} \bar{\mu}_a &= \int \mathcal{P}(\lambda) \mu_a(\lambda) d\lambda = \frac{1}{2} \left[\int \mathcal{P}(\lambda) d\lambda + \int \mathcal{P}(\lambda) \operatorname{Re}\{C_0 e^{i\phi + \delta\phi(\lambda)}\} d\lambda \right] \\ &= \frac{1}{2} \left[1 + \operatorname{Re}\left\{ e^{i\phi} \int \mathcal{P}(\lambda) C_0 e^{i\delta\phi(\lambda)} d\lambda \right\} \right], \\ \bar{\mu}_a &= \frac{1}{2} \left[1 + \bar{C} \operatorname{Re}\{ e^{i(\phi + \bar{\delta}\phi)} \} \right] = \frac{1}{2} \left[1 + \bar{C} \cos(\phi + \bar{\delta}\phi) \right]. \end{aligned} \quad (4.102)$$

In the last line of this equation, we have introduced the average contrast and average phase shift

$$\bar{C} e^{i\bar{\delta}\phi} \equiv \int \mathcal{P}(\lambda) C_0 e^{i\delta\phi(\lambda)} d\lambda, \quad (4.103)$$

where the contrast is simply defined by

$$\begin{aligned} \bar{C} &\equiv \left| \int \mathcal{P}(\lambda) C_0 e^{i(\phi + \delta\phi(\lambda))} d\lambda \right| = C_0 \left| \int \mathcal{P}(\lambda) e^{i\delta\phi(\lambda)} d\lambda \right| \\ &= C_0 \left[\left(\int \mathcal{P}(\lambda) e^{i\delta\phi(\lambda)} d\lambda \right) \left(\int \mathcal{P}(\lambda) e^{-i\delta\phi(\lambda)} d\lambda \right) \right]^{\frac{1}{2}} \\ \bar{C} &= C_0 \left[\left(\int \mathcal{P}(\lambda) \cos(\delta\phi(\lambda)) d\lambda \right)^2 + \left(\int \mathcal{P}(\lambda) \sin(\delta\phi(\lambda)) d\lambda \right)^2 \right]^{\frac{1}{2}}. \end{aligned} \quad (4.104)$$

In addition, we can define the average phase shift, $\bar{\delta}\phi$, using the identities

$$\bar{C} e^{i\bar{\delta}\phi} \equiv \int \mathcal{P}(\lambda) C_0 e^{i(\delta\phi(\lambda))} d\lambda \quad (4.105)$$

$$\Leftrightarrow \bar{C} (\cos(\bar{\delta}\phi) + i \sin(\bar{\delta}\phi)) \equiv \int \mathcal{P}(\lambda) C_0 \cos(\delta\phi(\lambda)) d\lambda + i \int \mathcal{P}(\lambda) C_0 \sin(\delta\phi(\lambda)) d\lambda. \quad (4.106)$$

By comparing the coefficients, the following relationships can be determined

$$\bar{C} \cos(\bar{\delta}\phi) = \int \mathcal{P}(\lambda) C_0 \cos(\delta\phi(\lambda)) d\lambda, \quad (4.107)$$

$$\bar{C} \sin(\bar{\delta}\phi) = \int \mathcal{P}(\lambda) C_0 \sin(\delta\phi(\lambda)) d\lambda, \quad (4.108)$$

the quotient of which yields

$$\tan(\bar{\delta\phi}) = \frac{\sin(\bar{\delta\phi})}{\cos(\bar{\delta\phi})} = \frac{\int \mathcal{P}(\lambda) \sin(\delta\phi(\lambda)) d\lambda}{\int \mathcal{P}(\lambda) \cos(\delta\phi(\lambda)) d\lambda}. \quad (4.109)$$

Assuming that the perturbative phase shift is small so that $\sin(\delta\phi(\lambda)) \approx \delta\phi(\lambda)$, and assuming that the probability distribution is symmetric, $\mathcal{P}(\lambda) = \mathcal{P}(-\lambda)$, while the shift itself is an asymmetric function, $\delta\phi(\lambda) = -\delta\phi(-\lambda)$, with $\left(\int \mathcal{P}(\lambda) \sin(\delta\phi(\lambda)) d\lambda\right)^2 \approx 0$, we find

$$\bar{C} \approx C_0 \int \mathcal{P}(\lambda) \cos(\delta\phi(\lambda)) d\lambda. \quad (4.110)$$

This expression has been used, e.g., in Refs. [85, 227] to characterize the exponential contrast decay due to random phase shifts $\delta\phi = 2 k_{\text{eff}} \delta v T$. In these cases, the velocity variations δv were caused by speckle patterns on the laser beams and characterized by a Lorentzian probability distribution $\mathcal{P}(\delta v)$. To model the contrast loss in the twin-lattice interferometer, we combine the expression for the single-particle contrast in Eq. (4.99) with the result in Eq. (4.110):

From a semiclassical point of view, our main idea is that we can interpret the center-of-mass trajectories in Fig. 4.7 as representatives for ensembles of single-particle trajectories, all of which have slightly different starting positions located within the finite spatial distribution of the atomic cloud at the beginning of the interferometer. This motivates introducing the starting coordinates $\mathbf{x}_0 = (x_0, y_0, z_0) \in \{\mathbf{x} \in \mathbb{R}^3 | 0 \leq |\psi(\mathbf{x}, t=0)|^2\}$ determined by the spatial probability distribution $|\psi(\mathbf{x}, t=0)|^2$. The contrast of the ensemble is then obtained by averaging over the initial positions,

$$\begin{aligned} C &= \int d^3\mathbf{x}_0 |\psi(\mathbf{x}_0, t=0)|^2 C_0(\mathbf{x}_0, t) \\ &\approx \int d^3\mathbf{x}_0 |\psi(\mathbf{x}_0, t=0)|^2 \left| \int d^3\mathbf{x} \exp\left(\frac{i}{\hbar} \left(\delta\mathbf{p}(\mathbf{x}_0) - \frac{M}{t_{\text{TOF}}} \delta\mathbf{x}(\mathbf{x}_0) \right) \cdot \mathbf{x} \right) |\psi(\mathbf{x}, t_{\text{TOF}})|^2 \right|. \end{aligned} \quad (4.111)$$

Since we assume that the relative displacement between the two arms of the interferometer depends on the initial starting position within the atomic cloud, $(\delta\mathbf{x}, \delta\mathbf{p}) = (\delta\mathbf{x}(\mathbf{x}_0), \delta\mathbf{p}(\mathbf{x}_0))$, both $|\psi(\mathbf{x}_0, t=0)|^2$ and $|\psi(\mathbf{x}, t_{\text{TOF}})|^2$ determine the value of the integrals in Eq.(4.111). In principle, the initial conditions of the trajectories additionally depend on the velocity distribution of the atomic ensemble at the start of the interferometer. Conceptually, however, this makes little difference and is therefore neglected to reduce the complexity of our model.

In the next section, we evaluate the contrast integral in Eq. (4.111) assuming that the phase shifts are caused by dipole forces resulting from intensity fluctuations of the lattice beam. Moreover, Eq. (4.109) implies that systematic phase shifts, $\bar{\delta\phi}$, can also be a consequence of the inhomogeneous phase shifts accumulated during the interrogation. In atom

interferometry, such shifts occur mainly as a consequence of wavefront errors and are often discussed in the context of atom interferometers using laser cooled atoms due to the large cloud sizes relative to the dimensions of the laser beams [66–68, 89]. In many of these cases, the dephasing is the result of different parts of the atomic cloud interacting with different parts of the phase fronts of the three-dimensional laser, either because the cloud is expanding or because it is moving off-axis. In the QUANTUS-1 experiment, effects due to the finite curvature of the wavefronts or the Gouy phase of the Gaussian beam used could possibly be exacerbated by the fact that the atomic cloud falls vertically through the horizontally aligned beam and therefore samples a significant portion of the laser profile off-axis (see Fig. 4.4). Conversely, because of its inherent symmetry, the twin-lattice scheme should be inherently insensitive to phase fluctuations of the laser, and, to some extent, to imperfections of the laser profile, especially when a large and well-collimated beam and a comparatively small atomic cloud with low expansion rates are used.

4.6.4 Distorted Light-field Model

To assess the impact of a distorted light field on the signal of the interferometer, we estimate contrast loss due to dephasing as predicted by Eq. (4.111). Perturbations of the intensity profile of the laser can result, e.g., from diffraction on the edge of the atom chip (see Fig. 4.4) and induce spatially variable dipole forces [85, 86]. Fundamentally, we interpret the atomic cloud as an ensemble of single-particle trajectories with different initial conditions determined by $|\psi(\mathbf{x}_0, t = 0)|^2$. As the twin-lattice sequence progresses, the trajectories of the individual atoms in this semiclassical picture interact with slightly different parts of the laser via the dipole force, which can prevent the individual paths from perfectly overlapping at $t = 2T$, leading to phase variations in the wave packet.

First, we set $\delta\mathbf{x} = 0$, simplifying the expression in Eq. (4.111). This is based on the experimental observation that a non-ideal spatial overlap, especially in the direction of the twin lattice, can be excluded, since it would introduce a dependence on the asymmetry δT in the determination of the contrast, which is not confirmed by the measurements (see Sec. 5.1.3 in Ref. [208]). Second, to calculate the phases caused by imperfect overlap in momentum space, e.g., in the direction of the beam splitter, δp_y , we determine the path-dependent dipole forces resulting from the gradient of the lattice beam potential,

$$U(\mathbf{x}, t; \Delta p) = U_0(\Delta p) \frac{I(\mathbf{x}, t)}{I_0(t)}. \quad (4.112)$$

Here, $I_0(t) := \max_{\mathbf{x} \in \mathbb{R}^3} \{I(\mathbf{x}, t)\}$ is the peak intensity of the diffracted twin-lattice laser and $U_0(\Delta p) = V_0(\Delta p)/(1 - \sigma_{\text{pol}})$ is the maximum depth of the dipole potential, which depends on Δp via $V_0(\Delta p)$ [see Fig. 4.8(c)]. The experimental setup in Fig. 4.4 features several potential sources of diffraction, such as apertures (vacuum windows etc.) or the edge of

the atom chip. For our theoretical analysis, we assume that the incoming Gaussian beam is diffracted at a metallic edge representing the atom chip [228], as shown in Fig. 4.9(a). We calculate the differential momentum between the two arms, $\delta p_{x_j} := p_{x_j, \text{arm1}} - p_{x_j, \text{arm2}}$

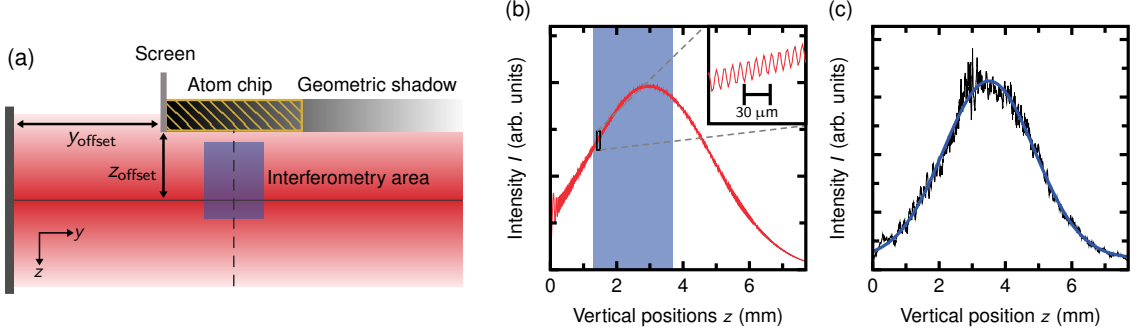


Figure 4.9: **Schematic of simulated light field and measured beam profile.** (a) Horizontal Gaussian beam refracted on a single metallic edge, which represents the atomic chi (not to scale) in Fig. 4.4 in our simplified model. (b) Vertical cross-section of the calculated intensity profile along the center of the interferometry area shown in Fig. 4.7, where the falling distance of the interferometer arms is shaded in blue [corresponding to a cut through the blue region in (a)]. The diffraction at the edge causes a clearly visible diffraction pattern with oscillations of $\sim 1\%$ on length scales smaller than the Thomas-Fermi radii of the BEC of about $30\ \mu\text{m}$ (see inset). (c) Vertical slice through the center of the experimentally determined intensity profile of the twin-lattice beam (black line), taken with a beam profile camera after passing through the vacuum chamber. The blue line represents a Gaussian fit to the data showing intensity variations in the order of $\sim 10\%$. Figures (b) and (c) adapted from *M. Gebbe et al.*, Nat. Comm. **12**(1):2544 (Ref. [96]), CC BY 4.0, <https://creativecommons.org/licenses/by/4.0/>.

with $x_j = x, y, z$, by integrating the dipole force along the single-particle trajectories for each arm, $\mathbf{x}_{\text{arm}} = \mathbf{x}_{\text{arm}}(\mathbf{x}_0, t; \Delta p)$, yielding

$$\begin{aligned} p_{x_j, \text{arm}}(\mathbf{x}_0, 2T; \Delta p) &= - \int_0^{2T} \frac{\partial}{\partial x_j} U(\mathbf{x}_{\text{arm}}, t; \Delta p) dt, \\ &= -U_0(\Delta p) \int_0^{2T} \frac{\partial}{\partial x_j} \frac{I(\mathbf{x}_{\text{arm}}, t; \Delta p)}{I_0(t)} dt. \end{aligned} \quad (4.113)$$

We assume that the trajectories, $\mathbf{x}_{\text{arm}}(\mathbf{x}_0, t; \Delta p)$, adiabatically follow the motion of the twin-lattice illustrated by the paths in Fig. 4.7. Thus, each path is determined by the twin-lattice sequences (and thereby Δp , see right-hand side of Fig. 4.7) and their initial conditions at $t = 0$, $\mathbf{x}_0 = (x_0, y_0, z_0)$. Furthermore, since the twin-lattice laser beam is well collimated and the atomic motion in the x -direction is negligible compared to the other directions, we set $\delta p_x = 0$ and assume that the motion in the x direction makes no relevant contribution to the contrast loss. As a result, it is sufficient for our model to find the two-dimensional

intensity distribution, $I(y, z, t) = |E(y, z, t)|^2$, of a single Gaussian beam propagating in positive y -direction with wave number $k = \frac{\pi}{\lambda_L}$

$$E_{\text{Gauss}}(y, z, t) = E_0(t) \left(\frac{w_0}{w(y)} \right) \exp \left(\frac{-(z - z_{\text{offset}})^2}{w^2(y)} \right) \exp \left(-i \left[ky + k \frac{(z - z_{\text{offset}})^2}{2R(y)} + \zeta(y) \right] \right), \quad (4.114)$$

that is clipped at a metallic edge acting as a screen, see Fig. 4.9(a). We proceed by solving the Fresnel integral for the diffracted electric field numerically [228],

$$E(y, z, t) = \frac{1}{\sqrt{2\pi}} \int_{-k}^k \exp \left\{ i \left(k_z z + y \sqrt{k^2 - k_z^2} \right) \right\} \text{Ker}(k_z, y, z) \mathcal{F}(E_{\text{Gauss}}(y, z, t)) dk_z, \quad (4.115)$$

with the help of the Fourier transformation in z -direction

$$\mathcal{F}(E_{\text{Gauss}}(y, z, t))(y, k_z, t) = \frac{1}{\sqrt{2\pi}} \int_{-\infty}^{+\infty} E_{\text{Gauss}}(y, z, t) \exp\{-ik_z z\} dz, \quad (4.116)$$

and the approximate integration kernel $\text{Ker}(k_z, y, z)$ suggested in Eq. (9) of Ref. [228]. The incoming Gaussian beam in Eq.(4.114) is characterized by its waist $w(y)$, a phase front curvature $R(y)$ and a Gouy phase $\zeta(y)$, which are determined by the beam parameters in Tab. 4.3 using the relations

$$w(y) = w_0 + y \tan(\theta_{\text{div}}), \quad (4.117a)$$

$$R(y) = y \left[1 + \left(\frac{y_R}{y} \right)^2 \right], \quad (4.117b)$$

$$\zeta(y) = \arctan \left(\frac{y}{y_R} \right). \quad (4.117c)$$

We show in Fig. 4.9(a) that the incoming beam travels a distance of $y_{\text{offset}} \approx 238$ mm before it is diffracted on the edge. Since the diffracted beam originates from this edge, we have

| Parameter | Symbol | Value |
|-------------------|-----------------------|----------------|
| Laser wavelength | λ_L | 780.2412 nm |
| Beam waist | w_0 | 3.5 mm |
| Rayleigh range | y_R | ≈ 60 m |
| Divergence angle | θ_{div} | 0.008° |
| Horizontal offset | y_{offset} | 238.5 mm |
| Vertical offset | z_{offset} | 3 mm |

Table 4.3: **Diffraction model input parameters.** The input parameters for our model for a light field diffracted on a metallic edge, see Fig. 4.9(a). The Gaussian beam parameters correspond to those used in the QUANTUS-1 experiment.

shifted the origin in y -direction accordingly $y \rightarrow y + y_{\text{offset}}$ to simplify our notation. Because of its large waist and the fact that the axis of the Gaussian beam is offset only a few millimeters below the edge, the vertical cross section of the intensity profile in Fig. 4.9(b) clearly shows that diffraction at the edge causes local variations of the intensity profile on top of the Gaussian envelope. While the blue shaded region indicates the vertical distance traveled by the atoms in free fall during interrogation, the zoom in the inset highlights that the typical length scale of the fluctuations in the z direction ($\sim \mu\text{m}$) is much smaller than the radii of the atomic cloud ($\sim 30 \mu\text{m}$), possibly enhancing the dephasing due to locally varying gradients. Using the intensity of the light field in Eq. (4.115), we can evaluate $\delta\mathbf{p} = \delta\mathbf{p}(\mathbf{x}_0, 2T; \Delta p) = (0, \delta p_y, \delta p_z)$ via Eq. (4.113) and predict the contrast loss due to a distorted light field,

$$C_L(\Delta p) := \int d^3\mathbf{x}_0 |\psi_{\text{TF}}(\mathbf{x}_0, 0)|^2 \left| \int d^3\mathbf{x} \exp\left(\frac{i}{\hbar} \delta\mathbf{p}(\mathbf{x}_0) \cdot \mathbf{x}\right) |\psi_{\text{TF}}(\mathbf{x}, t_{\text{TOF}})|^2 \right|. \quad (4.118)$$

To do so, we approximate the density distributions of the atomic cloud via the Thomas-Fermi solutions in Eq. (4.20). We define the density of the wave function via the Thomas-Fermi Radii, which we calibrate to measurements giving us $\mathbf{R}_{\text{TF}}(t = 0) = (22, 25, 20) \mu\text{m}$ and $\mathbf{R}_{\text{TF}}(t = t_{\text{TOF}}) = (33, 39, 30) \mu\text{m}$.

Comparison between Figs. 4.9(b) and (c) suggests that in our model intensity perturbations, $|I(\mathbf{x}, t) - I_{\text{Gauss}}(\mathbf{x}, t)|/I_0(t) \sim 1\%$, are much weaker than in the experiment, where measurements behind the experimental chamber show intensity fluctuations in the order of 10%. However, this discrepancy is to be expected as our model assumes diffraction on a single edge, which underestimates the experimental imperfections, where multiple sources of diffraction and potentially reflections play a role. Nevertheless, using the absolute magnitude of the intensity fluctuations as our only fit parameter we will combine the model for the contrast loss due to a distorted light field in Eq.(4.118) with the atom loss model $C_A(\Delta p)$ in Eq. (4.88) to compare to the experimental data in the next section.

4.7 Combined Contrast Model and Conclusions

Figure 4.10(a) compares the results of our theoretical analysis and the experimental data for the contrast we have already shown in Fig. 4.8(a). Starting with the predictions of the atom loss model $C_A(\Delta p)$ [see Eq. (4.88)] represented by the green diamonds in Fig. 4.10(a), we see that contrast is continuously lost due to increasing separations Δp because the number of coherent atoms is reduced by LZ losses and spontaneous scattering. However, this model by itself significantly overestimates the remaining contrast and, in particular, does not explain the strong contrast decrease already for Bragg-Bloch interferometers with modest Δp . The comparatively large confidence intervals result from the 10% uncertainty in the measured lattice depth $V_0(\Delta p)$ shown in Fig. 4.8(c) and are due to the sensitivity of $C_A(\Delta p)$ to

spontaneous emission losses [see Eq. (4.86)]. The results of the dephasing model, $C_L(\Delta p)$, have been obtained enhancing the perturbations of the laser profile to about 9 %, which provides good agreement with the experimentally measured fluctuations in the order of 10 % as discussed in the previous section. The corresponding data points in Fig. 4.10(a) (red triangles) clearly show that increasingly random velocity variations due to path-dependent dipole forces can lead to a dramatic loss in contrast even in the twin-lattice configuration. For our simulated light field, we obtain average differential velocities $\delta v = \delta p/M$ in the order of tens of nm/s (a few $\mu\text{m/s}$) in the y -direction (in z -direction), amounting to negligible average phase shifts. However, their standard deviations range from tens of $\mu\text{m/s}$ for $\Delta p = 24 \hbar k$ up to several hundreds of $\mu\text{m/s}$ for $\Delta p = 408 \hbar k$. This leads to uncertainties in the phase ranging from a few hundred mrad ($\Delta p = 24 \hbar k$) up to 2 rad ($\Delta p = 408 \hbar k$) across the cloud, for which the contrast has almost disappeared. Combining the models for atom loss and dephasing processes, $C(\Delta p) = C_L(\Delta p) \cdot C_A(\Delta p)$ (orange pentagons), allows us to reproduce the measured contrast loss. This provides strong evidence that the motion of the atoms through the distorted light field is one of the primary sources of the contrast decay with Δp in the QUANTUS-1 experiment. With this in mind, our contrast calculations for clouds with different sizes in Fig. 4.10(b) indicate that the twin-lattice interferometer benefits greatly from the small spatial extent of the collimated BEC with Thomas-Fermi radii of $\mathbf{R}_{\text{TF}} = (33, 39, 30) \mu\text{m}$ at the end of the interferometer. Without delta-kick collimation, the radii of the ensemble in the QUANTUS-1 experiment would increase by a factor of three in the y and z -directions, which has a significant impact as shown by the open violet circles in both panels of Fig. 4.10. The corresponding data points in (a) even overestimate the contrast of the uncollimated BEC, since we assume the same efficiencies for DBD and BO as for the collimated delta-kick BECs.

To experimentally check the influence of the spatial profile of the light field, the largest twin-lattice interferometer, $\Delta p = 408 \hbar k$, was realized with a beam diameter ($w_0 = 1.65 \text{ mm}$) about a factor of two smaller than that defined in Tab. 4.3. The blue square in Fig. 4.10(a) shows that contrast is tripled, $C(\Delta p = 408 \hbar k) = 0.14$, as the smaller diameter reduces light field distortions caused by diffraction at the atom chip and other apertures to about 5 % (cf. Sec. 5.3 in Ref. [208]). This is still worse than predicted by our theoretical model, where the same reduction of the beam diameter leads to an almost unperturbed beam, so that contrast is mainly determined by atom loss [green diamonds in Fig. 4.10(a)]. However, as already mentioned, this discrepancy is to be expected because the assumption of a beam clipped on a single chip edge oversimplifies the experimental situation in Fig. 4.4. A more detailed study tailored to the experiment is beyond the scope of this work as it would require a three-dimensional simulation of propagation of the lattice beam, including retroreflection.

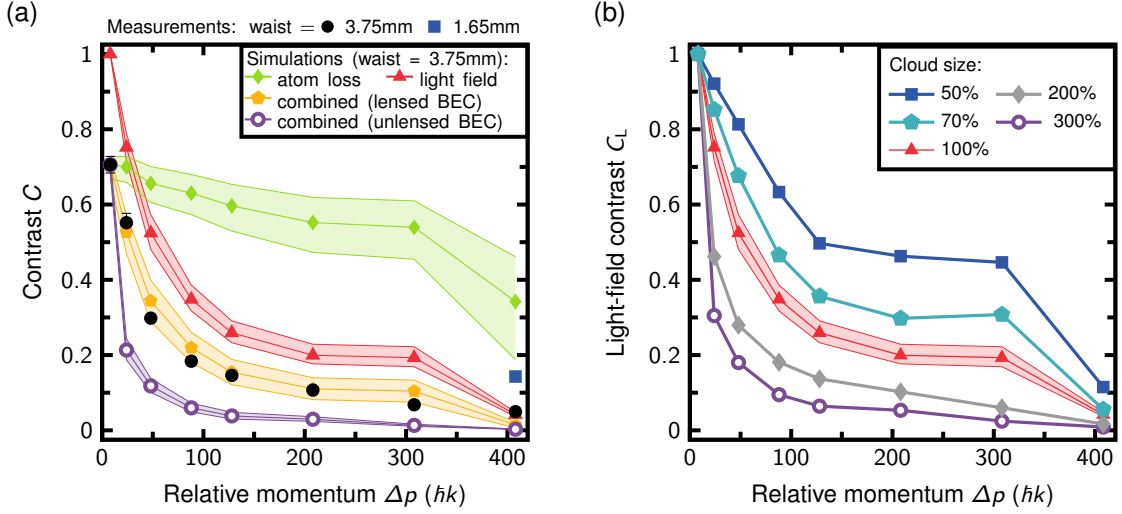


Figure 4.10: **Theoretical contrast analysis.** (a) Experimental [black circles, same as in Fig. 4.8(a)] and theoretical contrast C . Our model assumes atom loss (green diamonds) and local inhomogeneous dipole forces due to light field distortions (red triangles) to contribute to the decay of $C(\Delta p)$. Combining both effects (orange pentagons) we reach reasonable agreement with the experimental data. The shaded areas represent confidence intervals of the simulation, determined by atom number and lattice depth uncertainty [see Fig. 4.8(c)]. In addition, our model predicts a significantly lower contrast for an uncollimated BEC (open violet circles) because of its larger cloud size (see main text). Reducing the beam waist of the twin-lattice laser in the experiment leads to better contrast (blue square). (b) Simulated light-field contrast $C_L(\Delta p)$ for different cloud sizes. We compare the collimated BEC (100 % cloud size, red triangles) different cloud sizes using otherwise identical input parameters. An increase in size by 200 % or 300 % (gray diamonds, violet circles) leads to a significant contrast reduction. Smaller sizes, on the other hand, improve the contrast, highlighting the benefit of a well-collimated atom source in the presence of distortions of the light field. Figure (a) adapted from *M. Gebbe et al.*, Nat. Comm. **12**(1):2544 (Ref. [96]), CC BY 4.0, <https://creativecommons.org/licenses/by/4.0/>.

Conclusions

The main goal of this chapter was to understand the limitations of the spatial coherence of twin-lattice interferometers realized in the QUANTUS-1 experiment, which at the time of writing has demonstrated the largest differential momentum splitting of $\Delta p = 408 \hbar k$ between the interferometer arms. The symmetric combination of DBD and BO not only enables separations that exceed those of other symmetric schemes without BO by about a factor of 50 [94, 176], but the high efficiency of BO per recoil also significantly reduces atomic losses compared to the previous benchmark LMT experiment in Ref. [97]. Instead, our above analysis strongly suggests that the current beam splitter efficiency, and in general the scalability of this method, is primarily limited by technical reasons, in particular due to

spatial distortions of the twin lattice. It is therefore reasonable to assume that separations of > 400 photon recoils are possible despite these shortcomings, since the symmetric geometry reduces the laser power requirements compared to an asymmetric scheme involving BO. For the same momentum transfer and in the same amount of time, accelerating only one interferometer arm would require a greater potential depth, resulting not only in higher atomic losses due to spontaneous scattering, but also in even lower contrast due to light field distortions.

In the ideal case of an undisturbed Gaussian lattice beam, on the other hand, the experimental observations and our theoretical model imply that neither the LZ losses nor the differential dipole force arising due to the Gaussian waist are critical. For a twin lattice featuring spatial intensity fluctuations in the order of 0.5 % of V_0 our model predicts a contrast of more than 90 % at $\Delta p = 408 \hbar k$. Therefore, in addition to using a smaller beam, the benefits of which are already evident from the single data point in Fig. 4.10(a), adding a light field with opposite detuning with respect to the D2-line of ^{87}Rb , Δ , can reduce the effects of local distortions of the beam profile and improve the contrast by compensating for absolute Stark shifts [23, 124].

In conclusion, twin-lattice atom interferometry appears to provide the scalability required for future LMT applications. This technique not only brings within reach relative momentum separations of one thousand photon recoils or more, as envisioned in current designs of terrestrial detectors for infrasonic gravitational waves [37], in particular MIGA [36], ELGAR [38], and MAGIS [40]. Beyond that, the ability to enclose large areas in a comparably short time and volume makes the twin-lattice scheme attractive for inertial measurement applications in the real world, e.g., in the form of gyroscopes [122, 218], gradiometers [112, 142], or tilt meters [94, 217].

In general, it is reasonable to assume that addressing both interferometry arms symmetrically with two optical lattices derived from a single laser strongly suppresses diffraction phases due to light shifts [110, 150]. Nonetheless, this was not verified in the QUANTUS-1 experiment because no stable fringes could be observed due to inertial noise. It is important to recall in this context one of the main motivations for our work in Chapter 3: To benefit metrologically from the implementation of LMT beam splitters, one needs to understand and control systematic phase shifts below the mrad level. To this end, theoretical studies similar to ours but analyzing diffraction phases in Bragg-Bloch interferometers at the μrad -level will need to be performed in the future to ensure corresponding metrological gain. Important work has already been done investigating light shifts associated with BO [88, 150, 179]. Many of the existing studies, and most recently the predictions of *K. McAlpine* et al. [150] rely on Bloch states to describe the dynamics of atoms in accelerated optical lattices. As we have described here, this formalism is well suited to describe the acceleration of atoms in shallow optical lattices [108] but can also be extended to a

go beyond single-band physics [229]. LMT beam splitters with $\Delta p \sim 1000 \hbar k$ necessarily operate in the tight-binding regime, $V_0 \gg 20 E_r$ [24, 175, 179, 207], where the single-band approximation of the usual Bloch description fails. Thus, it will be interesting to see in the future, whether the above picture of Bloch states or a formalism based on Wannier-Stark states [199] is more appropriate to describe the acceleration of atoms in moving optical lattices in the LMT regime.

Finally, this also raises once again the question of the role of spontaneous emission for the phase of the interferometer. In our basic model of the QUANTUS-1 experiment, we have simply assumed that spontaneously scattered atoms are lost because of the negligible confinement in transverse direction due to the collimated beam. Nevertheless, it is not clear *ab initio*, what role spontaneous emission plays with respect to the coherence of the atomic ensemble in the tight-binding regime, where scattered atoms cannot leave the atomic cloud because of their strong confinement in the optical lattice. A thorough theoretical understanding of these mechanisms is of paramount importance, especially when considering to combine these novel LMT schemes with nonclassical BEC sources [163, 164, 230, 231].

5

Summarizing Statements and Outlook

Since the first experiments on Bragg scattering of atomic beams using light gratings about thirty years ago, numerous experiments have demonstrated that elastic scattering of atoms by laser light is a valuable technique for atom interferometry. It is noteworthy that these efforts have gone beyond mere proofs of principle, as currently one of the state-of-the-art measurements of the fine structure constant [23] as well as the best quantum test of the equivalence principle [32] are based on Bragg diffraction. Moreover, it is not difficult to envision the disruptive potential of this method as the basis for large-momentum-transfer beam splitters that can increase the sensitivity of modern atom interferometers by orders of magnitude. Therefore, Bragg diffraction is not only an important factor in the pursuit of fundamental scientific goals such as the detection of infrasound gravitational waves [33–40] or the search for ultralight dark matter [40, 46, 47], but also a key component in the development of accurate and robust inertial sensors that are well suited for real-world applications [60]. To date, few Bragg atom interferometers have demonstrated metrological gain [23, 32, 112, 113] using large momentum transfer despite their desirable properties. Their sensitivity appears to be constrained by the limited control of manipulating atomic wave packets with laser potentials.

The goal of this work was to promote a deeper understanding of the interaction between light and matter that is essential in order to overcome current sensitivity limitations. In its two main parts this thesis addressed atom interferometers operating between the Bragg and the Raman-Nath regimes, and the current limits of symmetric momentum transfer realized by twin-lattice interferometry in the QUANTUS-1 experiment.

5.1 Bragg Diffraction from Pulsed Optical Lattices

The first part began with Chapter 2, in which a brief overview of the current descriptions of the scattering process derived from the theory of light diffraction by thick (Bragg) or

thin (Raman-Nath) phase gratings in combination with Rabi oscillations in a two-level system was given. In contrast, we proposed to reinterpret the time evolution of elementary atom optical elements such as beam splitters or mirrors realized by Bragg diffraction from a single optical lattice in terms of the adiabatic theorem. From this perspective, an ideal Bragg pulse affects only the relative phase between the symmetric and antisymmetric components of the incoming matter wave, which can be understood in a frame that comoves with the optical lattice. This makes the dynamics fundamentally different from the diabatic transitions between atomic hyperfine states that occur in Raman diffraction. Furthermore it shows a close relationship to the image of Bloch bands normally used to describe Bloch oscillations. Furthermore, it allowed us to find an analytical solution for the time evolution of the Bragg pulse and to derive a scattering matrix relating the incoming to the outgoing wave packet in the asymptotic limit, starting from the one-dimensional optical lattice Hamiltonian in a moving frame.

Considering atomic wave packets with momentum uncertainties much smaller than the lattice recoil. Assuming that the optical lattice velocity is fixed, we have represented the Bragg Hamiltonian in eigenstates of the momentum operator exploiting the fact that a Bragg pulse couples only even (odd) to even (odd) momentum components via one or more two-photon transitions. Specifically, we treated an incoming plane wave with discrete momentum $-n\hbar k$ relative to the optical lattice, coupled to the outgoing wave with $n\hbar k$ and perturbatively included the effects of the finite momentum width of the wave packets. Thus, we were able to exploit the fact that the Bragg Hamiltonian is block diagonal when represented in the symmetric and antisymmetric components of plane waves. Assuming that the laser intensity follows a smooth temporal envelope required for adiabatic time evolution, we then formulated the scattering matrix adopting a block diagonal structure and connecting the incoming with the outgoing symmetric and antisymmetric components of the matter wave.

According to the adiabatic theorem, the time evolution of these components can be easily calculated by solving simple time integrals over eigenenergies of finite-dimensional matrices. Moreover, we related these eigenenergies of the Bragg Hamiltonian to specific points in the Bloch spectrum and saw that they determine the differential phase between symmetric and antisymmetric components of the diffracted wave. The Bragg pulse acts as a beam splitter or mirror depending on how this phase is controlled by the duration and intensity of the pulse. Thus, the differential phase can be understood as an analogue of the pulse area in the description of Rabi oscillations in a two-level system.

In addition to the adiabatic phase evolution, our final expression for the scattering matrix also includes corrections to the phase and amplitudes of the diffracted states. These Landau-Zener phases and Landau-Zener losses to other momentum states can be derived

from nonadiabatic couplings in an effective two-level system in most cases. Our perturbative treatment of the finite momentum width has shown that a Doppler shift that is small compared to the recoil frequency $\omega_r = \hbar k^2/2M$ leads to transitions between the symmetric and antisymmetric components of the outgoing matter wave, breaking the block-diagonal structure of the Bragg Hamiltonian. For a wave packet with average momentum $-n \hbar k$ this leads primarily to reduced diffraction efficiencies.

Finally, we compared the predictions of our analytical model with numerical solutions of the Schrödinger equation, assuming pulses with Gaussian intensity envelopes that transferred up to ten photon recoils. This diffraction order strikes a reasonable balance between the laser power and pulse duration required to change the differential phase to the desired value ($\pi/2$ in the case of a beam splitter and π for a mirror) and spontaneous emission according to Ref. [69]. To this end, we introduced the measurement of the fidelity of a Bragg beam splitter and a mirror and found that our model is in very good quantitative agreement with the numerical results. In particular, our study demonstrated that high-fidelity pulses with Gaussian shapes are always adiabatic and that adiabaticity is a necessary condition for efficient Bragg diffraction with smooth pulse shapes in general.

5.2 Large-momentum-transfer Bragg Interferometry

Finally, in preparation for Chapter 3 we included the dominant spurious diffraction orders populated by Landau-Zener transitions in our scattering matrix. This is required to adequately capture the multimode properties of Bragg atom interferometers previously observed in experiments [117, 118, 135, 147]. The presence of multiple nearby momentum states, which can be occupied by nonadiabatic transitions even at good diffraction efficiencies, arguably makes the estimation of the associated systematic effects more complex than for Raman interferometers.

Since the relative phase in atom interferometers must be inferred indirectly via measurements of an observable (in this case, the relative population detected in the two primary output ports), these effects must be understood in the context of the theory of parameter estimation. Therefore, at the beginning of Chapter 3 we gave a brief overview of some of the basic concepts of phase estimation including the method of moments, the Cramér-Rao bound, and the quantum Cramér-Rao bound. We then proceeded to the main focus of this chapter, which was to investigate the systematic effects arising from the multistage properties of the scattering process and the subsequent multipath interferences. In an effort to complement previous studies [98, 116, 118, 119], we extended our description of individual Bragg pulses into an analytical framework that allows the study of systematic effects in Bragg atom interferometers.

In extending our formalism, we took advantage of the fact that modern ultracold atomic sources, in particular BECs, have very narrow momentum distributions. Thus, we were able to unambiguously assign trajectories in space-time to the various momentum states that are populated by the scattering process. This description allows us to describe arbitrary interferometry geometries composed of our Bragg scattering matrices in a basis of these unique paths and to compute analytical results for the interferometer signal that depend on the pulse parameters.

To demonstrate the usefulness of our method, we treated the example of a Mach-Zehnder interferometer with two beam splitters and a mirror pulse between them. We included the dominant spurious paths and output ports that occur due to the atom-light interaction for diffraction order three or higher. In our example, the relative phase accumulated between pulses during free evolution was determined by a linear acceleration parallel to the wave vector of the optical lattice, as would be the case in a gravimeter setup.

Unlike a standard two-mode interferometer, Landau-Zener losses during the initial beam splitter interaction can cause spurious interferometry paths to overlap with the main interferometry arms at the time of the last beam splitter. We saw that the dominant spurious transitions populate parasitic interferometers enclosing reduced space-time areas. Furthermore, it became clear that multipath interference actually renders their contribution to the signal dependent on the pulse separation time T , which has already been observed experimentally before [118, 147]. We also learned that in the case of Mach-Zehnder geometry, the Bragg mirror pulse plays a crucial role. For the parasitic interferometers to close at all they must be reflected by the mirror pulse. Additionally, we saw that even in cases, where the mirror does not reflect these unwanted paths at all, the multiport nature of Bragg beam splitters leads to phase shifts and potential deformations of the signal fringes. Similar observations have been made previously [117, 118] and can now be quantified in terms of the pulse parameters of the Bragg beam splitters using our model.

This provided us with the opportunity to show that it is possible to find optimal pulse configurations that mitigate the adverse effects of parasitic paths and undetected output ports.

Based on our findings, we formulated a phase estimation strategy that takes into account the multiport properties of Bragg beam splitters and applied it in numerical experiments realizing fifth-order Bragg Mach-Zehnder interferometers. We then assessed the accuracy of our model by evaluating the systematic shift between the true value of the signal phase as determined in the numerical simulations and the result of our estimation strategy. We defined this shift as the diffraction phase. Scanning pulse parameters for beam splitting losses up to 10 %, we saw that the systematic errors due to the diffraction phase can be as large as several mrad and that they can be greatly reduced down to few μrad by our adapted

estimation strategy. This was particularly the case when mirror parameters were used to specifically suppress the formation of parasitic interferometers.

Finally, we analyzed the effects of multiple paths and ports on the statistical uncertainty of the measurement in detail. In particular, we evaluated the shot noise of our phase estimation strategy based on the method of moments that we had applied to the numerical simulations. We then compared this result with the fundamental bounds given by the analytic Cramér-Rao bound and the quantum Cramér-Rao bound. This analysis made it clear that there is a tradeoff between the nonadiabatic losses and the effects of the finite momentum width of the ensemble when choosing the parameter sets of the Bragg pulses to optimize the performance of the atom interferometer.

In summary, we are confident that the analytical framework presented in the first part of this thesis pertaining single Bragg operations with smooth pulse shapes [120] and their composition to large-momentum-transfer Bragg interferometers with μrad -accuracy [121] will be instrumental in improving the performance of current and future Bragg atom interferometers. In addition, it is more than likely that future sensors based on atom interferometry will employ large-momentum-transfer beam splitters that combine Bragg diffraction with other methods such as Bloch oscillations to create separations of several hundred or even thousands of photon recoils.

5.3 Scalability of Twin-lattice Atom Interferometers

In the second part of this work we provide a better understanding of the limitations of the state-of-the-art LMT beam splitters realized in the QUANTUS-1 experiment. Using "twin-lattice interferometry" it recently demonstrated the creation of Mach-Zehnder-type atom interferometers with momentum separations of up to $408 \hbar k$ [96], the largest at the time of writing. Combining collimated Bose-Einstein condensates with double Bragg diffraction and subsequent Bloch oscillations in accelerated optical lattices, this method promises efficient and symmetric momentum transfer.

After introducing the necessary theoretical concepts to adequately describe the acceleration of Bose-Einstein condensates in optical lattices, we first investigated the measured Bloch transfer efficiencies produced by two optical lattices moving in opposite directions. In the QUANTUS-1 experiment, the measurements deviate significantly from the predictions of the standard Landau-Zener formalism. A numerical simulation of the acceleration of the condensate in the twin lattice revealed that this was in fact not caused by the twin lattice potential itself. Instead, we showed that the experimental data can be reproduced assuming an additional stationary parasitic optical lattice potential, which is likely caused by errors in the polarization of the light fields in combination with the retroreflective setup in the experiment. Moreover, our simulations confirmed that the effects of the standing

lattice can be successfully circumvented when increasing the initial momentum splitting to eight photon recoils. This can be achieved implementing two consecutive first-order double Bragg pulses at the start of the interferometer sequence. As a result the Doppler detuning relative to the stationary potential is increased, which facilitates Bloch efficiencies in the order of 99.9 % [208].

Following the introduction of the twin-lattice interferometer sequence, we focused on modeling the experimentally observed contrast decay from $\sim 70\%$ for a momentum separation of $8\hbar k$ to about 5 % for the largest interferometer at $408\hbar k$. Due to the high transfer efficiencies about one-third of the original atom number remains even for the largest separation, which means that the contrast loss cannot be explained by atom loss alone as was the case in previous benchmark experiments [97].

Based on our analysis we conclude that there are two main sources of contrast loss in the QUANTUS-1 experiment. First, the signal is affected by nonadiabatic losses during Bloch oscillations as well as losses due to spontaneous emission. Second, distortions of the twin-lattice laser profile due to diffraction along the beam path lead to spatial intensity variations of the optical potential. Since the atomic ensembles interact with the distorted potential over the course of the interferometer their spatial coherence is diminished and thus the signal contrast is reduced. To estimate the second effect the atomic wave packets traveling along the trajectories of the twin lattice are semiclassically sampled as they move through the intensity distribution of a simplified light field modeled by a Gaussian laser beam diffracted at a single metallic edge. The averaging over the separation phases caused by the interaction with the dipole potential then showed that the contrast of the atomic ensemble decreases as the area explored by the atoms increases. After fitting the magnitude of the distortions in our calculations to experimental measurements of the twin-lattice laser profile and combining our two models for contrast loss, very good agreement was obtained with the experimental contrast data.

Our results are a clear indication that the current limits on the scalability of the twin-lattice interferometer realized in the QUANTUS-1 apparatus are technical in nature, strongly suggesting that this system is suitable for realizing Bose-Einstein condensate interferometry with momentum separations of a thousand photon recoils or more in the near future. However, as we pointed out, a thorough understanding of the systematic shifts at the μrad -level is required to translate such improvements in sensitivity into a metrological gain.

5.4 Future Prospects

We are confident that the work presented here will make a significant contribution to improving the accuracy of current and future Bragg atom interferometers, allowing them to

take full advantage of large momentum separations. Moreover, our results facilitate future studies of the optical elements of atom interferometers with great accuracy and utility.

First, our study of the Mach-Zehnder geometry has shown that it is possible to suppress multipath interference efficiently via the Bragg mirror. Nevertheless, for Bragg order $n = 5$ the formation of parasitic interferometers cannot be completely prevented, because the atom-light interaction couples multiple diffraction orders. Therefore, it will be interesting to see, whether the adapted Bragg mirror is even more effective when applied to third-order pulses since in this case and for comparable nonadiabatic losses only transitions to $n-2 = 1$ are significant. At the same time, the diffraction phases could be larger overall due to their inverse scaling with the Bragg order n (see Sec. 3.6). Second, experimental observations have shown that Bragg beam splitters populating multiple ports and interferometry paths play an important role in modern h/M measurements with large diffraction orders [23, 117, 118]. Previous studies based on numerical solutions of the atom-light interaction have shown that the relative magnitude of the associated diffraction phases can be significantly suppressed by the inclusion of Bloch oscillations [117, 118], which is a unique feature of the conjugate Ramsey-Bordé interferometer. However, it will be interesting to characterize the multipath interference effects and evaluate the optimization potential for this geometry using our analytical formalism.

In the context of the work presented here, we considered only Bragg pulses with Gaussian temporal pulse shapes which suppress nonadiabatic transitions. However, it is not difficult to imagine that there are innovative pulse configurations that, e.g., use more than one control parameter and can be tailored specifically to meet the requirements of modern atom interferometry devices. Along these lines, the authors Kovachy et al. [104] have shown that the velocity selectivity of Bragg mirrors can be improved by combining a hyperbolic tangent intensity profile (\tanh) with a linear sweep of the velocity of the Bragg lattice across the resonance for the duration of the pulse creating an adiabatic rapid passage. It is reasonable to assume that coupling to undesired momentum states or manipulation of parasitic interferometer paths also offer unexplored optimization potential. In the near future, such research efforts can undoubtedly be facilitated by the application of optimal control algorithms, the potential of which is best illustrated by the recent successful application of this technique to Raman diffraction [232–234].

Yet, it is also clear from our analysis that the resulting and potentially highly sophisticated experimental sequences will not only change the properties of the individual pulses. It will also affect the systematic and statistical properties of the entire interferometer. Therefore, such optimization routines must be considered in the context of the complete interferometer and not just a single operation. Our analytical framework has the potential to provide such a holistic perspective for Bragg atom interferometers and is therefore well suited to guide subsequent investigations.

In this context, a more comprehensive characterization of the phase response of the interferometer than we have provided here would be particularly desirable. The sensitivity function formalism is a powerful approach that goes beyond, e.g., our assumption of instantaneous interaction between the atoms and momentum with respect to phase [235]. Thus, integrating this method into our scattering matrix formalism developed here would certainly be extremely worthwhile, especially since it has already been successfully applied to large-momentum transfer interferometers based on sequential Bragg pulses [214].

As mentioned earlier, a thorough understanding of the systematic shifts as well as the statistical effects associated with the multistate nature of Bragg atom interferometers is essential in light of recent proposals to use entanglement and in particular squeezed states to overcome the standard quantum limit [141, 162–164]. In light interferometers the optimal squeezing operations depend on the quality of the optical operations (see , e.g., Ref. [236]). It will be interesting to determine these properties for multimode Bragg atom interferometers with nonclassical sources.

In summary, all of the above efforts aim to minimize or mitigate the multimode nature of Bragg scattering for atom interferometry. However, multimode interferometry has been proposed to improve the phase sensitivity of an interferometer [137] and has been successfully implemented in a contrast interferometer with three arms populated by a Raman-Nath pulse [98]. The unique multilevel structure of the diffraction process can therefore provide interesting opportunities for efficient multipoint beam splitting and the targeted study of multipath interference effects. In particular, the Bragg diffraction orders $n = 2$ and $n = 3$ seem to be suitable to realize 3- or 5-port beam splitters for matter waves simply by a suitable choice of parameters.

Beyond single Bragg pulses, recent proof-of-principle experiments have shown that future atom interferometers with momentum separations of several hundred or even thousand photon recoils will most likely be based on a symmetric momentum transfer setup [96, 142]. Therefore, it will certainly be worthwhile to investigate, whether the formalism of a scattering matrix can be advantageous to describe double Bragg diffraction [94, 105, 132]. We described in Chapter 4 that this technique allows for symmetric interferometer configurations with state-of-the-art momentum separations when paired with Bloch oscillations. Although the double-Bragg diffraction process is more complex than the single-Bragg case because of the second optical lattice, double-Bragg interferometers exhibit multipath properties similar to those described here (see Ref. [136]) and can therefore benefit from the insights gained from our description.

The goal should be of course to assess all aspects of modern large-momentum-transfer beam splitters with the same rigor as we have attempted in this work, which requires a theoretical framework that unifies the regimes of Bragg pulses and Bloch oscillations. The prospect of gaining analytical insights into how to seamlessly transition from one process

to another offers exciting new possibilities and seems feasible given the close relationship between these two techniques that we pointed out in Chapter 2.

Ultimately however, we have seen that any description of realistic experiments must include the three-dimensional nature of the atomic cloud and the light fields interacting with the atoms. For example, an important question that arises when studying Bragg interferometers with multiple paths and realistic light fields is how the different paths interact with the inhomogeneous wavefronts or intensity distributions. Finding satisfactory answers to these and related questions based on purely analytical calculations is certainly challenging. Nevertheless, such efforts can be complemented by efficient and robust numerical simulations (see, e.g., Ref. [237]) to provide accurate descriptions of atom interferometers in the future.

A

Appendices for Chapter 2

A.1 Analytical Landau-Zener (LZ) Transition Amplitudes

The results presented in this appendix are based on the work by *G. S. Vasilev and N. V. Vitanov* in Ref. [145]. We reproduce here the functions entering formula (2.93) for the LZ loss parameter γ_{2+} :

$$a_{\Theta}(\Omega, \tau) = 4\omega_r \sqrt{2\tau} \left\{ (\sqrt{\lambda^2 + 1} - 1) \sqrt{\frac{1}{2} \ln \frac{\lambda^2}{[1 + \nu_{\Theta}(\sqrt{\lambda^2 + 1} - 1)]^2 - 1}} \right. \\ \left. + \frac{1}{2} \sqrt{\sqrt{\left[\ln \frac{\lambda^2}{\mu_{\Theta}(2 - \mu_{\Theta})} \right]^2 + \pi^2} + \ln \frac{\lambda^2}{\mu_{\Theta}(2 - \mu_{\Theta})}} \right\} \quad (\text{A.1a})$$

and

$$b_{\Theta}(\Omega, \tau) = \frac{4\omega_r}{2} \sqrt{2\tau} \sqrt{\sqrt{4 \ln(m_{\Theta}\lambda)^2 + \pi^2} - 2 \ln(m_{\Theta}\lambda)}, \quad (\text{A.1b})$$

with

$$\lambda \equiv \sqrt{2} \frac{\Omega}{4\omega_r}.$$

These equations correspond to formulas (53) and (44) in Ref. [145], respectively, where we inserted the asymptotic energy difference between the states $|2, +\rangle$ and $|0, +\rangle$:

$$\lim_{t \rightarrow \pm\infty} \frac{E_{2,+}(t) - E_{0,+}(t)}{\hbar} = 4\omega_r. \quad (\text{A.2})$$

Eq. (2.93) from the main text follows from Eq. (59) in [145]. All formulas have been adapted to the notation used here. This requires in particular to identify the basic Hamiltonian in Eq. (2) in [145] with our Eq. (2.84). Note, that the latter features an increased

coupling strength $\sqrt{2}\Omega$ in comparison to the former. Following the logic of *Vasilev and Vitanov*, we can find values for the set of free parameters $\mu_\Theta, \nu_\Theta, m_\Theta$ in Eqs. (A.1) to match the exact numerical results as presented in Fig. 2.7 and in Fig. 2.8 in Sec. 2.6.3:

$$\begin{aligned} m_{\frac{\pi}{2}} &= 0.918028; & \nu_{\frac{\pi}{2}} &= 0.693525; & \mu_{\frac{\pi}{2}} &= 0.790483 \\ m_\pi &= 0.983601; & \nu_\pi &= 0.596432; & \mu_\pi &= 0.822102. \end{aligned} \quad (\text{A.3})$$

The Θ dependence results from the fact that the basic Hamiltonian in Eq. (2) of Ref. [145] applies to a constant energy offset between the two levels. The inclusion of more states than $|2, \pm\rangle$ and $|0, +\rangle$ required for our analysis, however, leads to ac Stark shifts such that the energy offset becomes $\Omega^2(t)$ dependent. We do not include this as the adaptation of the LZ-formula proposed in Ref. [145] is beyond the scope of this thesis. To account for the different ac Stark shifts in case of a beam splitter and mirror pulse, we have optimized the parameters in Eq. (A.3) separately.

A.2 Doppler Detuning

The first-order correction is described by

$$\langle +, n, p | Z_\alpha | -, n, p \rangle = \int_{-\infty}^{\infty} dt \frac{e^{i\Theta(t)} \langle +, n, p; t | V_\alpha(t) | -, n, p; t \rangle}{\hbar}, \quad (\text{A.4a})$$

where

$$\Theta(t) = \int_{-\infty}^t dt_1 [E_{n+}(t_1) - E_{n-}(t_1)]. \quad (\text{A.4b})$$

Note, this phase is related to the differential phase in Eq. (2.65) by $\lim_{t \rightarrow +\infty} \Theta(t) = \Theta$. The matrix element on the right-hand side of Eq. (A.4a) can be further simplified by noting that we can rewrite $V_\alpha(t)$ in Eq. (2.44b) as

$$\begin{aligned} V_\alpha(t) &= i2\omega_r t \hbar \Omega(t) \sum_{n \in \mathbb{Z}_\alpha} (e^{2i\phi_L} \hat{\sigma}_{n+2, n} - \text{H.c.}) \\ &= i2\omega_r t \left[D_\alpha, \sum_{n \in \mathbb{Z}_\alpha} \frac{\hbar \Omega(t)}{2} (e^{2i\phi_L} \hat{\sigma}_{n+2, n} + \text{H.c.}) \right] \\ &= i2\omega_r t [D_\alpha, H_\alpha(t) - \mathcal{L}_\alpha] \\ &= i2\omega_r t [D_\alpha, H_\alpha(t)] \end{aligned} \quad (\text{A.5})$$

where $H_\alpha(t)$ and \mathcal{L}_α are given in Eqs. (2.44a) and (2.37), respectively, and we introduced the operator $D_\alpha = \sum_{n \in \mathbb{N}_\alpha} n \hat{\sigma}_{n, n}$. This operator acts on the (anti)symmetric states (for $n > 0$) as $D_\alpha |\pm, n, p\rangle = n |\mp, n, p\rangle$, and thus changes their parity. It also commutes with \mathcal{L}_α , which

we used in the last equality in (A.5). Taking into account the eigenvalue equation (2.70) one finds

$$\langle +, n, p; t | V_\alpha(t) | -, n, p; t \rangle = -i2\omega_r t [E_{n+}(t) - E_{n-}(t)] \langle +, n, p; t | D_\alpha | -, n, p; t \rangle. \quad (\text{A.6})$$

This expression also shows that the diagonal matrix elements $\langle \pm, n, p; t | V_\alpha(t) | \pm, n, p; t \rangle$ are proportional to $[E_{n\pm}(t) - E_{n\pm}(t)] = 0$. Interpreting $\langle +, n, p; t | D_\alpha | -, n, p; t \rangle$ one can consider an expansion of the instantaneous energy eigenstates in terms of the asymptotic eigenstates, $|\pm, n, p; t\rangle = \sum_n c_{n\pm}(t) |\pm, n, p\rangle$. Using the fact that D_α flips the parity of the asymptotic eigenstates, one finds $\langle +, n, p; t | D_\alpha | -, n, p; t \rangle = \sum_n n c_{n+}^*(t) c_{n-}(t)$. Due to the asymptotics of the energy eigenstates Eq. (2.71) we have

$$\lim_{t \rightarrow \pm\infty} \langle +, n, p; t | D_\alpha | -, n, p; t \rangle = n. \quad (\text{A.7})$$

Inserting (A.6) into Eq. (A.4a) we arrive at

$$\langle +, n, p | Z_\alpha | -, n, p \rangle = 2n\tau^2 \omega_r^2 z_{n,\Theta}(\Omega_0) e^{i\Theta/2}. \quad (\text{A.8})$$

which is Eq. (2.100) from the main text. Here, Θ is the differential phase from Eq. (2.65) and $z_{n,\Theta}$ is

$$\begin{aligned} z_{n,\Theta}(\Omega_0) &= -i \int_{-\infty}^{\infty} d\zeta \zeta \frac{E_{n+}(\zeta\tau) - E_{n-}(\zeta\tau)}{\hbar\omega_r} \\ &\quad \times \frac{\langle +, n, p; \zeta\tau | D_\alpha | -, n, p; \zeta\tau \rangle e^{i[\Theta(\zeta\tau) - \Theta/2]}}{n} \\ &\approx -i \int_{-\infty}^{\infty} d\zeta \zeta \frac{E_{n+}(\zeta\tau) - E_{n-}(\zeta\tau)}{\hbar\omega_r} e^{i[\Theta(\zeta\tau) - \Theta/2]}. \end{aligned} \quad (\text{A.9})$$

In the last line of Eq. (A.9), we have approximated the rescaled matrix element to be unity. With this, our theory relies only on the simple calculation of instantaneous eigenenergies instead of the more involved computation of instantaneous energy eigenstates and their overlaps.

The time integral and the integrand have been scaled to dimensionless units such that the value of z_n is positive and on the order of unity as can be seen in Fig. 2.4. The pulse length is τ and ζ denotes a dimensionless time. The phase in Eq. (A.9) has been adapted such as to assure that z_n is real. In order to see this, we note that the argument of the exponential, $\Theta(\zeta\tau) - \Theta/2$, is an odd function in ζ since, for a Gaussian pulse, $\Theta(t)$ is essentially an error function. Because the rest of the integrand is an odd function in time, only the imaginary part of the exponential contributes to the integral in (A.9), which makes $z_{n,\Theta}$ real.

A.3 Hilbert Space Dimensionality and Numerical Integration

The results presented in this thesis are the product of calculations in truncated finite dimensional Hilbert spaces. This is true both for our analytics, which requires a diagonalization of finite-dimensional Hamiltonians to compute their spectra [see Eqs. (2.70)], and for the full numerical integration of the Schrödinger equation. In each case, we truncate the momentum state basis like

$$\{|-m_{\max}\hbar k + p\rangle, |(-m_{\max} + 2)\hbar k + p\rangle, \dots, |(m_{\max} - 2)\hbar k + p\rangle, |m_{\max}\hbar k + p\rangle\}, \quad (\text{A.10})$$

where m_{\max} is even (odd) if the diffraction order n is even (odd) and perform the same truncation of the Hamiltonians in Eqs. (2.55) in the (anti)symmetric basis. The truncations applied for our calculations are $m_{\max} = 6, 7, 8, 11$ for the different Bragg orders $n = 2, 3, 4, 5$ respectively. The codes that generate the results presented in Figs. 2.2-2.8 and Fig. 2.11 are available online [120]. Throughout this study, we compute time integrals and numerically solve the Schrödinger equations using the truncations above. To ensure that these calculations reflect the asymptotic nature of scattering theory on which our model is based on, we choose time intervals (expressed here in units of ω_r^{-1}) $\zeta \in [-22, 22]$ accordingly.

Note, that these truncations are adequate for the analysis performed in the context of the work presented in Sec. 2.6 chapter 2. Calculation of atom interferometer phases may require increased accuracy and therefore higher truncations. We further comment on this in chapter 3 and point out that our analytic model only relies on the computation of the spectra of these Hamiltonians. An increase in dimensionality will therefore not add significantly to the complexity of the model. As an example, *Gochbauer* et al. [119] successfully calculate effective Rabi frequencies and diffraction phases in a similar fashion and find good agreement with their experimental data taking into account nine states for a second-order Bragg mirror pulse provides sufficient convergence (see Ref. [34] in [119]).

A.4 Four-mode Bragg Scattering Matrix ($n = 2$)

In Sec. 2.7 we state the scattering matrix for single Bragg pulses with $n \geq 3$ including the dominantly populated parasitic diffraction order. Here, we reproduce the corresponding expressions for $n = 2$. As explained in the above section, the extended state space for second-order Bragg diffraction includes a single LZ state

$$\begin{aligned} |s_j(p)\rangle &\in \{|p, 2, \pm\rangle, |p, 0, +\rangle\}, \\ |q_j(p)\rangle &\in \{|\pm 2\hbar k + p\rangle, |p\rangle\}. \end{aligned} \quad (\text{A.11})$$

The generalized projection of the scattering matrix (2.61) for the enlarged (anti)symmetric state space reads

$$\mathcal{S}_\alpha = \sum_{j,l} S_{jl} |s_j\rangle\langle s_l|, \quad (\text{A.12})$$

with

$$S = S_{\text{LZ}} \cdot S_{\text{ad}} = \begin{pmatrix} e^{-\gamma_{2+}} & -e^{i\xi_+} \sqrt{1 - e^{-2\gamma_{2+}}} & 0 \\ e^{-i\xi_+} \sqrt{1 - e^{-2\gamma_{2+}}} & e^{-\gamma_{2+}} & 0 \\ 0 & 0 & 1 \end{pmatrix} \begin{pmatrix} e^{-i\theta_{2+}} & 0 & 0 \\ 0 & e^{-i\theta_{0+}} & 0 \\ 0 & 0 & e^{-i\theta_{2-}} \end{pmatrix}, \quad (\text{A.13})$$

in zeroth order of the (quasi)momentum p . Following the reasoning in Sec. 2.7, we take into account finite-velocity effects only for the main diffraction order as described before and write

$$S(p) = S \cdot \frac{1}{\sqrt{1 + \eta^2(p)}} \begin{pmatrix} 1 & 0 & i\eta(p)e^{i\Theta_2/2} \\ 0 & \sqrt{1 + \eta^2(p)} & 0 \\ i\eta(p)e^{-i\Theta_2/2} & 0 & 1 \end{pmatrix}. \quad (\text{A.14})$$

According to the second line in Eq. (A.11), the scattering matrix in the momentum eigenstate basis for $n = 2$ will have the form

$$S(\Omega, \tau) = \int_{-\hbar k/2}^{\hbar k/2} dp \sum_{j,l} [B(p, \Omega, \tau)]_{jl} |q_j(p)\rangle\langle q_l(p)|, \quad (\text{A.15a})$$

where

$$B(p, \Omega, \tau) = \begin{pmatrix} S_{-2,-2} & B_{-2,0} & B_{-2,+2} \\ B_{0,-2} & B_{0,0} & B_{0,+2} \\ B_{+2,-2} & B_{+2,0} & B_{+2,+2} \end{pmatrix}, \quad (\text{A.15b})$$

An expression for $B(p, \Omega, \tau)$ is obtained in this case by performing the change in basis using the transformation

$$T = \frac{1}{\sqrt{2}} \begin{pmatrix} e^{i2\phi_L} & 0 & e^{-i2\phi_L} \\ 0 & \sqrt{2} & 0 \\ e^{i2\phi_L} & 0 & -e^{-i2\phi_L} \end{pmatrix} \quad (\text{A.16})$$

We write in analogy to Eq. (2.121),

$$B(p, \Omega, \tau, \phi_L) := T^\dagger S(p)T = \mathcal{M}(\Omega, \tau, \phi_L) \cdot \mathcal{N}(p, \Omega, \tau, \phi_L), \quad (\text{A.17a})$$

where

$$\mathcal{M}(\Omega, \tau, \phi_L) = \left(\begin{array}{c|c|c} e^{\frac{-i}{2}(\Phi_2 - i\gamma_{2+})} \cos\left(\frac{\Theta_2 - i\gamma_{2+}}{2}\right) & -e^{-i(\theta_{0+} - \xi_+ + 2\phi_L)} \sqrt{e^{-\gamma_{2+}} \sinh(\gamma_{2+})} & -ie^{-i4\phi_L} e^{\frac{-i}{2}(\Phi_2 - i\gamma_{2+})} \sin\left(\frac{\Theta_2 - i\gamma_{2+}}{2}\right) \\ \hline e^{\frac{-i}{2}(\Theta_2 + 2\xi_+ + \Phi_2 - 4\phi_L)} \sqrt{e^{-\gamma_{2+}} \sinh(\gamma_{2+})} & e^{-i(\theta_{0+} - \gamma_{2+})} & e^{\frac{-i}{2}(\Theta_2 + 2\xi_+ + \Phi_2 + 4\phi_L)} \sqrt{e^{-\gamma_{2+}} \sinh(\gamma_{2+})} \\ \hline -ie^{i4\phi_L} e^{\frac{-i}{2}(\Phi_2 - i\gamma_{2+})} \sin\left(\frac{\Theta_2 - i\gamma_{2+}}{2}\right) & -e^{-i(\theta_{0+} - \xi_+ - 2\phi_L)} \sqrt{e^{-\gamma_{2+}} \sinh(\gamma_{2+})} & e^{\frac{-i}{2}(\Phi_2 - i\gamma_{2+})} \cos\left(\frac{\Theta_2 - i\gamma_{2+}}{2}\right) \end{array} \right), \quad (\text{A.17b})$$

and

$$\mathcal{N}(p, \Omega, \tau, \phi_L) = \left(\begin{array}{c|c|c} \frac{1+i\eta(p) \cos(\Theta_2/2)}{\sqrt{1+\eta^2(p)}} & 0 & ie^{-i22\phi_L} \frac{i\eta(p) \sin(\Theta_2/2)}{\sqrt{1+\eta^2(p)}} \\ \hline 0 & 1 & 0 \\ \hline -ie^{+i4\phi_L} \frac{i\eta(p) \sin(\Theta_2/2)}{\sqrt{1+\eta^2(p)}} & 0 & \frac{1-i\eta(p) \cos(\Theta_2/2)}{\sqrt{1+\eta^2(p)}} \end{array} \right). \quad (\text{A.17c})$$

The scattering matrix $\mathcal{M}(\Omega, \tau, \phi_L)$ contains in addition to the scattering phase θ_{0+} (2.91) of the energy eigenstate state $|+, 0\rangle$ also the LZ transition phase ξ_+ . We explain in Sec. 2.7, how this phase can be inferred for given pulse parameters $\{\Omega, \tau\}$ from numerical solutions of the Schrödinger equation with respect to the Hamiltonians in Eq. (2.44a).

B

Appendix for Chapter 3

Free Propagation Operator

We solve the time evolution of the momentum eigenstates $|q_j\rangle_j$ during free propagation to derive the propagation phases $\vartheta(g, t, q_j)$ (3.24). In doing so, we will reproduce the results presented by *Kritsotakis* et al. in the appendix A of Ref. [166] for the convenience of the reader. First, we use that the momentum operator $\hat{\mathbf{p}}$ in

$$\hat{U}(t) = \exp\left[-\frac{it}{\hbar}\left(\frac{\hat{\mathbf{p}}^2}{2M} + Mg\hat{z}\right)\right], \quad (\text{B.1})$$

is diagonal in the states acting on $|q_j\rangle_j$, $\hat{\mathbf{p}}|q_j\rangle_j = \hat{p}_z|q_j\rangle_j = q_j|q_j\rangle_j$. The effect of the operator $\exp[\pm ik\hat{z}]$ on those states is also well known (e.g., see appendix C.1 of [195]): Let $|q\rangle$ and $|z\rangle$ be eigenstate of the momentum operator \hat{p}_z and the position operator \hat{z} respectively. In this case, we find that

$$e^{\pm ik\hat{z}} \equiv \int_{-\infty}^{+\infty} dq |q \pm \kappa\rangle\langle q|, \quad (\text{B.2})$$

where we have used the identity

$$\langle z|e^{\pm ik\hat{z}}|q\rangle = e^{\pm ikz} \langle z|q\rangle = e^{\pm ikz} \frac{1}{\sqrt{2\pi\hbar}} e^{iqz/\hbar} = \frac{1}{\sqrt{2\pi\hbar}} e^{iz(q \pm \hbar\kappa)/\hbar} = \langle z|q \pm \kappa\rangle. \quad (\text{B.3})$$

To use this result, we first need to isolate the operators in Eq. (B.1) via the application of the Baker-Campbell-Hausdorff lemma:

$$e^{\hat{X}+\hat{Y}} = e^{\hat{X}} e^{\hat{Y}} e^{-[\hat{X},\hat{Y}]/2} e^{(2[\hat{Y},[\hat{X},\hat{Y}]]+[\hat{X},[\hat{X},\hat{Y}]])/6}, \quad (\text{B.4})$$

which is true for operators \hat{X}, \hat{Y} fulfilling

$$[[[\hat{X}, \hat{Y}], \hat{X}], \hat{X}] = [[[\hat{X}, \hat{Y}], \hat{X}], \hat{Y}] = [[[\hat{X}, \hat{Y}], \hat{Y}], \hat{Y}] = 0.$$

In our case $\hat{X} = -\frac{i}{\hbar} \frac{\hat{\mathbf{p}}^2}{2M}$ and $\hat{Y} = -\frac{i}{\hbar} Mg\hat{z}$, so that

$$[\hat{X}, \hat{Y}] = \frac{igt^2}{\hbar} \hat{p}_z, \quad [\hat{Y}, [\hat{X}, \hat{Y}]] = \frac{iMg^2t^3}{\hbar}, \quad \text{and} \quad [\hat{X}, [\hat{X}, \hat{Y}]] = 0, \quad (\text{B.5})$$

where we have used the fundamental commutation relations $[\hat{z}, \hat{p}_z] = i\hbar = [\hat{z}, \hat{\mathbf{p}}]$. Thus, we are allowed to apply Eq. (B.4) to transform $\hat{U}(t)$, yielding

$$\hat{U}(t) = e^{-\frac{i}{\hbar} \left(\frac{\hat{\mathbf{p}}^2}{2M} + Mg\hat{z} \right)} = e^{\frac{iMg^2t^3}{3\hbar}} e^{-\frac{i}{\hbar} \frac{\hat{\mathbf{p}}^2}{2M}} e^{-\frac{i}{\hbar} Mg\hat{z}} e^{-\frac{igt^2}{2\hbar} \hat{p}_z}. \quad (\text{B.6})$$

With this, we can show for the time evolution during the free propagation time T

$$\begin{aligned} \hat{U}(T) |q_j\rangle_j &= e^{\frac{iMg^2T^3}{3\hbar}} e^{-\frac{iT}{\hbar} \frac{\hat{\mathbf{p}}^2}{2M}} e^{-\frac{iT}{\hbar} Mg\hat{z}} e^{-\frac{igT^2}{2\hbar} \hat{p}_z} |q_j\rangle_j = e^{\frac{iMg^2T^3}{3\hbar}} e^{-\frac{igT^2}{2\hbar} q_j} e^{-\frac{iT}{\hbar} \frac{\hat{\mathbf{p}}^2}{2M}} |q_j - MgT\rangle_j \\ &= e^{i\vartheta(g, T, q_j)} |q_j - MgT\rangle_j. \end{aligned} \quad (\text{B.7})$$

At this point, we recall that, while the momenta q_j are affected by the effective gravitational acceleration, due to $|g| \ll \hbar k / (MT)$ we assume this effect to be negligible on the level of the trajectories as explained in Sec. 3.4. Moreover, we have introduced the propagation phase

$$\vartheta(g, T, q_j) = M \frac{g^2 T^3}{3\hbar} - \frac{gT^2}{2\hbar} q_j - \frac{T}{2M\hbar} (q_j - MgT)^2. \quad (\text{B.8})$$

It will be useful to evaluate this phase once for a discrete momentum of $q_j = 2m_j \hbar k$ with $m_j \in \mathbb{Z}$. In this case, we find

$$\begin{aligned} \vartheta(g, T, 2m_j \hbar k) &= M \frac{g^2 T^3}{3\hbar} - \frac{gT^2}{2\hbar} 2m_j \hbar k - \frac{T}{2M\hbar} (2m_j \hbar k - MgT)^2 \\ &= \dots = -M \frac{g^2 T^3}{6\hbar} - 4m_j^2 \frac{\hbar k^2}{2M} T + m_j kgT^2 \\ &= -M \frac{g^2 T^3}{6\hbar} - 4m_j^2 \omega_r T + m_j \phi_g, \end{aligned} \quad (\text{B.9})$$

where in the last line we have introduced the recoil frequency $\omega_r = \hbar k^2 / 2M$ and the phase $\phi = kgT^2$. Seeing the above result we can simply write

$$\vartheta_j := \theta_j + m_j \phi, \quad (\text{B.10})$$

with

$$\theta_j := -M \frac{g^2 T^3}{6\hbar} - 4m_j^2 \omega_r T. \quad (\text{B.11})$$

List of Figures

| | | |
|------|--|-----|
| 1.1 | Space-time diagram of a three-pulse Mach-Zehnder (MZ) matter wave interferometer. | 4 |
| 2.1 | Single Bragg diffraction setup. | 15 |
| 2.2 | Bloch energy bands. | 20 |
| 2.3 | Eigenenergies of the Bragg Hamiltonian. | 32 |
| 2.4 | Dimensionless Bragg diffraction parameters. | 34 |
| 2.5 | Nonnormalized Bragg diffraction fidelities. | 46 |
| 2.6 | Normalized Bragg diffraction fidelities. | 48 |
| 2.7 | Bragg beam splitter fidelity. | 51 |
| 2.8 | Bragg mirror fidelity. | 53 |
| 2.9 | Spurious beam splitter population and LZ amplitudes for Bragg order $n = 5$ | 60 |
| 2.10 | Dominant spurious beam splitter population for Bragg order $n = 5$ | 63 |
| 2.11 | Bloch energy bands and eigenenergies of the Bragg Hamiltonian. | 67 |
| 3.1 | Space-time diagram of a three-pulse MZ interferometer and sample interference signal. | 70 |
| 3.2 | Space-time diagram of the MZ geometry showing dominant parasitic paths of Bragg orders $n \geq 3$ | 80 |
| 3.3 | Pulse parameters and mirror reflectivity for Bragg order $n = 5$ | 91 |
| 3.4 | Population loss for a fifth-order Bragg beam splitter. | 93 |
| 3.5 | Space-time diagrams of the MZ geometry showing parasitic paths. | 94 |
| 3.6 | Signal phase scan of the MZ interferometer. | 95 |
| 3.7 | Phase offset γ/n of the MZ interferometer. | 98 |
| 3.8 | Phase estimation error for different pulse separation times T | 100 |
| 3.9 | Suppression of the diffraction phases in the MZ geometry at mid fringe, $\phi_0 = \frac{3\pi}{2} \frac{1}{5}$ | 101 |
| 3.10 | Suppression of the diffraction phases at the alternative mid-fringe position, $\phi_0 = \frac{\pi}{2} \frac{1}{5}$ | 103 |
| 3.11 | Sensitivity bound of multiport Bragg interferometers with uncorrelated particles. | 110 |
| 4.1 | Double Bragg diffraction (DBD) setup. | 123 |

| | | |
|------|--|-----|
| 4.2 | Spectra of the Bloch Hamiltonian. | 129 |
| 4.3 | Bloch oscillations in the Bloch-band picture. | 133 |
| 4.4 | Experimental twin-lattice setup. | 137 |
| 4.5 | Fidelity of one Bloch oscillation (BO) in the twin lattice. | 139 |
| 4.6 | Fidelity of one Bloch oscillation (BO) in the twin lattice for different DBD splittings. | 141 |
| 4.7 | Twin-lattice interferometer scheme. | 144 |
| 4.8 | Twin-lattice interferometer contrast data. | 147 |
| 4.9 | Schematic of simulated light field and measured beam profile. | 159 |
| 4.10 | Theoretical contrast analysis. | 163 |

List of Tables

| | | |
|-----|--|-----|
| 2.1 | Parameters to determine the LZ phases. | 37 |
| 2.2 | Bragg scattering matrix parameters. | 44 |
| 4.1 | GPE simulation parameters. | 143 |
| 4.2 | Twin-lattice sequence parameters | 145 |
| 4.3 | Diffraction model input parameters. | 160 |

Bibliography

- [1] L. de Broglie. Radiations - ondes et quanta. *Comp. Rend. Ac. Sci.*, 177(507), 1923. (cit. on page 1).
- [2] C. J. Davisson and L. H. Germer. Reflection and Refraction of Electrons by a Crystal of Nickel. *Proceedings of the National Academy of Sciences*, 14(8):619–627, August 1928. doi:10.1073/pnas.14.8.619. (cit. on page 1).
- [3] G. P. Thomson and J. J. Thomson. Experiments on the diffraction of cathode rays. *Proceedings of the Royal Society of London. Series A, Containing Papers of a Mathematical and Physical Character*, 117(778):600–609, February 1928. doi:10.1098/rspa.1928.0022. (cit. on page 1).
- [4] S. A. Werner, J. L. Staudenmann, and R. Colella. Effect of Earth’s Rotation on the Quantum Mechanical Phase of the Neutron. *Physical Review Letters*, 42(17):1103–1106, April 1979. doi:10.1103/PhysRevLett.42.1103. (cit. on page 1).
- [5] D. M. Greenberger and A. W. Overhauser. Coherence effects in neutron diffraction and gravity experiments. *Reviews of Modern Physics*, 51(1):43–78, January 1979. doi:10.1103/RevModPhys.51.43. (cit. on page 1).
- [6] O. Carnal and J. Mlynek. Young’s double-slit experiment with atoms: A simple atom interferometer. *Physical Review Letters*, 66(21):2689–2692, May 1991. doi:10.1103/PhysRevLett.66.2689. (cit. on pages 1 and 2).
- [7] D. W. Keith, C. R. Ekstrom, Q. A. Turchette, and D. E. Pritchard. An interferometer for atoms. *Physical Review Letters*, 66(21):2693–2696, May 1991. doi:10.1103/PhysRevLett.66.2693. (cit. on pages 1 and 2).
- [8] F. Riehle, Th. Kisters, A. Witte, J. Helmcke, and Ch. J. Bordé. Optical Ramsey spectroscopy in a rotating frame: Sagnac effect in a matter-wave interferometer. *Physical Review Letters*, 67(2):177–180, July 1991. doi:10.1103/PhysRevLett.67.177. (cit. on pages 1, 2, and 7).
- [9] M. Kasevich and S. Chu. Atomic interferometry using stimulated Raman transitions. *Physical Review Letters*, 67(2):181–184, July 1991. doi:10.1103/PhysRevLett.67.181. (cit. on pages 1, 2, 7, and 69).

- [10] A. D. Cronin, J. Schmiedmayer, and D. E. Pritchard. Optics and interferometry with atoms and molecules. *Reviews of Modern Physics*, 81(3):1051–1129, July 2009. doi:[10.1103/RevModPhys.81.1051](https://doi.org/10.1103/RevModPhys.81.1051). (cit. on page 1).
- [11] M. Arndt and K. Hornberger. Testing the limits of quantum mechanical superpositions. *Nature Physics*, 10(4):271–277, April 2014. doi:[10.1038/nphys2863](https://doi.org/10.1038/nphys2863). (cit. on page 1).
- [12] P. Meystre. *Atom Optics*. In *Atom Optics*, chapter 4, pages 57–68. Springer Germany, 3 edition, 2009. (cit. on pages 1, 12, 14, 16, and 118).
- [13] T. H. Maiman. Stimulated Optical Radiation in Ruby. *Nature*, 187(4736):493–494, August 1960. doi:[10.1038/187493a0](https://doi.org/10.1038/187493a0). (cit. on page 1).
- [14] S. Chu. Nobel Lecture: The manipulation of neutral particles. *Reviews of Modern Physics*, 70(3):685–706, July 1998. doi:[10.1103/RevModPhys.70.685](https://doi.org/10.1103/RevModPhys.70.685). (cit. on page 1).
- [15] C. N. Cohen-Tannoudji. Nobel Lecture: Manipulating atoms with photons. *Reviews of Modern Physics*, 70(3):707–719, July 1998. doi:[10.1103/RevModPhys.70.707](https://doi.org/10.1103/RevModPhys.70.707). (cit. on page 1).
- [16] W. D. Phillips. Nobel Lecture: Laser cooling and trapping of neutral atoms. *Reviews of Modern Physics*, 70(3):721–741, July 1998. doi:[10.1103/RevModPhys.70.721](https://doi.org/10.1103/RevModPhys.70.721). (cit. on page 1).
- [17] E. A. Cornell and C. E. Wieman. Nobel Lecture: Bose-Einstein condensation in a dilute gas, the first 70 years and some recent experiments. *Reviews of Modern Physics*, 74(3):875–893, August 2002. doi:[10.1103/RevModPhys.74.875](https://doi.org/10.1103/RevModPhys.74.875). (cit. on page 1).
- [18] W. Ketterle. Nobel lecture: When atoms behave as waves: Bose-Einstein condensation and the atom laser. *Reviews of Modern Physics*, 74(4):1131–1151, November 2002. doi:[10.1103/RevModPhys.74.1131](https://doi.org/10.1103/RevModPhys.74.1131). (cit. on page 1).
- [19] S. Bose. Plancks Gesetz und Lichtquantenhypothese. *Zeitschrift für Physik*, 26(1):178–181, December 1924. doi:[10.1007/BF01327326](https://doi.org/10.1007/BF01327326). (cit. on pages 1 and 117).
- [20] A. Einstein. Quantentheorie des einatomigen idealen Gases. volume 1 of 3. Sitzungsberichte Der Preuss. Akad. Der Wissenschaften, 1925. (cit. on pages 1 and 117).

- [21] G. M. Tino and M. A. Kasevich, editors. *Atom Interferometry*. Societ' a Italiana di Fisica and IOS Press, Amsterdam, 2014. (cit. on page 2).
- [22] A. Arvanitaki, S. Dimopoulos, A. A. Geraci, J. Hogan, and M. Kasevich. How to test atom and neutron neutrality with atom interferometry. *Physical Review Letters*, 100(12):120407, March 2008. doi:10.1103/PhysRevLett.100.120407. (cit. on page 2).
- [23] R. H. Parker, C. Yu, W. Zhong, B. Estey, and H. Müller. Measurement of the fine-structure constant as a test of the Standard Model. *Science*, April 2018. doi:10.1126/science.aap7706. (cit. on pages 2, 8, 11, 69, 85, 111, 114, 164, 167, and 173).
- [24] L. Morel, Z. Yao, P. Cladé, and S. Guellati-Khélifa. Determination of the fine-structure constant with an accuracy of 81 parts per trillion. *Nature*, 588(7836):61–65, December 2020. doi:10.1038/s41586-020-2964-7. (cit. on pages 2, 8, 85, 114, 134, 135, and 165).
- [25] G. M. Tino. Testing gravity with cold atom interferometry: Results and prospects. *Quantum Science and Technology*, 6(2):024014, March 2021. doi:10.1088/2058-9565/abd83e. (cit. on page 2).
- [26] G. Rosi, F. Sorrentino, L. Cacciapuoti, M. Prevedelli, and G. M. Tino. Precision measurement of the Newtonian gravitational constant using cold atoms. *Nature*, 510(7506):518–521, June 2014. doi:10.1038/nature13433. (cit. on page 2).
- [27] A. Bonnin, N. Zahzam, Y. Bidel, and A. Bresson. Simultaneous dual-species matter-wave accelerometer. *Physical Review A: Atomic, Molecular, and Optical Physics*, 88(4):043615, October 2013. doi:10.1103/PhysRevA.88.043615. (cit. on page 2).
- [28] D. Schlippert, J. Hartwig, H. Albers, L. L. Richardson, C. Schubert, A. Roura, W. P. Schleich, W. Ertmer, and E. M. Rasel. Quantum test of the universality of free fall. *Physical Review Letters*, 112(20):203002, May 2014. doi:10.1103/PhysRevLett.112.203002. (cit. on page 2).
- [29] L. Zhou, S. Long, B. Tang, X. Chen, F. Gao, W. Peng, W. Duan, J. Zhong, Z. Xiong, J. Wang, Y. Zhang, and M. Zhan. Test of Equivalence Principle at 10^{-8} Level by a Dual-Species Double-Diffraction Raman Atom Interferometer. *Physical Review Letters*, 115(1):013004, July 2015. doi:10.1103/PhysRevLett.115.013004. (cit. on page 2).

- [30] B. Barrett, L. Antoni-Micollier, L. Chichet, B. Battelier, T. Lévèque, A. Landragin, and P. Bouyer. Dual water-mave inertial sensors in weightlessness. *Nature Communications*, 7(1):13786, December 2016. doi:[10.1038/ncomms13786](https://doi.org/10.1038/ncomms13786). (cit. on page 2).
- [31] C. Overstreet, P. Asenbaum, T. Kovachy, R. Notermans, J. M. Hogan, and M. A. Kasevich. Effective Inertial Frame in an Atom Interferometric Test of the Equivalence Principle. *Physical Review Letters*, 120(18):183604, May 2018. doi:[10.1103/PhysRevLett.120.183604](https://doi.org/10.1103/PhysRevLett.120.183604). (cit. on page 2).
- [32] P. Asenbaum, C. Overstreet, M. Kim, J. Curti, and M. A. Kasevich. Atom-Interferometric Test of the Equivalence Principle at the 10^{-12} Level. *Physical Review Letters*, 125(19):191101, November 2020. doi:[10.1103/PhysRevLett.125.191101](https://doi.org/10.1103/PhysRevLett.125.191101). (cit. on pages 2, 8, 69, and 167).
- [33] S. Dimopoulos, P. W. Graham, J. M. Hogan, M. A. Kasevich, and S. Rajendran. Gravitational wave detection with atom interferometry. *Physics Letters B*, 678(1):37–40, 2009. doi:[10.1016/j.physletb.2009.06.011](https://doi.org/10.1016/j.physletb.2009.06.011). (cit. on pages 2 and 167).
- [34] N. Yu and M. Tinto. Gravitational wave detection with single-laser atom interferometers. *General Relativity and Gravitation*, 43(7):1943–1952, July 2011. doi:[10.1007/s10714-010-1055-8](https://doi.org/10.1007/s10714-010-1055-8). (cit. on pages 2 and 167).
- [35] J. M. Hogan, et al. An atomic gravitational wave interferometric sensor in low earth orbit (AGIS-LEO). *General Relativity and Gravitation*, 43(7):1953–2009, July 2011. doi:[10.1007/s10714-011-1182-x](https://doi.org/10.1007/s10714-011-1182-x). (cit. on pages 2 and 167).
- [36] B. Canuel, et al. Exploring gravity with the MIGA large scale atom interferometer. *Scientific Reports*, 8(1):14064, September 2018. doi:[10.1038/s41598-018-32165-z](https://doi.org/10.1038/s41598-018-32165-z). (cit. on pages 2, 164, and 167).
- [37] C. Schubert, D. Schlippert, S. Abend, E. Giese, A. Roura, W. P. Schleich, W. Ertmer, and E. M. Rasel. Scalable, symmetric atom interferometer for infrasound gravitational wave detection. *arXiv:1909.01951*, 2019. arXiv:[1909.01951](https://arxiv.org/abs/1909.01951). (cit. on pages 2, 113, 164, and 167).
- [38] B. Canuel, et al. ELGAR—a European Laboratory for Gravitation and Atom-interferometric Research. *Classical and Quantum Gravity*, 37(22):225017, October 2020. doi:[10.1088/1361-6382/aba80e](https://doi.org/10.1088/1361-6382/aba80e). (cit. on pages 2, 113, 164, and 167).

- [39] M.-S. Zhan, et al. ZAIGA: Zhaoshan long-baseline atom interferometer gravitation antenna. *International Journal of Modern Physics D*, 29(04):1940005, March 2020. doi:10.1142/S0218271819400054. (cit. on pages 2 and 167).
- [40] M. Abe, et al. Matter-wave Atomic Gradiometer Interferometric Sensor (MAGIS-100). *Quantum Science and Technology*, 6(4):044003, July 2021. doi:10.1088/2058-9565/abf719. (cit. on pages 2, 113, 164, and 167).
- [41] M. Zych, F. Costa, I. Pikovski, and Č. Brukner. Quantum interferometric visibility as a witness of general relativistic proper time. *Nature Communications*, 2(1):505, October 2011. doi:10.1038/ncomms1498. (cit. on page 2).
- [42] S. Loriani, et al. Interference of clocks: A quantum twin paradox. *Science Advances*, 5(10):eaax8966, October 2019. doi:10.1126/sciadv.aax8966. (cit. on page 2).
- [43] A. Roura. Gravitational Redshift in Quantum-Clock Interferometry. *Physical Review X*, 10(2):021014, April 2020. doi:10.1103/PhysRevX.10.021014. (cit. on page 2).
- [44] A. Roura, C. Schubert, D. Schlippert, and E. M. Rasel. Measuring gravitational time dilation with delocalized quantum superpositions. *Physical Review D*, 104(8):084001, October 2021. doi:10.1103/PhysRevD.104.084001. (cit. on page 2).
- [45] F. Di Pumpo, C. Ufrecht, A. Friedrich, E. Giese, W. P. Schleich, and W. G. Unruh. Gravitational Redshift Tests with Atomic Clocks and Atom Interferometers. *PRX Quantum*, 2(4):040333, November 2021. doi:10.1103/PRXQuantum.2.040333. (cit. on page 2).
- [46] L. Badurina, et al. AION: An atom interferometer observatory and network. *Journal of Cosmology and Astroparticle Physics*, 2020(05):011–011, May 2020. doi:10.1088/1475-7516/2020/05/011. (cit. on pages 2 and 167).
- [47] I. Alonso, et al. Cold Atoms in Space: Community Workshop Summary and Proposed Road-Map, January 2022. arXiv:2201.07789, doi:10.48550/arXiv.2201.07789. (cit. on pages 2, 116, 136, and 167).
- [48] K. Bongs, M. Holynski, J. Vovrosh, P. Bouyer, G. Condon, E. Rasel, C. Schubert, W. P. Schleich, and A. Roura. Taking atom interferometric quantum sensors from the laboratory to real-world applications. *Nature Reviews Physics*, 1(12):731–739, December 2019. doi:10.1038/s42254-019-0117-4. (cit. on pages 2 and 6).

- [49] V. Ménoret, P. Vermeulen, N. Le Moigne, S. Bonvalot, P. Bouyer, A. Landragin, and B. Desruelle. Gravity measurements below $10^{-9}g$ with a transportable absolute quantum gravimeter. *Scientific Reports*, 8(1):12300, August 2018. doi:[10.1038/s41598-018-30608-1](https://doi.org/10.1038/s41598-018-30608-1). (cit. on page 2).
- [50] X. Wu, Z. Pagel, B. S. Malek, T. H. Nguyen, F. Zi, D. S. Scheirer, and H. Müller. Gravity surveys using a mobile atom interferometer. *Science Advances*, 5(9):eaax0800, 2019. doi:[10.1126/sciadv.aax0800](https://doi.org/10.1126/sciadv.aax0800). (cit. on page 2).
- [51] B. Stray, et al. Quantum sensing for gravity cartography. *Nature*, 602(7898):590–594, February 2022. doi:[10.1038/s41586-021-04315-3](https://doi.org/10.1038/s41586-021-04315-3). (cit. on page 2).
- [52] R. Geiger, et al. Detecting inertial effects with airborne matter-wave interferometry. *Nature Communications*, 2(1):474, September 2011. doi:[10.1038/ncomms1479](https://doi.org/10.1038/ncomms1479). (cit. on pages 2, 6, 136, and 147).
- [53] P. Cheiney, L. Fouché, S. Templier, F. Napolitano, B. Battelier, P. Bouyer, and B. Barrett. Navigation-Compatible Hybrid Quantum Accelerometer Using a Kalman Filter. *Physical Review Applied*, 10(3):034030, September 2018. doi:[10.1103/PhysRevApplied.10.034030](https://doi.org/10.1103/PhysRevApplied.10.034030). (cit. on page 2).
- [54] R. Geiger, A. Landragin, S. Merlet, and F. Pereira Dos Santos. High-accuracy inertial measurements with cold-atom sensors. *AVS Quantum Science*, 2(2):024702, June 2020. doi:[10.1116/5.0009093](https://doi.org/10.1116/5.0009093). (cit. on pages 2, 5, 8, 69, 71, 72, 94, 111, 113, 116, and 122).
- [55] P. Storey and C. Cohen-Tannoudji. The Feynman path integral approach to atomic interferometry. A tutorial. *Journal de Physique II*, 4(11):1999–2027, November 1994. doi:[10.1051/jp2:1994103](https://doi.org/10.1051/jp2:1994103). (cit. on pages 4, 70, and 88).
- [56] C. J. Bordé. Quantum Theory of Atom-Wave Beam Splitters and Application to Multidimensional Atomic Gravito-Inertial Sensors. *General Relativity and Gravitation*, 36(3):475–502, March 2004. doi:[10.1023/B:GERG.0000010726.64769.6d](https://doi.org/10.1023/B:GERG.0000010726.64769.6d). (cit. on pages 4, 70, and 88).
- [57] G. D. McDonald and C. C. N. Kuhn. Space-Time Area in Atom Interferometry, July 2014. arXiv:[1312.2713](https://arxiv.org/abs/1312.2713), doi:[10.48550/arXiv.1312.2713](https://doi.org/10.48550/arXiv.1312.2713). (cit. on pages 4, 88, and 146).
- [58] W. M. Itano, J. C. Bergquist, J. J. Bollinger, J. M. Gilligan, D. J. Heinzen, F. L. Moore, M. G. Raizen, and D. J. Wineland. Quantum projection noise: Population fluctuations in two-level systems. *Physical Review A*, 47(5):3554–3570, May 1993. doi:[10.1103/PhysRevA.47.3554](https://doi.org/10.1103/PhysRevA.47.3554). (cit. on page 5).

- [59] J. M. Hogan, D. M. S. Johnson, and M. A. Kasevich. Light-pulse atom interferometry. *Proc. Int. School Phys. Enrico Fermi*, 168:411–446, 2009. doi:[10.3254/978-1-58603-990-5-411](https://doi.org/10.3254/978-1-58603-990-5-411). (cit. on pages 5 and 155).
- [60] F. A. Narducci, A. T. Black, and J. H. Burke. Advances toward fieldable atom interferometers. *Advances in Physics: X*, 7(1):1946426, December 2022. doi:[10.1080/23746149.2021.1946426](https://doi.org/10.1080/23746149.2021.1946426). (cit. on pages 5, 72, 111, and 167).
- [61] J. Kwolek, C. Fancher, M. Bashkansky, and A. Black. Three-Dimensional Cooling of an Atom-Beam Source for High-Contrast Atom Interferometry. *Physical Review Applied*, 13(4):044057, April 2020. doi:[10.1103/PhysRevApplied.13.044057](https://doi.org/10.1103/PhysRevApplied.13.044057). (cit. on page 5).
- [62] T. L. Gustavson, A. Landragin, and M. A. Kasevich. Rotation sensing with a dual atom-interferometer Sagnac gyroscope. *Classical and Quantum Gravity*, 17(12):2385, June 2000. doi:[10.1088/0264-9381/17/12/311](https://doi.org/10.1088/0264-9381/17/12/311). (cit. on page 5).
- [63] J. Rudolph, et al. A high-flux BEC source for mobile atom interferometers. *New Journal of Physics*, 17(6):065001, June 2015. doi:[10.1088/1367-2630/17/6/065001](https://doi.org/10.1088/1367-2630/17/6/065001). (cit. on pages 5, 6, 116, and 136).
- [64] T. Kovachy, J. M. Hogan, A. Sugarbaker, S. M. Dickerson, C. A. Donnelly, C. Overstreet, and M. A. Kasevich. Matter Wave Lensing to Picokelvin Temperatures. *Physical Review Letters*, 114(14):143004, April 2015. doi:[10.1103/PhysRevLett.114.143004](https://doi.org/10.1103/PhysRevLett.114.143004). (cit. on pages 6, 7, 11, 18, 33, 78, 111, and 116).
- [65] C. Deppner, et al. Collective-Mode Enhanced Matter-Wave Optics. *Physical Review Letters*, 127(10):100401, August 2021. doi:[10.1103/PhysRevLett.127.100401](https://doi.org/10.1103/PhysRevLett.127.100401). (cit. on pages 6, 7, 18, 78, 111, 114, 116, and 136).
- [66] V. Schkolnik, B. Leykauf, M. Hauth, C. Freier, and A. Peters. The effect of wavefront aberrations in atom interferometry. *Applied Physics B*, 120(2):311–316, August 2015. doi:[10.1007/s00340-015-6138-5](https://doi.org/10.1007/s00340-015-6138-5). (cit. on pages 6, 8, 152, and 158).
- [67] A. Trimeche, M. Langlois, S. Merlet, and F. Pereira Dos Santos. Active Control of Laser Wavefronts in Atom Interferometers. *Physical Review Applied*, 7(3):034016, March 2017. doi:[10.1103/PhysRevApplied.7.034016](https://doi.org/10.1103/PhysRevApplied.7.034016). (cit. on pages 6, 8, 152, and 158).
- [68] R. Karcher, A. Imanaliev, S. Merlet, and F. P. D. Santos. Improving the accuracy of atom interferometers with ultracold sources. *New Journal of Physics*, 20(11):113041, November 2018. doi:[10.1088/1367-2630/aaf07d](https://doi.org/10.1088/1367-2630/aaf07d). (cit. on pages 6, 8, 152, and 158).

- [69] S. S. Szigeti, J. E. Debs, J. J. Hope, N. P. Robins, and J. D. Close. Why momentum width matters for atom interferometry with Bragg pulses. *New Journal of Physics*, 14(2):023009, February 2012. doi:[10.1088/1367-2630/14/2/023009](https://doi.org/10.1088/1367-2630/14/2/023009). (cit. on pages 6, 7, 17, 18, 23, 33, 44, 63, 65, 90, 135, and 169).
- [70] N. P. Robins, P. A. Altin, J. E. Debs, and J. D. Close. Atom lasers: Production, properties and prospects for precision inertial measurement. *Physics Reports*, 529(3):265–296, August 2013. doi:[10.1016/j.physrep.2013.03.006](https://doi.org/10.1016/j.physrep.2013.03.006). (cit. on page 6).
- [71] F. Schreck and K. van Druten. Laser cooling for quantum gases. *Nature Physics*, 17(12):1296–1304, December 2021. doi:[10.1038/s41567-021-01379-w](https://doi.org/10.1038/s41567-021-01379-w). (cit. on pages 6 and 116).
- [72] C. Gross, T. Zibold, E. Nicklas, J. Estève, and M. K. Oberthaler. Nonlinear atom interferometer surpasses classical precision limit. *Nature*, 464(7292):1165–1169, April 2010. doi:[10.1038/nature08919](https://doi.org/10.1038/nature08919). (cit. on pages 6 and 116).
- [73] M. F. Riedel, P. Böhi, Y. Li, T. W. Hänsch, A. Sinatra, and P. Treutlein. Atom-chip-based generation of entanglement for quantum metrology. *Nature*, 464(7292):1170–1173, April 2010. doi:[10.1038/nature08988](https://doi.org/10.1038/nature08988). (cit. on pages 6 and 116).
- [74] L. Pezzé and A. Smerzi. Entanglement, Nonlinear Dynamics, and the Heisenberg Limit. *Physical Review Letters*, 102(10):100401, March 2009. doi:[10.1103/PhysRevLett.102.100401](https://doi.org/10.1103/PhysRevLett.102.100401). (cit. on pages 6 and 76).
- [75] S. S. Szigeti, O. Hosten, and S. A. Haine. Improving cold-atom sensors with quantum entanglement: Prospects and challenges. *Applied Physics Letters*, 118(14):140501, April 2021. doi:[10.1063/5.0050235](https://doi.org/10.1063/5.0050235). (cit. on page 6).
- [76] A. Hinton, et al. A portable magneto-optical trap with prospects for atom interferometry in civil engineering. *Philosophical Transactions of the Royal Society A: Mathematical, Physical and Engineering Sciences*, 375(2099):20160238, August 2017. doi:[10.1098/rsta.2016.0238](https://doi.org/10.1098/rsta.2016.0238). (cit. on page 6).
- [77] S. Ravenhall, B. Yuen, and C. Foot. High-flux, adjustable, compact cold-atom source. *Optics Express*, 29(14):21143–21159, July 2021. doi:[10.1364/OE.423662](https://doi.org/10.1364/OE.423662). (cit. on pages 6 and 116).
- [78] J. Lee, et al. A compact cold-atom interferometer with a high data-rate grating magneto-optical trap and a photonic-integrated-circuit-compatible laser system. *Nature Communications*, 13(1):5131, September 2022. doi:[10.1038/s41467-022-31410-4](https://doi.org/10.1038/s41467-022-31410-4). (cit. on page 6).

- [79] J. E. Debs, P. A. Altin, T. H. Barter, D. Döring, G. R. Dennis, G. McDonald, R. P. Anderson, J. D. Close, and N. P. Robins. Cold-atom gravimetry with a Bose-Einstein condensate. *Physical Review A*, 84(3):033610, September 2011. doi:10.1103/PhysRevA.84.033610. (cit. on pages 6, 115, and 116).
- [80] H. Müntinga et al. Interferometry with Bose-Einstein condensates in microgravity. *Physical Review Letters*, 110(9):093602, February 2013. doi:10.1103/PhysRevLett.110.093602. (cit. on pages 6, 116, and 136).
- [81] M. D. Lachmann, et al. Ultracold atom interferometry in space. *Nature Communications*, 12(1):1317, February 2021. doi:10.1038/s41467-021-21628-z. (cit. on pages 6, 126, and 136).
- [82] D. C. Aveline, J. R. Williams, E. R. Elliott, C. Dutenhoffer, J. R. Kellogg, J. M. Kohel, N. E. Lay, K. Oudrhiri, R. F. Shotwell, N. Yu, and R. J. Thompson. Observation of Bose–Einstein condensates in an Earth-orbiting research lab. *Nature*, 582(7811):193–197, June 2020. doi:10.1038/s41586-020-2346-1. (cit. on pages 6 and 136).
- [83] K. Frye, et al. The Bose-Einstein Condensate and Cold Atom Laboratory. *EPJ Quantum Technology*, 8(1):1–38, December 2021. doi:10.1140/epjqt/s40507-020-00090-8. (cit. on pages 6 and 136).
- [84] P. Cladé, S. Guellati-Khélifa, C. Schwob, F. Nez, L. Julien, and F. Biraben. A promising method for the measurement of the local acceleration of gravity using Bloch oscillations of ultracold atoms in a vertical standing wave. *Europhysics Letters*, 71(5):730, August 2005. doi:10.1209/epl/i2005-10163-6. (cit. on pages 6 and 8).
- [85] R. Charrière, M. Cadoret, N. Zahzam, Y. Bidel, and A. Bresson. Local gravity measurement with the combination of atom interferometry and Bloch oscillations. *Physical Review A: Atomic, Molecular, and Optical Physics*, 85(1):013639, January 2012. doi:10.1103/PhysRevA.85.013639. (cit. on pages 6, 8, 114, 116, 152, 155, 157, and 158).
- [86] X. Zhang, R. P. del Aguila, T. Mazzoni, N. Poli, and G. M. Tino. Trapped-atom interferometer with ultracold Sr atoms. *Physical Review A*, 94(4):043608, October 2016. doi:10.1103/PhysRevA.94.043608. (cit. on pages 6, 8, 114, 116, 152, 155, and 158).

- [87] V. Xu, M. Jaffe, C. D. Panda, S. L. Kristensen, L. W. Clark, and H. Müller. Probing gravity by holding atoms for 20 seconds. *Science*, 366(6466):745–749, November 2019. doi:10.1126/science.aay6428. (cit. on pages 6, 114, 152, and 155).
- [88] C. D. Panda, M. Tao, J. Egelhoff, M. Ceja, V. Xu, and H. Müller. Minute-scale gravimetry using a coherent atomic spatial superposition, May 2023. arXiv:2210.07289, doi:10.48550/arXiv.2210.07289. (cit. on pages 6, 8, 114, 116, 152, 155, and 164).
- [89] T. Hensel, S. Loriani, C. Schubert, F. Fitzek, S. Abend, H. Ahlers, J.-N. Siemß, K. Hammerer, E. M. Rasel, and N. Gaaloul. Inertial sensing with quantum gases: A comparative performance study of condensed versus thermal sources for atom interferometry. *The European Physical Journal D*, 75(3):108, March 2021. doi:10.1140/epjd/s10053-021-00069-9. (cit. on pages 6, 8, 115, 116, and 158).
- [90] D. Becker, et al. Space-borne Bose–Einstein condensation for precision interferometry. *Nature*, 562(7727):391–395, October 2018. doi:10.1038/s41586-018-0605-1. (cit. on pages 6 and 136).
- [91] QUANTengase unter Schwerelosigkeit (QUANTUS) collaboration. URL: <https://quantus.zarm.uni-bremen.de/>. (cit. on page 6).
- [92] German Aerospace Center (DLR). URL: https://www.dlr.de/DE/Home/home_node.html. (cit. on pages 6 and 136).
- [93] T. van Zoest et al. Bose-Einstein condensation in microgravity. *Science (New York, N.Y.)*, 328:1540, 2010. doi:10.1126/science.1189164. (cit. on pages 6, 116, and 136).
- [94] H. Ahlers, et al. Double Bragg Interferometry. *Physical Review Letters*, 116(17):173601, April 2016. doi:10.1103/PhysRevLett.116.173601. (cit. on pages 7, 11, 17, 18, 33, 109, 113, 123, 125, 127, 136, 146, 149, 163, 164, and 174).
- [95] S. Abend, M. Gebbe, M. Gersemann, H. Ahlers, H. Müntinga, E. Giese, N. Gaaloul, C. Schubert, C. Lämmerzahl, W. Ertmer, W. P. Schleich, and E. M. Rasel. Atom-chip fountain gravimeter. *Physical Review Letters*, 117(20):203003, November 2016. doi:10.1103/PhysRevLett.117.203003. (cit. on pages 7, 124, and 136).
- [96] M. Gebbe, J.-N. Siemß, M. Gersemann, H. Müntinga, S. Herrmann, C. Lämmerzahl, H. Ahlers, N. Gaaloul, C. Schubert, K. Hammerer, S. Abend, and E. M. Rasel. Twin-lattice atom interferometry. *Nature Communications*, 12(1):2544, May 2021. doi:10.1038/s41467-021-22823-8. (cit. on pages 7, 8, 11, 33, 50, 114, 115, 136, 137, 141, 144, 147, 159, 163, 171, and 174).

- [97] S.-w. Chiow, T. Kovachy, H.-C. Chien, and M. A. Kasevich. $102\hbar k$ large Area Atom Interferometers. *Physical Review Letters*, 107(13), September 2011. doi:[10.1103/PhysRevLett.107.130403](https://doi.org/10.1103/PhysRevLett.107.130403). (cit. on pages 7, 11, 33, 50, 113, 145, 148, 163, and 172).
- [98] B. Plotkin-Swing, D. Gochnauer, K. E. McAlpine, E. S. Cooper, A. O. Jamison, and S. Gupta. Three-Path Atom Interferometry with Large Momentum Separation. *Physical Review Letters*, 121(13):133201, September 2018. doi:[10.1103/PhysRevLett.121.133201](https://doi.org/10.1103/PhysRevLett.121.133201). (cit. on pages 7, 8, 11, 17, 30, 33, 50, 66, 70, 72, 113, 145, 169, and 174).
- [99] T. Wilkason, M. Nantel, J. Rudolph, Y. Jiang, B. E. Garber, H. Swan, S. P. Carman, M. Abe, and J. M. Hogan. Atom Interferometry with Floquet Atom Optics. *Physical Review Letters*, 129(18):183202, October 2022. doi:[10.1103/PhysRevLett.129.183202](https://doi.org/10.1103/PhysRevLett.129.183202). (cit. on page 7).
- [100] D. A. Steck. Rubidium 87 D Line Data, 2003. URL: <https://steck.us/alkalidata/>. (cit. on pages 7, 94, and 139).
- [101] P. J. Martin, B. G. Oldaker, A. H. Miklich, and D. E. Pritchard. Bragg scattering of atoms from a standing light wave. *Physical Review Letters*, 60(6):515–518, February 1988. doi:[10.1103/PhysRevLett.60.515](https://doi.org/10.1103/PhysRevLett.60.515). (cit. on pages 7, 11, 64, and 69).
- [102] D. M. Giltner, R. W. McGowan, and S. A. Lee. Atom Interferometer Based on Bragg Scattering from Standing Light Waves. *Physical Review Letters*, 75(14):2638–2641, October 1995. doi:[10.1103/PhysRevLett.75.2638](https://doi.org/10.1103/PhysRevLett.75.2638). (cit. on pages 7, 11, and 64).
- [103] H. Müller, S.-w. Chiow, Q. Long, S. Herrmann, and S. Chu. Atom Interferometry with up to 24-Photon-Momentum-Transfer Beam Splitters. *Physical Review Letters*, 100(18):180405, May 2008. doi:[10.1103/PhysRevLett.100.180405](https://doi.org/10.1103/PhysRevLett.100.180405). (cit. on pages 7, 8, 11, 113, and 147).
- [104] T. Kovachy, S.-w. Chiow, and M. A. Kasevich. Adiabatic-rapid-passage multiphoton Bragg atom optics. *Physical Review A*, 86(1):011606, July 2012. doi:[10.1103/PhysRevA.86.011606](https://doi.org/10.1103/PhysRevA.86.011606). (cit. on pages 7, 11, 33, and 173).
- [105] J. Küber, F. Schmaltz, and G. Birkl. Experimental realization of double Bragg diffraction: Robust beamsplitters, mirrors, and interferometers for Bose-Einstein condensates, March 2016. arXiv:[1603.08826](https://arxiv.org/abs/1603.08826), doi:[10.48550/arXiv.1603.08826](https://doi.org/10.48550/arXiv.1603.08826). (cit. on pages 7, 11, 18, 113, 125, and 174).

- [106] M. Ben Dahan, E. Peik, J. Reichel, Y. Castin, and C. Salomon. Bloch Oscillations of Atoms in an Optical Potential. *Physical Review Letters*, 76(24):4508–4511, June 1996. doi:[10.1103/PhysRevLett.76.4508](https://doi.org/10.1103/PhysRevLett.76.4508). (cit. on pages 7, 11, 19, 114, and 127).
- [107] S. R. Wilkinson, C. F. Bharucha, K. W. Madison, Q. Niu, and M. G. Raizen. Observation of Atomic Wannier-Stark Ladders in an Accelerating Optical Potential. *Physical Review Letters*, 76(24):4512–4515, June 1996. doi:[10.1103/PhysRevLett.76.4512](https://doi.org/10.1103/PhysRevLett.76.4512). (cit. on pages 7, 11, 19, 114, and 127).
- [108] E. Peik, M. Ben Dahan, I. Bouchoule, Y. Castin, and C. Salomon. Bloch oscillations of atoms, adiabatic rapid passage, and monokinetic atomic beams. *Physical Review A*, 55(4):2989–3001, April 1997. doi:[10.1103/PhysRevA.55.2989](https://doi.org/10.1103/PhysRevA.55.2989). (cit. on pages 7, 11, 19, 114, 127, 130, 132, 134, and 164).
- [109] H. Müller, S.-w. Chiow, S. Herrmann, and S. Chu. Atom Interferometers with Scalable Enclosed Area. *Physical Review Letters*, 102(24):240403, June 2009. doi:[10.1103/PhysRevLett.102.240403](https://doi.org/10.1103/PhysRevLett.102.240403). (cit. on pages 7, 11, 33, and 114).
- [110] P. Cladé, S. Guellati-Khélifa, F. Nez, and F. Biraben. Large Momentum Beam Splitter Using Bloch Oscillations. *Physical Review Letters*, 102(24):240402, June 2009. doi:[10.1103/PhysRevLett.102.240402](https://doi.org/10.1103/PhysRevLett.102.240402). (cit. on pages 7, 11, 114, and 164).
- [111] G. D. McDonald, C. C. N. Kuhn, S. Bennetts, J. E. Debs, K. S. Hardman, M. Johnson, J. D. Close, and N. P. Robins. $80\hbar k$ momentum separation with Bloch oscillations in an optically guided atom interferometer. *Physical Review A*, 88(5):053620, November 2013. doi:[10.1103/PhysRevA.88.053620](https://doi.org/10.1103/PhysRevA.88.053620). (cit. on pages 7, 11, 33, and 114).
- [112] P. Asenbaum, C. Overstreet, T. Kovachy, D. D. Brown, J. M. Hogan, and M. A. Kasevich. Phase Shift in an Atom Interferometer due to Spacetime Curvature across its Wave Function. *Physical Review Letters*, 118(18):183602, May 2017. doi:[10.1103/PhysRevLett.118.183602](https://doi.org/10.1103/PhysRevLett.118.183602). (cit. on pages 8, 69, 164, and 167).
- [113] C. Overstreet, P. Asenbaum, J. Curti, M. Kim, and M. A. Kasevich. Observation of a gravitational Aharonov-Bohm effect. *Science*, 375(6577):226–229, January 2022. doi:[10.1126/science.abl7152](https://doi.org/10.1126/science.abl7152). (cit. on pages 8, 69, and 167).
- [114] A. Peters, K. Y. Chung, and S. Chu. High-precision gravity measurements using atom interferometry. *Metrologia*, 38(1):25–61, February 2001. doi:[10.1088/0026-1394/38/1/4](https://doi.org/10.1088/0026-1394/38/1/4). (cit. on pages 8, 122, and 124).

- [115] D. S. Weiss, B. C. Young, and S. Chu. Precision measurement of \hbar/m_{Cs} based on photon recoil using laser-cooled atoms and atomic interferometry. *Applied Physics B*, 59(3):217–256, September 1994. doi:[10.1007/BF01081393](https://doi.org/10.1007/BF01081393). (cit. on page 8).
- [116] M. Büchner, R. Delhuille, A. Miffre, C. Robilliard, J. Vigué, and C. Champenois. Diffraction phases in atom interferometers. *Physical Review A*, 68(1):013607, July 2003. doi:[10.1103/PhysRevA.68.013607](https://doi.org/10.1103/PhysRevA.68.013607). (cit. on pages 8, 19, 30, 66, 72, 113, and 169).
- [117] B. Estey, C. Yu, H. Müller, P.-C. Kuan, and S.-Y. Lan. High-Resolution Atom Interferometers with Suppressed Diffraction Phases. *Physical Review Letters*, 115(8):083002, August 2015. doi:[10.1103/PhysRevLett.115.083002](https://doi.org/10.1103/PhysRevLett.115.083002). (cit. on pages 8, 66, 72, 73, 78, 84, 96, 97, 169, 170, and 173).
- [118] R. H. Parker, C. Yu, B. Estey, W. Zhong, E. Huang, and H. Müller. Controlling the multiport nature of Bragg diffraction in atom interferometry. *Physical Review A*, 94(5), November 2016. doi:[10.1103/PhysRevA.94.053618](https://doi.org/10.1103/PhysRevA.94.053618). (cit. on pages 8, 17, 54, 66, 73, 78, 83, 86, 87, 92, 93, 96, 100, 102, 152, 153, 169, 170, and 173).
- [119] D. Gochnauer, K. E. McAlpine, B. Plotkin-Swing, A. O. Jamison, and S. Gupta. Bloch-band picture for light-pulse atom diffraction and interferometry. *Physical Review A*, 100(4):043611, October 2019. doi:[10.1103/PhysRevA.100.043611](https://doi.org/10.1103/PhysRevA.100.043611). (cit. on pages 8, 16, 19, 20, 30, 65, 66, 113, 169, and 180).
- [120] J.-N. Siemß, F. Fitzek, S. Abend, E. M. Rasel, N. Gaaloul, and K. Hammerer. Analytic theory for Bragg atom interferometry based on the adiabatic theorem. *Physical Review A*, 102(3):033709, September 2020. doi:[10.1103/PhysRevA.102.033709](https://doi.org/10.1103/PhysRevA.102.033709). (cit. on pages 8, 12, 20, 32, 34, 44, 46, 48, 51, 53, 67, 171, and 180).
- [121] J.-N. Kirsten-Siemß, F. Fitzek, C. Schubert, E. M. Rasel, N. Gaaloul, and K. Hammerer. Large-Momentum-Transfer Atom Interferometers with μrad -Accuracy Using Bragg Diffraction. *Physical Review Letters*, 131(3):033602, July 2023. doi:[10.1103/PhysRevLett.131.033602](https://doi.org/10.1103/PhysRevLett.131.033602). (cit. on pages 8 and 171).
- [122] D. Savoie, M. Altorio, B. Fang, L. A. Sidorenkov, R. Geiger, and A. Landragin. Interleaved atom interferometry for high-sensitivity inertial measurements. *Science Advances*, 4(12), 2018. doi:[10.1126/sciadv.aau7948](https://doi.org/10.1126/sciadv.aau7948). (cit. on pages 8, 146, and 164).
- [123] G. Tackmann, P. Berg, C. Schubert, S. Abend, M. Gilowski, W. Ertmer, and E. M. Rasel. Self-alignment of a compact large-area atomic Sagnac interferometer. *New*

- Journal of Physics*, 14(1):015002, January 2012. doi:[10.1088/1367-2630/14/1/015002](https://doi.org/10.1088/1367-2630/14/1/015002). (cit. on page 8).
- [124] T. Kovachy, P. Asenbaum, C. Overstreet, C. A. Donnelly, S. M. Dickerson, A. Sugarbaker, J. M. Hogan, and M. A. Kasevich. Quantum superposition at the half-metre scale. *Nature*, 528(7583):530–533, December 2015. doi:[10.1038/nature16155](https://doi.org/10.1038/nature16155). (cit. on pages 8, 147, 148, 152, 155, and 164).
- [125] J. M. Hogan, D. M. S. Johnson, and M. A. Kasevich. Proceedings of the International School of Physics “Enrico Fermi. In E. Arimondo, W. Ertmer, W. P. Schleich, and E. M. Rasel, editors, *Proceedings of the International School of Physics “Enrico Fermi*, pages 411–447. Societ‘a Italiana di Fisica and IOS Press, Amsterdam, 2009. (cit. on pages 11, 30, 64, and 69).
- [126] P. L. Gould, G. A. Ruff, and D. E. Pritchard. Diffraction of atoms by light: The near-resonant Kapitza-Dirac effect. *Physical Review Letters*, 56(8):827–830, February 1986. doi:[10.1103/PhysRevLett.56.827](https://doi.org/10.1103/PhysRevLett.56.827). (cit. on page 11).
- [127] E. M. Rasel, M. K. Oberthaler, H. Batelaan, J. Schmiedmayer, and A. Zeilinger. Atom wave interferometry with diffraction gratings of light. *Physical Review Letters*, 75(14):2633–2637, October 1995. doi:[10.1103/PhysRevLett.75.2633](https://doi.org/10.1103/PhysRevLett.75.2633). (cit. on pages 11 and 17).
- [128] B. Dubetsky and P. R. Berman. Atom gratings produced by large-angle atom beam splitters. *Physical Review A: Atomic, Molecular, and Optical Physics*, 64(6):063612, November 2001. doi:[10.1103/PhysRevA.64.063612](https://doi.org/10.1103/PhysRevA.64.063612). (cit. on page 11).
- [129] T. Albash and D. A. Lidar. Adiabatic quantum computation. *Reviews of Modern Physics*, 90(1):015002, January 2018. doi:[10.1103/RevModPhys.90.015002](https://doi.org/10.1103/RevModPhys.90.015002). (cit. on pages 12 and 22).
- [130] H. Müller, S.-w. Chiow, and S. Chu. Atom-wave diffraction between the Raman-Nath and the Bragg regime: Effective Rabi frequency, losses, and phase shifts. *Physical Review A*, 77(2):023609, February 2008. doi:[10.1103/PhysRevA.77.023609](https://doi.org/10.1103/PhysRevA.77.023609). (cit. on pages 12, 15, 16, 17, 18, 19, 50, 64, 65, 91, and 113).
- [131] C. Keller, J. Schmiedmayer, A. Zeilinger, T. Nonn, S. Dürr, and G. Rempe. Adiabatic following in standing-wave diffraction of atoms. *Applied Physics B: Photophysics and Laser Chemistry*, 69(4):303–309, October 1999. doi:[10.1007/s003400050810](https://doi.org/10.1007/s003400050810). (cit. on pages 16, 18, and 65).

- [132] E. Giese, A. Roura, G. Tackmann, E. M. Rasel, and W. P. Schleich. Double Bragg diffraction: A tool for atom optics. *Physical Review A*, 88(5):053608, November 2013. doi:[10.1103/PhysRevA.88.053608](https://doi.org/10.1103/PhysRevA.88.053608). (cit. on pages [16](#), [17](#), [18](#), [65](#), [113](#), [114](#), [123](#), [125](#), [126](#), and [174](#)).
- [133] S. Szigeti. *Controlled Bose-Condensed Sources for Atom Interferometry*. PhD thesis, Australian Nation University, July 2013. doi:[10.25911/5d514a57ce679](https://doi.org/10.25911/5d514a57ce679). (cit. on pages [16](#) and [18](#)).
- [134] S. Hartmann, J. Jenewein, E. Giese, S. Abend, A. Roura, E. M. Rasel, and W. P. Schleich. Regimes of atomic diffraction: Raman versus Bragg diffraction in retroreflective geometries. *Physical Review A*, 101(5):053610, May 2020. doi:[10.1103/PhysRevA.101.053610](https://doi.org/10.1103/PhysRevA.101.053610). (cit. on pages [17](#) and [141](#)).
- [135] A. Béguin, T. Rodzinka, J. Vigué, B. Allard, and A. Gauguier. Characterization of an atom interferometer in the quasi-Bragg regime. *Physical Review A*, 105(3):033302, March 2022. doi:[10.1103/PhysRevA.105.033302](https://doi.org/10.1103/PhysRevA.105.033302). (cit. on pages [17](#), [30](#), [54](#), [65](#), [78](#), [83](#), [86](#), [87](#), [102](#), [113](#), and [169](#)).
- [136] J. Jenewein, S. Hartmann, A. Roura, and E. Giese. Bragg-diffraction-induced imperfections of the signal in retroreflective atom interferometers. *Physical Review A*, 105(6):063316, June 2022. doi:[10.1103/PhysRevA.105.063316](https://doi.org/10.1103/PhysRevA.105.063316). (cit. on pages [17](#), [113](#), [114](#), [126](#), and [174](#)).
- [137] W. Li, T. He, and A. Smerzi. Multimode Kapitza-Dirac Interferometry with Trapped Cold Atoms. *Physical Review Letters*, 113(2):023003, July 2014. doi:[10.1103/PhysRevLett.113.023003](https://doi.org/10.1103/PhysRevLett.113.023003). (cit. on pages [17](#), [105](#), and [174](#)).
- [138] M. V. Fedorov. The kapitza-dirac effect in a strong radiation field. *Sov.Phys. JETP*, 25(5):952–959, November 1967. (cit. on page [19](#)).
- [139] M. Horne, I. Jex, and A. Zeilinger. Schrödinger wave functions in strong periodic potentials with applications to atom optics. *Physical Review A: Atomic, Molecular, and Optical Physics*, 59(3):2190–2202, March 1999. doi:[10.1103/PhysRevA.59.2190](https://doi.org/10.1103/PhysRevA.59.2190). (cit. on page [19](#)).
- [140] C. Champenois, M. Büchner, R. Delhille, R. Mathevet, C. Robilliard, C. Rizzo, and J. Vigué. Atomic diffraction by a laser standing wave: Analysis using Bloch states. *The European Physical Journal D - Atomic, Molecular, Optical and Plasma Physics*, 13(2):271–278, January 2001. doi:[10.1007/s100530170276](https://doi.org/10.1007/s100530170276). (cit. on page [19](#)).

- [141] A. Shankar, L. Salvi, M. L. Chiofalo, N. Poli, and M. J. Holland. Squeezed state metrology with Bragg interferometers operating in a cavity. *Quantum Science and Technology*, 4(4):045010, October 2019. doi:[10.1088/2058-9565/ab455d](https://doi.org/10.1088/2058-9565/ab455d). (cit. on pages 24, 77, and 174).
- [142] Z. Pagel, W. Zhong, R. H. Parker, C. T. Olund, N. Y. Yao, and H. Müller. Symmetric Bloch oscillations of matter waves. *Physical Review A*, 102(5):053312, November 2020. doi:[10.1103/PhysRevA.102.053312](https://doi.org/10.1103/PhysRevA.102.053312). (cit. on pages 26, 114, 124, 139, 164, and 174).
- [143] D. Xiao, M.-C. Chang, and Q. Niu. Berry phase effects on electronic properties. *Reviews of Modern Physics*, 82(3):1959–2007, July 2010. doi:[10.1103/RevModPhys.82.1959](https://doi.org/10.1103/RevModPhys.82.1959). (cit. on page 35).
- [144] G. Rigolin, G. Ortiz, and V. H. Ponce. Beyond the quantum adiabatic approximation: Adiabatic perturbation theory. *Physical Review A*, 78(5), November 2008. doi:[10.1103/PhysRevA.78.052508](https://doi.org/10.1103/PhysRevA.78.052508). (cit. on page 36).
- [145] G. S. Vasilev and N. V. Vitanov. Coherent excitation of a two-state system by a Gaussian field. *Physical Review A: Atomic, Molecular, and Optical Physics*, 70(5):053407, November 2004. doi:[10.1103/PhysRevA.70.053407](https://doi.org/10.1103/PhysRevA.70.053407). (cit. on pages 39, 40, 51, 63, 177, and 178).
- [146] G. S. Vasilev and N. V. Vitanov. Coherent excitation of a two-state system by a linearly chirped Gaussian pulse. *The Journal of Chemical Physics*, 123(17):174106, November 2005. doi:[10.1063/1.2090260](https://doi.org/10.1063/1.2090260). (cit. on pages 40 and 63).
- [147] P. A. Altin, et al. Precision atomic gravimeter based on Bragg diffraction. *New Journal of Physics*, 15(2):023009, February 2013. doi:[10.1088/1367-2630/15/2/023009](https://doi.org/10.1088/1367-2630/15/2/023009). (cit. on pages 54, 78, 83, 84, 85, 86, 87, 100, 102, 106, 155, 169, and 170).
- [148] J. P. Davis. Nonadiabatic transitions induced by a time-dependent Hamiltonian in the Semiclassical/Adiabatic limit: The two-state case. *Journal of Chemical Physics*, 64(8):3129, 1976. doi:[10.1063/1.432648](https://doi.org/10.1063/1.432648). (cit. on page 63).
- [149] A. M. Dykhne. Adiabatic perturbation of discrete spectrum states. *Soviet Physics–JETP [translation of Zhurnal Eksperimentalnoi i Teoreticheskoi Fiziki]*, 14(4):941, 1962. (cit. on page 63).

- [150] K. E. McAlpine, D. Gochnauer, and S. Gupta. Excited-band Bloch oscillations for precision atom interferometry. *Physical Review A*, 101(2):023614, February 2020. doi:[10.1103/PhysRevA.101.023614](https://doi.org/10.1103/PhysRevA.101.023614). (cit. on pages 66, 131, and 164).
- [151] D. M. Giltner, R. W. McGowan, and S. A. Lee. Theoretical and experimental study of the Bragg scattering of atoms from a standing light wave. *Physical Review A*, 52(5):3966–3972, November 1995. doi:[10.1103/PhysRevA.52.3966](https://doi.org/10.1103/PhysRevA.52.3966). (cit. on page 69).
- [152] S. M. Dickerson, J. M. Hogan, A. Sugarbaker, D. M. S. Johnson, and M. A. Kasevich. Multi-axis Inertial Sensing with Long-Time Point Source Atom Interferometry. *Physical Review Letters*, 111(8):083001, August 2013. doi:[10.1103/PhysRevLett.111.083001](https://doi.org/10.1103/PhysRevLett.111.083001). (cit. on pages 70, 122, and 124).
- [153] Ch. J. Bordé. Atomic interferometry with internal state labelling. *Physics Letters A*, 140(1):10–12, September 1989. doi:[10.1016/0375-9601\(89\)90537-9](https://doi.org/10.1016/0375-9601(89)90537-9). (cit. on page 70).
- [154] W. Ketterle, D. S. Durfee, and D. M. Stamper-Kurn. Making, probing and understanding Bose-Einstein condensates. *Bose-Einstein Condensation in Atomic Gases*, pages 67–176, 1999. doi:[10.3254/978-1-61499-225-7-67](https://doi.org/10.3254/978-1-61499-225-7-67). (cit. on pages 70 and 117).
- [155] L. Pezzè, A. Smerzi, M. K. Oberthaler, R. Schmied, and P. Treutlein. Quantum metrology with nonclassical states of atomic ensembles. *Reviews of Modern Physics*, 90(3):035005, September 2018. doi:[10.1103/RevModPhys.90.035005](https://doi.org/10.1103/RevModPhys.90.035005). (cit. on pages 72, 73, and 77).
- [156] M. Fréchet. Sur l’extension de certaines évaluations statistiques au cas de petits échantillons. *Revue de l’Institut International de Statistique / Review of the International Statistical Institute*, 11(3/4):182–205, 1943. arXiv:[1401114](https://arxiv.org/abs/1401114), doi:[10.2307/1401114](https://doi.org/10.2307/1401114). (cit. on pages 72 and 76).
- [157] H. Cramér. *Mathematical Methods of Statistics*. Princeton University Press, 1946. (cit. on pages 72 and 76).
- [158] C. R. Rao. Information and the Accuracy Attainable in the Estimation of Statistical Parameters. In S. Kotz and N. L. Johnson, editors, *Breakthroughs in Statistics: Foundations and Basic Theory*, Springer Series in Statistics, pages 235–247. Springer, New York, NY, 1945. doi:[10.1007/978-1-4612-0919-5_16](https://doi.org/10.1007/978-1-4612-0919-5_16). (cit. on pages 72 and 76).

- [159] C. W. Helstrom. Quantum detection and estimation theory. *Journal of Statistical Physics*, 1(2):231–252, June 1969. doi:[10.1007/BF01007479](https://doi.org/10.1007/BF01007479). (cit. on page 72).
- [160] R. Demkowicz-Dobrzanski, M. Jarzyna, and J. Kolodynski. Quantum limits in optical interferometry. *arXiv:1405.7703 [quant-ph]*, 60:345–435, 2015. arXiv:[1405.7703](https://arxiv.org/abs/1405.7703), doi:[10.1016/bs.po.2015.02.003](https://doi.org/10.1016/bs.po.2015.02.003). (cit. on pages 73 and 77).
- [161] L. Pezze’ and A. Smerzi. Quantum theory of phase estimation. *arXiv:1411.5164 [cond-mat, physics:quant-ph]*, November 2014. arXiv:[1411.5164](https://arxiv.org/abs/1411.5164). (cit. on page 75).
- [162] L. Salvi, N. Poli, V. Vuletić, and G. M. Tino. Squeezing on Momentum States for Atom Interferometry. *Physical Review Letters*, 120(3):033601, January 2018. doi:[10.1103/PhysRevLett.120.033601](https://doi.org/10.1103/PhysRevLett.120.033601). (cit. on pages 77 and 174).
- [163] S. S. Szigeti, S. P. Nolan, J. D. Close, and S. A. Haine. High-Precision Quantum-Enhanced Gravimetry with a Bose-Einstein Condensate. *Physical Review Letters*, 125(10):100402, September 2020. doi:[10.1103/PhysRevLett.125.100402](https://doi.org/10.1103/PhysRevLett.125.100402). (cit. on pages 77, 111, 165, and 174).
- [164] R. Corgier, N. Gaaloul, A. Smerzi, and L. Pezzè. Delta-Kick Squeezing. *Physical Review Letters*, 127(18):183401, October 2021. doi:[10.1103/PhysRevLett.127.183401](https://doi.org/10.1103/PhysRevLett.127.183401). (cit. on pages 77, 111, 165, and 174).
- [165] A. Bertoldi, F. Minardi, and M. Prevedelli. Phase shift in atom interferometers: Corrections for nonquadratic potentials and finite-duration laser pulses. *Physical Review A*, 99(3):033619, March 2019. doi:[10.1103/PhysRevA.99.033619](https://doi.org/10.1103/PhysRevA.99.033619). (cit. on page 78).
- [166] M. Kritsotakis, S. S. Szigeti, J. A. Dunningham, and S. A. Haine. Optimal matter-wave gravimetry. *Physical Review A*, 98(2):023629, August 2018. doi:[10.1103/PhysRevA.98.023629](https://doi.org/10.1103/PhysRevA.98.023629). (cit. on pages 81 and 183).
- [167] R. Bösche. Theory of Atom Interferometers in the Bragg Regime. Master’s thesis, Leibniz Universität Hannover, Hannover, 2022. (cit. on pages 87 and 90).
- [168] S.-w. Chiow, S. Herrmann, S. Chu, and H. Müller. Noise-Immune Conjugate Large-Area Atom Interferometers. *Physical Review Letters*, 103(5):050402, July 2009. doi:[10.1103/PhysRevLett.103.050402](https://doi.org/10.1103/PhysRevLett.103.050402). (cit. on page 90).

- [169] F. Fitzek, J.-N. Siemß, S. Seckmeyer, H. Ahlers, E. M. Rasel, K. Hammerer, and N. Gaaloul. Universal atom interferometer simulation of elastic scattering processes. *Scientific Reports*, 10(1):22120, December 2020. doi:[10.1038/s41598-020-78859-1](https://doi.org/10.1038/s41598-020-78859-1). (cit. on pages 94 and 119).
- [170] M. D. Feit, J. A. Fleck, and A. Steiger. Solution of the Schrödinger equation by a spectral method. *Journal of Computational Physics*, 47(3):412–433, September 1982. doi:[10.1016/0021-9991\(82\)90091-2](https://doi.org/10.1016/0021-9991(82)90091-2). (cit. on pages 94 and 119).
- [171] M. A. Kristensen, M. B. Christensen, M. Gajdacz, M. Iglicki, K. Pawłowski, C. Klempt, J. F. Sherson, K. Rzążewski, A. J. Hilliard, and J. J. Arlt. Observation of Atom Number Fluctuations in a Bose-Einstein Condensate. *Physical Review Letters*, 122(16):163601, April 2019. doi:[10.1103/PhysRevLett.122.163601](https://doi.org/10.1103/PhysRevLett.122.163601). (cit. on page 106).
- [172] S. A. Haine and M. T. Johnsson. Dynamic scheme for generating number squeezing in Bose-Einstein condensates through nonlinear interactions. *Physical Review A*, 80(2):023611, August 2009. doi:[10.1103/PhysRevA.80.023611](https://doi.org/10.1103/PhysRevA.80.023611). (cit. on page 106).
- [173] M. O. Scully and M. S. Zubairy. *Quantum Optics*. Cambridge University Press, Cambridge, 1997. doi:[10.1017/CB09780511813993](https://doi.org/10.1017/CB09780511813993). (cit. on page 106).
- [174] P. Hamilton, M. Jaffe, J. M. Brown, L. Maisenbacher, B. Estey, and H. Müller. Atom Interferometry in an Optical Cavity. *Physical Review Letters*, 114(10):100405, March 2015. doi:[10.1103/PhysRevLett.114.100405](https://doi.org/10.1103/PhysRevLett.114.100405). (cit. on page 111).
- [175] B. Canuel, et al. Technologies for the ELGAR large scale atom interferometer array, July 2020. arXiv:[2007.04014](https://arxiv.org/abs/2007.04014), doi:[10.48550/arXiv.2007.04014](https://doi.org/10.48550/arXiv.2007.04014). (cit. on pages 113, 134, and 165).
- [176] T. Lévêque, A. Gauguet, F. Michaud, F. Pereira Dos Santos, and A. Landragin. Enhancing the Area of a Raman Atom Interferometer Using a Versatile Double-Diffraction Technique. *Physical Review Letters*, 103(8):080405, August 2009. doi:[10.1103/PhysRevLett.103.080405](https://doi.org/10.1103/PhysRevLett.103.080405). (cit. on pages 114 and 163).
- [177] N. Malossi, Q. Bodart, S. Merlet, T. Lévêque, A. Landragin, and F. P. D. Santos. Double diffraction in an atomic gravimeter. *Physical Review A*, 81(1):013617, January 2010. doi:[10.1103/PhysRevA.81.013617](https://doi.org/10.1103/PhysRevA.81.013617). (cit. on pages 114 and 124).

- [178] P. Cladé, E. de Mirandes, M. Cadoret, S. Guellati-Khélifa, C. Schwob, F. Nez, L. Julien, and F. Biraben. Determination of the Fine Structure Constant Based on Bloch Oscillations of Ultracold Atoms in a Vertical Optical Lattice. *Physical Review Letters*, 96(3):033001, January 2006. doi:[10.1103/PhysRevLett.96.033001](https://doi.org/10.1103/PhysRevLett.96.033001). (cit. on page 114).
- [179] P. Cladé, E. de Mirandes, M. Cadoret, S. Guellati-Khélifa, C. Schwob, F. Nez, L. Julien, and F. Biraben. Precise measurement of h/m_{Rb} using Bloch oscillations in a vertical optical lattice: Determination of the fine-structure constant. *Physical Review A*, 74(5):052109, November 2006. doi:[10.1103/PhysRevA.74.052109](https://doi.org/10.1103/PhysRevA.74.052109). (cit. on pages 114, 116, 135, 152, 164, and 165).
- [180] P. Cladé, T. Plisson, S. Guellati-Khélifa, F. Nez, and F. Biraben. Theoretical analysis of a large momentum beamsplitter using Bloch oscillations. *The European Physical Journal D*, 59(3):349–360, September 2010. doi:[10.1140/epjd/e2010-00198-0](https://doi.org/10.1140/epjd/e2010-00198-0). (cit. on pages 114 and 140).
- [181] R. Bouchendira, P. Cladé, S. Guellati-Khélifa, F. Nez, and F. Biraben. New Determination of the Fine Structure Constant and Test of the Quantum Electrodynamics. *Physical Review Letters*, 106(8):080801, February 2011. doi:[10.1103/PhysRevLett.106.080801](https://doi.org/10.1103/PhysRevLett.106.080801). (cit. on page 114).
- [182] M. Andia, R. Jannin, F. Nez, F. Biraben, S. Guellati-Khélifa, and P. Cladé. Compact atomic gravimeter based on a pulsed and accelerated optical lattice. *Physical Review A*, 88(3):031605, September 2013. doi:[10.1103/PhysRevA.88.031605](https://doi.org/10.1103/PhysRevA.88.031605). (cit. on page 114).
- [183] K. S. Hardman, C. C. N. Kuhn, G. D. McDonald, J. E. Debs, S. Bennetts, J. D. Close, and N. P. Robins. Role of source coherence in atom interferometry. *Physical Review A*, 89(2):023626, February 2014. doi:[10.1103/PhysRevA.89.023626](https://doi.org/10.1103/PhysRevA.89.023626). (cit. on page 115).
- [184] S. Loriani, D. Schlippert, C. Schubert, S. Abend, H. Ahlers, W. Ertmer, J. Rudolph, J. M. Hogan, M. A. Kasevich, E. M. Rasel, and N. Gaaloul. Atomic source selection in space-borne gravitational wave detection. *New Journal of Physics*, 21(6):063030, June 2019. doi:[10.1088/1367-2630/ab22d0](https://doi.org/10.1088/1367-2630/ab22d0). (cit. on page 116).
- [185] M. FATTORI, B. DEISLER, C. D’ERRICO, M. JONA-LASINIO, M. MODUGNO, G. ROATI, L. SANTOS, A. SIMONI, M. ZACCANTI, M. INGUSCIO, and G. MODUGNO. ATOM INTERFEROMETRY WITH A WEAKLY INTERACTING BOSE-EINSTEIN CONDENSATE. In *Pushing the Frontiers of Atomic*

- Physics*, pages 251–262. WORLD SCIENTIFIC, March 2009. doi:10.1142/9789814273008_0025. (cit. on page 116).
- [186] M. R. Andrews, C. G. Townsend, H.-J. Miesner, D. S. Durfee, D. M. Kurn, and W. Ketterle. Observation of Interference Between Two Bose Condensates. *Science*, January 1997. doi:10.1126/science.275.5300.637. (cit. on page 116).
- [187] E. W. Hagley, L. Deng, M. Kozuma, M. Trippenbach, Y. B. Band, M. Edwards, M. Doery, P. S. Julienne, K. Helmerson, S. L. Rolston, and W. D. Phillips. Measurement of the Coherence of a Bose-Einstein Condensate. *Physical Review Letters*, 83(16):3112–3115, October 1999. doi:10.1103/PhysRevLett.83.3112. (cit. on page 116).
- [188] H. Ammann and N. Christensen. Delta Kick Cooling: A New Method for Cooling Atoms. *Physical Review Letters*, 78(11):2088–2091, March 1997. doi:10.1103/PhysRevLett.78.2088. (cit. on pages 116 and 136).
- [189] J. Hartwig, S. Abend, C. Schubert, D. Schlippert, H. Ahlers, K. Posso-Trujillo, N. Gaaloul, W. Ertmer, and E. M. Rasel. Testing the universality of free fall with rubidium and ytterbium in a very large baseline atom interferometer. *New Journal of Physics*, 17(3):035011, March 2015. doi:10.1088/1367-2630/17/3/035011. (cit. on page 116).
- [190] C. J. Pethick and H. Smith. *Bose–Einstein Condensation in Dilute Gases*. Cambridge university press, 2008. (cit. on page 117).
- [191] M. E. Peskin and D. V. Schroeder. *An Introduction to Quantum Field Theory*, 1995. (cit. on page 118).
- [192] J. Rogel-Salazar. The Gross–Pitaevskii equation and Bose–Einstein condensates. *European Journal of Physics*, 34(2):247, January 2013. doi:10.1088/0143-0807/34/2/247. (cit. on page 118).
- [193] L. Salasnich, A. Parola, and L. Reatto. Effective wave equations for the dynamics of cigar-shaped and disk-shaped Bose condensates. *Physical Review A*, 65(4):043614, April 2002. doi:10.1103/PhysRevA.65.043614. (cit. on pages 119 and 120).
- [194] H. Müntinga. *Matter-Wave Interferometry for Space-Borne Inertial Sensors*. PhD thesis, Universität Bremen, Bremen, February 2019. (cit. on pages 125 and 136).
- [195] E. Giese. Mechanisms of matter-wave diffraction and their application to interferometers. *Fortschritte der Physik*, 63(6):337–410, 2015. doi:10.1002/prop.201500020. (cit. on pages 125 and 183).

- [196] N. W. Ashcroft and N. D. Mermin. *Solid State Physics*. Saunders College Publ., Philadelphia [u.a.], 1976. (cit. on page 128).
- [197] E. Kaxiras. *Atomic and Electronic Structure of Solids*. Cambridge Univ. Press, Cambridge [u.a.], 2003. (cit. on page 128).
- [198] P. Cladé, M. Andia, and S. Guellati-Khélifa. Improving efficiency of Bloch oscillations in the tight-binding limit. *Physical Review A*, 95(6):063604, June 2017. doi:10.1103/PhysRevA.95.063604. (cit. on pages 130, 134, and 138).
- [199] M. Glück, A. R. Kolovsky, and H. J. Korsch. Wannier–Stark resonances in optical and semiconductor superlattices. *Physics Reports*, 366(3):103–182, August 2002. doi:10.1016/S0370-1573(02)00142-4. (cit. on pages 130, 134, and 165).
- [200] J. H. Denschlag, J. E. Simsarian, H. Häffner, C. McKenzie, A. Browaeys, D. Cho, K. Helmerson, S. L. Rolston, and W. D. Phillips. A Bose-Einstein condensate in an optical lattice. *Journal of Physics B: Atomic, Molecular and Optical Physics*, 35(14):3095–3110, July 2002. doi:10.1088/0953-4075/35/14/307. (cit. on page 131).
- [201] O. Morsch and M. Oberthaler. Dynamics of Bose-Einstein condensates in optical lattices. *Reviews of Modern Physics*, 78(1):179–215, February 2006. doi:10.1103/RevModPhys.78.179. (cit. on page 131).
- [202] C. Zener and R. H. Fowler. A theory of the electrical breakdown of solid dielectrics. *Proceedings of the Royal Society of London. Series A, Containing Papers of a Mathematical and Physical Character*, 145(855):523–529, July 1934. doi:10.1098/rspa.1934.0116. (cit. on pages 133 and 134).
- [203] S. Kling, T. Salger, C. Grossert, and M. Weitz. Atomic Bloch-Zener Oscillations and Stückelberg Interferometry in Optical Lattices. *Physical Review Letters*, 105(21):215301, November 2010. doi:10.1103/PhysRevLett.105.215301. (cit. on page 134).
- [204] D. Gochnauer. *Vertical Contrast Interferometry and Bloch-Band Approach to Atom Optics*. PhD thesis, University of Washington, Washington, 2020. (cit. on page 134).
- [205] T. Hartmann, F. Keck, H. J. Korsch, and S. Mossmann. Dynamics of Bloch oscillations. *New Journal of Physics*, 6:2–2, January 2004. doi:10.1088/1367-2630/6/1/002. (cit. on page 134).

- [206] C. Sias, A. Zenesini, H. Lignier, S. Wimberger, D. Ciampini, O. Morsch, and E. Arimondo. Resonantly Enhanced Tunneling of Bose-Einstein Condensates in Periodic Potentials. *Physical Review Letters*, 98(12):120403, March 2007. doi: [10.1103/PhysRevLett.98.120403](https://doi.org/10.1103/PhysRevLett.98.120403). (cit. on page 134).
- [207] L. Morel. *High Sensitivity Matter-Wave Interferometry : Towards a Determination of the Fine Structure Constant below 10-10*. PhD thesis, Sorbonne Université, September 2019. (cit. on pages 135 and 165).
- [208] M. Gebbe. *Atom Interferometry in a Twin Lattice*. PhD thesis, Universität Bremen, March 2020. doi: [10.26092/elib/19](https://doi.org/10.26092/elib/19). (cit. on pages 135, 136, 137, 138, 140, 142, 147, 148, 149, 151, 158, 162, and 172).
- [209] R. Grimm, M. Weidemüller, and Y. B. Ovchinnikov. Optical Dipole Traps for Neutral Atoms. In B. Bederson and H. Walther, editors, *Advances In Atomic, Molecular, and Optical Physics*, volume 42, pages 95–170. Academic Press, January 2000. doi: [10.1016/S1049-250X\(08\)60186-X](https://doi.org/10.1016/S1049-250X(08)60186-X). (cit. on page 135).
- [210] E. R. Elliott, M. C. Krutzik, J. R. Williams, R. J. Thompson, and D. C. Aveline. NASA’s Cold Atom Lab (CAL): System development and ground test status. *npj Microgravity*, 4(1):1–7, August 2018. doi: [10.1038/s41526-018-0049-9](https://doi.org/10.1038/s41526-018-0049-9). (cit. on page 136).
- [211] T. van Zoest. *Realisierung erster quantenentarteter Gase unter Schwerelosigkeit*. doctoralThesis, Hannover : Gottfried Wilhelm Leibniz Universität Hannover, 2008. doi: [10.15488/7153](https://doi.org/10.15488/7153). (cit. on page 136).
- [212] W. Lewoczko-Adamczyk. *Bose-Einstein Condensation in Microgravity*. doctoralThesis, Humboldt-Universität zu Berlin, Mathematisch-Naturwissenschaftliche Fakultät I, July 2009. doi: [10.18452/15970](https://doi.org/10.18452/15970). (cit. on page 136).
- [213] M. Krutzik. *Matter Wave Interferometry in Microgravity*. doctoralThesis, Humboldt-Universität zu Berlin, Mathematisch-Naturwissenschaftliche Fakultät I, October 2014. doi: [10.18452/17050](https://doi.org/10.18452/17050). (cit. on page 136).
- [214] B. Décamps, M. Bordoux, J. Alibert, B. Allard, and A. Gauguet. Phase response of atom interferometers based on sequential Bragg diffractions. *Journal of Physics B: Atomic, Molecular and Optical Physics*, 52(1):015003, January 2019. doi: [10.1088/1361-6455/aaf0be](https://doi.org/10.1088/1361-6455/aaf0be). (cit. on pages 145 and 174).

- [215] G. D. McDonald, C. C. N. Kuhn, S. Bennetts, J. E. Debs, K. S. Hardman, J. D. Close, and N. P. Robins. A faster scaling in acceleration-sensitive atom interferometers. *Europhysics Letters*, 105(6):63001, March 2014. doi:[10.1209/0295-5075/105/63001](https://doi.org/10.1209/0295-5075/105/63001). (cit. on page 146).
- [216] M. Zimmermann, M. A. Efremov, W. Zeller, W. P. Schleich, J. P. Davis, and F. A. Narducci. Representation-free description of atom interferometers in time-dependent linear potentials. *New Journal of Physics*, 21(7):073031, July 2019. doi:[10.1088/1367-2630/ab2e8c](https://doi.org/10.1088/1367-2630/ab2e8c). (cit. on page 146).
- [217] W.-J. Xu, M.-K. Zhou, M.-M. Zhao, K. Zhang, and Z.-K. Hu. Quantum tiltmeter with atom interferometry. *Physical Review A*, 96(6):063606, December 2017. doi:[10.1103/PhysRevA.96.063606](https://doi.org/10.1103/PhysRevA.96.063606). (cit. on pages 146 and 164).
- [218] J. K. Stockton, K. Takase, and M. A. Kasevich. Absolute Geodetic Rotation Measurement Using Atom Interferometry. *Physical Review Letters*, 107(13):133001, September 2011. doi:[10.1103/PhysRevLett.107.133001](https://doi.org/10.1103/PhysRevLett.107.133001). (cit. on pages 146 and 164).
- [219] S. Abend. *Atom-Chip Gravimeter with Bose-Einstein Condensates*. doctoralThesis, Hannover : Gottfried Wilhelm Leibniz Universität Hannover, 2017. doi:[10.15488/8921](https://doi.org/10.15488/8921). (cit. on page 147).
- [220] A. Roura, W. Zeller, and W. P. Schleich. Overcoming loss of contrast in atom interferometry due to gravity gradients. *New Journal of Physics*, 16(12):123012, December 2014. doi:[10.1088/1367-2630/16/12/123012](https://doi.org/10.1088/1367-2630/16/12/123012). (cit. on pages 148, 152, 153, 154, and 155).
- [221] L. P. Parazzoli, A. M. Hankin, and G. W. Biedermann. Observation of Free-Space Single-Atom Matter Wave Interference. *Physical Review Letters*, 109(23):230401, December 2012. doi:[10.1103/PhysRevLett.109.230401](https://doi.org/10.1103/PhysRevLett.109.230401). (cit. on pages 148 and 155).
- [222] S. Bade, L. Djadaojee, M. Andia, P. Cladé, and S. Guellati-Khelifa. Observation of Extra Photon Recoil in a Distorted Optical Field. *Physical Review Letters*, 121(7):073603, August 2018. doi:[10.1103/PhysRevLett.121.073603](https://doi.org/10.1103/PhysRevLett.121.073603). (cit. on page 152).
- [223] D. A. Kokorowski, A. D. Cronin, T. D. Roberts, and D. E. Pritchard. From Single- to Multiple-Photon Decoherence in an Atom Interferometer. *Physical Review Letters*, 86(11):2191–2195, March 2001. doi:[10.1103/PhysRevLett.86.2191](https://doi.org/10.1103/PhysRevLett.86.2191). (cit. on pages 152 and 155).

- [224] W. Zeller. *The Impact of Wave-Packet Dynamics in Long-Time Atom Interferometry*. PhD thesis, Universität Ulm, Ulm, 2017. (cit. on page 154).
- [225] C. R. Ekstrom. *Experiments with a Separated Beam Atom Interferometer*. Thesis, Massachusetts Institute of Technology, 1993. (cit. on page 156).
- [226] P. R. Berman. *Atom Interferometry*. Academic Press, San Diego, 1997. (cit. on page 156).
- [227] K. Zhang, W. Chen, M. Bhattacharya, and P. Meystre. Hamiltonian chaos in a coupled BEC–optomechanical-cavity system. *Physical Review A*, 81(1):013802, January 2010. doi:10.1103/PhysRevA.81.013802. (cit. on page 157).
- [228] S. P. Anokhov, R. A. Lymarenko, and A. I. Khizhnyak. Wide-angle diffraction of the laser beam by a sharp edge. *Radiophysics and Quantum Electronics*, 47(10):926–932, October 2004. doi:10.1007/s11141-005-0034-5. (cit. on pages 159 and 160).
- [229] N. Lörch, F. V. Pepe, H. Lignier, D. Ciampini, R. Mannella, O. Morsch, E. Arimondo, P. Facchi, G. Florio, S. Pascazio, and S. Wimberger. Wavefunction-renormalization effects in resonantly enhanced tunneling. *Physical Review A*, 85(5):053602, May 2012. doi:10.1103/PhysRevA.85.053602. (cit. on page 165).
- [230] J. Estève, C. Gross, A. Weller, S. Giovanazzi, and M. K. Oberthaler. Squeezing and entanglement in a Bose–Einstein condensate. *Nature*, 455:1216–1219, 2008. doi:10.1038/nature07332. (cit. on page 165).
- [231] K. Lange, J. Peise, B. Lücke, I. Kruse, G. Vitagliano, I. Apellaniz, M. Kleinmann, G. Tóth, and C. Klempt. Entanglement between two spatially separated atomic modes. *Science (New York, N.Y.)*, 360(6387):416–418, 2018. doi:10.1126/science.aao2035. (cit. on page 165).
- [232] J. C. Saywell, I. Kuprov, D. Goodwin, M. Carey, and T. Freegarde. Optimal control of mirror pulses for cold-atom interferometry. *Physical Review A*, 98(2):023625, August 2018. doi:10.1103/PhysRevA.98.023625. (cit. on page 173).
- [233] J. Saywell, M. Carey, M. Belal, I. Kuprov, and T. Freegarde. Optimal control of Raman pulse sequences for atom interferometry. *Journal of Physics B: Atomic, Molecular and Optical Physics*, 53(8):085006, March 2020. doi:10.1088/1361-6455/ab6df6. (cit. on page 173).

- [234] J. Saywell, M. Carey, N. Dedes, I. Kuprov, and T. Freegarde. Efficient state-symmetric beamsplitters and mirrors for atom interferometers using optimized pulses. *Journal of Physics B: Atomic, Molecular and Optical Physics*, 55(20):205501, September 2022. doi:10.1088/1361-6455/ac8cc3. (cit. on page 173).
- [235] P. Cheinet, B. Canuel, F. Pereira Dos Santos, A. Gauguet, F. Yver-Leduc, and A. Landragin. Measurement of the Sensitivity Function in a Time-Domain Atomic Interferometer. *IEEE Transactions on Instrumentation and Measurement*, 57(6):1141–1148, June 2008. doi:10.1109/TIM.2007.915148. (cit. on page 174).
- [236] E. Oelker, G. Mansell, M. Tse, J. Miller, F. Matichard, L. Barsotti, P. Fritschel, D. E. McClelland, M. Evans, and N. Mavalvala. Ultra-low phase noise squeezed vacuum source for gravitational wave detectors. *Optica*, 3(7):682–685, July 2016. doi:10.1364/OPTICA.3.000682. (cit. on page 174).
- [237] A. Neumann, M. Gebbe, and R. Walser. Aberrations in (3+1)-dimensional Bragg diffraction using pulsed Laguerre-Gaussian laser beams. *Physical Review A*, 103(4):043306, April 2021. doi:10.1103/PhysRevA.103.043306. (cit. on page 175).

ACADEMIC CURRICULUM VITAE

PERSONAL DATA

NAME: Jan-Niclas Kirsten-Siemß, née Siemß
BORN: 14 Dezember 1991 in Lübeck, Deutschland
ADDRESS: Rosenbergstraße 19, 30163 Hannover

EDUCATION

| | |
|-----------------|---|
| In progress | Doktor der Naturwissenschaften, Dr. rer. nat. Leibniz Universität Hannover Thesis: <i>Theory of Large-Momentum-Transfer Atom Interferometry in the Quasi-Bragg Regime</i> Supervisor: Prof. Dr. K. Hammerer |
| 01/2017–present | PhD student at the Institute of Theoretical Physics, Leibniz Universität Hannover |
| 12/2016 | MASTER OF SCIENCE (PHYSICS) Leibniz Universität Hannover Thesis: <i>Simulations of Bose-Einstein condensate dynamics in Optical Lattices for Large Momentum Transfer Experiments</i> Supervisor: Prof. Dr. E. M. Rasel |
| 11/2014–12/2016 | Master studies at Leibniz Universität Hannover |
| 11/2014 | BACHELOR OF SCIENCE (PHYSICS) Leibniz Universität Hannover Thesis: <i>Aufbau und Stabilisierung einer optischen Dipolfalle und Evaporation aus einer Magnetfalle zur Vorbereitung einer Hybridfalle</i> Supervisor: Prof. Dr. Ernst M. Rasel |
| 10/2011–11/2014 | Bachelor studies at Leibniz Universität Hannover |
| 2002–2011 | ABITUR Thomas-Mann-Schule Lübeck |

COMPLETE LIST OF PUBLICATIONS

F. Fitzek, **J.-N. Kirsten-Siemß**, E. M. Rasel, N. Gaaloul, and K. Hammerer, *Accurate and efficient Bloch-oscillation-enhanced atom interferometry*, [arXiv:2306.09399](#) (2023).

J.-N. Kirsten-Siemß, F. Fitzek, C. Schubert, E. M. Rasel, N. Gaaloul, and K. Hammerer, *Large-Momentum-Transfer Atom Interferometers with μ rad-Accuracy Using Bragg Diffraction*, *Phys. Rev. Lett.* **131**, 033602 (2023).

P. Boegel, M. Meister, **J.-N. Siemß**, N. Gaaloul, M. A. Efremov, and W. P. Schleich, *Diffractional focusing of a uniform Bose–Einstein condensate*, *J. Phys. B, At. Mol. Opt. Phys.* **54** 185301 (2021).

M. Gebbe, **J.-N. Siemß**, et al., *Twin-lattice atom interferometry*, *Nature Communications*, **12**(1):2544 (2021).

T. Hensel, S. Loriani, C. Schubert, F. Fitzek, S. Abend, H. Ahlers, **J.-N. Siemß**, K. Hammerer, E. M. Rasel, and N. Gaaloul, *A comparative performance study of condensed versus thermal sources for atom interferometry*, *The European Physical Journal D*, **75**(3):108 (2021).

F. Fitzek, **J.-N. Siemß**, S. Seckmeyer, H. Ahlers, E. M. Rasel, K. Hammerer, and N. Gaaloul, *Universal atom interferometer simulation of elastic scattering processes*, *Scientific Reports*, **10**(1):22120 (2020).

B. Canuel, et al., *ELGAR—a European Laboratory for Gravitation and Atom-interferometric Research*, *Classical and Quantum Gravity*, **37**(22):225017 (2020).

J.-N. Siemß, F. Fitzek, S. Abend, E. M. Rasel, N. Gaaloul, and K. Hammerer, *Analytic theory for Bragg atom interferometry based on the adiabatic theorem*, *Phys. Rev. A*, **102**(3):033709 (2020).

B. Canuel, et al., *Technologies for the ELGAR large scale atom interferometer array*, [arXiv:2007.04014](#) (2020). [arXiv:2007.04014](#) (2020).